



TECHNISCHE  
UNIVERSITÄT  
WIEN

Vienna University of Technology

# Application of microfluidic devices for time resolved FTIR spectroscopy

A thesis submitted for the degree of

**Doctor of Technology**

at the

Vienna University of Technology

Faculty of Technical Chemistry

Institute of Chemical Technologies and Analytics

under the supervision of

**a.o. Prof. DI Dr. Bernhard Lendl**

defended by

**Christoph Karl Wagner**

**Matrikelnummer: 0025964**

**Dammstraße 21/46**

**A-1200 Vienna**

Vienna, August 2012



for my parents and my fiancée Wilhelmine

*"I am a firm believer that without speculation there is no good and original observation."*

CHARLES DARWIN





# Deutsche Kurzfassung

Im Rahmen dieser Arbeit wurden mikrofluidische Mischer, welche im kontinuierlichen Durchfluss betrieben wurden, zur zeitaufgelösten Untersuchung von chemischen Reaktionen in wässrigen Lösungen mit Hilfe der FTIR-Spektroskopie genutzt. Der Vorteil dieser Messtechnik liegt darin, dass sich alle chemischen Reaktionen untersuchen lassen, die durch das Mischen von zwei Reagenzien gestartet werden können. Hierbei dient der Mischkanal des mikrofluidischen Mixers auch gleichzeitig als Messkanal für die Infrarotmessungen. Die Messungen werden entlang dieses Kanals an definierten Positionen durchgeführt: Je weiter der Messpunkt ( $100 \times 100 \mu\text{m}^2$ ) vom Anfang in Richtung Ende des Kanals verschoben wird, desto weiter ist die Reaktionszeit der ablaufenden Reaktion fortgeschritten. Die erreichbare zeitliche Auflösung des Experiments hängt von zwei Faktoren ab: Erstens von der Fließgeschwindigkeit im Kanal und zweitens vom räumlichen Abstand zwischen den aufeinanderfolgenden Messpunkten. Unter Verwendung eines FTIR-Mikroskops lassen sich bei hohen Flussraten Zeitaufösungen im Submillisekunden-Bereich erreichen. Verwendet man hingegen langsame Flussraten, kann die messbare Reaktionszeit auf bis zu 1000 ms ausgedehnt werden.

Zu Beginn dieser Arbeit wurde die Mischzeit des verwendeten Mikromixers mit Hilfe einer schnellen Reaktion evaluiert und belief sich auf rund 5 ms. Zusätzlich wurde die gleichmäßige räumliche Verteilung der Flüssigkeiten im Kanal evaluiert.

Im Anschluss wurde der H/D Austausch an Zuckern, die komplexe Reaktion von Formaldehyd mit Sulfit und die Faltung des Proteins Ubiquitin, welches durch die Mischung mit angesäuertem Methanol vom natürlichen in den "A" Zustand umgewandelt wird, vermessen. Für die Reinigung des Mixers nach einem Experiment wurde ein automatisiertes Fließsystem verwendet, welches durch ein neu entwickeltes LabVIEW Programm, namens ATLAS, gesteuert wurde.

Zusätzlich dazu wurde die Mikromischer-Technologie mit der Step-Scan Messtechnik kombiniert. Hierfür wurde eine externe Fokussiereinrichtung

verwendet um das IR Licht des Spektrometers auf den Mischer zu fokussieren (Durchmesser des Messpunkts rund 1 mm). Gleichzeitig wurde ein Laser, welcher zur Anregung der Reaktion im Mischer benötigt wird, mittels eines dichroitischen Spiegels eingekoppelt und auf den Messpunkt fokussiert. Wird die Probe im Messpunkt zwischen zwei Anregungen durch den Laser durch einen kontinuierlichen Fluss im Kanal komplett ausgetauscht, so können auch nicht-zyklische Reaktion mittels der Step-Scan Technik vermessen werden.

Mittels dieses Messaufbaus wurde die Rückbindungskinetik von Kohlenstoffmonoxid an Myoglobin (Mb), nach der Photodissoziation des Mb–CO Komplexes, evaluiert und ein bi-exponentielles Verhalten sowohl für die Rückbindung als auch für die Veränderungen an der Sekundärstruktur des Proteins ermittelt. Die Vermessung des Photozyklus der Cytochrom-c-Oxidase scheiterte allerdings, da die maximal mögliche Konzentration des Proteins in Lösung zu niedrig war um bei einer Absorptionsstrecke von 10  $\mu\text{m}$  des Mischers ein messbares Signal des Proteins im Bereich der Amid Banden zu erhalten.

Als dritter Ansatz für die zeitaufgelöste Messung von Reaktionen wurden MOEMS Spektrometer evaluiert, welche eine sehr hohe Messgeschwindigkeit pro Spektrum ermöglichen. Durch den frühen Entwicklungsstand der zur Verfügung stehenden Prototypen konnte allerdings keine ausreichendes Signal/Rauschverhältnis ohne starke Mittelwertbildung erreicht werden, wodurch der Geschwindigkeitsvorteil gegenüber klassischen FTIR Spektrometern nicht genutzt werden konnte.

---

**Schlagworte:** Zeitaufgelöste FTIR-Spektroskopie · Step-Scan Spektroskopie · Mikrofluidische Mischer · MOEMS Spektrometer · Formaldehyd Sulfid Reaktion · H/D Austausch · Protein Faltung · Ubiquitin · Myoglobin · Cytochrom-c-Oxidase

# Abstract

Within this thesis, micro fluidic mixers, operated in continuous flow mode, were used for time resolved FTIR studies of chemical reactions in aqueous solution. Any chemical reaction, which can be started upon mixing two reagents, can be examined with this technique. The mixing channel also serves as the observation window for the IR measurements. The actual measurements take place at well defined spots along this channel, corresponding to specific reaction times: moving the measurement spot ( $100 \times 100 \mu\text{m}^2$ ) towards the entry yields shorter reaction times, moving it towards the channel's end gives longer reaction times. The temporal resolution of the experiment depends on the flow rate inside the mixing channel and the spacing between subsequent measurement points. Fast flow rates, limited by the back pressure of the mixer leading to leakages, allow time resolutions in the sub-millisecond time range using a standard FTIR microscope, whereas slow flow rates allow the measurement of reaction times up to 1000 ms.

Evaluating the mixer using a fast chemical reaction resulted in mixing times of approximately 5 ms and a homogeneous distribution of the liquids across the width of the mixing channel.

The mixer was then used for the measurement of the H/D exchange on carbohydrates, the complex formaldehyde sulfite clock reaction, and the folding of the protein ubiquitin from its native to the "A" state, induced by mixing it with an acidified methanol solution. For cleaning the mixer a software tool, called ATLAS, was developed in LabVIEW, which was used to automatize the necessary cleaning steps performed by a dedicated flow system.

Additionally, the micro mixer technology was combined with the step scan measurement technique using a beam condenser focusing the IR beam of an FTIR spectrometer down to a spot size of 1 mm diameter and through the mixer. The laser light, initiating the chemical reaction inside the mixing channel, was coupled into the focusing unit using a dichroic mirror. By continuously flowing sample through the measurement spot only fresh sample was excited for each measurement cycle, allowing the measurement of non-

cyclic reactions. The rebinding kinetics of carbon monoxide to myoglobin, after photo dissociation of the carbonmonoxy myoglobin complex, was successfully investigated, showing bi-exponential reaction kinetics for the rebinding of the carbon monoxide and the relaxation of the induced changes in the protein's secondary structure. Measurements of the photo cycle of cytochrome c oxidase, however, failed due to physical limitations, such as the maximum possible concentration of cytochrome c oxidase and the path length of 10  $\mu\text{m}$  needed to be able to measure the Amide I band of proteins in aqueous solution.

As a third approach to time resolved measurements, fast scanning MOEMS spectrometers were evaluated. Poor signal to noise ratios, due to the early stage of the used prototypes, forced the use of intensive signal averaging, which nullified the advantage of faster scan rates, compared to standard FTIR spectrometers.

---

**Keywords:** Time resolved FTIR spectroscopy · Step Scan spectroscopy · Micro fluidic mixers · MOEMS spectrometers · Formaldehyde sulfite clock reaction · H/D exchange · Protein folding · Ubiquitin · Myoglobin · Cytochrome c oxidase

# Acknowledgement

During the progress of this work I did not only gain invaluable knowledge and experience but also met a lot of amiable, supportive people, some of who became friends.

I want to say *thank you* ...

- ... to my supervisor *Bernhard Lendl* for giving me the opportunity to work in such an enjoyable environment beginning with a short laboratory course, which led to a stay of several years in the CAVS workgroup, his enduring support, as well as supplying all necessary resources needed for this Ph.D. thesis.
- ... to *Prof. Michael Vellekoop* from the Institute of Sensor and Actuator Systems including *Andreas Rigler* and *Wolfgang Buchegger* for designing and fabricating the mixers used in this thesis.
- ... to *Martin Kraft* from Carinthian Tech Research AG for his invaluable input on writing publications, scientific discussions and proofreading this thesis.
- ... to *Prof. Heberle* for giving me the opportunity to perform the step scan experiments at the Bielefeld University as well as at the Freie Universität Berlin.
- ... to *Michael Schleegeer* for all his knowledge on proteins and the time we spent together accomplishing the step scan experiments.
- ... to *Georg Ramer*, *Greta Lindermuth* and *Karin Wieland* contributing with their bachelor theses to this work.
- ... to the members and former members of the CAVS workgroup including *Alison Hobro*, *Andreas Genner*, *Andreas Wagner*, *Bernhard Zachhuber*, *Christoph Gasser*, *Christoph Reidl-Leuthner*, *Cosima Koch*, *Engelene Chrysostom*, *Eric González García*, *eVa Aguilera*, *Guillermo Quintas*,

*Harald Moser, Johannes Frank, Johannes Schnöller, Julia Kuligowski, Markus Brandstetter, Nina Kaun, Paul Waclawek, Sergio Armenta, Stefan Radel, Thomas Furch, Wolfgang Ritter, Wolfgang Tomischko and Verena Wessely* for all the discussions and help on scientific topics. But also for a lot of fun we had together after work or during work ...

... to *Christoph Straif* for supplying the L<sup>A</sup>T<sub>E</sub>X class files used to write this thesis.

... to all my *friends*.

... to my fiancée *Wilhelmine* for her patience and all the support during the last years.

... to, last but not least, my father *Karl Wagner*, my mother *Ursula Wagner* and my brother *Gabriel Wagner*, who always supported me.

For the financial support of this project I gratefully acknowledge *Carinthian Tech Research AG* within the *COMET Competence Center Program* of the Austrian Government.



# Contents

<b>Deutsche Kurzfassung</b>	<b>iii</b>
<b>Abstract</b>	<b>v</b>
<b>Acknowledgement</b>	<b>vii</b>
<b>Abbreviations</b>	<b>xiii</b>
<b>Symbols</b>	<b>xv</b>
<b>1 Introduction</b>	<b>1</b>
1.1 Theory of infrared spectroscopy . . . . .	3
<b>2 Instrumentation for infrared spectroscopy used in this thesis</b>	<b>7</b>
2.1 FTIR spectroscopy . . . . .	7
2.1.1 Rapid scanning – standard IR bench . . . . .	8
2.1.2 Rapid scanning – MOEMS spectrometer . . . . .	13
2.1.3 Step-scanning . . . . .	19
2.2 FTIR microscopy . . . . .	22
2.2.1 FTIR microscopy using a thermal radiation source . . .	24
<b>3 Time resolved (TR) FTIR spectroscopy of chemical reactions in aqueous phase</b>	<b>33</b>
3.1 FTIR spectroscopy of aqueous solutions . . . . .	33
3.2 General concepts of TR-FTIR spectroscopy . . . . .	36
3.3 Mixing induced TR-FTIR spectroscopy . . . . .	38
<b>4 Micro-machined mixers for TR-FTIR spectroscopy used in this thesis</b>	<b>43</b>
4.1 Two fluid layer "old" micro-mixer design . . . . .	44
4.2 Four fluid layer "new" micro-mixer design . . . . .	45
4.2.1 Design and fabrication . . . . .	46
4.2.2 Mixer support holder . . . . .	49
4.2.3 Experimental characterization . . . . .	50
4.2.4 Encountered difficulties in mixer life-time . . . . .	57

---

<b>5</b>	<b>Advanced Total Lab Automation System (ATLAS)</b>	<b>59</b>
5.1	All-In-One program . . . . .	62
5.2	Master / Client system . . . . .	63
5.2.1	The master . . . . .	64
5.2.2	The clients . . . . .	66
5.2.3	Communication principle . . . . .	67
5.2.4	Two Example Clients . . . . .	69
<b>6</b>	<b>Evaluation of MOEMS spectrometers</b>	<b>75</b>
6.1	Grating spectrometer . . . . .	75
6.1.1	Determination of CO <sub>2</sub> in aqueous solution . . . . .	75
6.2	FTIR spectrometer . . . . .	77
6.2.1	Determination of CO <sub>2</sub> in aqueous solution . . . . .	77
<b>7</b>	<b>Step-scan TR-FTIR spectroscopy in a micro-fluidic system</b>	<b>81</b>
7.1	Experimental setup . . . . .	82
7.1.1	Optical setup . . . . .	82
7.1.2	Data acquisition . . . . .	83
7.2	Measurements on myoglobin . . . . .	84
7.2.1	Sample preparation . . . . .	84
7.2.2	Measurements . . . . .	86
7.3	Measurements on cytochrome c oxidase . . . . .	90
7.3.1	Sample preparation . . . . .	93
7.3.2	Measurements . . . . .	94
<b>8</b>	<b>Rapid scan TR-FTIR spectroscopy in a micro-fluidic system</b>	<b>97</b>
8.1	Experimental set-up . . . . .	97
8.2	Formaldehyde sulfite clock reaction . . . . .	98
8.3	H/D exchange on carbohydrates . . . . .	103
8.4	Protein folding reactions . . . . .	108
<b>9</b>	<b>Conclusion &amp; Outlook</b>	<b>113</b>
	<b>Bibliography</b>	<b>115</b>



---

<b>A</b>	<b>Published scientific papers</b>	<b>127</b>
	Publication I . . . . .	127
	Publication II . . . . .	139
	Publication III . . . . .	147
	Publication IV . . . . .	157
	Publication V . . . . .	177
	Publication VI . . . . .	183
	Publication VII . . . . .	195
	Publication VIII . . . . .	207
<b>B</b>	<b>List of available clients for ATLAS</b>	<b>221</b>
<b>C</b>	<b>Curriculum Vitae</b>	<b>225</b>



# Abbreviations

ADC	Analog Digital Converter
ATLAS	Advanced Total Lab Automation System
ATP	Adenosine TriPhosphate
ATR	Attenuated Total Reflection
CAVS	Chemical Analysis and Vibrational Spectroscopy
CE	Capillary Electrophoreses
CFD	Computational Fluid Dynamics
DTGS	Deuterated TriGlycine Sulfate
FPA	Focal Plane Array
FTIR	Fourier Transform InfraRed
GUI	Graphical User Interface
IR	InfraRed
MCT	Mercury Cadmium Telluride
MOEMS	Micro Opto Electro Mechanical System
NA	Numerical Aperture
NI	National Instruments
NIR	Near InfraRed
OPO	Optical Parametric Oscillator
PDMS	PolyDiMethylSiloxane
PEEK	PolyEtherEtherKetone
PP	Peak to Peak

RMS	Root Mean Square
S/N	Signal to Noise
TCP/IP	Transmission Control Protocol / Internet Protocol
TR-FTIR	Time resolved Fourier Transform InfraRed
TTL	Transistor Transistor Logic
UV	Ultra Violet
VI	Virtual Instrument

# Symbols

$\rho$	.....	Density [kg/m <sup>3</sup> ]
D	.....	Diffusion coefficient [m <sup>2</sup> /s]
$\eta$	.....	Dynamic Viscosity [Pa s], [kg/m s]
E	.....	Energy [J]
$\nu$	.....	Frequency [s <sup>-1</sup> ]
$d_h$	.....	Hydraulic Diameter [m]
k	.....	Imaginary Refractive Index
h	.....	Planck constant ( $6.62606957 \times 10^{-34}$ J s)
n	.....	Real Refractive Index
c	.....	Speed of light (299792458 m s <sup>-1</sup> )
t	.....	Time [s]
$v$	.....	Velocity [m/s]
$\lambda$	.....	Wavelength [nm]
$\tilde{\nu}$	.....	Wavenumber [cm <sup>-1</sup> ]



# Introduction

---

Mid InfraRed (IR) spectroscopy is a well recognized technique in modern analytical chemistry since mid IR spectra directly give access to *structural information* of the sample molecule. Each molecule has its characteristic *fingerprint spectrum* and can thereby be identified easily. Due to its simple measurement technique IR spectroscopy has found its way into industry for routine analysis. However if it comes to Time Resolved Fourier Transform InfraRed (TR-FTIR) spectroscopy, instrumentation becomes more challenging and measurements are limited by a number of factors.

Over the past years the technique of TR-FTIR spectroscopy applying micro fluidic devices was steadily improved in the Chemical Analysis and Vibrational Spectroscopy (CAVS) workgroup of Prof. Lendl, beginning with Peter Hinsmann [1], who developed a micro mixer, which was used in stopped flow mode in 2002. His successor Nina Kaun [2] developed a continuous flow micro mixer together with Michael Harasek from the Institute of Chemical Engineering in 2006, improving the mixing time and therefore its applicability to faster chemical reactions. Peter Hinsmann's original design generated a sequence of 50 alternating 20  $\mu\text{m}$  thick fluid layers from two inlets, resulting in a mixing time of 200 ms. A later design sandwiched two 10  $\mu\text{m}$  thick fluid layers horizontally improving the mixing time to 100 ms. Nina Kaun further improved this design by reducing the layer thickness to 5  $\mu\text{m}$  and hence reducing the mixing time down to 45 ms.

The scope of this work was to tie in with this enhancements and to further improve the micro mixer and its handling. These improvements were achieved in cooperation with Prof. Vellekoop's work group at the Institute of Sensor and Actuator Systems of the Vienna University of Technology.

Beyond improving the mixer also other ways to conduct TR-FTIR measurements were evaluated. This includes the application of Micro Opto Electro Mechanical System (MOEMS) spectrometers. Using a MOEMS spectrometer allows the reduction of the mirror weight and therefore faster mirror movements resulting in faster scanning speeds compared to standard bench-top spectrometers. To further increase the time resolution a technique called *step-scan spectroscopy* can be employed. This technique is normally limited to *cyclic reactions* only since the chemical system under investigation needs to be measurement thousands of times to generate a whole spectral data set.

In this work we combined step-scan spectroscopy with micro mixers widening the applicability of the step-scan technique to *non-cyclic systems*. This enables time-resolved experiments where two chemicals need rapid mixing before starting the actual reaction by an external trigger, which is a standard experiment in UV/VIS spectroscopy called flow-flash experiment. However, in IR spectroscopy of aqueous solutions, where path lengths are limited by the strong absorption of water, such an experiment underlies various limitations. Usually those UV/VIS *flow-flash experiments* are conducted in a *stopped-flow manner*. The reagents are mixed rapidly in a turbulent mixer, pumped into the measurement cell, where the reaction is started by an external trigger, such as a laser flash, and measured afterwards. In IR spectroscopy, however, a stopped-flow experiment in aqueous solution can't be achieved easily since path lengths below 10  $\mu\text{m}$  are needed for transmission measurements with standard bench-top Fourier Transform InfraRed (FTIR) spectrometers. In such dimensions high pressures are needed to pump solutions through flow cells and stopping the liquid abruptly before excitation becomes difficult. To overcome this limitation a micro mixer in *continuous flow mode* was used in such a way that fresh sample is provided in the measurement spot before the excitation triggers the measurement and only 10 percent of the excited sample is exchanged during data recording.



## 1.1 Theory of infrared spectroscopy

In IR spectroscopy the physical phenomenon of absorption of light in the infrared region of the electromagnetic spectrum by a target molecule is used to gain information on its structural properties. By this the target molecule gets excited to *vibrational* / *rotational states* and the transferred energy contains information on functional groups, intra- and intermolecular interactions.

Light or radiation in general is characterized by its *energy* ( $E$  given in equation 1.1 with  $h$  being the Planck constant and  $\nu$  the light frequency). More commonly, however, scientists use *wavelength* ( $\lambda$ , equation 1.2,  $c$  denotes the speed of light) to specify the energy of radiation. More particularly, scientists working in the field of IR spectroscopy prefer *wavenumber* ( $\tilde{\nu}$ , equation 1.3) over wavelength, which is directly proportional to the light frequency ( $\nu$ ).

$$E = h \cdot \nu \quad (1.1)$$

$$\lambda = \frac{c}{\nu} \quad (1.2)$$

$$\tilde{\nu} = \frac{1}{\lambda} \quad (1.3)$$

The IR region is split into different sections (table 1.1) according to different modes excited by IR radiation. The region with the most prominent bands is the mid-IR region where typical stretching and bending modes are excited. Using higher energies results in the excitation of combination vibrations and overtones of mid-IR vibrations giving broader bands in the near-IR region. Irradiation of the sample with light of the wavelength longer than 100  $\mu\text{m}$  mainly results in skeletal, intermolecular vibrations as well as pure rotations in gases.

Those IR bands are the result of an energy uptake of the molecule and an accompanying transition between quantized vibrational energy states  $V_{iv}$ . This energy states can be described by the model of an *harmonic oscillator* in equation 1.4.

**Table 1.1:** *Classification of the IR spectral region*

	Region	
	Wavenumber ( $\tilde{\nu}$ )	Wavelength ( $\lambda$ )
Near IR	12500 – 4000 $\text{cm}^{-1}$	0.8 – 2.5 $\mu\text{m}$
Mid IR	4000 – 400 $\text{cm}^{-1}$	2.5 – 25 $\mu\text{m}$
Far IR	400 – 1 $\text{cm}^{-1}$	25 – 10000 $\mu\text{m}$
THz region	100 – 1 $\text{cm}^{-1}$	100 – 10000 $\mu\text{m}$

$$V_{iv} = h \cdot \nu_i \cdot \left( v_i + \frac{1}{2} \right) \quad (1.4)$$

$V_{iv}$  denotes the vibrational energy states,  $\nu_i$  the fundamental energy of a specific vibration and  $v_i$  the vibrational quantum number of that vibration ( $v_i = 0, 1, 2, \dots$ ). This harmonic model is only approximately valid for low vibrational quantum numbers. For larger quantum numbers the model of the *anharmonic oscillator*, equation 1.5, has to be used, which takes the dissociation of molecules into account.

$$V_{iv} = h \cdot \nu_i \cdot \left( v_i + \frac{1}{2} \right) + h \cdot \nu_i \cdot x_i \left( v_i + \frac{1}{2} \right)^2 \quad (1.5)$$

$x_i$  is the *anharmonicity constant*, a dimensionless number typically ranging from -0.001 to -0.02. This anharmonic model not only allows for vibrational modes ( $v_i \pm 1$ ) but also combination vibrations ( $\Delta v_i = 1$  and  $\Delta v_j = 1$  with  $j$  representing a second vibrational mode) and overtones ( $\Delta v_i = 2, 3, \dots$ ) as mainly observed in the Near InfraRed (NIR) region.

The number of possible vibrational modes can be derived from the number of atoms in a molecule as follows: For every atom ( $N$ ) the molecule has three degrees of freedom ( $3 \cdot N$ ). Of those degrees three represent the translational motion along the three axis (x,y,z) and three the rotational motion about the three axis giving a total number of degrees of freedom of  $3 \cdot N - 6$ . In a linear molecule the rotation about the axis of the molecule doesn't displace any of the atoms causing such a molecule to loose only two degrees of freedom and

therefore has  $3 \cdot N - 5$  vibrational modes. For a diatomic molecule such as HCl this gives only one possible vibration.

However, the IR spectrum of HCl in the gas phase contains various bands due to *rotational states*. Those bands arise from the fact that the rotations of molecules are quantized like vibrational modes and the *rotational quantum number*,  $J$  also has to change by  $\pm 1$  upon absorption of light. A pure vibrational transition ( $\Delta v_i = 1, J = 0$ ) is therefore forbidden resulting in a gap of the gas phase spectrum of HCl at the energy level of the vibrational transition. In liquid phase spectra those fine structures can't be observed because collisions of molecules, hence energy transfer between them, occur at a greater rate than the rotational frequency [3].

The optical behaviour of a material is described by its complex refractive index

$$\tilde{n}(\tilde{\nu}) = n(\tilde{\nu}) + ik(\tilde{\nu}) \quad (1.6)$$

where  $n$  is the real and  $k$  is the imaginary part. The imaginary refractive index  $k$  – often called absorption index – describes the absorption of light whereas the real refractive index  $n$  is the ratio of the velocity of light in vacuum to the velocity of light in the described material where no absorption is taking place ( $k = 0$ ) [4]. Figure 1.1 shows both the real and imaginary refractive indices of water in the mid-IR range. The imaginary refractive index rises at wavenumbers where absorption of light takes place. The real refractive index, however, increases gently approaching an absorption band from lower wavenumbers sharply decreasing right before the maximum of  $k$  and starting to gently rise again after passing the maximum. This phenomenon is called *anomalous* dispersion. Normal dispersion, on the other hand, describes the steady increase of  $n$  with increasing wavenumbers in regions of absorption.

From the Maxwell's equation of electromagnetism formula 1.7 can be derived [4], calculating the attenuation of light of the intensity  $I$  after travelling the distance  $l$  through an absorbing medium.

$$I = I_0 \cdot e^{-4\pi\tilde{\nu}kl} \quad (1.7)$$

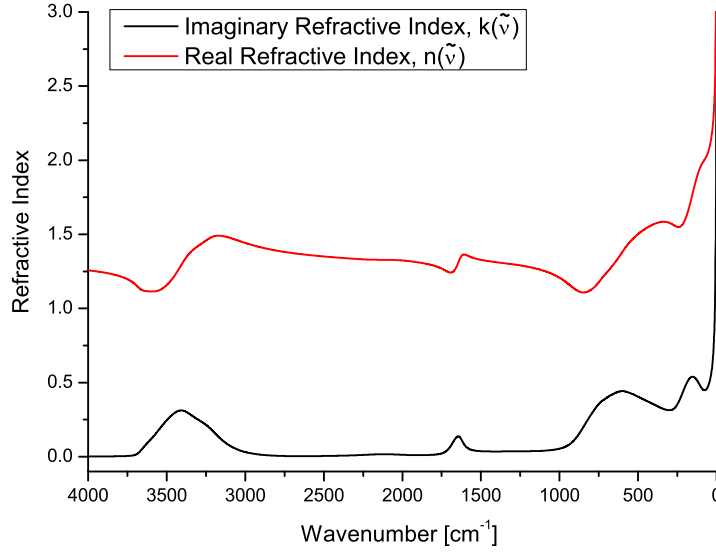


**Figure 1.1:** Real and imaginary refractive indices of water over the far and mid-IR spectral region. [5]

$I_0$  denotes the intensity of the incident light beam and the absorption of the material is characterized by the imaginary refractive index  $k$  of the absorbing material. Replacing  $4\pi\tilde{\nu}k$  by the linear absorption coefficient  $\alpha$  the absorption of a medium can be written as

$$A(\tilde{\nu}) = -\ln \frac{I(\tilde{\nu})}{I_0(\tilde{\nu})} = \alpha \cdot l \quad (1.8)$$

Replacing  $\alpha$  with the decadic molar absorption coefficient

$$k_c = \frac{\alpha}{\ln(10)c} \quad (1.9)$$

introduces the concentration ( $c$ ) dependence giving the Lambert Beer law:

$$A(\tilde{\nu}) = -\log \frac{I(\tilde{\nu})}{I_0(\tilde{\nu})} = k_c(\tilde{\nu}) \cdot c \cdot l \quad (1.10)$$

$k_c$  only accounts for *absorption effects* of the material and not for potential losses due to reflections at the measurement cell windows or absorptions of the cell window material.

# Instrumentation for infrared spectroscopy used in this thesis

---

## 2.1 FTIR spectroscopy

The measurement of  $I$  and  $I_0$  in dependence of the wavenumber to be used in formula 1.10 is achieved by the use of a spectrometer. First of all the sample cell without the analyt is measured to obtain  $I_0$  and afterwards the sample of interest ( $I$ ) is measured. In the simplest way a dispersive element, such as gratings or prisms, disperses the light, passing the sample. By turning this element all wavenumbers are scanned over the detector element giving the intensity spectrum or *single channel spectrum* of the sample. However, since this technique is time consuming in modern laboratories *Fourier transform infrared spectrometers* are used instead. These instruments have three advantages over dispersive spectrometers:

1. The *Fellgett's advantage* or *multiplex advantage* describes the fact that all wavenumbers are measured simultaneously in an FTIR spectrometer. Therefore the Signal to Noise (S/N) ratio of a spectrum recorded in the same time on an FTIR spectrometer exceeds the S/N ratio of the same spectrum measured on a grating spectrometer by a factor of  $\sqrt{N}$  with  $N$  spectral resolution elements.
2. The *Jacquinot's advantage* or *throughput advantage* describes that the optical throughput of an FTIR spectrometer is superior to that of dispersive instruments. A dispersive spectrometer has to use a slit to define the spectral resolution and therefore the optical throughput is getting

reduced for higher spectral resolutions, while for the FTIR spectrometer the optical path difference (details in chapter 2.1.1) is increased, which doesn't affect the optical throughput.

3. The *Connes' advantage* or *calibration advantage* describes the fact that a FTIR spectrometer uses the interferogram of a HeNe laser for reading the position of the movable mirror. In addition this interferogram is used as an internal wavenumber standard for higher wavenumber accuracy compared to dispersive spectrometers.

Combining the Fellgett's and Jaquinot's advantage a FTIR spectrometer is *2000 times more sensitive* than a dispersive spectrometer [6, p.173]. The Connes' advantage additionally enables the improvement of the S/N ratio by a factor of  $\sqrt{N}$  by co-adding  $N$  spectra.

### 2.1.1 Rapid scanning – standard IR bench

Peter Griffiths defines a *Rapid Scanning Interferometer* as an interferometer that translates the moving mirror at a constant velocity faster than  $0.1 \text{ cm} \cdot \text{s}^{-1}$  [6, p.20] including all up-to-date commercially available spectrometers.

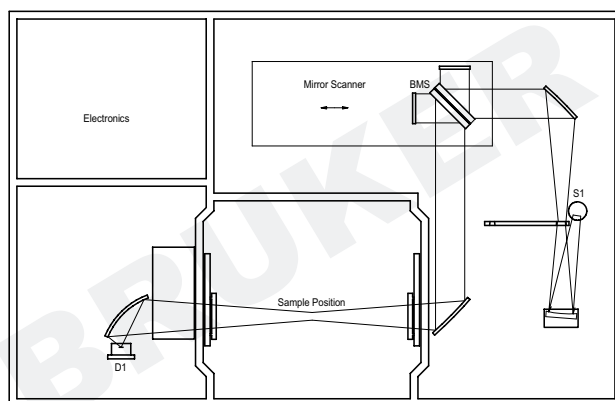


**Figure 2.1:** Layout of a Bruker IFS66 spectrometer. The light travels from the source ( $S1$ ) through an aperture into the interferometer. After the beamsplitter ( $BMS$ ) the light is focused through the sample onto the detector ( $D1$ ).

Figure 2.1 shows the layout of a classic FTIR spectrometer with a Michelson type interferometer. The light source (S1) used for the mid-IR spectral region is a rod made of *silicon carbide*, which is electrically heated to temperatures of 1200 – 1500 K. The radiation emitted by such a *blackbody* is characterized by Planck’s law giving its *spectral energy density* [6, p.161]:

$$U_{\tilde{\nu}}(T) = \frac{C_1 \cdot \tilde{\nu}^3}{e^{(C_2 \cdot \tilde{\nu})/T} - 1} \quad (2.1)$$

with  $C_1$  and  $C_2$  being the first and second radiation constants:  $C_1 = 2 \cdot h \cdot c^2 = 1.191 \times 10^{-12} \text{ W} \cdot \text{cm}^{-2} \cdot \text{sr}(\text{cm}^{-1})$ ,  $C_2 = \frac{h \cdot c}{k} = 1.439 \text{ K} \cdot \text{cm}$  with  $k$  being the Boltzmann constant.

After passing the interferometer, which will be described in detail later in this chapter, and being absorbed by the sample according to equation 1.7 the remaining intensity is detected. Two types of detectors are used throughout IR spectroscopy. The Deuterated TriGlycine Sulfate (DTGS) detector is a thermal detector directly responding to the *incident radiation power* of the light. On the other hand Mercury Cadmium Telluride (MCT) detectors are used giving a signal proportional to the number of photons hitting the detector element. Due to the low energy of mid-IR photons MCT detectors have to be operated at low temperatures – often cooled by liquid nitrogen – to reduce the thermal agitation of the detector element. Cooling also reduces noise originating from the readout circuitry.

In terms of *specific detectivity*  $D^*$  – usually used to compare IR detectors – MCT detectors are 10 to 50 times more sensitive than DTGS detectors [6, p.149] also allowing for faster response times at the cost of a narrower detection range.

$$D^* = \frac{\sqrt{A_D}}{NEP} \quad (2.2)$$

with  $NEP$  being the noise equivalent power, which can be calculated by dividing the Root Mean Square (RMS) noise voltage of the detector (in  $\text{V} \cdot \sqrt{\text{Hz}}$ ) by the voltage responsivity of the detector (in  $\text{V} \cdot \text{W}^{-1}$ ).  $A_D$  denotes the area of the detector element [6, p.161].

The centrepiece of an FTIR *spectrometer*, however, is its *interferometer*, which was invented by Albert Michelson in 1891. An interferometer, as drafted

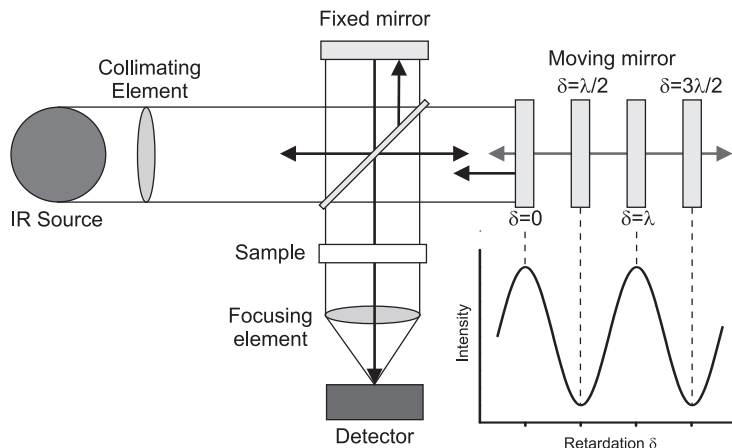


**Figure 2.2:** Schematic of a Michelson Interferometer with its main components. In the lower right corner an interferogram for a monochromatic light source is plotted with the according mirror positions for constructive and destructive interferences.

in figure 2.2, splits a collimated beam of light into two halves by reflecting one part towards a *fixed mirror* and transmitting the second part towards a *movable mirror*. After being reflected by the mirrors the two halves are recombined at the beamsplitter and directed through the sample to the detector. At the *zero path difference*, where both mirrors are located equidistantly from the *beamsplitter*, *constructive interference* occurs and all light is transmitted towards the detector. Is the movable mirror displaced by  $\frac{1}{4}\lambda$ , leading to an optical path difference of  $\delta = \frac{1}{2}\lambda$ , the two beams are out of phase (phase change  $180^\circ$ ) and *destructive interference* occurs. At that point all light is returning to the source.

Moving the mirror at *constant velocity* leads to a *sinusoidal modulation* of the light for a monochromatic light source. The detector records the temporal intensity changes, called *interferogram*, in dependence of the position of the moving mirror position. For a poly chromatic light source the measured interferogram is a combination of all interferograms, which exhibits very high intensity – called *centerburst* – at the zero path difference where all wavelengths interfere constructively. The frequency of the sinusoidal wave for a single wavelength is called *Fourier frequency*  $f_{\nu}$  and can be calculated according to formula 2.3. The interference of the light of an HeNe laser at



632 nm, coupled into the interferometer in addition to the IR radiation, is used to monitor the position of the moving mirror by counting the *zero crossings* of the HeNe laser interferogram.

$$f_{\tilde{\nu}} = 2 \cdot V \cdot \tilde{\nu} \quad (2.3)$$

$V$  denotes the speed of the moving mirror in  $\text{cm} \cdot \text{s}^{-1}$ .

The spectral resolution<sup>1</sup> that can be achieved by an interferometer is another important criterion for a spectrometer. It is indirectly proportional to the optical path difference generated by the moving mirror:

$$\Delta\tilde{\nu} = \delta^{-1} \quad (2.4)$$

Measuring one spectrum therefore means moving the mirror from the centerburst position to the maximum necessary optical path difference for the chosen spectral resolution. Using the *double sided forward backward acquisition mode* of the FTIR spectrometer yields *four spectra* in one complete mirror movement.

As can be seen from the description above the *temporal resolution* in a dynamic experiment, such as recording the kinetics of chemical reactions, with a *rapid scanning* FTIR spectrometer strongly depends on the maximum speed the interferometer can move its mirror as well as the lowest, still tolerable, spectral resolution. Additionally the digitization of the signal has to be considered and the *Nyquist theorem* has to be obeyed, stating that a signal has to be digitized with at least twice the frequency of the highest frequency of the signal. This also implies that the sampling frequency of the digitization electronics has to be high enough to suffice the Nyquist theorem. Assuming that the highest wavenumber reaching the detector is  $\tilde{\nu}_{max}$  the electronics of the detector has to sample at a rate of  $2 \cdot V \cdot \tilde{\nu}_{max}$ . If the maximum sampling rate of the detector is lower than this limit aliasing artefacts can occur in the spectra. These can be avoided by lowering  $\tilde{\nu}_{max}$  using optical filters.

---

<sup>1</sup>The spectral resolution gives the spacing between two absorption lines in a spectrum that can still be resolved by the spectrometer.

However, the effective time resolution that can be achieved by a rapid scanning spectrometer is limited by its *duty cycle efficiency*. The moving mirror has to be accelerated to the constant scan speed and decelerated after the necessary retardation of the mirror is reached for a certain spectral resolution. After the mirror has halted it has to be accelerated again in the other direction, reducing the active scan time dramatically:

$$\text{duty cycle efficiency} = \frac{\text{data acquisition time}}{\text{time between start of scans}} \quad (2.5)$$

The time needed for stopping and accelerating the mirror depends on the maximum force that can be generated by the voice-coil of the interferometer. C. Manning showed that measuring a spectrum with  $4 \text{ cm}^{-1}$  spectral resolution within 1 ms at a mirror weight of 30 g would need a force of 375 N [7]. For a conventional system this force is in the range of 1 – 2 N with mirror masses of 5 – 500 g [6, p.98] and therefore limiting the scan speed of the interferometer. For the high-end Bruker Vertex 80V spectrometer a maximum scan speed of 320 kHz can be achieved. Usually the speed of the moving mirror is given as the Fourier frequency ( $f_{\nu}$ ) of the HeNe laser interferogram. Calculating the effective speed of the mirror can be achieved by inserting the wavenumber of the HeNe laser<sup>2</sup> and calculating the optical velocity ( $V$ ) using formula 2.3. The speed of the moving mirror is then half the optical velocity. For the case of the Bruker Vertex 80V spectrometer this gives a maximum speed of the moving mirror of  $10.13 \text{ cm} \cdot \text{s}^{-1}$ .

In figure 2.3 the scans per second at given spectral resolutions are plotted for the Bruker Vertex 80V spectrometer<sup>3</sup> For example at a spectral resolution of  $8 \text{ cm}^{-1}$  a maximum time resolution of 12.5 ms can be achieved. Dividing the distance moved by the mirror<sup>4</sup> needed for a spectral resolution of  $8 \text{ cm}^{-1}$  from formula 2.4 and dividing it by the maximum mirror speed gives the *active scan time* of the instrument. According to formula 2.5 the Bruker Vertex 80V reaches a *duty cycle efficiency* of 49.4 % at a spectral resolution of  $8 \text{ cm}^{-1}$ .

<sup>2</sup>The HeNe laser emits light at 632.8 nm corresponding to  $15800 \text{ cm}^{-1}$

<sup>3</sup>Taken from the S129 "Option for Rapid Scan, Time-Resolved Spectroscopy (TRS) using a FT-IR Spectrometer of the VERTEX Series" manual.

<sup>4</sup>The way of the moving mirror is half the optical path difference.

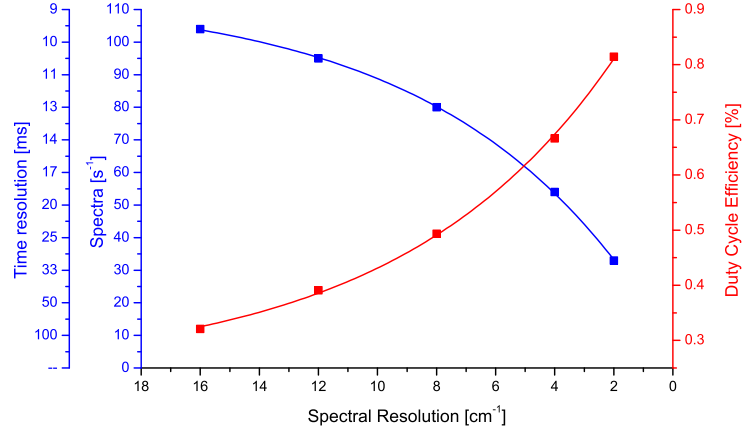


**Figure 2.3:** Number of spectra measured by the Bruker Vertex 80V spectrometer operating at a mirror speed of 320 kHz in dependence of the chosen spectral resolution plotted versus the duty cycle efficiency.

Faster time resolutions down to 1 ms were shown by replacing the moving mirror by a rotating disc [8]. In this *ultra-rapid-scanning* FTIR spectrometer the *optical path difference* is generated by a wedge shaped rotating mirror. The angle of the mirror gives the *spectral resolution*, which was chosen to be  $4 \text{ cm}^{-1}$ . Rotating the mirror at a maximum rate of 500 Hz gives two interferograms per full turn and a time resolution of 1 ms. The drawback of this design is the way to change the *spectral resolution*, which can be done by changing the rotating mirror to another angle or to move the point of incident of the light beam on the surface of the mirror closer or further away from the center.

### 2.1.2 Rapid scanning – MOEMS spectrometer

As described in chapter 2.1.1 the scan speed of a spectrometer is mainly limited by the weight of the moving mirror which has to be accelerated by the voice-coil of the interferometer. By miniaturizing the interferometer the weight of the mirror can be reduced to a minimum enabling scan times as little as 0.2 ms for one spectrum [9]. However reducing the mirror size will also reduce the possible throughput of the interferometer ( $\Theta_I$ ) as can be seen in formula 2.6 with  $A_M$  being the area of the mirror,  $\Delta\tilde{\nu}$  the spectral resolution and  $\tilde{\nu}_{max}$  the

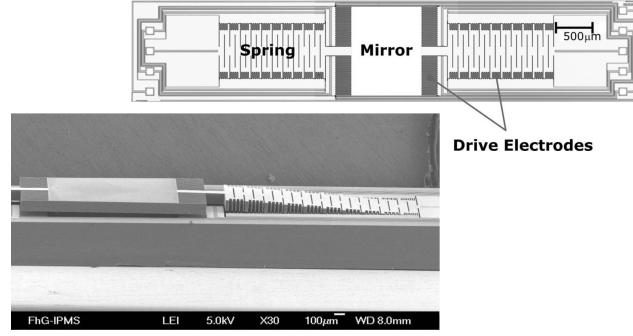


**Figure 2.4:** Layout and photograph of a 1<sup>st</sup> generation MOEMS FTIR mirror with an area of 1.65 mm<sup>2</sup> suspended at two bending springs.

maximum wavenumber of interest in the spectrum. As a consequence reducing the mirror size limits the S/N ratio that can be achieved.

$$\Theta_I = \frac{2\pi \cdot A_M \cdot \Delta\tilde{\nu}}{\tilde{\nu}_{max}} \cdot \text{sr} \quad (2.6)$$

Applying microelectronic fabrication processes, such as *lithography* or *etching steps*, those mirrors on the *micro scale* can be produced. Such devices combine micro electro mechanical aspects with micro optics and are therefore called *Micro Opto Electro Mechanical Systems* (MOEMS).

The main reason, however, to develop MOEMS type FTIR spectrometers is the possibility to produce small and reliable systems in large quantities at admissible production costs for harsh environments [10], which would lead to a higher distribution of IR spectroscopy in industrial process environments.

### 2.1.2.1 MOEMS FTIR spectrometer

The MOEMS FTIR spectrometer evaluated in this thesis utilizes a square mirror of  $1.1 \times 1.5 \text{ mm}^2$  which is suspended on two long bending springs (figure 2.4). The MOEMS mirror was designed and fabricated by the Fraunhofer Institute for Photonic Microsystems (FIPM) and integrated by Carinthian Tech Research AG into an FTIR spectrometer prototype. The prototype uses the classical Michelson interferometer design. Due to the compact mirror size and the accompanying size limitations the HeNe laser is coupled to the

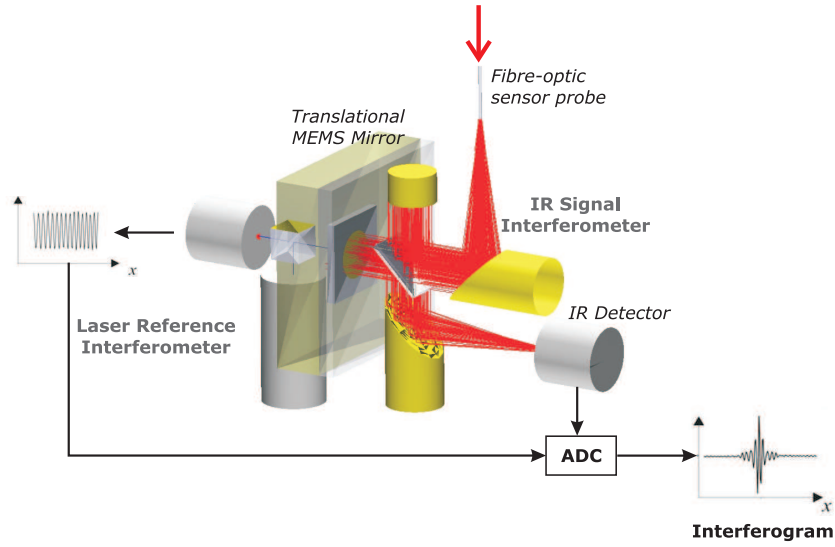


**Figure 2.5:** Schematic of the MOEMS FTIR spectrometer. The reference laser is coupled to the back side of the micro mirror to save space for the infrared beam on the front side.

backside of the MOEMS mirror. A schematic of the optical layout of the prototype is given in figure 2.5.

The mirror itself is produced by standard micromachining techniques on a 150 mm diameter SOI (silicon on insulator) wafer with a device thickness of 100  $\mu\text{m}$ . To enhance the reflectivity of the mirror it is coated with a thin layer of aluminium [10].

The movement of the mirror is electrostatically induced by a rectangular shaped voltage oscillation applied to the drive electrodes. The amplitude and frequency of the movement depends on the pressure surrounding the mirror as well as the drive voltage. The frequency of the excitation is nearly twice the mechanical resonance frequency of the mirror at a duty cycle of 50% [10].

This design is capable of a mirror movement of  $\pm 100 \mu\text{m}$  at a driving voltage of 40 V resulting in a spectral resolution of around  $50 \text{ cm}^{-1}$ . For a stable mirror movement, however, a pressure of 10 Pa has to be maintained by connecting the vacuum packaging of the mirror to a vacuum pump.

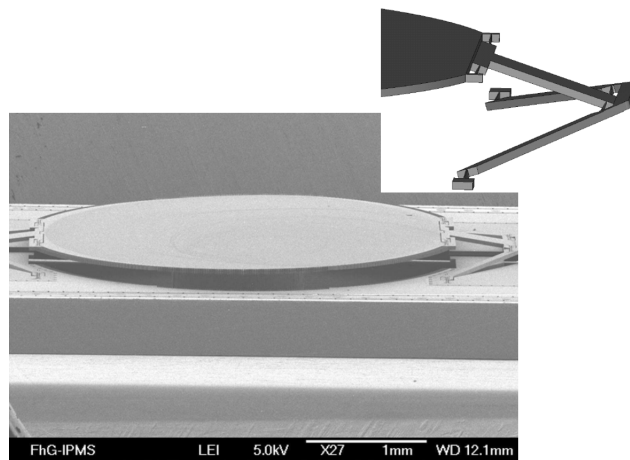


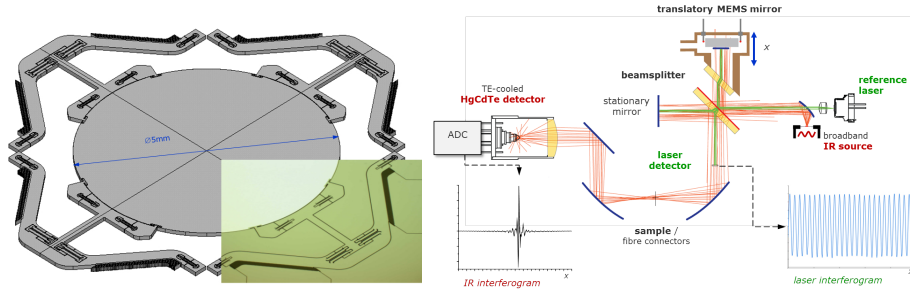
**Figure 2.6:** Photograph of a 2<sup>nd</sup> generation MOEMS FTIR mirror suspended on two pantograph-type levers.

The applicability of this first MOEMS spectrometer prototype is limited by its small mirror diameter limiting the light throughput and the poor spectral resolution that can be achieved. Additionally the mirror exhibits a dynamic mirror deformation at the turning points of between 600 nm and 900 nm [10] causing problems with the dynamic symmetry of the interferograms [11].

In this thesis a first test of the applicability of this MOEMS spectrometer was conducted by measuring CO<sub>2</sub> in aqueous solutions (see chapter 6.2).

In a latter design the mirror suspension was adopted to a *pantograph type lever* and the diameter was optimized for better light throughput at the cost of a reduced scan rate. The first pantograph type mirror had a diameter of 3 mm increasing the mirror surface by a factor of 4.3 compared to the initial design. The mirror plate was suspended on two sides of the mirror with the pantograph levers shown in figure 2.6 allowing for a larger deflection of the mirror at less dynamic deformation of the mirror plane [10]. A first prototype FTIR spectrometer utilizing this mirror was built and tested giving an *optical path difference* of 250  $\mu\text{m}$  yielding a spectral resolution of 42  $\text{cm}^{-1}$  at a resonant frequency of the mirror of 518 Hz [12].

The mirror design was further improved within the MEMFIS project of the 7<sup>th</sup> framework program of the European Union by suspending it on four pantograph springs, as can be seen from figure 2.7(a), and further increasing



(a) MOEMS FTIR mirror with four pantograph-type suspensions. (b) Optical layout of the spectrometer

**Figure 2.7:** *MOEMS FTIR spectrometer developed within the MEMFIS project with a spectral resolution of  $13 \text{ cm}^{-1}$ .*

the mirror diameter to 5 mm [13]. The implementation of the MOEMS mirror into the FTIR spectrometer, shown in figure 2.7(b), was also adopted so that the reference laser is coupled to the same side of the mirror as the IR light.

### 2.1.2.2 MOEMS grating spectrometer

Carinthian Tech Research also developed a MOEMS *grating spectrometer* for the near infrared region [14] which was adapted for the mid infrared region by changing the *diffraction angle* of the grating to  $\beta = 66.5^\circ$  enabling the measurement of dissolved  $\text{CO}_2$  in aqueous solutions to evaluate its performance, which can be found in chapter 6.1. However, the grating was optimized for the spectral region of  $1.2 - 2.5 \mu\text{m}$  resulting in grating efficiency of only 0.4 for the mid-infrared which, however, seemed sufficient for testing purposes compared to the effort needed to produce a new grating for the mid-IR region.

In such *dispersive spectrometers* the wavelength reaching the detector is chosen by the angle of the dispersive element, such as prisms, or in this case the grating. By rotating the grating different wavelengths are scanned over the detector element. For a MOEMS device, however, it is favorable to oscillate the micro-grating around its central axis instead of rotating it. The MOEMS grating, developed by the the Fraunhofer Institute for Photonic Microsystems (IPMS), used in this spectrometer achieves this oscillation by applying a pulsed

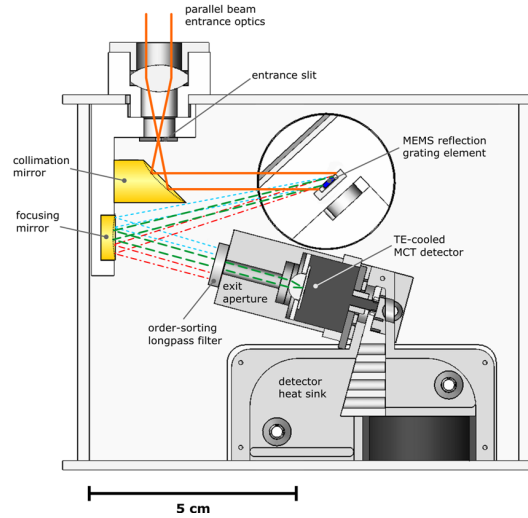


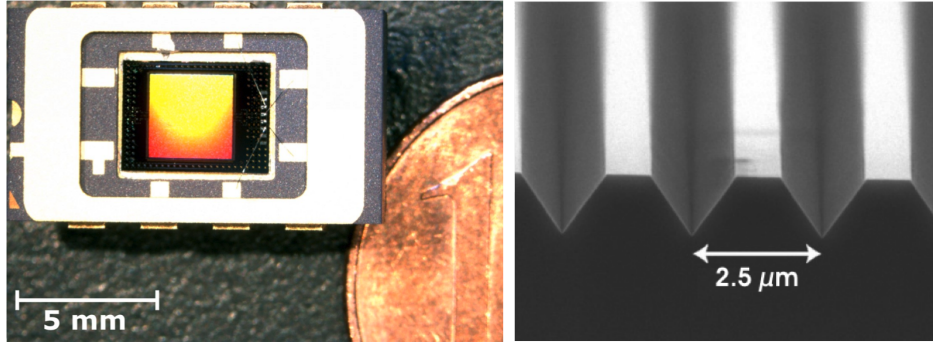
**Figure 2.8:** *Czerny-Turner monochromator layout of the MOEMS grating spectrometer with the MOEMS grating as the core element. Optimizations resulted in a refracted beam being deflected by the grating under a total angle of  $15^\circ$  from the incident beam.*

voltage to in-plane comb electrodes resulting in large deflection angles at low driving voltages [15]. The grating structure is applied to the mirror surface by anisotropic wet etching [16] and coating the grating afterwards with a thin layer of aluminum to enhance its reflectivity in the mid-IR spectral region.

The spectrometer utilizes the *Czerny-Turner monochromator* configuration [17, 18], see figure 2.8, reducing aberrations resulting from the collimating mirror. The light entering the spectrometer through a slit is collimated onto the *MOEMS grating* by an off-axis parabolic mirror with a focal length of 10 mm. The *first order diffraction* of the grating is focused by a round mirror through a order-sorting filter and the exit slit onto a thermo-electrically cooled MCT detector [19].

The MOEMS grating, shown in figure 2.9, with a size of  $3 \times 3 \text{ mm}^2$  and  $400 \text{ grooves} \cdot \text{mm}^{-1}$  is driven at a pulsed voltage of 36 V resulting in a mechanical deflection angle of  $\pm 7^\circ$ . Due to the *diffraction angle* of  $66.5^\circ$ , necessary for reaching the spectral region of the  $\text{CO}_2$  band at  $2343 \text{ cm}^{-1}$ , the effective grating aperture is reduced to  $1.2 \times 3 \text{ mm}^2$ . Oscillating at a frequency of 130 Hz the spectral range of  $2500 - 2222 \text{ cm}^{-1}$  could be scanned in 7.7 ms.





(a) Packaged MOEMS grating.

(b) 400 grooves/mm grating.

**Figure 2.9:** *MOEMS grating with a mirror area of  $3 \times 3 \text{ mm}^2$ .*

### 2.1.3 Step-scanning

In the last chapters the time resolution limitations of the classical rapid scan interferometer, which is limited by the speed of the moving mirror or in rare cases by the maximum sampling frequency of the Analog Digital Converter (ADC) board have been discussed. The half-life of the kinetic event being observed should be at least a factor of 10 longer lived than the duration of one scan. Otherwise the intensity changes on the detector due to the kinetic event will contribute heavily to interferogram points recorded at the beginning of an event and less for later interferogram points [7]. This overlap will directly transform into spectral noise and needs to be avoided.

Therefore, *decoupling the time resolution of the experiment from the mirror movement* is desirable, which is achieved by the *step-scan technique* developed by Sakai et al. [21]. Consequently, the moving mirror isn't scanning continuously but is moving step wise halting at each mirror position corresponding to an interferogram point, illustrated in figure 2.10. At each stop the temporal development of the evolving system is initiated and recorded. After all necessary interferogram points have been recorded the data set is rearranged from the temporal evolution at each point in that manner that interferograms spaced in time are obtained. From these interferograms the spectra at each time can be calculated.

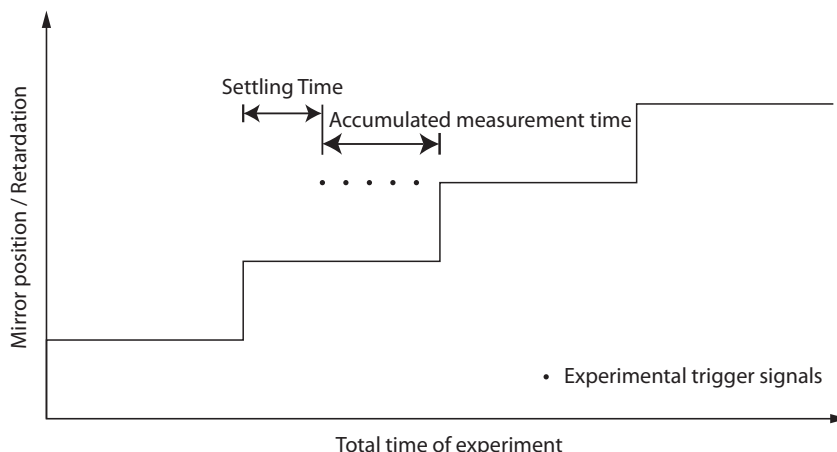


**Figure 2.10:** In a step-scan experiment the mirror is moving stepwise. After stopping at a position the mirror stabilizes during the settling time. Then the actual data recording is triggered by the experiment's master. The data acquisition is repeated until enough co-additions have been recorded for a sufficient  $S/N$  ratio. Graph based on [20].

The temporal resolution that can be achieved in a step-scan experiment only depends on the *rise time* of the detector and the *speed of digitization* of the ADC. Modern MCT detectors allow for rise times in the region of a few nanoseconds and ADC boards with band widths greater than 500 MHz are available enabling TR-FTIR measurements on the *nanosecond time scale*.

From the way the data acquisition is conducted in a step-scan experiment it is apparent that the *kinetic event* under investigation needs to be *reproduced for every time trace* that needs to be recorded. To improve the  $S/N$  ratio of the data set signal averaging will often be needed further increasing the number of repetitions of the experiment, which can lead to measurement times of several hours in the worst case. This need to precisely trigger the kinetic event certainly limits the use of the step-scan technique.

One classical biochemical system studied by step-scan spectroscopy is the membrane protein *bacteriorhodopsin* which undergoes a photocycle upon light excitation of 5 ms with defined intermediates appearing in the ps to ms time range. Since bacteriorhodopsin is a very stable protein, it can be illuminated

many thousand times making it a thoroughly studied and well understood protein often serving as a benchmark system for testing step-scan setups [22].

Rödig et al. used *bacteriorhodopsin* to systematically study potential errors and artifacts that can occur during a *step-scan measurement* [23]. They identified two main sources of noise contribution: *mirror fluctuations* and *signal fluctuations*. For their Bruker IFS 88 spectrometer, using a home built vacuum optical bench, mirror fluctuations in the region of 1.3 nm<sub>pp</sub> were observed, causing only little distortions in the recorded spectra. Commercially available step-scan spectrometers nowadays reach a RMS positional uncertainties of better than 1 nm [6, p.128]. However, it is clearly necessary to avoid any external disturbances, such as vibrations of the whole instrument, which would further disturb the mirror.

The second contribution arising from *signal fluctuations* is attributed to two effects. Triggering the chemical reaction is often done by light illumination. Using pulsed lasers, as light trigger, the fluctuations between two pulses can cause a different amount of sample to be excited, leading to different amplitudes of the recorded time trace. Saturating the excited state of the sample by choosing high enough laser powers cannot always be achieved especially if the sample is degraded by too high laser powers. On the other hand the energy of the laser gets absorbed by the sample which leads to a temperature increase. This increase also induces fluctuations in the IR signal reaching the detector.

These artefacts can be eliminated by averaging a larger number of spectra. However, this may lead to impractically long measurement times. Artefacts from fluctuating laser energies can best be compensated by additionally measuring the intensity of every laser pulse and correcting the signal accordingly. Temperature dependent changes can be measured by blocking the IR light of the spectrometer and initiating the reaction by the laser. Signal changes detected in that manner only arise from heating the sample by the laser. The obtained spectrum can now be subtracted from the IR data set eliminating the temperature induced signal fluctuations.

Developments expanding the step-scan technology to non-cyclic reactions would allow the measurement of a larger variety of bio(chemical) systems:

Using a microscope to probe only a small portion of a 15 mm diameter sample of bacteriorhodopsin, which was squeezed to a 4  $\mu\text{m}$  thick film, Rammelsberg et al. [24] were able to provide fresh sample for every step of the experiment by moving the sample stage to a fresh sample position prior to the excitation. Kauffmann et al. followed the ring-opening reaction of 1,3-cyclohexadiene using a steady flow of  $12.5 \text{ cm} \cdot \text{s}^{-1}$  using a standard IR flow cell to excite fresh sample at a rate of 10 Hz [25]. Cheng et al. also used a continuous flow device to study the release rate of caged glutamate a potential biologically active substance [26].

For step-scan measurements within this thesis a *Bruker IFS 66v/S* spectrometer was used. The whole instrument was mounted on a vibration-cushioned optical table to avoid any disturbances of the mirror. The signal was measured with an MCT detector and digitized using a 16 bit 200 kHz ADC. The optical bench was evacuated down to a residual pressure of  $< 3 \text{ mbar}$ . The typical experimental setting were a spectral resolution of  $4.5 \text{ cm}^{-1}$  at a mirror speed of 60 kHz in the single sided, fast return mode. The *Blackman-Harris-3-Term* apodization function was used with a zero-filling factor of 2 and *Mertz / No Peak Search* (phase resolution:  $32 \text{ cm}^{-1}$ ) was used for phase correction of the interferograms.

## 2.2 FTIR microscopy

FTIR microscopy, the combination of IR spectroscopy with microscopy, gets favourable as soon as the sample under investigation becomes smaller than the IR beam diameter in the sample compartment (around 12 mm) of a classical FTIR spectrometer. Focusing down the IR beam to the dimensions of the sample increases the photon throughput and therefore enhances the S/N ratio compared to the standard bench top spectrometer.

The *spatial resolution* of a microscope as well as the minimum spot size of a focused beam is limited by *diffraction*. If light passes through a circular aperture smaller than the wavelength of the incident light beam a diffraction pattern is observed. This *Airy pattern* is called after Georg Biddell Airy who depicted the phenomenon theoretically in 1835. It describes a bright central

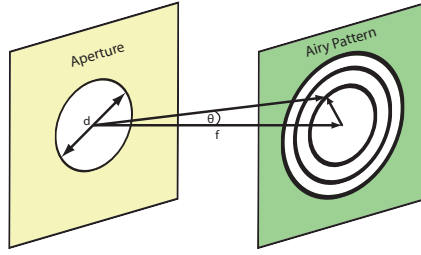


**Figure 2.11:** The diameter of the Airy disk is observed for an aperture of the diameter  $d$  at a distance  $l$  occurring under and angle  $\theta$ .

region, called Airy disk, and concentric bright rings around it with decreasing intensities called Airy pattern, shown in figure 2.11.

The angle defining the diameter of the Airy disc observed for an aperture of a diameter  $d$  depends on the wavelength of the incident light ( $\lambda$ ) and can be written as shown in formula 2.7.

$$\sin\theta = 1.22 \cdot \frac{\lambda}{d} \quad (2.7)$$

The possibility of an optical system to resolve two structures is described by the *Rayleigh criterion*: As soon as the Airy disc of the first object coincides with the first minimum of the Airy pattern of the second object the two objects can be resolved. The spatial resolution ( $\Delta l$ ) can be calculated by multiplying formula 2.7 with the distance ( $f$ ) between the aperture and the object (2.8).

$$\Delta l = 1.22 \cdot \frac{f \cdot \lambda}{d} \quad (2.8)$$

In photography the factor  $\frac{f}{d}$  is called *f-number* (N). In microscopy, however, it is more common to use the Numerical Aperture (NA) (equation 2.9) of the microscope's objective instead of the f-number.

$$NA = n \cdot \sin\gamma = n \cdot \sin\left(\arctan\frac{d}{2 \cdot f}\right) \approx n \cdot \frac{d}{2 \cdot f} \quad (2.9)$$

$\gamma$  denotes the half angle of the objective, as can be seen from figure 2.12(b). Replacing  $\frac{f}{d}$  in formula 2.8 with the NA gives equation 2.10 assuming the use in air ( $n=1$ ).

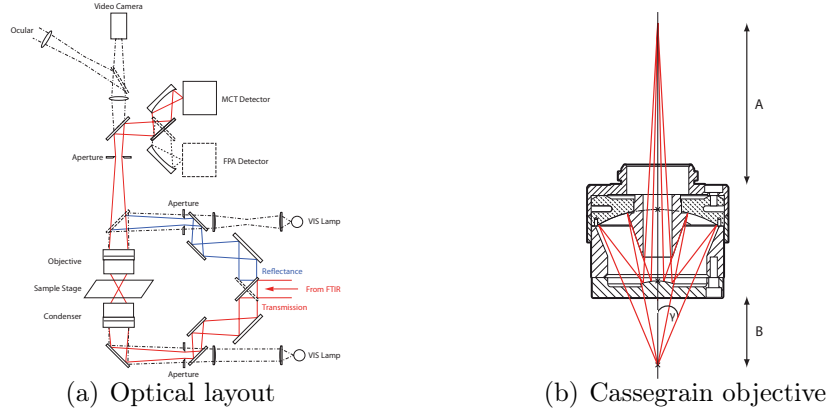


**Figure 2.12:** The Bruker Hyperion 3000 IR microscope uses two Cassegrain objectives in transmission mode to focus the IR beam through the sample onto the single point or FPA detector. The Cassegrain objectives have a back focal length of 160 mm (A) and a working distance of 24 mm (B).

$$\Delta l = \frac{0.61 \cdot \lambda}{NA} \quad (2.10)$$

In most IR microscopes the largest NA that can be achieved is around 0.6 resulting in a spatial resolution approximately in the region of the wavelength of the incident radiation ( $2.5 - 25 \mu\text{m}$  for the mid-IR region) [6, p.306]. This fundamental considerations of spatial resolution, however, are in practice often limited by the S/N ratio that can be achieved by the FTIR microscope getting worse if the aperture, shown in figure 2.12(a) right before the detectors, is reduced to increase the spatial resolution.

## 2.2.1 FTIR microscopy using a thermal radiation source

### 2.2.1.1 Single point detector

For an IR microscope with a single element detector the S/N ratio can be written as

$$S/N \text{ Ratio} = \frac{U_{\tilde{\nu}}(T) \cdot \Theta \cdot \Delta \tilde{\nu} \cdot \sqrt{t} \cdot \xi \cdot D^*}{\sqrt{A_D}} \quad (2.11)$$

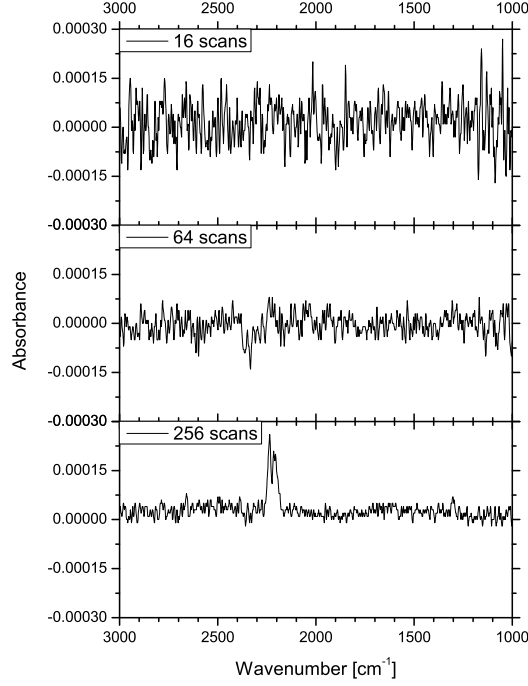


**Figure 2.13:** 100 % lines of the empty beam path attenuated by the 80 % attenuator of the Hyperion 3000 microscope measured with the single point MCT detector at a mirror velocity of 40 kHz and a spectral resolution of  $4 \text{ cm}^{-1}$ .

where  $U_{\tilde{\nu}}(T)$  is the spectral energy density of the globar, discussed in chapter 2.1.1,  $\Theta$  the throughput,  $\Delta\tilde{\nu}$  the spectral resolution of the FTIR spectrometer,  $t$  the measurement time,  $\xi$  the total optical system efficiency,  $D^*$  the specific detectivity and  $A_D$  the area of the detector.

From equation 2.11 it is obvious that the S/N ratio will be higher for larger  $D^*$  and for smaller detector sizes. It is crucial to attune the size of the detector element to the image size of the sample being projected onto the detector. For example, if a sample of  $100 \times 100 \text{ }\mu\text{m}^2$  is imaged onto a  $250 \times 250 \text{ }\mu\text{m}^2$  detector element without further magnification, only 16 % of the total area is illuminated and generating a signal from the sample. The remaining detector area is detecting background noise only. Larger detector elements, on the other hand, are beneficial for the alignment of the microscope as well as for reflection measurements. MCT detectors used in FTIR microscopes, therefore,

have often an area of  $250 \times 250 \mu\text{m}^2$  as compromise. Figure 2.13 shows the performance of the MCT detector of the Hyperion microscope.

The throughput of the instrument will in most cases be limited by the sample size and not by the spectrometer<sup>5</sup> itself [27]. The sample area interrogated by the light beam is limited by closing an aperture commonly located in the first image plane after the sample. Closing this aperture to the dimension of the incident wavelength will cause diffraction and therefore dramatically decrease the throughput.

The optical efficiency of a standard FTIR rapid scan spectrometer is normally assumed to be 0.1. For an IR microscope this factor needs to be reduced to 0.06 due to the additional mirrors needed to divert the light through the microscope [28].

### 2.2.1.2 Focal plane array detector

In contrast to a single detector element a *focal plane array (FPA) detector* comprises several detector elements arranged in a matrix of  $n \times m$  elements, each of which has its own readout circuitry. The FPA detector installed in the *Bruker Hyperion 3000* microscope used in this thesis featured  $64 \times 64$  pixel elements at a total detector size of  $2.5 \times 2.5 \text{ mm}^2$ , resulting in a detector size of a single pixel of only  $39 \times 39 \mu\text{m}^2$ .

As a consequence, the area illuminated by the optics of the microscope cannot be designed for maximum light throughput at the smallest possible focal point any more. It is rather important to evenly illuminate a larger area of the sample to guarantee a homogeneous light distribution on all the detector elements. Additionally, the optics of the microscope need to be designed very carefully reducing chromatic aberrations to a minimum.

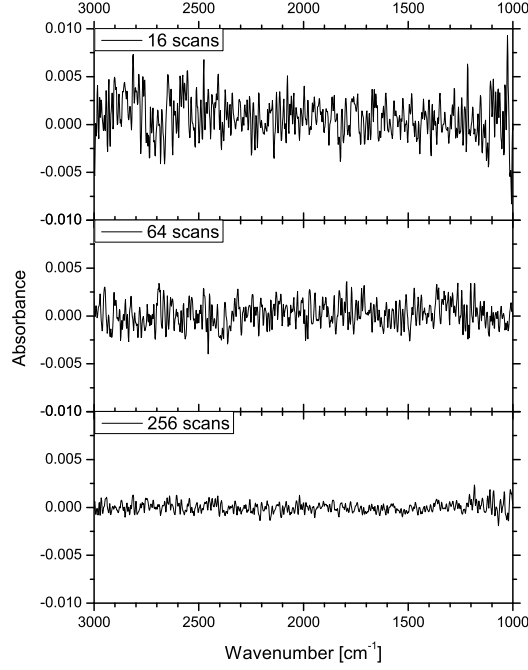
In analogy to formula 2.11, Snively and Koenig [28] state the S/N ratio of an imaging FTIR instrument as

$$S/NRatio = \frac{0.12 \cdot \pi \cdot A \cdot \left[1 - \sqrt{1 - (NA)^2}\right] \cdot U_{\tilde{\nu}}(T) \cdot \Delta\tilde{\nu} \cdot D^* \cdot \sqrt{t}}{\sqrt{A_D}} \quad (2.12)$$

---

<sup>5</sup>See [6] for throughput limiting factors of FTIR spectrometers.



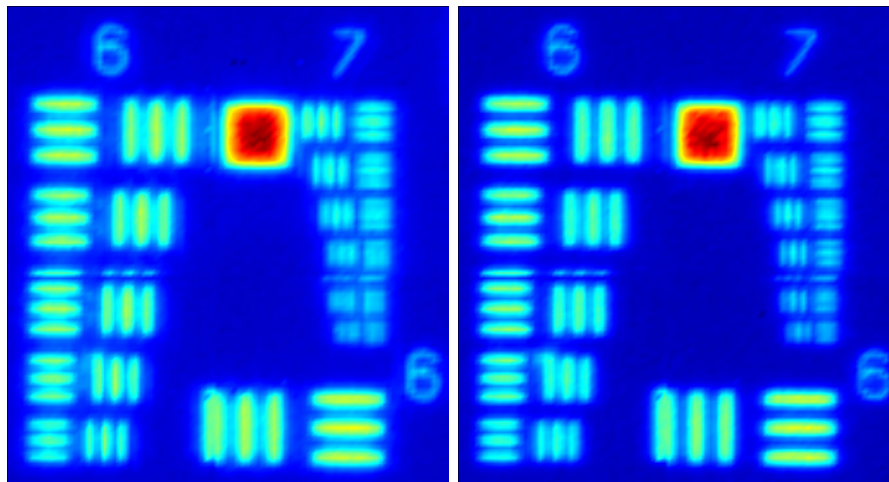


**Figure 2.14:** 100 % lines from one pixel located in the center of the  $64 \times 64$  px FPA detector of the Hyperion 3000 microscope measured at a mirror velocity of 1.6 kHz and a spectral resolution of  $4 \text{ cm}^{-1}$ . The FPA settings were an integration time of  $0.191625 \text{ } \mu\text{s}$  at Gain 1 and an offset of 255.

with  $\xi$  being set to 0.06 and taking the throughput ( $\Theta$ ) of an imaging spectrometer as

$$\Theta = 2 \cdot \pi \cdot A \cdot \left[ 1 - \sqrt{1 - (NA)^2} \right] \quad (2.13)$$

$A$  gives the sample area and  $NA$  the numerical aperture of the objective and the condenser of the microscope (see figure 2.12(a)). The reduction of size of one single detector element of the FPA array in comparison to the size of the single element detector of the Hyperion 3000 microscope should result in enhancement of the S/N ratio by a factor of  $\approx 6$ . However, comparing the 100 % lines, shown in figure 2.14, with the measurements performed with the MCT detector (figure 2.13) shows that the performance of the FPA detector is

(a) Measurement at  $2300\text{ cm}^{-1}$ (b) Measurement at  $3800\text{ cm}^{-1}$ 

**Figure 2.15:** Measurements of groups 6 and 7 of the USAF resolution target performed on the Bruker Hyperion 3000 using the FPA detector at a spectral resolution of  $4\text{ cm}^{-1}$  averaging 1024 scans. The image was recorded as a  $2 \times 2$  map and shows artifacts from incorrect stitching, which can be seen between elements 4 and 5 of group 7 for example. Blue color denotes high transmission, red color low transmission.

40 times<sup>6</sup> worse than the MCT detector, possibly caused by a lower  $D^*$  value of the FPA compared to the MCT detector.

In such an *imaging system* the *spatial resolution* isn't determined by the *spot size* of the beam, or a limiting aperture, anymore. Rather is the *spatial resolution* given by the *pixel size* of the FPA detector and the imaging optics. Using the 15 fold objectives of the *Hyperion 3000* microscope a sample area of  $175 \times 175\text{ }\mu\text{m}^2$  is projected onto the detector resulting in a *pixel resolution* of  $2.7\text{ }\mu\text{m}$  at a pixel size of the FPA of  $39 \times 39\text{ }\mu\text{m}^2$ . Hence, the area seen by one pixel of the FPA detector is smaller than the wavelength of the incident beam.

Peter Lasch and Dieter Naumann thoroughly investigated the *spatial resolution* of a Hyperion 3000 microscope equipped with 15 and 36 fold Cassegrain objectives [29] by measuring a USAF resolution target (see figure 2.15) in

<sup>6</sup>Peak to Peak Noise calculated in the range from  $2100 - 1900\text{ cm}^{-1}$  for the 256 scan lines.

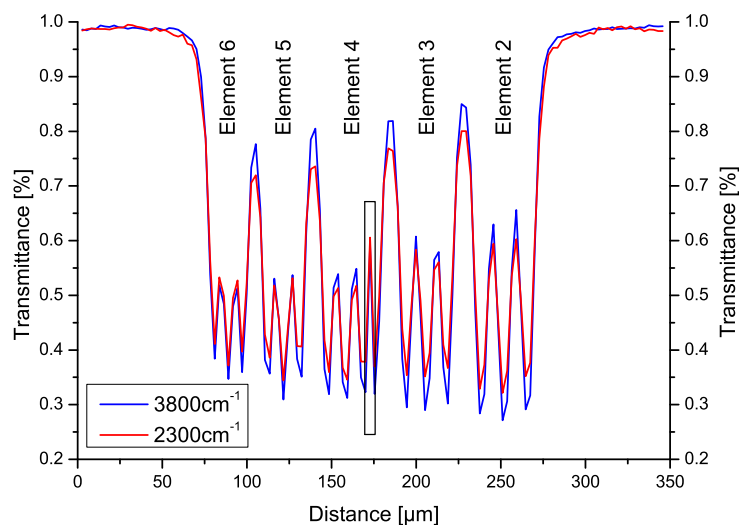
**Table 2.1:** *Number of line pairs per mm of the USAF resolution target for groups 5 to 7. The higher the group and element number the more lines are present.*

	<i>Group</i>		
<i>Element</i>	<i>5</i>	<i>6</i>	<i>7</i>
<i>1</i>	32	64	128
<i>2</i>	36	71.8	144
<i>3</i>	40.3	80.6	161
<i>4</i>	45.3	90.5	181
<i>5</i>	50.8	102	203
<i>6</i>	57	111	228

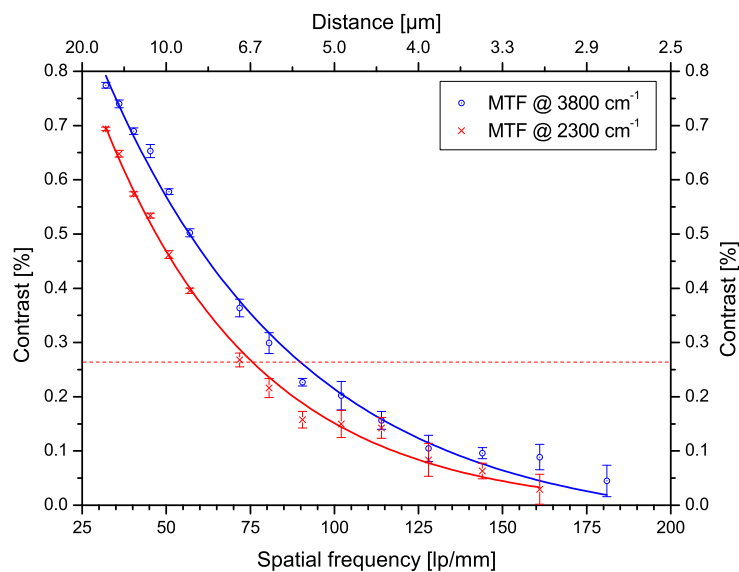
transmission mode. This USAF resolution target consists of a chromium pattern of periodically alternating bars of chromium with zero transmission and spaces with 100 % transmission on a *soda lime glass* substrate, which can unfortunately only be used for wavenumbers of  $2300\text{ cm}^{-1}$  or higher. The pattern itself is divided into several groups each featuring 6 elements of alternating bars. The width of the bars and spaces gets smaller with higher group and element number and is given as *line pairs per millimeter* ( $\text{lp} \cdot \text{mm}^{-1}$ ), also called spatial frequency. The sizes of the used elements for the analysis of the resolution of the Bruker Hyperion 3000 microscope are given in table 2.1.

Analysing the images shown in figure 2.15 it can be clearly seen that the separation of dark and bright parts in the images decreases the smaller the elements get. It can also be seen that for smaller wavelengths (or higher wavenumbers) the separation is better. This visual observation can be mathematically expressed as the contrast between dark and bright parts in the image. For a periodic pattern, with equal widths for dark and bright parts, the sum of maximum and minimum transmittance values should be equal to 100. The contrast can therefore be written as

$$C(\lambda) = \frac{T(\text{bright}) - T(\text{dark})}{100} \cdot 100\% \quad (2.14)$$



(a) Transmission distribution along a line through elements 2 to 6 of group 6. A stitching error of the FPA image is marked in black.



(b) MTF function as a result of the transmission patterns of groups 5 to 7 at  $3800\text{ cm}^{-1}$  in blue and  $2300\text{ cm}^{-1}$  in red. The dotted red line marks the Rayleigh criterion (26.4 % contrast).

**Figure 2.16:** *USAF resolution target evaluation of the Bruker Hyperion 3000 microscope using the  $64 \times 64$  pixel FPA detector.*

Figure 2.16(a) shows the obtained transmittance values versus the distance on the FPA area for 5 elements of group 6 of the USAF target for two wavelengths. From every element four contrast values were derived and averaged. Plotting this values versus the spatial frequency gives figure 2.16(b) showing the so called *modulation transfer function* derived from groups 5 to 7 from the USAF target. At a contrast level of 26.4 % the Rayleigh criterion is reached and two structures can still be resolved. The resulting spatial resolutions are summarized in table 2.2

**Table 2.2:** *Measured spatial resolutions for the Bruker Hyperion 3000 microscope. The theoretical limits applying the Rayleigh criterion were calculated according to formula 2.10 with a given NA of 0.5 for the used 15× objective.*

Wavenumber	Measured spatial resolution	Rayleigh limit
3800 cm <sup>-1</sup> (2.63 μm)	5.6 μm 89.9 lp · mm <sup>-1</sup>	3.2 μm
2300 cm <sup>-1</sup> (4.35 μm)	6.6 μm 75.7 lp · mm <sup>-1</sup>	5.3 μm

For comparison: Peter Lasch and Dieter Naumann found a *spatial resolution* for the 15 fold objective at 4000 cm<sup>-1</sup> (2.5 μm) of 5.1 μm and 6.6 μm at 2300 cm<sup>-1</sup> (4.35 μm) for their Bruker Hyperion 3000 microscope. For the 36 fold objective a *spatial resolution* of 2.4 μm was measured being better than the theoretical limit (see equation 2.10) of 3.05 μm for the given NA of 0.5 of the objective. They attributed this finding to the precise, but unknown, optical configuration of the Hyperion 3000 microscope.



# Time resolved (TR) FTIR spectroscopy of chemical reactions in aqueous phase

---

## 3.1 FTIR spectroscopy of aqueous solutions

One of the most important substances on earth is liquid water. Huge areas of our planet's surface is covered with water. It is essential for life as we know it and serves as the solvent in biochemical studies. Nina Kaun cited Martin Chaplin's website<sup>1</sup>, which offers an extensive compendium of information about water, with the words "... Martin Chaplin citing about one thousand publications ..." in 2006 [2]. In February 2012 the number of citations has climbed above 1700. This impressive number already gives some idea about the complexity of the nature of water, its structure and its effect on our environment.

This complexity can be attributed to the ability of the water molecule to form hydrogen-bonds with surrounding molecules. In ice each water molecule forms two hydrogen-bonds to its neighbors and accepts two more hydrogen-bonds from two more H<sub>2</sub>O neighbors [30]. The hydrogen-bonding network formed that way can be found in a nearly identical way in liquid water. IR spectroscopy has shown that the same tetrahedral structure exists in liquid water, only in a more distorted way than in ice [30].

---

<sup>1</sup><http://www.lsbu.ac.uk/water/>

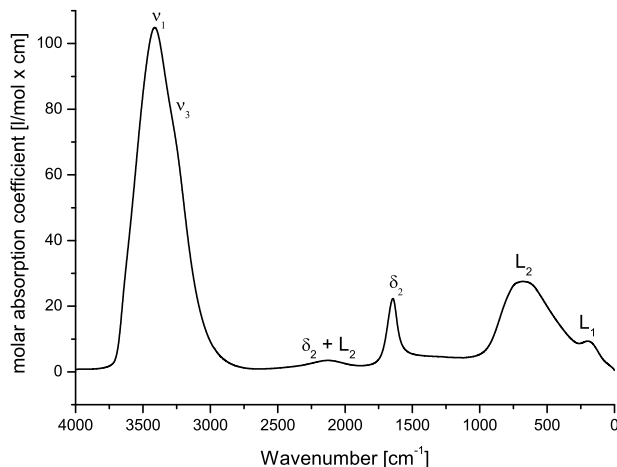


**Figure 3.1:** Molar absorption coefficient of  $H_2O$  [5].  $\nu_1$  and  $\nu_3$  represent the symmetric and asymmetric stretch vibrations,  $\delta_2$  the bending vibration and  $L_{1,2}$  libration modes.

Despite the value of IR spectroscopy to gain insights into the nature of water, water itself is of great importance to IR spectroscopists due to its high absorption coefficients (see figure 3.1) in the mid-infrared. This fact has to be considered especially if water is used as a solvent for proteins: The amide I band of proteins, a marker band for the protein secondary structure [31], highly overlaps with the bending vibration ( $\delta_2$ ) of water.

Assuming that an absorption of 1 gives a satisfying S/N ratio one can calculate the maximum allowed path length for the measurement of the amide I band by inserting the molar absorption coefficient at the maximum of the bending vibration of water ( $1644\text{ cm}^{-1}$  taken from [5]) into the Lambert Beer's law (equation 1.10) giving equation 3.1.

$$\frac{1 \text{ Absorbance}}{55.5 \text{ mol/l} \times 22.3_{1644 \text{ cm}^{-1}} \text{ l/mol} \cdot \text{cm}} = 8.08 \cdot 10^{-4} \text{ cm} \approx 8 \text{ } \mu\text{m} \quad (3.1)$$

According to that calculation a path length of  $8\text{ } \mu\text{m}$  or less has to be used for protein measurements in  $H_2O$ . As an alternative, water as the solvent can be exchanged by  $D_2O$  shifting the absorption bands to lower wavenumbers due to the higher mass of deuterium. However, remaining  $H_2O$  molecules react



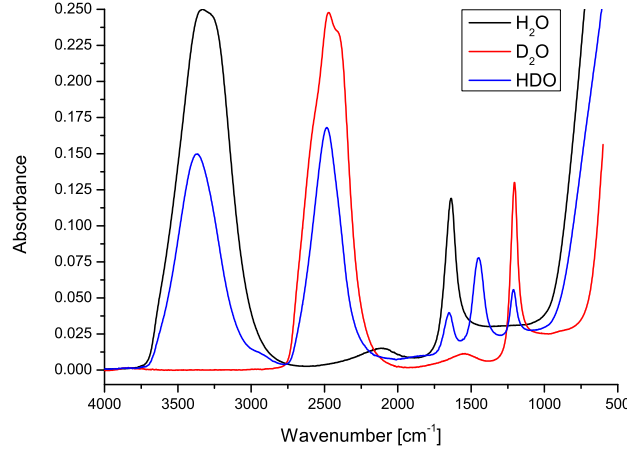


**Figure 3.2:** Spectra of  $H_2O$ ,  $HDO$  and  $D_2O$  measured on a one-bounce diamond ATR crystal. Band assignments are summarized in table 3.1

with  $D_2O$  to  $HDO$  according to equation 3.2, giving rise to a bending vibration of  $HDO$ , as can be seen in figure 3.2.



For  $H_2O$  and  $D_2O$  a coupling effect between the symmetric and asymmetric stretching vibrations is observed leading to a broadening of the observed absorption bands around  $2500 \text{ cm}^{-1}$  for  $D_2O$  and around  $3330 \text{ cm}^{-1}$  for  $H_2O$ .  $HDO$  on the other hand doesn't show this effect.

From the spectra measured with a one-bounce diamond Attenuated Total Reflection (ATR) crystal, shown in figure 3.2, band positions for IR active absorptions are derived and summarized in table 3.1.

The measured ATR spectra of  $H_2O$ ,  $HDO$  and  $D_2O$  will vary slightly in absorption and band position from spectra measured in transmission due to the changing penetration depth across the spectral region as can be seen from formula 3.3.

$$d_p = \frac{\lambda}{2\pi n_1 \sqrt{\sin^2 \theta - \left(\frac{n_2}{n_1}\right)^2}} \quad (3.3)$$

**Table 3.1:** Absorption maxima measured for  $H_2O$ ,  $D_2O$  and  $HDO$  with a one-bounce diamond ATR crystal. The measurement of the libration mode below  $600\text{ cm}^{-1}$  wasn't possible due to restriction of the spectrometer used.

	$H_2O$	$HDO$	$D_2O$
bending vibration ( $\delta_2$ )	1636.6 $\text{cm}^{-1}$	1652.1 $\text{cm}^{-1}$ ( $H_2O$ ) 1448.9 $\text{cm}^{-1}$ ( $HDO$ ) 1211.1 $\text{cm}^{-1}$ ( $D_2O$ )	1204.3 $\text{cm}^{-1}$
combination of $\delta_2$ + libration mode $L_2$	2099.3 $\text{cm}^{-1}$	—	1541.2 $\text{cm}^{-1}$
combination of sym. ( $\nu_1$ ), asym. ( $\nu_3$ ) stretching vibrations + overtone of $\delta_2$	3331.9 $\text{cm}^{-1}$	3364.7 $\text{cm}^{-1}$ (OH) 2484.6 $\text{cm}^{-1}$ (OD)	2472.8 $\text{cm}^{-1}$
libration mode	below $600\text{ cm}^{-1}$		

$n_1$  is the refractive index of the ATR crystal,  $n_2$  the refractive index of the sample and  $\theta$  the angle of incidence under which the light hits the ATR crystal.

Additionally, the refractive index (see figure 1.1 for refractive indices of water) strongly changes in the area of strong absorption bands due to *anomalous dispersion*. The refractive index, however, changes the penetration depth of the IR light using an ATR crystal, altering the measured absorption. Higher refractive indices of the ATR crystal reduce this effect since  $n_2$  has less influence on the term  $\sin^2\theta - (\frac{n_2}{n_1})^2$  in formula 3.3.

## 3.2 General concepts of TR-FTIR spectroscopy

In FTIR spectroscopy two well established techniques are known for time resolved measurements. The first, *rapid scanning*, utilizes a standard interferometer

at very high mirror speeds. The interferograms are stored and co-added in a *data acquisition processor* and the Fourier-transform calculations are done at the end of the experiment saving time during the experimental run. The time resolution limiting element is the speed of the moving mirror, see chapter 2.1.1 for further details.

The second, *step-scanning* [6, p.400], decouples the time resolution from the moving mirror by moving the mirror step-wise and recording time traces at every interferogram position. As a consequence the time resolution only depends on the rise time of the detector and the speed of the ADC. Less well known techniques are stroboscopic [6, p.407] and asynchronous [6, p.408] TR-FTIR spectrometry, which both use classical rapid scanning spectrometers together with advanced sampling techniques to increase the achievable time resolution.

All techniques share one challenge: *precisely starting the reaction* and synchronizing it to the start of the data acquisition process. For *step-scanning*, *stroboscopic spectrometry* and *asynchronous spectrometry* it is even necessary to repeat the measurement several times with very precise timing to record a whole time resolved data set. For *rapid scanning* this isn't necessary since the whole spectrum is recorded at once. However if the S/N ratio is insufficient spectral averaging is required and the reaction under investigation also needs to be repeated.

External triggers used to start chemical reactions can be light pulses from lasers or light emitting diodes directly initiating photochemical reactions or releasing caged compounds, temperature jumps or electrical fields. Kötting et al. [32] investigated the potential interactions of small molecules with Ras-GTP using the rapid scanning approach by caging GTP and releasing it upon 308 nm laser flashes. All components of the reaction were provided as a static sample between two CaF<sub>2</sub> windows. After excitation each forward-backward movement of the mirror resulting in four spectra, which were averaged, gave one spectrum and no further averaging was needed.

Coupling a rapid-scanning spectrometer to a potentiostat Zhou et al. recorded the oxidation of methanol on a nano structured platinum electrode. At the beginning of the potential scan a trigger signal started the FTIR data

acquisition. Spectra were recorded along the cyclic voltammogram and spectra from nine voltammograms were averaged to improve the signal to noise ratio of the IR spectra [33].

The intrinsic need of the step-scanning experiment to be repeated at least once at every interferogram point corresponding to one mirror position limited its use mainly to cyclic reactions. Examples range from the measurement of photocycles [22] to excited states of metal complexes [34, 35]. It can also be applied to visualize the emission characteristics of infra-red lasers [36]. Extending the applicability of the step-scan technique to non-cyclic reactions can be achieved by supplying fresh sample for every excitation at the cost of higher sample consumption. This can be achieved by the use of a flow cell and replacing the sample inside the cell after excitation [25, 26]. This method, however, has a high sample consumption making it unsuitable for the measurement of biological or biochemical system where sample volumes are often limited. Klaus Gerwert circumvented this drawback by coupling the excitation laser into an FTIR microscope and supplying fresh sample for every excitation by means of moving the XY-stage of the microscope to a spot with fresh sample [24]. The downside of both techniques is that only reactions of stable chemicals can be monitored since all reactants need to be in direct contact well prior to excitation.

The simplest and most convenient way to start a chemical reaction is to mix two or more chemicals together and follow the progress of the reaction. For slow reactions this is for example possible by the use of an ATR fibre probe measuring inline of the reaction vessel [37]. However, for fast chemical reactions special techniques have to be applied, which are discussed in the following chapter.

### 3.3 Mixing induced TR-FTIR spectroscopy

The disadvantage of the before mentioned time resolved techniques is their need for an external trigger to start the reaction, limiting their applicability. Simply bringing the reactants in close contact and following the course of the reaction is therefore favourable. A well known way for mixing induced

time resolved experiments is the *stopped flow technique* [38,39]. Two or more reactants are rapidly mixed and pumped into the measurement cell. The flow is stopped as soon as the mixture has filled the cell and the measurement is initiated. Such systems are commercially available and mostly equipped with Ultra Violet (UV)-Vis or fluorescence detection. The temporal resolution of the experiment depends on the speed of the applied measurement technique, the mixing time and the *dead time* needed to pump the prepared sample to the measurement cell.

Moving to IR spectroscopy the detection principle poses a challenge since the path lengths of the measurement cell have to be significantly reduced compared to UV-Vis spectroscopy. Wharton et al. constructed a stopped flow apparatus in combination with a 50  $\mu\text{m}$  flow cell achieving mixing times below 40 ms and a transfer time between the mixer and the measurement cell of 15 ms. The operating pressure of this device was around 19 MPa, which has to be withstood by all components of the system. A similar system was constructed by Dunn and Eyring using a Y-shaped mixer. The system, however, can't be used for aqueous solutions since NaCl windows were used [40]. Further reducing the path length enables the measurement in the spectral region of the bending vibration of water, which led to the development of an ATR stopped flow system [41]. Using the ATR measurement technique, the path length is determined by the ATR crystal allowing for thicker channels and therefore reducing the backpressure of the system leading to faster mixing times due to higher flow rates. The *dead time* of this system proved to be of approximately 150 ms.

If organic solvents, such as  $\text{CH}_2\text{Cl}_2$ , can be used, IR spectroscopy can be coupled to commercial stopped flow systems. Manning et al. used one of those in combination with a 500  $\mu\text{m}$  path length cell achieving *dead times* of 12 ms and *time resolutions* of 5 ms [42].

All previously mentioned techniques share the drawback of some *dead time* needed to bring the sample to the measurement spot after mixing. Peter Hinsmann combined the mixing unit with the measurement cell into a "*spaghetti type*" [43] and a "*lasagne type*" [44] micro mixing device for time-resolved FTIR measurements, eliminating any transfer time between the mixer and the

measurement cell. Both designs were optimized for an optical path length of 20  $\mu\text{m}$ . Those small dimensions resulted in *laminar flow conditions* inside the microfluidic device. The absence of any *turbulent flow* results in a *diffusion based mixing process*. The rather slow diffusional process is described by Fick's law:

$$c(x, t) = \frac{c_0}{\sqrt{\pi \cdot D \cdot t}} \cdot e^{-\frac{x^2}{4Dt}} \quad (3.4)$$

$c_0$  denotes the initial concentration of the diffusing species at the time  $t = 0$ , the diffusion distance  $x = 0$  and the *diffusion coefficient*  $D$ . Simplifying formula 3.4 one can write

$$t \propto \frac{x^2}{D} \quad (3.5)$$

showing that the mixing time can only be decreased constructively<sup>2</sup> by reducing the *diffusion distance*.

In the "spaghetti type" mixer two feeding channels produce an alternating horizontal sequence of 50 streams with a thickness of 20  $\mu\text{m}$  each with a height of 20  $\mu\text{m}$ , resulting in mixing times of 200 ms. The latter "lasagne type" design improved the mixing time to 100 ms by stacking two 10  $\mu\text{m}$  thick fluid layers vertically. Both designs were operated in *stopped flow mode* by means of pumping the chemicals through the micromixer at very high speed (100 - 200  $\mu\text{L} \cdot \text{min}^{-1}$ ) giving the solutions little time for premixing. After stopping the flow diffusional mixing started and the reaction was observed directly through the mixing channel with an FTIR spectrometer operated in *rapid scan mode*. The diffusional mixing process is a very uniform process allowing to repeat the mixing very precisely by switching the flow on and off again. Therefore, the experiment can be repeated several times and by synchronizing the stopping of the flow and the start of data acquisition several runs can be co-added to improve the S/N ratio.

Is the flow rate inside the mixing channel reduced to a level where the fluid streams are completely mixed shortly after entering the channel, the mixer

---

<sup>2</sup>The diffusion coefficient is temperature depended. Higher temperatures lead to faster diffusion

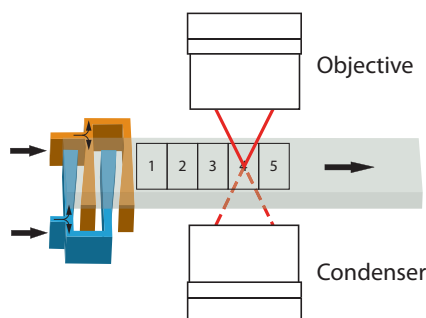


**Figure 3.3:** *Continuous flow operating mode of a micro mixer: By moving the micro mixer along its measurement channel within the measurement spot of an IR microscope subsequent spectra (1, 2, 3, ...) are recorded. Moving away from the inlet side of the mixer gives longer reaction times.*

is operated in *continuous flow mode* and the reaction of interest is observed along the mixing channel as outlined in figure 3.3. Moving the observation window away from the mixing spot gives longer reaction times. The *time resolution* in *continuous flow mode* now doesn't depend on the speed of the FTIR spectrometer used for the measurements any more as it does in *stopped flow mode*. The *age of the chemical solution* inside the mixing channel can be calculated by dividing the *mixers cross section* by the *flow rate inside the channel* and multiplying it by the *distance from the mixing spot*.

The *time resolution* now depends on the *size of the observation window*, the spacing between subsequent measurement spots and the *flow rate*: Smaller spot sizes of the probing IR beam with narrower spacing and faster flow rates enhance the time resolution. Using a FTIR microscope for the measurements the spot size can be controlled by closing the aperture until the S/N ratio is becoming a limiting factor. The upper limit of the flow rate is determined by the back pressure generated by the micro mixer causing leakages.

Within this thesis *two continuous flow micro mixers* were employed for time resolved measurements and will be discussed in the following chapter.





# Micro-machined mixers for TR-FTIR spectroscopy used in this thesis

---

Within this thesis two mixer designs were used: First a two flow sheet mixer developed by Nina Kaun [2] and a new mixer [45–47] designed in cooperation with the *Institute of Sensor and Actuator Systems* featuring four flow sheets reducing the diffusion lengths for faster mixing performances. Evaluating the two mixers can be done by comparing their flow properties.

In fluid mechanics the *Reynolds number* is used for characterizing and comparing different flow regimes and can be calculated using physical parameters of the flowing liquid (or gases):

$$Re = \frac{\rho \cdot v \cdot d_h}{\eta} \quad (4.1)$$

$\rho$  is the *density* of the medium,  $v$  is the *velocity*,  $\eta$  the *dynamic viscosity* both at a given temperature and pressure and  $d_h$  the *hydraulic diameter* which is defined, for non-circular channels as it is the case for our micro mixers, by:

$$d_h = \frac{4 \cdot A}{P} \quad (4.2)$$

with  $A$  being the *cross sectional area* and  $P$  the *wetted perimeter*<sup>1</sup>.

At low *Reynolds numbers* viscous forces are dominating and the *laminar flow regime* is prevailing. In laminar flow no cross currents perpendicular to the flow direction occur and all fluid elements flow in parallel to the side walls.

---

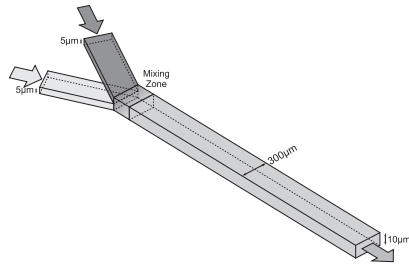
<sup>1</sup>The perimeter of the cross sectional area that is in contact with the flowing medium.

**Table 4.1:** Summarized Reynolds numbers for the old and new mixer design, calculated using the given channel dimensions and water as the flowing medium at a flow rate of  $10 \mu\text{L} \cdot \text{min}^{-1}$ .

	Old Mixer	New Mixer
Channel width	300 $\mu\text{m}$	200 $\mu\text{m}$
Channel height	10 $\mu\text{m}$	8 $\mu\text{m}$
Reynolds Number	$\approx 1$	$\approx 1.5$

At Reynolds numbers  $\geq 2300$  and  $\leq 4000$  a transition from the *laminar flow regime* to the *turbulent flow regime*, where *inertial forces* are dominating the flow, occurs. In table 4.1 the Reynolds numbers for the two mixers calculated for water<sup>2</sup> as the flowing medium are summarized.

## 4.1 Two fluid layer "old" micro-mixer design



(a) Schematic of the mixer



(b) Photograph of the mixer

**Figure 4.1:** 10  $\mu\text{m}$  path length, two flow sheet micro mixer.

The old mixer design used in this thesis was developed during the PhD thesis of Nina Kaun [2] and used for coupling micro fluidic mixing with the step-scan technique (see theory in chapter 2.1.3), presented in chapter 7 within this thesis.

The micro mixer, shown in figure 4.1, is built from two  $\text{CaF}_2$  plates serving as top and bottom windows and SU8 polymer as the spacer material between the

<sup>2</sup>Properties of water:  $\rho = 998.23 \text{ kg} \cdot \text{m}^{-3}$ ,  $\eta = 1.0 \times 10^{-3} \text{ kg} \cdot \text{m}^{-1} \cdot \text{s}^{-1}$  at  $20^\circ$  [48]

plates [49]. The two fluid streams containing the chemicals under investigation are fed to the mixer through two holes in the bottom  $\text{CaF}_2$  plate. A silver layer separates the two  $5\text{ }\mu\text{m}$  thick fluid layers until they reach the  $300\text{ }\mu\text{m}$  wide and  $11\text{ mm}$  long observation channel forming two laminar flow sheets. The end of the silver layer marks the starting point of the diffusion based mixing. The silver layer also masks the observation channel blocking all IR radiation which would pass the observation channel on either side.

Typical flow rates for this mixer design were  $0.5\text{ }\mu\text{Lmin}^{-1}$  resembling a linear flow velocity of  $0.006\text{ ms}^{-1}$  in the mixing channel. Computational Fluid Dynamics (CFD) simulations using a diffusion coefficient of  $D = 5 \times 10^{-10}\text{ m}^2 \cdot \text{s}^{-1}$  and viscosities of water resulted in a mixing distance of  $250\text{ }\mu\text{m}$ , corresponding to  $45\text{ ms}$ , for a mixing quality of  $100\text{ }\%$  [50]. The CFD simulation also showed that the laminar flow regime leads to a *velocity distribution* across the mixing channel's cross section with faster flow rates towards the middle of the channel. This expected behaviour leads to a further *deviation* between the *observed* and the *real reaction time*.

These uncertainties cause that only a *relative* and no *absolute time scale* for the reaction under investigation can be given.

## 4.2 Four fluid layer "new" micro-mixer design

Nina Kaun summarized different aspects of possible improvements on the *two fluid layer mixer design* in her thesis [2, p.55]. She stated that the mixer cross section should be reduced by downsizing the height of the mixing channel to  $8\text{ }\mu\text{m}$  to enable good measurements of the Amide I band in aqueous solutions. This would additionally lead to faster mixing due to reduced diffusion lengths. Further, the width of the channel should be reduced since state-of-the-art IR microscopes are capable of focusing the IR beam down to smaller spot sizes and the flow inside the channel would get more stable. By reducing the cross section of the mixer, lower pumping speeds would lead to the same time resolution at smaller sample consumption. By redesigning the inlet channels of the mixer a more homogeneous flow speed distribution across the width of the channel would be favourable.

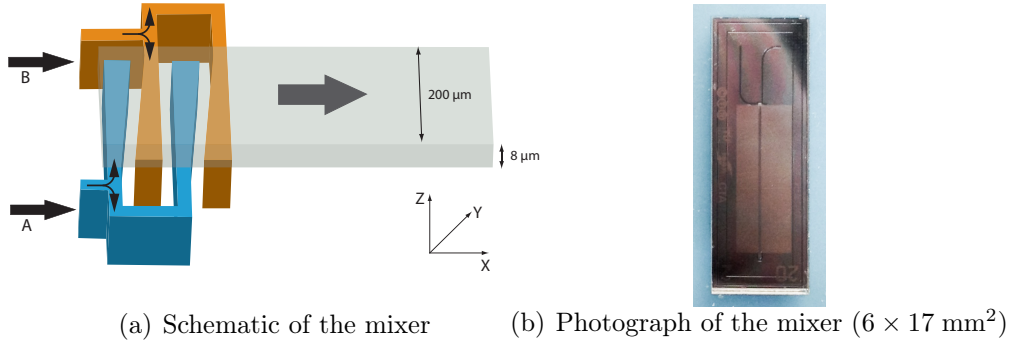


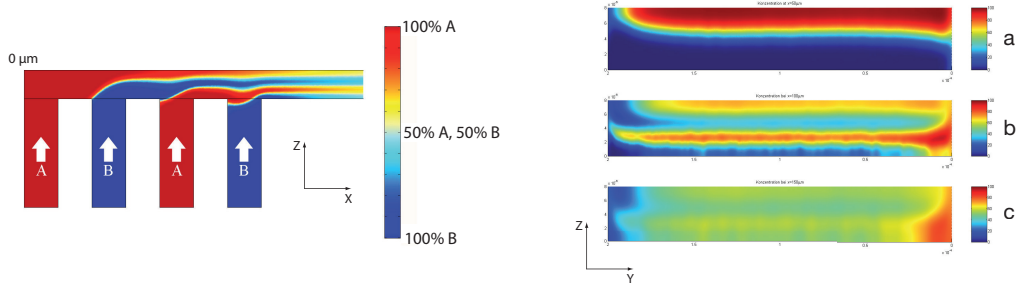
**Figure 4.2:** *New mixer design building four vertically stacked fluid layers in the  $8 \mu\text{m}$  thick mixing channel. The wedge-shaped inlet channels are optimized for a homogeneous distribution of the liquids A and B along the y-axis of the mixer.*

#### 4.2.1 Design and fabrication

The new mixer generation used in this thesis was developed by the *Institute for Sensor and Actuator Systems* in cooperation with the CAVS workgroup considering the experience on TR-FTIR measurements applying micro mixers accumulated by Peter Hinsmann [1] and Nina Kaun [2]. The new mixer features are a *reduced cross section* together with a *reduced path length* of  $8 \mu\text{m}$  for IR measurements in the Amide I region. Figure 4.2 shows a schematic of the mixer along side a photograph of the mixer chip.

The presented micro mixer is based on a design published by Kauffmann et al. [51] featuring three straight inlet channels. Feeding a protein solution in the middle channel and sandwiching it between buffer solution pumped through the outer channels in an  $8 \mu\text{m}$  thick channel a mixing time of  $0.4 \text{ ms}$  was calculated by CFD simulations. However, no experimental proof of the achieved mixing time was published. A disadvantage of the design is that all three channels reach the mixing channel from the same side, leading to a dead zone at that side of the mixing channel where only slow mixing occurs.

This inhomogeneous distribution of the liquids along the mixing channel, observed as the mentioned dead zone, is a result of a pressure drop along the feeding channel from the injection side to its far end. In our design, the velocity distribution of the liquids inside feeding channel network was optimized, using CFD simulations, resulting in a *wedge shaped broadening of the lamination*



(a) Cut along the mixing channel showing the four inlet channels forming four fluid layers inside the mixing channel. (b) Cut through the mixing channel at a) 50  $\mu\text{m}$ , b) 100  $\mu\text{m}$  and c) 150  $\mu\text{m}$  downstream.

**Figure 4.3:** *CFD simulations of the new mixer design with wedge shaped inlet channels widening from 10  $\mu\text{m}$  to 22  $\mu\text{m}$ .*

*inlets* towards the far end. A widening from 10  $\mu\text{m}$  to 22  $\mu\text{m}$  gave an optimal distribution of the liquids along the y-axis of the mixer. The feeding network, which splits two inlet channels into the four lamination inlets, was carefully designed to feed every inlet channel with a *different, optimized fluid velocity*. As a result the thickness of each layer inside the mixing channel is optimized for fastest mixing performance.

Figure 4.3 shows the obtained simulation results for the optimal wedge shaped feeding channels. In figure 4.3(b) the four fluid layers formed across the mixing channel are shown at three positions downstream the mixing channel. At the side walls small *dead zones* are formed, which can be seen as blue/red zones in part c. This is due to the – strictly laminar – flow profile formed by the fluids. However since the probing IR beam is smaller than the well mixed parts (width 160  $\mu\text{m}$ ), these zones do not interfere with the IR measurements.

The **fabrication process** of the mixer is based on silicon micromachining techniques structuring the feeding network on a 350  $\mu\text{m}$  thick, double sided polished, silicon nitride and silicon oxide covered,  $\langle 100 \rangle$  lattice oriented silicon wafer.

In a first step the backside of the silicon wafer is spincoated with a positive photoresist and the inlet channels for the fluid inlets are patterned. After

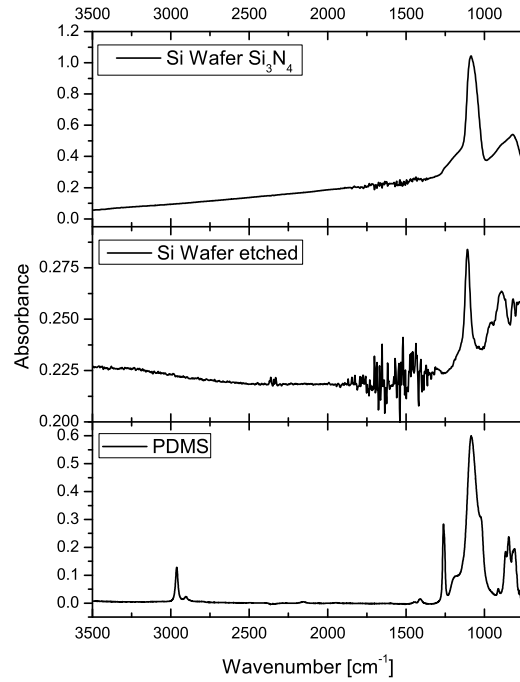


**Figure 4.4:** IR measurements in transmission of the  $\text{Si}_3\text{N}_4$  and  $\text{SiO}_2$  covered Si wafer before (top) and after the etching process (middle). At the bottom the spectrum of the used PDMS polymer defining the channel height of the mixing channel is shown.

removing the  $\text{Si}_3\text{N}_4$  layer by a plasma etching process, the inlet holes are wet-etched using KOH. In a next step the fluid network is photo-structured on the other side of the wafer and formed by *deep reactive ion etching*. Both sides are cleaned by an oxygen plasma etching step removing any remaining photoresist as well as the  $\text{Si}_3\text{N}_4$  layer.

The mixing channel itself was realized on a  $\text{CaF}_2$  wafer, with a thickness of 1 mm. In a first step a metal layer, serving as an aperture for the IR measurements, with a width of  $180\text{ }\mu\text{m}$ , masking the channel was applied. The aperture elements are structured using a photoresist before a thin metal layer is deposited on the  $\text{CaF}_2$  wafer forming the aperture. By spincoating a PDMS-like polymer onto the wafer resulting in an  $8\text{ }\mu\text{m}$  thick layer the height of the mixing channel is defined. After a soft baking process the channel

structures are patterned by UV-exposition and a development step removes the remaining unexposed PDMS polymer.

As can be seen from figure 4.4 removing the  $\text{Si}_3\text{N}_4$  layer from the Si wafer is an important step in the mixer production due to high absorptions caused around  $1100\text{ cm}^{-1}$ . In figure 4.4 the IR spectrum of the PDMS polymer is shown as well, which should be masked out in IR measurements by the deposited aperture.

The two wafers are cold bonded in a last step for several hours, due to different thermal expansion coefficients of silicon and  $\text{CaF}_2$ . On a 100 mm diameter wafer, 40 mixers can be fabricated. For experimental comparisons mixers with the *wedge shaped design* as well as *straight shaped inlet channels* of  $10\text{ }\mu\text{m}$  width have been produced.

On a later wafer also  $50\text{ }\mu\text{m}$  path length mixers were produced for the use with an external cavity quantum cascade laser, which however was beyond this thesis. Further information on the mixer design can be found in **Publication I** and for additional information on the fabrication refer to **Publication II**.

### 4.2.2 Mixer support holder

Using *micro fluidic devices* always comes with the need to connect them to the *macroscopic world*. For the micro mixer this connection means to connect the chip to a pump, which is driving the two liquids through the mixing channel. In the present work a kD-Scientific 100 syringe pump equipped with two Hamilton syringes was used. The support holder, shown in figure 4.5 was connected to the Hamilton syringes by PolyEtherEtherKetone (PEEK) capillaries to reduce the dead volume between the pump and the mixer. The design of the support holder becomes especially important if higher flow rates (up to  $30\text{ }\mu\text{L} \cdot \text{min}^{-1}$ ) are used producing *high back pressure* from the mixing chip causing *leakages* between the mixing chip and the support holder. Therefore, it is important to firmly press the mixer onto the support. Too high pressures, however, will inevitably lead to breaking the brittle mixer.

The used holder within this thesis is an improvement on the design introduced by Nina Kaun. By replacing the 1/4-28" fittings with thinner 10-32

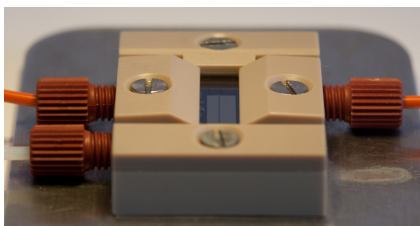


**Figure 4.5:** *Support holder for the micro mixer built from PEEK polymer*

fittings<sup>3</sup> the overall thickness of the holder could be reduced, resulting in *less dead volume* inside the holder. A second crucial improvement was removing the O-rings used by Nina Kaun between the mixing chip and the holder. Instead, a typically 200  $\mu\text{m}$  thick silicone foil was used as a sealing layer. This has the advantage of being a soft layer across the whole mixer's area, mitigating inhomogeneously applied pressure by the holding clamps pressing the mixer onto the holder. Additionally the clamps were redesigned allowing to hold the mixer from all four sides (instead of two in the previous design) by using only one screw per clamp, leading to an evenly distributed pressure along the clamp.

A last improvement deals with the *risk to contaminate the mixer* with particles leading to a disturbance in the laminar flow profile or in worst cases to the blockage of the mixer. By incorporating *titanium filter frits*<sup>4</sup> with a pore size of 0.2  $\mu\text{m}$  right beneath the silicone sealing layer into the support holder a prefiltering mechanism was implemented. The filters are now located as close to the mixer as possible.

### 4.2.3 Experimental characterization

Evaluating a mixing device designed for TR-FTIR spectroscopy means to measure the mixing performance. In comparison to the old mixer design the new mixer exhibits *unwanted premixing* due to the fact that the four fluid layers are superimposed already before the first possible measurement spot.

<sup>3</sup>Part number P-844 and P-840 at <http://webstore.idex-hs.com>

<sup>4</sup>Part number A-505 at <http://webstore.idex-hs.com>



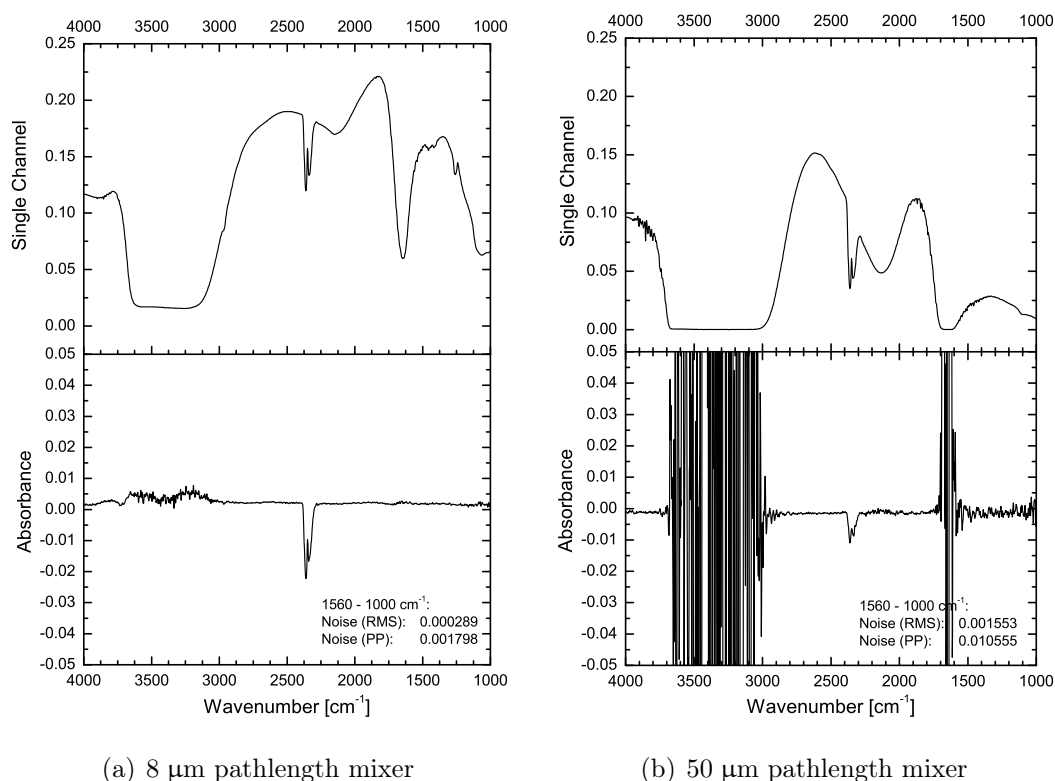


**Figure 4.6:** Single channel spectra (top) of the two different mixers filled with water after coadding 32 scans. The measurements were taken on the Bruker Hyperion 3000 microscope using the 15 fold lenses in transmisson mode using the single point MCT detector and an aperture size of  $150 \times 150 \mu\text{m}^2$ . The lower graphs show 100 % lines calculated from two consecutive measurements. The RMS noise is about 4.5 times higher for the 50  $\mu\text{m}$  than for the 8  $\mu\text{m}$  mixer in the range from  $1560 \text{ cm}^{-1}$  to  $1000 \text{ cm}^{-1}$

## 52 Chapter 4. Micro-machined mixers for TR-FTIR spectroscopy

It is therefore important to characterize this effect as well as the *mixing time* itself.

Additionally, experimental proof of the *spatial homogeneity* across the width of the mixing channel was obtained by taking FPA IR images of the mixing zone and comparing *straight shaped inlet channels* to the *optimal wedge shaped structured mixer*.

As a first benchmark for the new mixers 100 % lines were recorded by subsequently recording a background and a sample single channel spectrum and calculating the absorbance of mixers filled with pure water. As can be seen from figure 4.6(a), the mixers with 8  $\mu\text{m}$  path length exhibit only slightly higher noise in the region of the  $\text{H}_2\text{O}$  bending vibration (see chapter 3.1) compared to the rest of the finger print region whereas total absorption occurs for the bending vibration using the 50  $\mu\text{m}$  mixer (figure 4.6(b)).

The mixing and premixing times were analysed by using a very fast chemical reaction – an *acid-base neutralization* reaction.

### 4.2.3.1 Acid-base neutralization

Evaluating the mixing performance of the mixer needs a chemical reaction that proceeds faster than the expected mixing process itself. This pre-requirement is met by acid base neutralization reactions. Rini et al. used photoacids<sup>5</sup> to prepare unreactive acid-base pairs weakly bonded by a hydrogen bond. Upon an optical trigger pulse the acidity of the photoacid rises by several units of  $pK_a$  and the neutralization proceeds. The proton transfer was found to occur in the femtosecond time regime [53, 54] being much faster than the mixing process in our micro mixer.

As outlined in chapter 4.2.1, strong bases are used in the fabrication process of the mixer to etch the inlet holes through the silicon wafer. Strong acids on the other hand would dissolve the  $\text{CaF}_2$ . Therefore a neutralization reaction of a weak acid – acetic acid – with  $\text{NaOH}$  was chosen using only low concentrations to avoid any damage to the mixer.

---

<sup>5</sup>A photoacid exhibits an excited state which represents a stronger acid than the ground state and can be switched on by optical excitation [52].

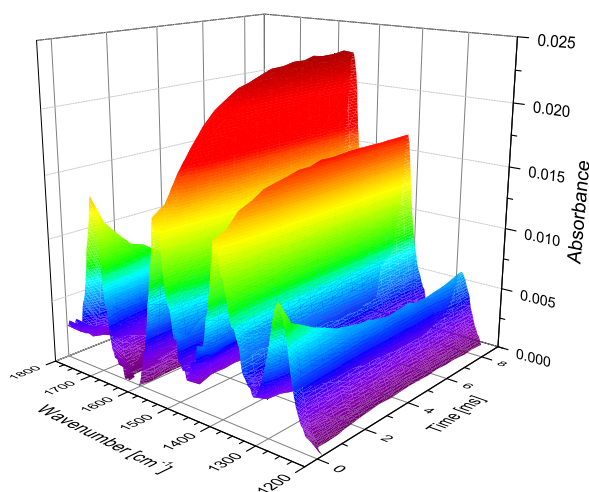


**Figure 4.7:** Neutralization reaction of 0.2 M acetic acid with 0.1 M sodium hydroxide solution using a reagent flow rate of  $10 \mu\text{L} \cdot \text{min}^{-1}$ .

Pumping 0.2 M acetic acid and 0.1 M NaOH through the mixer at a constant flow rate of  $10 \mu\text{L} \cdot \text{min}^{-1}$  for each reagent the acetate anion is formed according to equation 4.3.



The reaction is followed by using the Bruker Hyperion 3000 microscope set up to average 32 scans at an aperture size of  $100 \times 100 \mu\text{m}$  stepping  $100 \mu\text{m}$  after each spectrum is recorded. Calculating the absorbance using one sample run mixing water with water as the background single channel results in one time resolved IR data set shown in figure 4.7. The observed bands, plotted in figure 4.8(a), can be assigned to the asymmetric stretching vibration ( $1525 \text{ cm}^{-1}$ ), the symmetric stretching vibration ( $1416 \text{ cm}^{-1}$ ) of the acetate ion. The band at  $1710 \text{ cm}^{-1}$  is assigned to the stretching of the carbonyl band whereas the band at  $1286 \text{ cm}^{-1}$  arises from the C-O stretching vibration of the protonated acid.

Integrating and applying exponential fits (figure 4.8(b)) to data set for the acetic acid and the acetate ion results in time constants of 1.8 ms for both chemicals demonstrating the usability of the mixer. However, the data set also

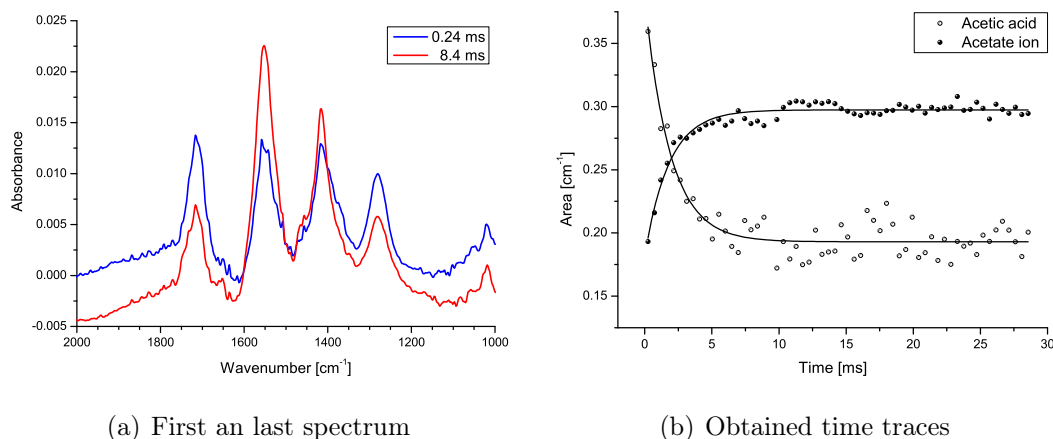


**Figure 4.8:** Evaluation of the obtained data set from figure 4.7. Integrated areas for the acetate band at  $1416\text{ cm}^{-1}$  and the acetic acid band at  $1710\text{ cm}^{-1}$  are evaluated by applying exponential fits resulting in time constants of 1.8 ms for both fits.

shows that bands originating from the acetate ion are well present already in the first spectrum recorded right after the last inlet channel. This shows that a significant amount of acid and base have already reacted due to premixing starting as soon as the first two inlet fluid layers are formed (figure 4.3).

The obtained exponential fit for the acetate band at  $1416\text{ cm}^{-1}$  has the formula  $y = -0.116 \cdot e^{\frac{-x}{1.801}} + 0.297$  and can be extrapolated to an acetate band area of  $y = 0$  assuming that no acetate ion<sup>6</sup> is present at the real starting point of the reaction. This gives an x-value of -1.698 meaning that the reaction starts 1.7 ms prior to the first measurement spot located  $50\text{ }\mu\text{m}$  downstream from the last inlet channel. Translating the obtained 1.7 ms back into an x-axis value of the mixer an impossible premixing distance of  $350\text{ }\mu\text{m}$  would be the result. Only slight changes of the exponential fit towards a steeper slope for the starting of the reaction would result in a shorter calculated premixing time. Therefore an overestimation of the premixing time caused by an inaccurate fit seems to be the most likely explanation for this unexpected result.

However, it can be clearly seen from the presented data that complete mixing of the acetic acid with NaOH is achieved in the order of 5 ms when the chemical reaction reaches an equilibrium state.

<sup>6</sup>The degree of ionization for a 0.2 M acetic acid solution in water ( $pH = 2.7$ ) is 0.9 %.

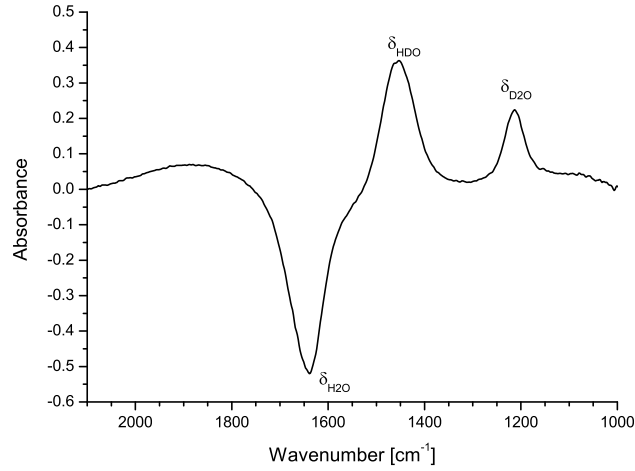


**Figure 4.9:** IR spectrum from one pixel of the FPA detector of the Hyperion 3000 microscope in the spectral region of the bending vibrations of  $H_2O$ ,  $D_2O$  and  $HDO$ .

#### 4.2.3.2 H/D exchange in water

In a second evaluation step the lateral distribution of the the two feed liquids was compared between a straight and a wedge shaped micro mixer. For this, pure  $H_2O$  was mixed with pure  $D_2O$  forming  $HDO$  according to formula 3.2. The proton exchange again occurs on the femtosecond time scale [55] and is therefore well suited for visualizing the mixing process.

By evaluating the  $H_2O/D_2O$  mixture and integrating the  $HDO$  bending vibration, shown in figure 4.9, between  $1335\text{ cm}^{-1}$  and  $1530\text{ cm}^{-1}$  after applying a baseline correction at  $2100\text{ cm}^{-1}$  data shown in figure 4.10 was obtained. The shown IR images were recorded as  $64 \times 64$  px images using the FPA detector of the Bruker Hyperion 3000 microscope. The images were recorded slightly overlapping with the last inlet channel and the aperture on the upper side of the mixer for positioning reasons. These overlapping pixels showing only noise were cut for the evaluation, resulting in an imaged area of  $166.8 \times 158.6\text{ }\mu\text{m}^2$  ( $X \times Y$ ).

From the shown data it can be concluded that the wedge shaped mixer geometry outperforms the straight mixer in terms of mixing time and homogeneity across the y-axis, proving CFD simulation results. Further experiments were therefore conducted only using the wedge shaped mixers.

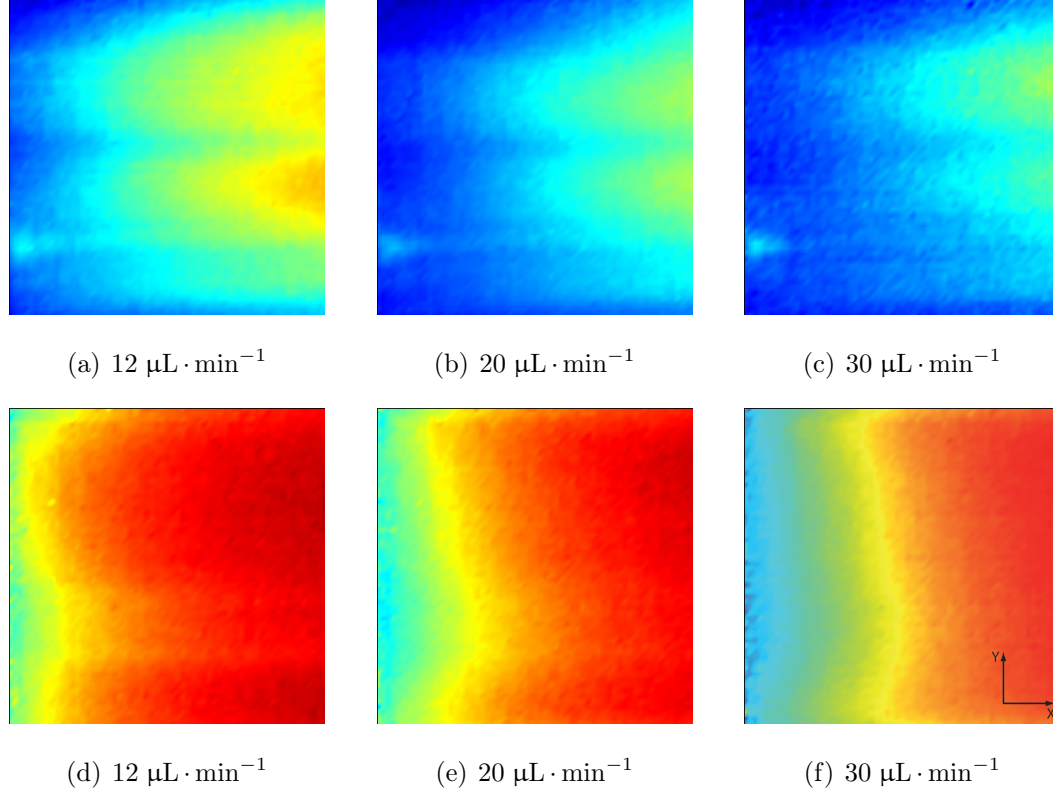


**Figure 4.10:** FPA images taken right after the last inlet channel in the top left corner of the mixing channel showing  $166.8 \times 158.6 \mu\text{m}^2$  at different channel flow rates. The top row shows images taken from a straight shaped inlet channel mixer whereas the bottom row shows a wedged shaped mixer with the optimal geometry of the inlet channels widening from  $10 \mu\text{m}$  to  $22 \mu\text{m}$ . The colors represent the band area of the HDO bending vibration from low (blue) to high (red) concentrations. It can be seen that the wedge shaped mixer shows significantly faster mixing as well as a homogeneous distribution across the width of the channel (Y-axis).

#### 4.2.4 Encountered difficulties in mixer life-time

Operating micro fluidic devices at laminar flow conditions goes hand in hand with small fluid channel dimension down to  $8\text{ }\mu\text{m}$  in the case of the newly developed micro mixers and to  $5\text{ }\mu\text{m}$  for the old design of Nina Kaun. Those small dimensions resulted in various difficulties encountered during the use of the mixers. Figure 4.11 illustrates those difficulties with photographs of the old and the new mixer designs taken after use.

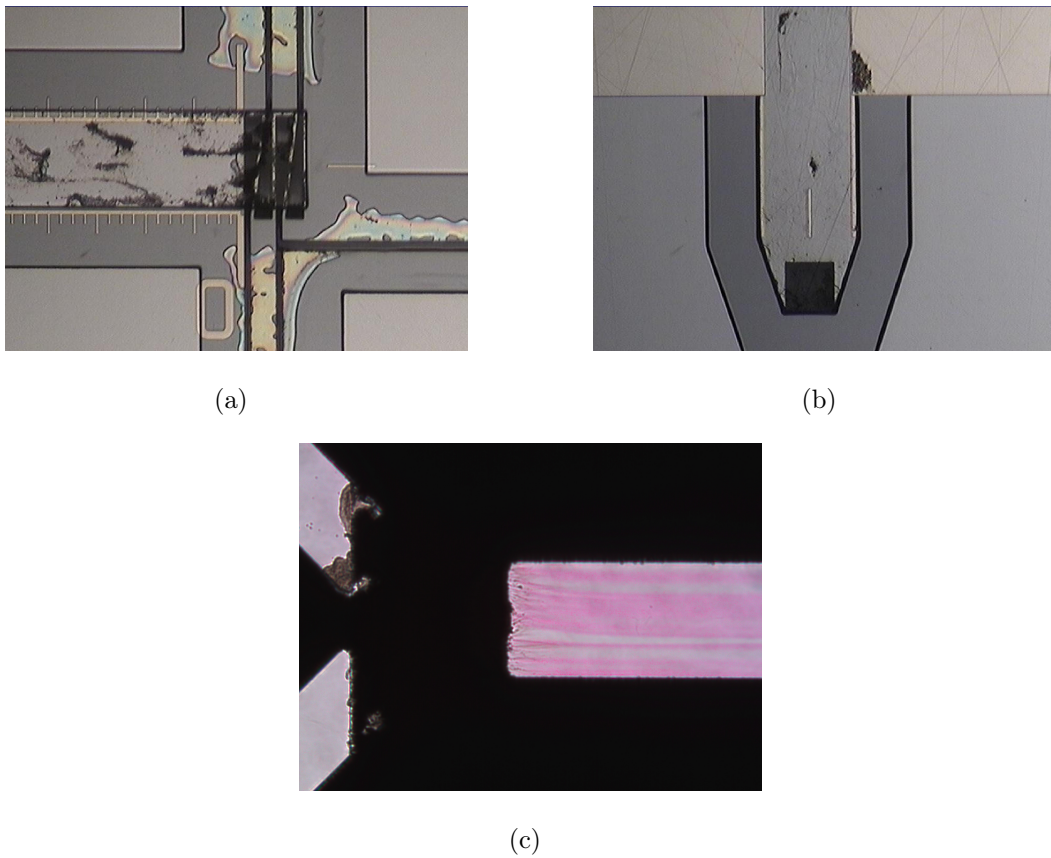


**Figure 4.11:** Figure (a) shows particle contamination inside the mixing channel, delamination of the PDMS and slight misalignment between the Si and CaF<sub>2</sub> wafer. Figure (b) shows corrosion of the metal aperture. Figure (c) illustrates the disturbed laminar flow caused by dirt particles in the inlet channels of an old-type mixer. No pink colouration shows zones where no reaction of the indicator phenolphthalein with NaOH took place due to a disturbed laminar flow.

Since every little particle inside the mixing channel disturbs the laminar flow deteriorating the mixing efficiency of the mixer (figure 4.11(c)), contamination of the mixer is the biggest difficulty encountered during its use. The implementation of the filter frits into the new support holder (see chapter 4.2.2) reduced that risk but couldn't eliminate it completely. Partly, the problem was exacerbated by the use of the silicone sealing layer due to particles sticking onto the adhesive surface of the polymer. *Intensive cleaning* of the sealing layer using iso-propanol was therefore inevitable before assembling the mixer and its support. The formation of salt crystals, caused by drying solvents in the mixing channel after use, was countered by an automated cleaning system consisting of valves and a syringe pump controlled by Advanced Total Lab Automation System (ATLAS) described in the next chapter.

Due to the fast mixing times of the new mixer high flow rates had to be used to extend the measurable reaction range resulting in *high pressures* acting on the mixer itself and the sealing layer, causing *leakages*. In some rare cases this led to *delamination* of the cold-bonded PDMS layer from the silicon or the  $\text{CaF}_2$  wafer, as shown in figure 4.11(a).

For some of the mixer chips a slight *misalignment* of the silicon wafer and the PDMS structures deposited on the  $\text{CaF}_2$  wafer was observed, probably affecting the mixing time. Those mixers were used in preliminary experiments only.

Figure 4.11(b) shows another issue experienced with the micro mixers: Sometimes the *aperture layer* masking the PDMS ridges *corroded*, forming dark spots. However, a negative influence on the quality of the obtained spectra is unlikely.

As expected the difficulties of particles inside the channel and leakages is significantly less severe with the 50  $\mu\text{m}$  mixers compared to the 8  $\mu\text{m}$  mixers.



# Advanced Total Lab Automation System (ATLAS)

---

As described in chapter 4.2.4, the micro mixing device is very susceptible to particles inside its narrow structures. Therefore, cleaning the mixer after use is essential to extend its lifetime. This cleaning process consists of many repetitive steps of rinsing the mixer with cleaning agents and deionized water followed by a drying step where the mixer is flushed with nitrogen. This step helps to minimize the risk of any liquid drying up inside the mixer forming any kinds of residues. Taking the maximum possible flow rates inside the mixer into account the cleaning can take more than an hour, making it favourable to automatize it.

Developing such an automation systems for one specific task using always the same sequence of cleaning steps can be easily achieved in various ways. However, if the sequences change or the whole experimental setup needs to be adapted, a flexible solution with regard to the control software is needed. Expanding the idea of a variable liquid handling system to a complete analytical measurement scenario increases the number of possible combinations by a large value. In a simple liquid handling system, for example, one valve or a pump might need to be changed. On the other hand in a more complex system the ADC board at the detector side may be exchanged for a better S/N ratio. All these changes often come together with the need to adapt the control software, which was programmed for e.g. a specific ADC board only, resulting in extra workload or costs for those changes.

In this workgroup, this issue was first perceived by Michael Haberkorn [56]. He developed a software package called Sagittarius, which consisted of a

server program, called master, and various clients, which communicated over Transmission Control Protocol / Internet Protocol (TCP/IP). All parts of this package were developed using Visual Basic 6.0 and mainly contained clients for liquid handling purposes.

Stephan Kulka [57] added two more clients to control a Dionex UV detector as well as a Spellman high voltage supply to build a Capillary Electrophoreses (CE) system using Sagittarius. However, writing the detector client was a great challenge – for a chemist – due to the fact that Visual Basic 6.0 didn't offer any predefined elements for displaying the obtained graph from the UV detector<sup>1</sup>.

However, the advantage of this distributed master/client system was its *scripting language* used to send commands from the server to the connected clients. Each client executed those commands at the connected hardware. In that fashion it was possible to realize different experimental setups without changing the client programs. Only the script, used for the specific setup, had to be rewritten.

Using Sagittarius was unfortunately not possible in the course of this thesis due to an inherent problem with Visual Basic, which always needs to compile a program to an executable before it can be used. Those executables were not usable anymore because of changes made to Windows handling the communication over RS232. Therefore, the Sagittarius clients couldn't connect to their hardware counterparts, rendering Sagittarius useless.

Looking for a new programming language overcoming these difficulties and making programs more prolonging, LabVIEW by National Instruments (NI) came up as the ideal development environment. LabVIEW is – in contrast to textual programming languages such as C++ – a graphical programming language, which is organized in functional blocks, each handling a specific task, called Virtual Instrument (VI). These VIs are connected through wires transporting data values (see fig. 5.1 for an example). Therefore, the flow of variables within a program is automatically visualized in the source code itself, making it easier to understand a program made by someone else. Altogether LabVIEW offers the following advantages:

---

<sup>1</sup>Private communication with Stephan Kulka

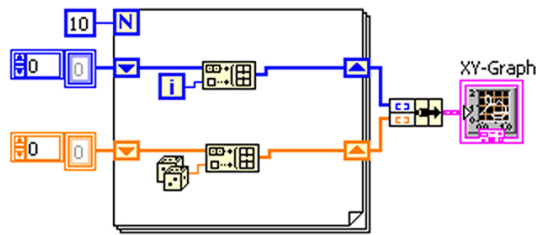


**Figure 5.1:** Simple example of LabVIEW's programming language, called "G", showing the generation of an XY graph in a for-loop using the number of iterations as the X and random values for the Y values. Different colors of the wires symbolize different variable types such as blue for integer, orange for double precision values and pink for LabVIEW specific clusters.

- On-the-fly compiler (one can directly run the source code of a program)
- Upwards compatibility (older programs will also run on newer software versions)
- Extensive support (also from third-parties) for different hardware by downloading drivers from the NI website<sup>2</sup>
- Wide range of different NI hardware for various measurement and control tasks directly supported by LabVIEW
- Easy-to-read source code
- Easy-to-learn for non-programmers
- Professional support even for complex problems

Within this thesis two LabVIEW based programs have been developed and are described below. First a simple All-In-One program was realized (**Publication III**), already using a scripting language, as proposed by Michael Haberkorn [56], giving flexibility in combining the available hardware components freely. After adding more and more components, the maintenance of the original All-In-One program had become a too big hassle, so I decided to

<sup>2</sup><http://www.ni.com/downloads/idnet/>

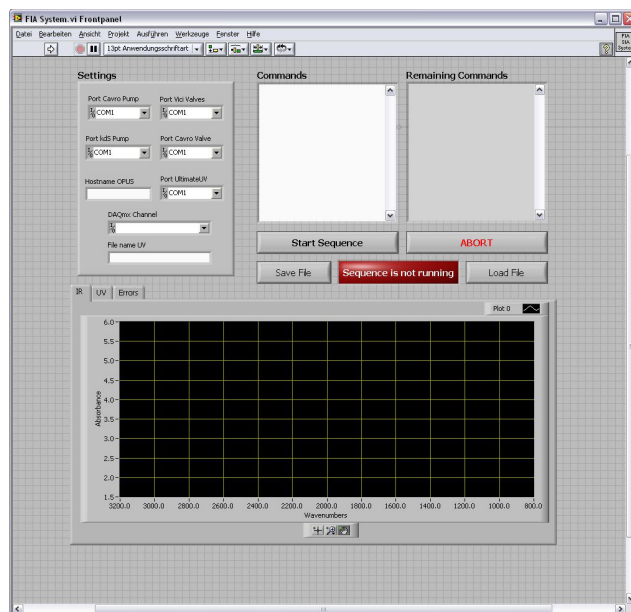


**Figure 5.2:** GUI of the All-In-One program showing on the top left the settings panel. The scripting commands are added to the Commands text field. Measured IR or UV data are displayed in the according tab in the lower part of the program window. After starting a script for execution the red indicator turns green indicating a running script. For the easier reuse of scripts they can be saved and loaded from within the program.

adopt Michael Haberkorn’s idea to distribute different hardware elements over different software counterparts. The outcome of this effort is a master / client software platform programmed in LabVIEW called ATLAS. ATLAS combines the easy expandability of Sagittarius with the advantages offered by LabVIEW (**Publication IV**).

## 5.1 All-In-One program

Out of the need to clean the mixers I developed my first LabVIEW program which supported valves from Vici Inc. and pumps from Cervo (now Tecan Trading AG). Using a *scripting language* as proposed by Michael Haberkorn [56] allowed to change the sequential arrangement of different cleaning steps as

well as the pumped volumes and times each cleaning agent remained inside the mixer. At this point a master/client based approach didn't seem necessary.

Over the time, however, colleagues wanted to use that program together with other hardware as well. At the beginning it was easy to implement the code needed but as the program grew the source code became harder to read and adapting the program was nearly impossible in the end. The possibilities of this extended program, shown in figure 5.2, were demonstrated by building a CE system [58] by combining an injection valve with a selection valve and a syringe pump forming a liquid handling system with a high voltage supply and an UV detector. The second analytical system built by Sergio Armenta [58] utilized the same program and was used to monitor enzymatic reactions with an FTIR spectrometer.

## 5.2 Master / Client system

By splitting the original All-In-One program into different clients and a master, the complexity of each program could be decreased, and it got easier to add new hardware components. Now it is only necessary to create a new client for the new hardware. The other clients and especially the master don't need any changes at all. On the other hand it became possible to run different clients on different computers, which is especially useful if the wiring to the connected hardware have to be kept short or if it is not possible to connect all hardware to the same PC.

One of the big advantages of this distributed approach, which is controlled by a scripting language, is also one of its disadvantages. The more complex a hardware component, such as a Daylight Solutions external cavity laser, becomes the more complex the scripting language has to be to cover all possibilities the hardware offers. This can be achieved by a large set of single commands or by combining different options into one command. Both of them hold the risk of confusing commands, which nobody can remember. Therefore the ATLAS platform offers the possibility to program the script on the master directly from each of the clients by interacting with its GUI. We call this mode the *programming mode* of the clients.

After a script is finished the clients are switched to the *server mode*. In this mode the clients are remote controlled by the master, which executes the programmed commands of the script in consecutive order. However, if someone wants to use only a single client this is also possible in the *local mode* where each user input is directly executed on the hardware.

### 5.2.1 The master

The master program, shown in figure 5.3, is the central communication element of the ATLAS platform. Its main duty is to govern the scripts used for different experimental setups. It allows to *create*, *save*, *load* and *execute* scripts. The script sequence itself is displayed in a text box which also allows editing the script directly. On the right side of the window a list of all connected clients also shows the status of each. While a *red* light indicates a busy client, a *green* light stands for an idle client, ready to accept a new command.

After starting the script execution the master starts sending the script commands (one command per line) to the according clients. Upon executing a script the master also automatically saves the complete script together with a timestamp of the execution start-time allowing to identify the script used for data recorded later on. Furthermore, the master also keeps a log of all commands sent to clients and their replies. This can be useful to find the cause of an error that occurred if a script is running unattended for several hours.

Huge scripts can become confusing quite easily. To help keeping a clear overview the master offers two possibilities to shorten scripts. First of all, predefined *aliases* can be added to a script with a single command. These aliases contain more scripting commands which are inserted into the script at the alias position prior to execution. Aliases are especially handy if a certain script sequence can be used within different scripts. An example for such an alias could be the cleaning sequence for a liquid handling system.

The second possibility comes handy for well known situations in experimental work where one task needs to be done over and over again. One could multiply the according commands and insert them many times into the script or use the more elegant way offered by ATLAS: Using *for-loops*

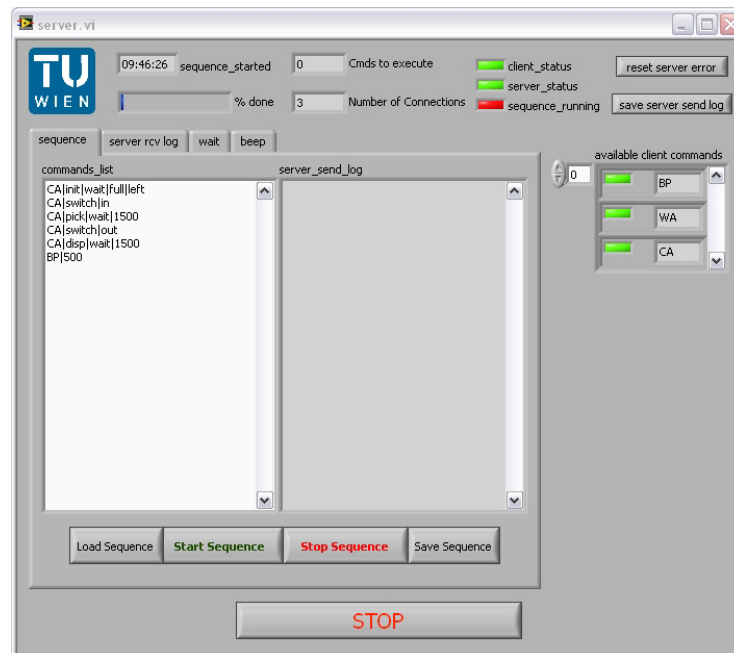


**Figure 5.3:** GUI of the ATLAS master showing a simple script in the textbox on the left and the server log of sent commands in the middle. On the right hand side the list of available clients shows three connected clients. The Wait client (WA), the Beep client (BP) and the Cavro syringe pump client (CA). See chapter 5.2.2 for further information on the clients.

allows to execute commands for a specified number of times by adding the script commands once within the for-loop construct. *For-loops* offer another significant advantage: the count of the actual repetition can be used within the script offering possibilities such as switching a valve through its ports 1 to 10 automatically in a liquid handling sequence.

In addition the master also offers a possibility if the user wants to switch the valve from the example above only through every second position: By using a VI supplied by National Instruments<sup>3</sup> the master program can calculate mathematical expressions and use their results within the script.

<sup>3</sup>[http://zone.ni.com/reference/en-XX/help/371361G-01/gmath/advanced\\_formula\\_vis/](http://zone.ni.com/reference/en-XX/help/371361G-01/gmath/advanced_formula_vis/)

### 5.2.2 The clients

As already mentioned in the introduction each client can be operated in three modes:

**Local:** The client only controls the connected hardware. Any user interaction is executed directly.

**Programming:** The client sends the generated scripting command to the master and the command is added at the cursor position of the script on the server.

**Server:** The client is connected to the master and awaits commands to execute. However, users can still directly interact with the hardware over the GUI.

As soon as a client is connected to the master a continuous communication between them starts as described later (chapter 5.2.3). The programming code handling the communication with the master is available as a template and new clients can easily be programmed by adding the hardware specific code to that template. In addition this template also contains code for a *steady state machine*<sup>4</sup> and a *producer consumer architecture*<sup>5</sup>. This *steady state machine* has three states:

**Init:** This state is called after starting the client and contains all necessary steps to initialize the client and especially the connected hardware

**Running:** This state contains all the code for the actual program including the *producer consumer architecture*

**State changed:** This state is called if the user changes the operating mode of the client, such as from *local* to *server* mode.

The *producer consumer architecture* within the *running state* handles all interactions of the user with the client over the GUI as well as the communication with the master. A typical *producer consumer architecture* consists of two

---

<sup>4</sup><http://zone.ni.com/devzone/cda/tut/p/id/2926>

<sup>5</sup><http://zone.ni.com/devzone/cda/tut/p/id/3023>



parts: the first one produces *commands* or *data* (producer) and the second one *executes* them or *evaluates* the data (consumer). The producer is linked to the consumer by a queue buffering commands or data if the consumer is slower than the producer. In our clients we expanded this architecture by a third loop in the following way:

**Event handler loop:** This first producer creates scripting commands upon user interaction and adds them to the *execution queue*.

**Server loop:** Acts as a producer or consumer. In *programming mode* it sends the commands generated by the *event handler loop* to the master filling the *Command list* whereas in *server mode* it adds script commands received from the master to the execution loop.

**Consumer loop:** This loop takes commands out of the *execution queue* and runs the commands on the hardware one after the other.

In chapter 5.2.4 two example clients are discussed highlighting two aspects of the client development. For a full list of available client refer to appendix B. The next chapter, however, will focus on the communication between the server and connected clients.

### 5.2.3 Communication principle

The communication between the master and the clients is handled only by the master. This is achieved by polling the clients with a time interval of 50 ms by sending the command *status* to the client. Upon the first reception of this status query a new client answers with *cmd:ID* where ID stands for a two letter alphanumerical code identifying the client. This ID is used in further communications between the master and that specific client to directly address this client only. Any further status query can be answered by the clients in three ways:

**status:ready:** Tells the master that the client is ready to accept new commands.

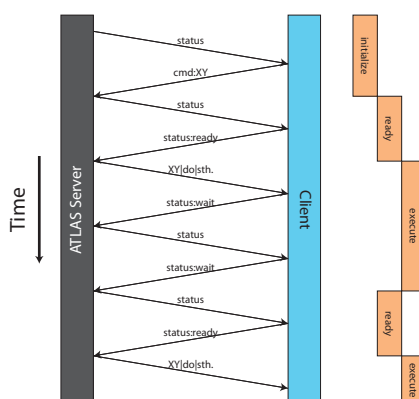


**Figure 5.4:** Communication between the master and one client during the execution of a script.

***status:wait:*** Tell the master that the client is executing a command and wants the server to wait until it is finished.

***status:error:*** Tells the master that an error occurred at the client side.

If the master is executing a script and receives a *status:wait* reply it doesn't execute the next command but keeps on querying the status of the clients until it receives *status:ready* from all clients. After that it continues executing the next command of the script by sending the next command from list to the according client, identified by its ID. The communication between the master and one client is exemplified in figure 5.4.

If a client replies with *status:error* the master distributes this error to all connected clients and terminates the execution of the running script. Each client is responsible to act on the error message by itself and measures can range from doing nothing, stopping a pump or executing a complex shutdown procedure consisting of many commands.

The transportation of the commands over TCP/IP is handled by the STM library<sup>6</sup> maintained by National Instruments. This library simplifies communication between more then two communication partners by offering a *communication manager*. Further it offers specialized VIs handling all necessary data manipulation to send and receive data over TCP/IP.

<sup>6</sup><http://zone.ni.com/devzone/cda/tut/p/id/4095>

### 5.2.4 Two Example Clients

In the following, two clients will be discussed in further detail, which both illustrate certain aspects and challenges of the client development process very clearly. First the client for controlling up to six valves from Vici AG is used to illustrate the usefulness of the *steady state machine* and secondly the client for syringe pumps from Tecan Inc. is discussed giving insights into the *code parallelization abilities* of LabVIEW.

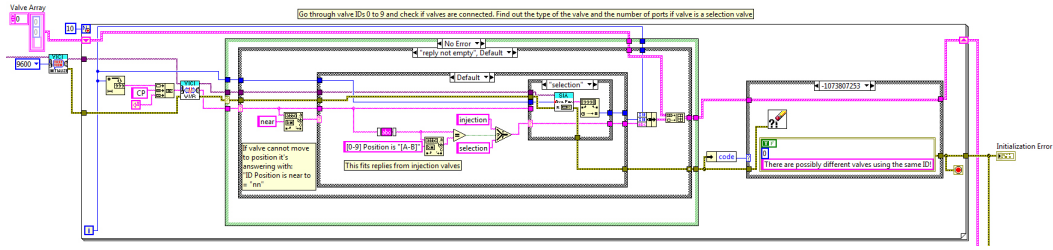
#### 5.2.4.1 Vici valve client

Vici AG valves are connected to the PC over a classical RS232 connection. However, the company decided to break the RS232 standard, which defines the connection between two connection partners only. Vici allows to connect up to ten valves to one RS232 port in parallel, where each of the valves is programmed by an unique ID number. Every command is sent to all connected valves, containing the ID number to address only one specific valve.

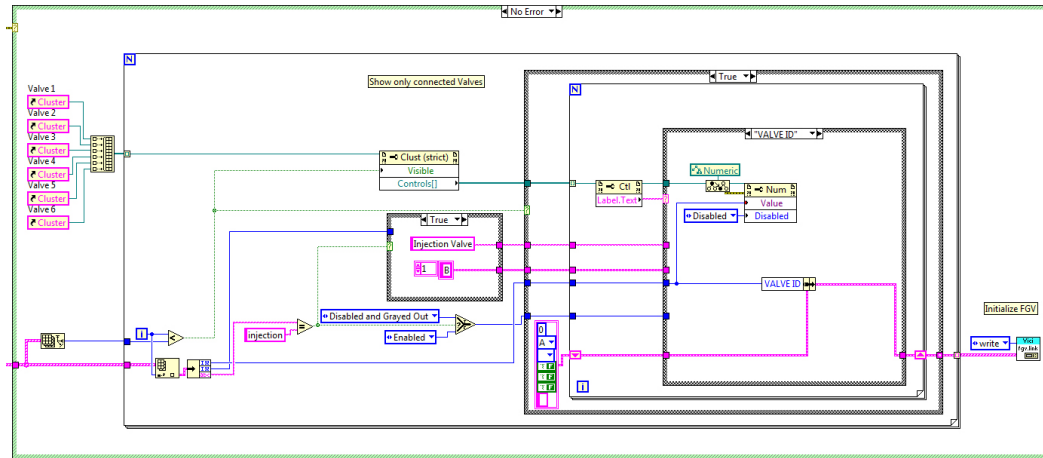
This fact is convenient because it reduces the number of RS232 connections needed. However, it also complicates the use of the valves because the IDs can be reprogrammed leading to errors if two valves use the same ID. Another layer of complexity is added due to the fact that two types of valves can be mixed on one RS232 port: injection and selection valves.

Therefore special thoughtfulness, while programming this client, was paid to the ease of use connecting more then one valve at once. If the user changes the COM Port in the GUI the *init state* of the *steady state machine* is called. As can be seen in figure 5.5 the *init state* connects to the specified COM port gathering information on the connected valves (a) and configuring the GUI afterwards.(b).

After the execution of the *init state* and the successful identification of connected valves the program changes into the running state and provides the user with the GUI, shown in figure 5.6 which only displays the actual connected valves along with their type and deactivates options not applicable for certain valves.



(a) First part of the *init state* of the Vici valve client aggregating information on connected valves at the specified COM port by sending the *CP* command, querying the current position of the valve, to all IDs from 0-9. If the reply contains "near" the queried valve has a positioning error, if the reply contains "A" or "B" the connected valve is an injection valve. In all other cases the program asks for the number of available ports of the selection valve. If a framing error (code -1073807253) occurs at any point during the communication with the valves it is most likely that two valves replied to the same query due to the identical *IDs*. The collected information is stored in a *cluster* and handed over to the program code shown in figure 5.5(b).



(b) By evaluating the cluster containing the information on connected valves only the GUI elements of the available valves are made visible by a *property node*. In the case structure further downstream all GUI elements not applicable for the connected valve are grayed out. After the GUI elements are configured the cluster containing the valve information is written to a *functional global variable* to make the information accessible in the *running state* of the *steady state machine* where it is used to assign *VALVE REFs* to the real *valve IDs*.

**Figure 5.5:** *G code of the init state of the Vici valve client*

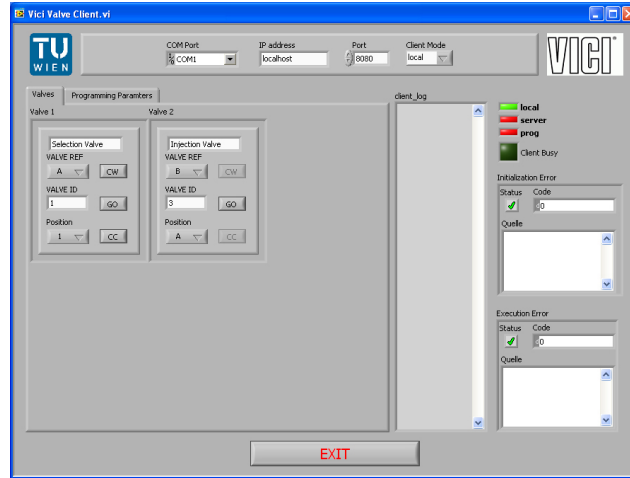


**Figure 5.6:** GUI of the ATLAS client for valves by Vici. The graph shows two connected valves, one selection and one injection valve. The selection valve can be switched to a different port by rotating clockwise (CW), counter clockwise (CC) or the valve can decide which way is faster (GO), whereas the injection valve only can switch between two states (GO).

As can be seen from figure 5.6, each valve is assigned with a *VALVE REF*, which is used to identify the valve in the *scripts*. This seems redundant at first since every valve already has an unique ID. However, this is necessary if one wants to use an old script with a new configuration of valves. In that case the *VALVE REF* can be changed in the GUI to match the *VALVE REF*s used in the old script so no changes need to be done in the script itself.

Using the *steady state machine architecture* a clear separation of the initialization routine and the rest of the program can be achieved. By searching the COM port for all connected valves right at the beginning, possible misconfigurations of the valves can be detected and the GUI is adjusted to actual connected hardware. By using the *steady state machine* it is very simple to re-run this initialization procedure if the user changes the COM port by simply calling this state of the *steady state machine* again. In addition to this advantage the *G code*<sup>7</sup> of the program is easier to read since the complex *G code* of the initialization is hidden while editing the rest of the program.

<sup>7</sup>The source code of a LabVIEW program is called G code.

#### 5.2.4.2 Tecan syringe pump client

One goal of the ATLAS platform was to give the user as much flexibility as possible writing scripts. One of the challenges arising from this ambition is the need to execute tasks on different connected hardware elements at the same time. Using the ATLAS platform this can be achieved quite easily by simply sending *status:ready* back to the *master* after starting the execution of a certain task even if the task is still active. Using a classical *producer consumer design pattern* (see chapter 5.2.2) on the client side, however, would *lock up* the client during the execution of this specific task making it *non-responsive* for input from the master and the GUI. If such a task is quick, such as switching a valve to a new port, this fact is of no consequence. If this task takes several seconds or even longer it needs to be decoupled from the interpretation and execution of new commands.

In the case of the *Tecan syringe pump* the command to pickup or deliver a defined volume just takes a few milliseconds to execute and is therefore executed directly in the *consumer loop* of the client. The time needed to pump the volume, however, takes much longer and since it is of great importance to monitor the movement of the plunger this monitoring task needs to be parallelized to the rest of the client program code. Only by doing so a possible failure of the pump can be detected and the *master* can be notified.

Using LabVIEW this *parallelization* is simply achieved by adding another loop parallel to existing loops. In figure 5.7 the *monitoring loop* for the pump movement can be seen right above the *producer loop* monitoring user input on the GUI. To minimize the CPU time used by this loop it is only executed upon request by the *consumer loop*, indicated by the partial loop structure at the very top of the figure. If a hardware error occurs the *monitoring loop* is stopped and the *master* is notified, which will distribute the error to all connected clients.

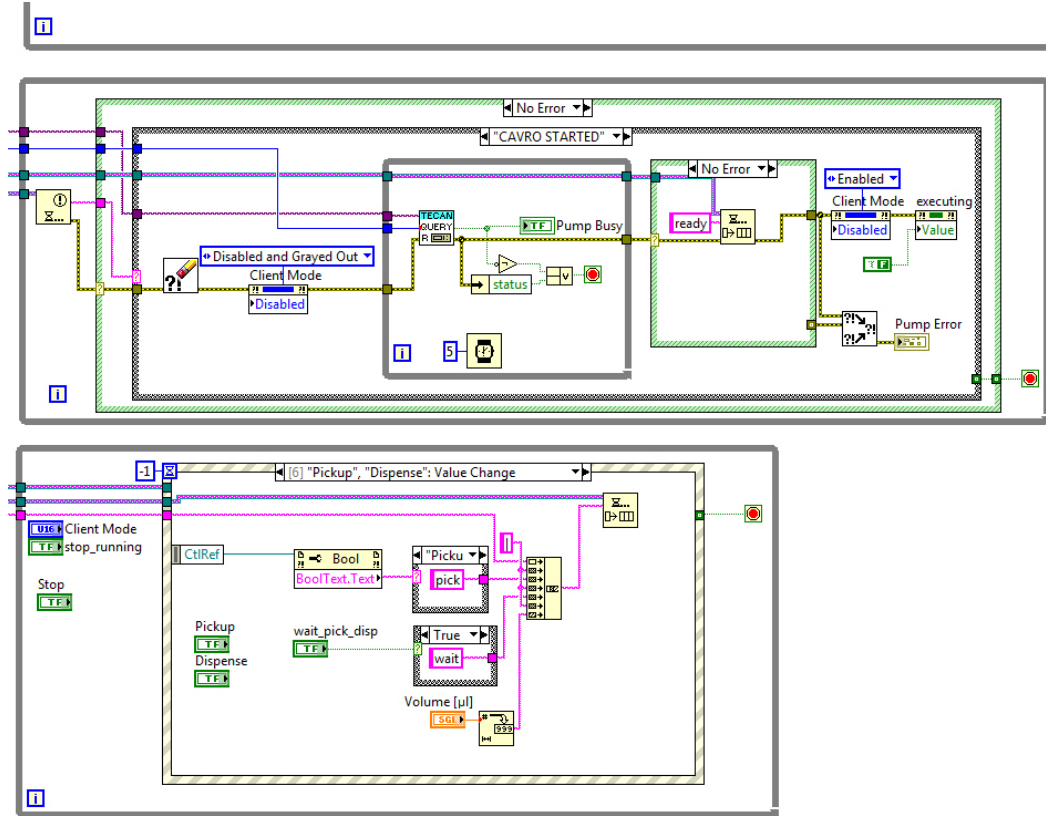


**Figure 5.7:** Partial G code of the Tecan syringe pump client showing the producer loop, the monitoring loop for the pump execution and the consumer loop indicated by the partial loop structure (from bottom to top) indicating parallel code by placing different loops next to each other. In the monitoring loop every 5 ms the status of the pump is queried by sending the appropriate command over the RS232 connection. As long as the pump answers that it is busy this loop keeps running. However as soon as the pump answers that it is ready or that an error occurred the loop stops and the master is notified.





# Evaluation of MOEMS spectrometers

---

## 6.1 Grating spectrometer

### 6.1.1 Determination of CO<sub>2</sub> in aqueous solution

The optical setup for the determination of dissolved carbon dioxide CO<sub>2(aq)</sub> in water consisted of a 20 W global IR source, an off-axis parabolic mirror, which focused the IR beam through a 25  $\mu\text{m}$  path length flow cell directly onto the entrance slit of the MOEMS grating spectrometer. To avoid interferences from water vapour and especially atmospheric CO<sub>2</sub>, the whole set up was encased in a plastic box flushed with nitrogen (5.0) from a gas bottle. For each spectrum 3000 scans were averaged directly by the spectrometer electronics, resulting in a measurement time of approximately 40 s per spectrum and an active scan time of 23 s, giving noise values summarized in table 6.1.

**Table 6.1:** *Typical noise values of the MOEMS grating spectrometer averaging 3000 scans*

Range	RMS	Peak to Peak (PP)
2500 – 2380 cm <sup>-1</sup>	0.011	0.048
2300 – 2215 cm <sup>-1</sup>	0.023	0.114

Due to the low solubility of carbon dioxide in water<sup>1</sup> the calibration standards had to be prepared in-situ to avoid out-gassing. Therefore different

---

<sup>1</sup>Solubility of CO<sub>2</sub> in water at 20°: 1.7 g · l<sup>-1</sup>

**Table 6.2:** *Equilibria reaction of carbon dioxide with water. Since only 0.1 % of the dissolved  $\text{CO}_{2(\text{aq})}$  forms carbonic acid the effective  $pK_{a1}$  value has to be calculated by  $pK_{a1} = 3.2 + 3.3 = 6.5$  resulting in a very weak acid.*

reaction	$pK_a$
$\text{CO}_{2(\text{g})} \rightleftharpoons \text{CO}_{2(\text{aq})}$	1.4
$\text{CO}_{2(\text{aq})} + \text{H}_2\text{O} \rightleftharpoons \text{H}_2\text{CO}_3$	3.2
$\text{H}_2\text{CO}_3 + \text{H}_2\text{O} \rightleftharpoons \text{H}_3\text{O}^+ + \text{HCO}_3^-$	3.3
$\text{HCO}_3^- + \text{H}_2\text{O} \rightleftharpoons \text{H}_3\text{O}^+ + \text{CO}_3^{2-}$	10.4

concentration of  $\text{NaHCO}_3$  were prepared and by *acidifying* them with citrate buffer (pH 3)  $\text{CO}_{2(\text{aq})}$  was released according to the equilibrium reaction of carbonic acid, shown in table 6.2. The mixing was achieved in a closed liquid handling system consisting of a peristaltic pump and a t-shaped junction as the mixing element.

To obtain the raw spectra of aqueous carbon dioxide, shown in figure 6.1(a) a mixture of pure water with citrate buffer solution was measured as a background before water was replaced by the  $\text{NaHCO}_3$  solution. As can be seen from the spectra baseline drifts and especially a tilting of the

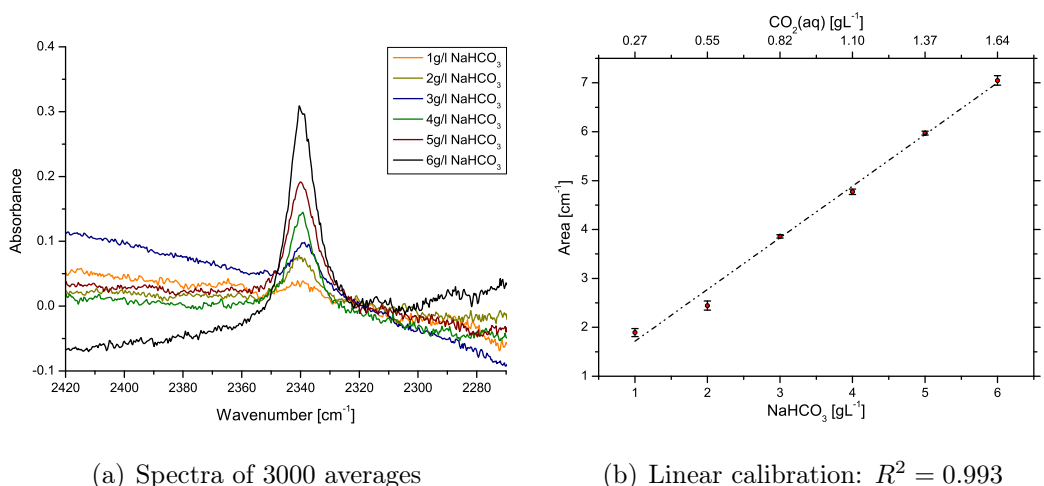


**Figure 6.1:** *Spectra and calibration curve of  $\text{CO}_{2(\text{aq})}$  obtained using the MOEMS grating spectrometer developed by Carinthian Tech Research AG*

baseline was observed. Those baseline variations can partially be contributed to the underlying absorption of water (combination of bending vibration  $\delta_2$  and libration mode  $L_2$ ) as well as to temperature effects on the MOEMS spectrometer caused by the powerful light source used in a closed environment.

Evaluating the spectra by applying a four point baseline correction<sup>2</sup> and integrating the band between  $2322\text{ cm}^{-1}$  and  $2359\text{ cm}^{-1}$  resulted in a linear calibration curve plotted in figure 6.1(b).

From the obtained data it has to be concluded that the MOEMS grating spectrometer is capable of measuring IR spectra in a limited spectral range at high speeds. However, the size of the grating (and in the case of the presented  $\text{CO}_{2(\text{aq})}$  measurements the angle of the grating) is a limiting factor in terms of energy throughput. The achieved S/N ratio allows for the quantification of dissolved carbon dioxide, however due to intensive averaging the advantage of speed is lost (**Publication V**).

Therefore the usability of this spectrometer for TR-FTIR measurements is limited to chemical reactions with strong absorptions and slow reaction kinetics.

## 6.2 FTIR spectrometer

### 6.2.1 Determination of $\text{CO}_2$ in aqueous solution

Within the time frame of this thesis only the MOEMS FTIR spectrometer of the first generation, described in chapter 2.1.2, could be evaluated. The experimental setup consisted of a 20 W IR source, a parabolic mirror focusing the light through the measurement cell onto a chalcogenide fibre leading to the spectrometer. The measurement cell consisted of two parallel  $\text{CaF}_2$  windows with an optical path length of  $100\text{ }\mu\text{m}$ . The movement of the scanning MOEMS mirror was limited to  $100\text{ }\mu\text{m}$  either side of the interferogram's centerburst, shown in figure 6.2 resulting in a spectral resolution of  $50\text{ cm}^{-1}$ . Averaging typically 512 scans for one spectrum resulted in a measurement time of approx.

---

<sup>2</sup>OPUS method E: baseline points at  $2221, 2291, 2389, 2510\text{ cm}^{-1}$

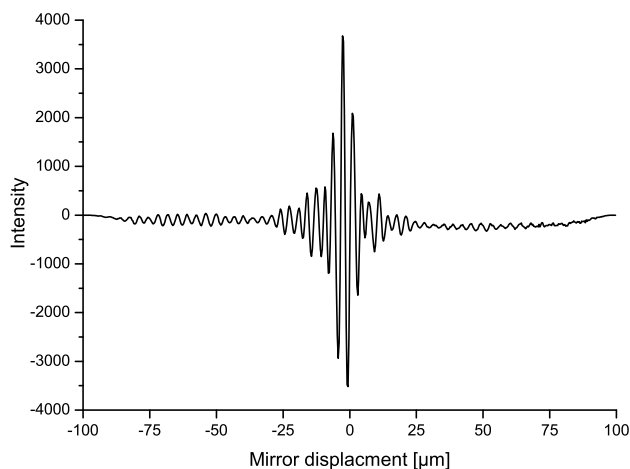


**Figure 6.2:** *Interferogram measured through 100  $\mu\text{m}$  of  $\text{H}_2\text{O}$ .*

0.7 s and gave noise values summarized in table 6.3 for the measurement of a 100 % line through 100  $\mu\text{m}$  of water.

**Table 6.3:** *Typical noise values of the MOEMS FTIR spectrometer averaging 512 scans in the spectral range  $2850 - 2420 \text{ cm}^{-1}$ .*

Range	RMS	PP
$2850 - 2420 \text{ cm}^{-1}$	0.023	0.102

Using the same sample preparation as for the evaluation of the MOEMS grating spectrometer, described in chapter 6.1, different calibration samples of  $\text{CO}_{2(\text{aq})}$  were prepared in-situ resulting in a linear calibration curve shown in figure 6.3.

Using a PFD Filling Device<sup>3</sup> from Anton Paar it was possible to measure real world samples avoiding out-gassing effects. This device pierces the cap of bottles or the bottom of cans immediately applying pressure to it through a compressed air supply. This overpressure not only keeps the  $\text{CO}_{2(\text{aq})}$  dissolved but it also presses the sample through the measurement cell.

Using this sampling system, spectra of mineral water, carbonated soft-drinks and beer were measured (figure 6.4(a)). Due to the extended spectral

<sup>3</sup>[http://www.anton-paar.com/Filling-Device-PFD/CO2-Meter/60\\_Corporate\\_en?product\\_id=309](http://www.anton-paar.com/Filling-Device-PFD/CO2-Meter/60_Corporate_en?product_id=309)

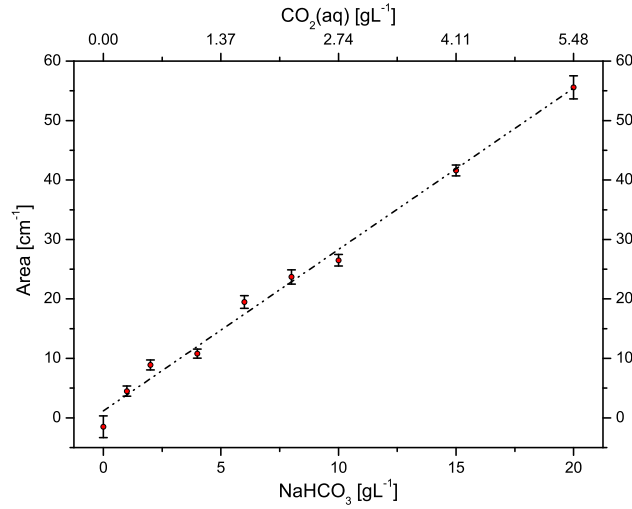
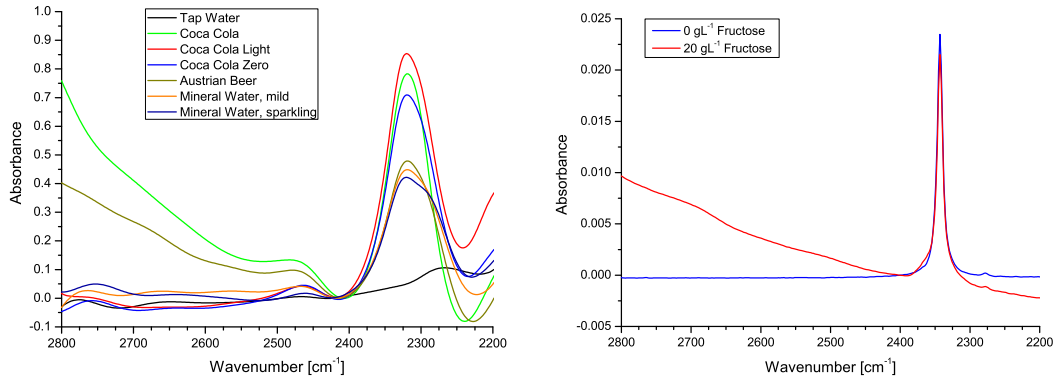


**Figure 6.3:** Linear calibration curve of  $\text{CO}_{2(\text{aq})}$  averaging 512 scans and integrating the  $\text{CO}_{2(\text{aq})}$  signal from  $2400 \text{ cm}^{-1}$  to  $2240 \text{ cm}^{-1}$ .

range of the MOEMS FTIR spectrometer, compared to the MOEMS grating spectrometer it was possible to additionally measure parts of the CH-stretching vibration region above  $2700 \text{ cm}^{-1}$ . The carbonated softdrink sample as well as beer show absorption in this spectral region indicating the presence of sugars.



(a) Beverage samples, 100  $\mu\text{m}$  path length      (b) Reference sample, 25  $\mu\text{m}$  path length

**Figure 6.4:** (a) IR spectra measured with the MOEMS FTIR spectrometer at a spectral resolution of  $50 \text{ cm}^{-1}$ . The spectra were baseline corrected at  $2410 \text{ cm}^{-1}$ . (b) IR spectra of  $\text{CO}_{2(\text{aq})}$  measured on a Bruker Tensor 27 spectrometer at a spectral resolution of  $2 \text{ cm}^{-1}$  showing the tilt of the baseline caused by dissolved carbohydrates.

Comparing the obtained spectra with a reference spectrum (figure 6.4(b)) measured on a Bruker Tensor 27 FTIR spectrometer using a spectral resolution of  $2\text{ cm}^{-1}$  shows that the maximum of the  $\text{CO}_{2(\text{aq})}$  band is red-shifted<sup>4</sup> which can be attributed to the low resolution of the MOEMS FTIR spectrometer.

In summary, the evaluated prototype with a spectral resolution of  $50\text{ cm}^{-1}$  is severely limited by the maximum achieved optical path difference of the interferometer. The high scan rate of this prototype again needs to be traded for longer scan times to achieve better S/N ratios (**Publication VI**). For time resolved studies, however, a higher spectral resolution is needed to be able to distinguish different species by their IR spectra. Further improvements of the MOEMS technology within the MEMFIS project already show improvements in terms of spectral resolution and could enable the use of MOEMS spectrometers for time resolved measurements in the near future.

---

<sup>4</sup>Band located at  $2320\text{ cm}^{-1}$  for the MOEMS FTIR spectrometer and at  $2343\text{ cm}^{-1}$  for the bench-top FTIR system.

# Step-scan TR-FTIR spectroscopy in a micro-fluidic system

---

As described in chapter 2.1.3, step-scan experiments on non-cyclic reactions need special experimental considerations. In this chapter the use of micro fluidic mixers for the measurement of non-cyclic reactions is discussed. Using a micro mixer instead of a standard flow cell, as used in classic IR spectroscopy, reduces the sample volume needed to a minimum, a pre-requirement for the measurement of biochemical samples. Using the micro mixer to mix two solutions right prior to the excitation for the step-scan experiment allows the usage of meta-stable reaction partners that would over time start reacting even without a trigger.

The developed measurement setup was intended for the infrared spectroscopic measurement of the reaction of cytochrome c oxidase with oxygen on the microsecond time scale. The reaction centre of the cytochrome c oxidase is reduced and deactivated by binding carbon monoxide to it. Using a light trigger the bound CO is released and the reaction is monitored.

The proposed "flow-flash" setup was evaluated using myoglobin as a test-molecule which was deactivated in the same way and the rebinding kinetics of the CO to the myoglobin molecule were monitored after photo-excitation under continuous flow conditions.

## 7.1 Experimental setup

### 7.1.1 Optical setup

The optical setup, shown in figure 7.1(a), for the step-scan measurements of aqueous protein samples consisted of an IR beamcondenser (schematics shown in figure 7.1(b)) connected to a Bruker IFS 66v/S spectrometer. The IR light was coupled out of the spectrometer through an exit port. Using a gold-coated parabolic off-axis mirror (D), with a focal length of 69 mm, the light was focused onto an X,Y,Z translational stage from beneath. The spot size on the micro mixer, mounted on the stage, was approximately 1 mm. The transmitted IR light was collimated by a second 69 mm parabolic off-axis mirror (C) and deflected downwards by a dichroic mirror (B) (Keveley Technologies, Chesterland, OH, USA) reflecting IR and transmitting visible light. A third off-axis parabolic mirror (focal length 43 mm finally focused the IR beam onto the MCT detector (E).

For the photo activation of the protein samples inside the micro mixer laser light was used, which was tuned to the right wavelength using an Optical Parametric Oscillator (OPO) (Opta GmbH, Bensheim, Germany) (A). The OPO was pumped by the third harmonic of a Nd:YAG laser (Quanta-Ray Lab-

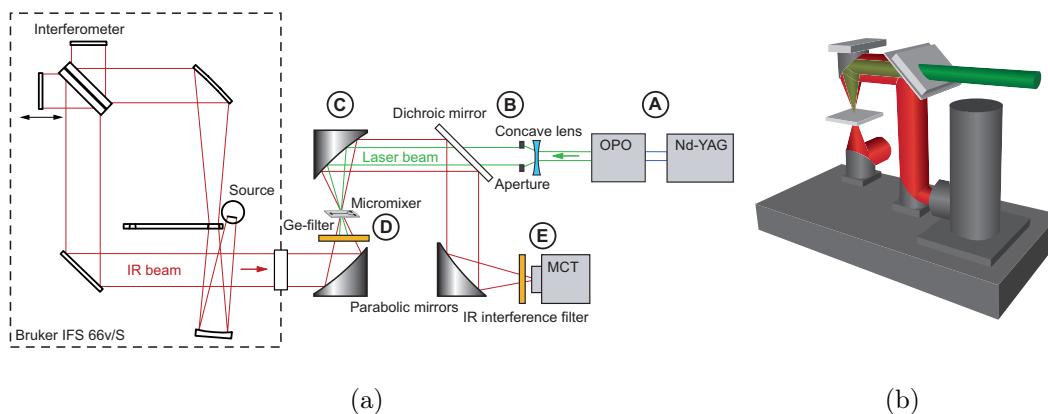


**Figure 7.1:** (a) Optical setup of the experimental set-up used for the Flow-Flash time resolved step-scan measurements. See the text for details. (b) 3D schematic of the used beamcondenser showing the IR beam path in red and the laser beam in green.



150, Spectra Physics, Mountain View, CA, USA). The laser light was directed towards the IR beamcondenser using dielectric mirrors. Before entering the beamcondenser the laser light was widened using a concave lens and a round aperture fully illuminating the parabolic mirror (C) to reduce the energy density down to approx.  $0.2 \text{ mJ} \cdot \text{cm}^{-2}$ . Otherwise the gold coated mirror would have been damaged due to absorptivity of gold in the visible spectral region. At the sample spot the focused laser beam had an energy density of around  $4 \text{ mJ} \cdot \text{cm}^{-2}$ .

To ensure that only sample, that was also probed by the IR light beam, was illuminated by the laser flashes, the mixer was covered with an additional metal aperture located on top of the mixer chip. The aperture had a rectangular shape of  $1 \times 1 \text{ mm}$  and was located at the end of the mixing channel. First the IR beam and the mixer position were optimized for maximum IR throughput. Afterwards the laser beam was adjusted using the last dielectric mirror to fully illuminate the area of the aperture hole.

Using the old mixer design, consisting of two  $\text{CaF}_2$  plates, the transmitted laser light through the mixer had to be blocked from entering the spectrometer. Using a Germanium filter (Laser Components, Olching, Germany) ensured blocking the laser without strongly attenuating the IR beam (D).

To *reduce* the number of *recorded data points*, necessary to suffice the Nyquist criterion, in the step-scan experiments the IR light reaching the detector was limited by a broadband filter (E) before reaching the detector. For measuring the fingerprint region of the protein samples a longpass filter ranging from  $1973 \text{ cm}^{-1}$  to  $0 \text{ cm}^{-1}$  was used, reducing the number of interferogram points to 1024 at a spectral resolution of  $4.5 \text{ cm}^{-1}$ . A bandpass filter from  $2429 \text{ cm}^{-1}$  to  $1669 \text{ cm}^{-1}$  was used for the measurement of the CO band region reducing the interferogram points to 169.

### 7.1.2 Data acquisition

The step-scan experiments had to be conducted at a repetition rate of 10 Hz, limited by the OPO. At that rate the Nd:YAG laser triggered its flash lamp and 180  $\mu\text{s}$  later the laser flash was emitted. Using a Transistor Transistor Logic

(TTL) signal provided by the Nd:YAG laser marking the ignition of the flash lamp, the data acquisition by the Bruker IFS 66v/S spectrometer was started. The MCT detector's pre-amplifier was connected to the external detector port of the spectrometer, which was used as a power supply for the pre-amplifier. The detector signal was amplified and the DC output of the pre-amplifier was off-set compensated using a specially designed electronic device. This signal was then digitized by the spectrometer's ADC at a resolution of 16 bit and a bandwidth of 200 kHz. For all measurements 1000 data points were acquired at a temporal resolution of 5  $\mu$ s. The first 36 spectra were recorded prior to the laser flash and their average was used as a reference spectrum to calculate the time resolved difference spectra.

The flow rate of the sample inside the mixing channel was chosen in a way that the sampled volume ( $10 \times 300 \times 1000 \mu\text{m} = 3 \text{ nL}$ ) was flushed four times between two subsequent laser flashes to ensure that only fresh sample was measured. Therefore the flowrate inside the channel was set to  $8 \mu\text{L} \cdot \text{min}^{-1}$ . Allowing that no more than 10 % of the sampled volume was exchanged during the measurement time only the first 2.5 ms of each time-resolved data set were used for data evaluation.

## 7.2 Measurements on myoglobin

### 7.2.1 Sample preparation

First 1 mL of 4 mM myoglobin solution from horse heart was prepared in a 25 mM phosphate buffer at pH 7.0. After centrifuging it at 14000 rpm the supernatant was filtered using a 0.2  $\mu\text{m}$  syringe filter. The solution was then carried over to a 25 mL bottle neck flask and sealed with a silicone septum. Afterwards the atmosphere inside the flask was exchanged with argon by applying five cycles of evacuating and aerating with argon under steady stirring of the solution.

The sample solution was then reduced by adding sodium dithionite to a final concentration of 16 mM under a counter current of argon through one of the bottlenecks. The reduced form of myoglobin, shown in figure 7.2(a) has a

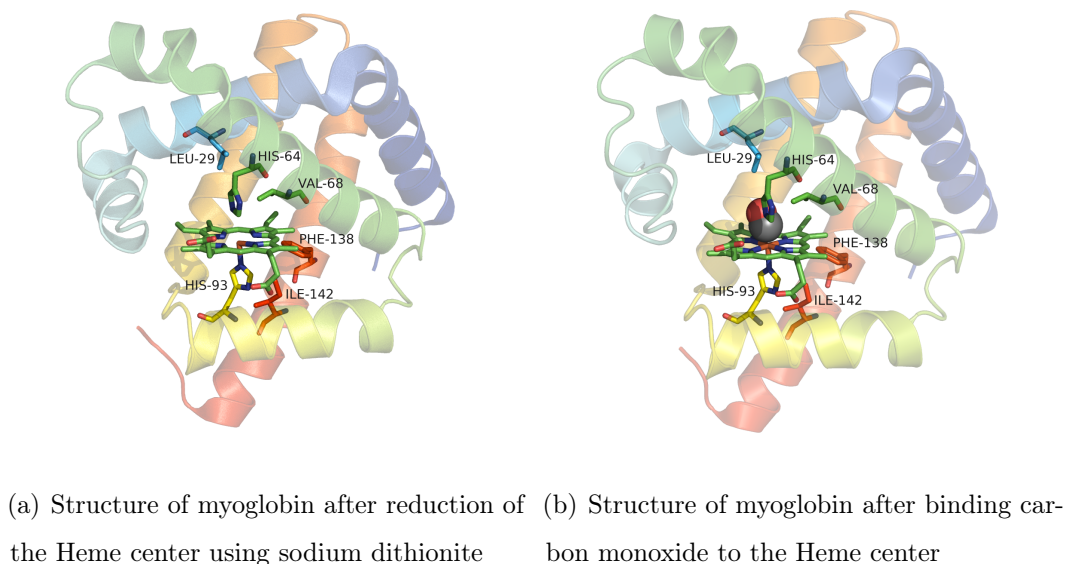


**Figure 7.2:** *Crystal structure of myoglobin.*

dark red colour compared to the brown colour of native myoglobin. Finally, the argon atmosphere was replaced with carbon monoxide using ten cycles of evacuating and aerating. The solution was then stirred for 30 min to form the carbonmonoxymyoglobin (Mb-CO), shown in figure 7.2(b) which has a bright red colour. The final solution was saturated with carbon monoxide at a concentration of approximately 1 mM.

The 3D models were calculated using the software package Pymol<sup>1</sup> using data from [59] for the deoxy-form and [60] for the Mb-CO data. Upon the uptake of the carbon monoxide, an out-of-plane movement of the Heme iron takes place, which leads to backbone displacements of various helices. As a consequence the histidine-64 amino acid moves into the Heme pocket and the side chain of the leucine-29 rotates slightly [61, 62].

The formation of the Mb-CO complex was verified by recording UV/VIS spectra before the sample was used. Figure 7.3 shows a comparison of myoglobin, deoxy-myoglobin and the Mb-CO complex showing a strong shift in

<sup>1</sup><http://www.pymol.org/>. Data downloaded from the Protein Data Bank: <http://www.pdb.org>

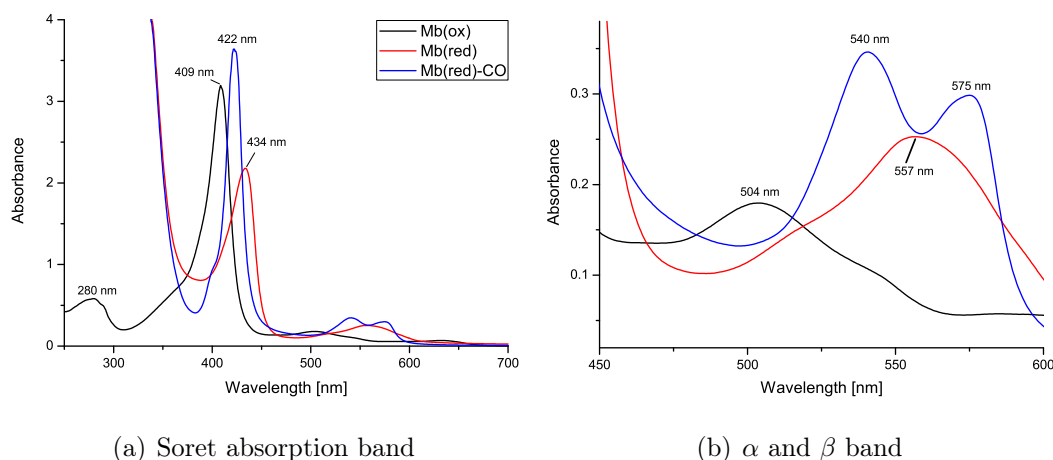


**Figure 7.3:** Typical UV/VIS spectra of the three forms of myoglobin. (a) shows the strong absorption of the Soret bands and (b) a zoomed in view of the spectral region of the  $\alpha$  and  $\beta$  bands.

the Soret absorption<sup>2</sup> (figure 7.3(a)) for the three different states. The absence of a shoulder at 434 nm in the spectrum of the Mb-CO complex shows that all reduced myoglobin was converted to the Mb-CO complex. However, a slight shoulder at 409 nm is evidence for remaining oxidized myoglobin.

Additionally to the shift in the Soret band the binding of carbon monoxide leads to a split of the  $\alpha$  band, shown in figure 7.3(b). Upon the binding of CO the  $\alpha$  band splits into a stronger  $\beta$  band at 540 nm and a remaining weaker  $\alpha$  band at 575 nm. For the initiation of the flow-flash experiment the laser was tuned to the maximum of the  $\beta$  band at 540 nm using the OPO system.

## 7.2.2 Measurements

The presented measurements on myoglobin have been recorded using the old micro mixer design described in chapter 4.1 with the purpose to evaluate the proposed flow-flash setup (see chapter 7.1).

As a first test a single-channel spectrum of the Mb-CO complex was recorded in AC-coupled mode, shown in figure 7.4(a), inside the mixing channel. At

<sup>2</sup>The spectral region of 400 to 500 nm is called Soret band and is widely used for spectrophotometric determination of metalloporphyrins [63].

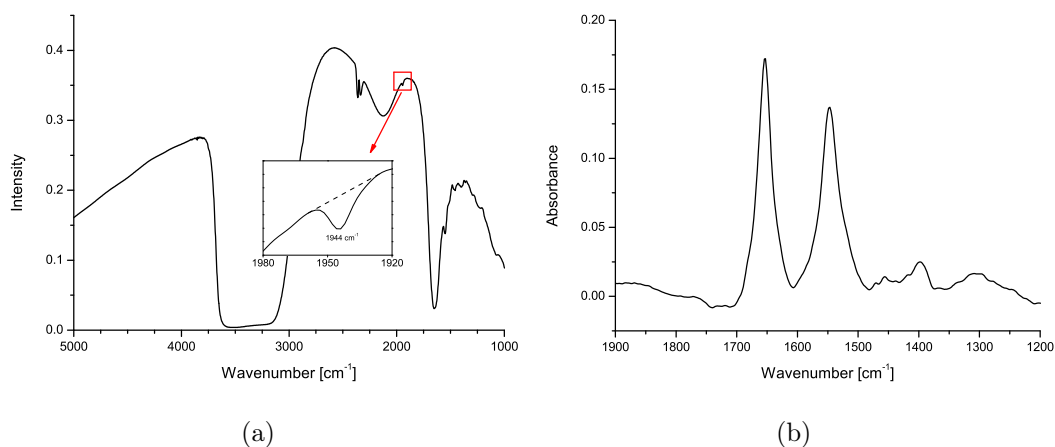


**Figure 7.4:** (a) Single channel spectrum of 4 mM Mb-CO solution recorded inside the micro mixer using the beamcondenser setup. The absorption at  $1944\text{ cm}^{-1}$  is the result of carbon monoxide. (b) Absorption spectrum of myoglobin measured inside the micro mixer showing the strong Amide I and II absorption features.

$1944\text{ cm}^{-1}$  the stretching vibration of carbon monoxide can clearly be seen. Recording a single channel spectrum of water inside the mixer allowed to calculate an absorption spectrum of the 4 mM myoglobin solution inside the mixer. However, due to the high concentration of myoglobin a negative absorbance at  $1644\text{ cm}^{-1}$  occurred as a result of the displaced water molecules. To obtain the absorption spectrum shown in figure 7.4(b) a spectrum of water was added to the absorption spectrum of myoglobin in such a way that the negative absorption of the combination vibration of water around  $2100\text{ cm}^{-1}$ , which doesn't interfere with the Amide I absorption of myoglobin, was minimized.

The data shows that recording decent protein spectra in the mixer is possible and also proves in addition to the UV/VIS measurements that the Mb-CO complex was formed successfully and is stable enough to be transferred to the syringes used to fill the mixer with the sample solution.

In a next step the flow flash setup was tested recording step-scan data using laser flashes at 540 nm to dissociate CO from myoglobin. The IR light reaching the detector was limited by a bandpass filter, which was mounted in front of the MCT detector. Averaging 40 time slices at each of the 169 interferogram

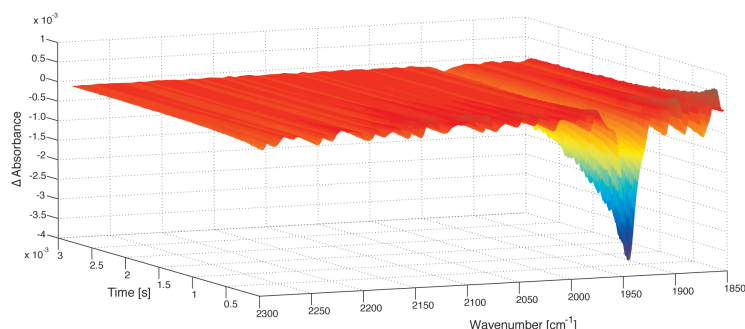


**Figure 7.5:** Result of a flow-flash experiment showing the rebinding of the carbon monoxide to the deoxy-myoglobin.

points, a whole time-resolved data set was recorded consuming just 22  $\mu\text{L}$  of the sample solution. Taking the average of the first 36 spectra, which were recorded prior to the excitation, and using their average as the background spectrum difference spectra were calculated. As a result, a 3 dimensional data set of the flow-flash experiment, shown in figure 7.5, was obtained. Allowing that only 10 % of the sample was exchanged during the measurement the evaluated time frame had to be reduced to 2.5 ms<sup>3</sup> being too short to follow the complete rebinding of the carbon monoxide.

The observed negative band at  $1943\text{ cm}^{-1}$  is the result of the dissociation of the Mb-CO complex after the laser excitation. The dissolved carbon monoxide in the solution is then rebinding to the Heme iron. Figure 7.6(a) shows the difference spectrum 10  $\mu\text{s}$  after excitation, extracted from the data shown in figure 7.5. Figure 7.6(b) shows the rebinding kinetics of the carbon monoxide to myoglobin. Applying a bi-exponential fit to the data results in time constants of  $\tau_1 = 185\text{ }\mu\text{s}$  and  $\tau_2 = 1\text{ ms}$ .

In figure 7.6(c) and (d) the order of the rebinding kinetics is evaluated. By plotting the inverse of the deoxy-myoglobin concentration against time results in a linear fit for second order reaction kinetics, whereas plotting the natural logarithm of the deoxy-myoglobin concentration against time gives a linear relation ship for first order kinetics.

<sup>3</sup>This value poses a compromise between the repetition rate of the laser, the time needed to flush the sample volume four times between two laser flashes and only 10 % of sample volume being exchange during the measurement.

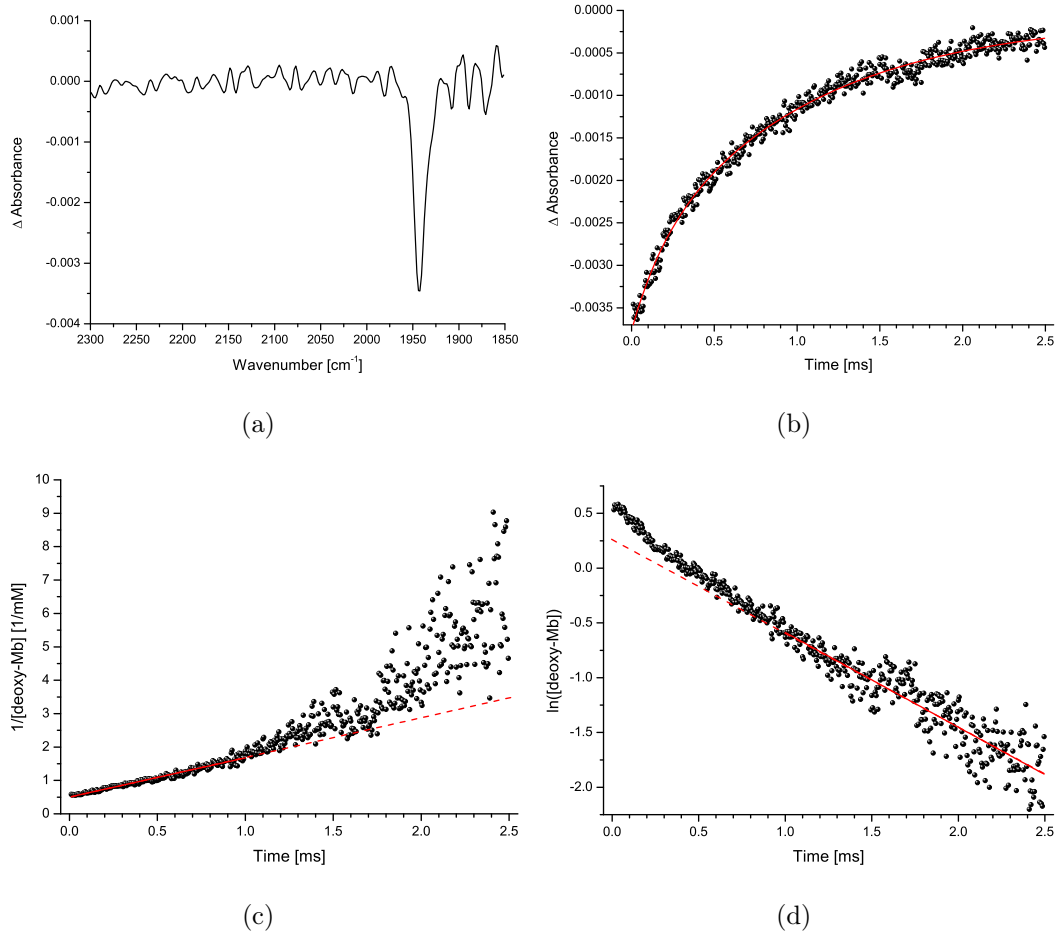


**Figure 7.6:** (a) Difference spectrum of the deoxy-myoglobin form observed after photo dissociation, showing negative absorption at the band position of the CO stretching vibration at  $1943 \text{ cm}^{-1}$ . (b) Bi-exponential fit for the CO band ( $\tau_1 = 185 \text{ }\mu\text{s}$ ,  $\tau_2 = 1 \text{ ms}$ ). (c) Plotting the reciprocal of the deoxy-myoglobin concentration against the reaction time indicates a second order reaction for reaction times  $< 1 \text{ ms}$ . (d) Plotting the natural logarithm of the deoxy-myoglobin concentration indicates a pseudo-first order reaction for reaction times  $> 1 \text{ ms}$ .

From figures 7.6(c) and (d) it is apparent that for reaction times up to approx. 1 ms the rebinding of carbon monoxide to the deoxy form of myoglobin follows a second order kinetic and a first order kinetic for reaction times  $> 1$  ms. This means that for the beginning of the rebinding the concentration of the deoxy-myoglobin as well as the concentration of the carbon monoxide in the sample solution are time limiting factors. After the dissociation of the Mb-CO complex the concentration of carbon monoxide in the solution is approximately 5 mM and much higher than the equilibrium concentration of dissolved carbon monoxide at room temperature (1 mM) resulting in a second order kinetic. For later time slices the concentration of carbon monoxide in the solution approaches the equilibrium concentration and the reaction is of pseudo-first order.

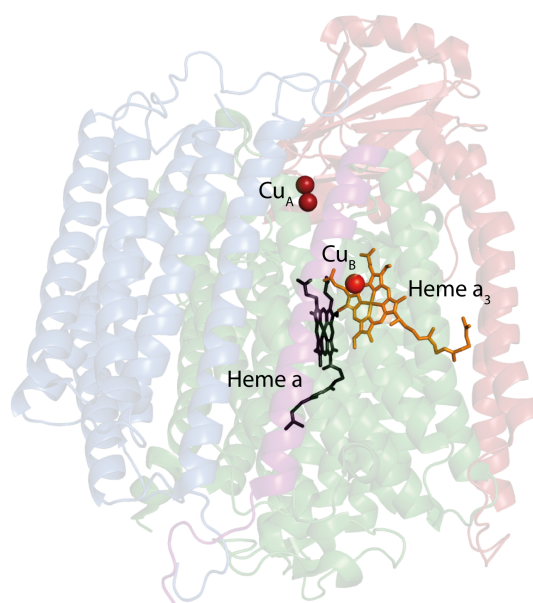
For the spectral region of the Amide bands of the protein a second experiment was conducted using an appropriate optical filter. Due to the lower S/N ratio in that region 150 scans had to be averaged, consuming 230  $\mu\text{L}$  of sample, and advanced signal processing techniques were required to extract the protein signals. Data presented in **Publication VII**.

The obtained kinetics for the CO rebinding are in good agreement with data from Dixon et al. [64], proving that the proposed flow-flash setup is capable of recording time-resolved data of proteins in flow if the exchanged sample volume is small enough during the measurement time of each time slice. In the presented case 10 % of the probed volume was exchange during the evaluated measurement time of 2.5 ms.

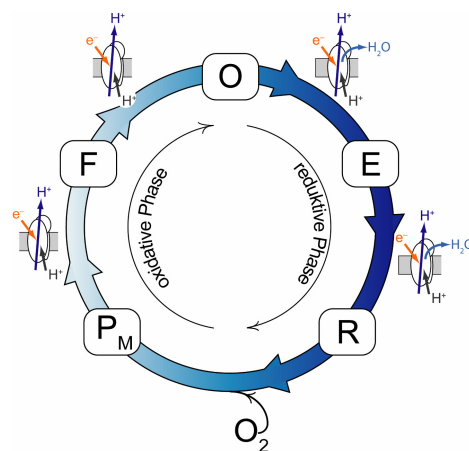
### 7.3 Measurements on cytochrome c oxidase

Cytochrome c oxidase is the complex IV of the electron transfer chain that generates chemical energy by producing Adenosine TriPhosphate (ATP). Cytochrome c oxidase takes four electrons from four cytochrome c molecules transferring them to one oxygen molecule, producing two molecules of water while pumping four protons across the inner cell membrane. Thus, it contributes to the proton gradient necessary to produce ATP by the ATP-synthase.





(a)



(b)

**Figure 7.7:** (a) Crystal structure of the cytochrome c oxidase, showing the subunits I (green), II (red), III (blue) and IV (purple). Electrons are being transferred from the  $\text{Cu}_A$  over the Heme a to the active reaction centre of the cytochrome c oxidase consisting of the Heme  $a_3$  and the  $\text{Cu}_B$ . (b) Reaction cycle of the cytochrome c oxidase. Refer to the text for a detailed description. The figure is reproduced with kind permission from Michael Schlegel [65].

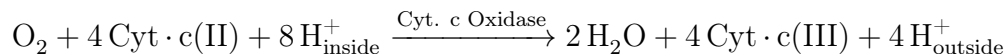
For the presented work, cytochrome c oxidase from *Rhodobacter spaeroides* [66] was used. A 3D model of the used cytochrome c oxidase rendered from crystallographic data is shown in figure 7.7(a). The different subunits (I-IV) are shown in different colours and the active centres of the cytochrome c oxidase located in subunit I (shown in green) consisting of the  $\text{Cu}_B$  ion and the Heme  $a_3$  are shown in red and orange. A  $\text{Cu}_A$  pair is located in subunit II (shown in red), which is accountable for the uptake of the electrons from the cytochrome c molecules. Additional co-factors of the cytochrome c oxidase are Ca and Mg ions located in subunit I.

A full reaction cycle of the cytochrome c oxidase is shown in figure 7.7(b) starting at the *state O* where all four redox centres are oxidized [65]:

- Transition  $O \rightarrow E$ : One electron is taken from a cytochrome c molecule and transferred by the  $\text{Cu}_A$  over the Heme a to the reactive center of the cytochrome c oxidase, reducing the  $\text{Cu}_B^{\text{II}}$  to  $\text{Cu}_B^{\text{I}}$ , pumping one proton across the membrane and taking up one proton in the reactive center. This proton is transferred to a hydroxyl-ligand and a water molecule is released.
- Transition  $E \rightarrow R_2$ : The uptake of a second electron reduces the iron center of the Heme  $a_3$  ( $\text{Fe}_{a_3}^{\text{III}} \rightarrow \text{Fe}_{a_3}^{\text{II}}$ ). Again, one proton is pumped and another proton is taken up again being most likely transferred to a hydroxyl-ligand and released as a water molecule. *Comment:* A fully reduced state of the cytochrome c oxidase, called  $R_4$  state, where all co-factors are reduced, is not observed in nature but can be produced artificially by using a reducing agent.
- Transition  $R_2 \rightarrow P_M$ : The Heme  $a_3$  binds one molecule of oxygen, breaking the  $\text{O}_2$  double bond to give an oxo-complex of the Heme iron ( $\text{Fe}_{a_3}^{\text{II}} \rightarrow \text{Fe}_{a_3}^{\text{IV}}$ ) and a hydroxyl-complex of the  $\text{Cu}_B^{\text{II}}$  ( $\text{Cu}_B^{\text{I}} \rightarrow \text{Cu}_B^{\text{II}}$ ). Four electrons are needed, three of which are provided by the metal centres and the fourth one coming from an amino acid (tyrosin 288) forming a radical.

- Transition  $P_M \rightarrow F$ : Another electron is taken up and transferred to the amino acid radical forming an anion in the F state.
- Transition  $F \rightarrow O$ : In this step another electron is used to reduce the Heme  $a_3$  iron ( $Fe_{a_3}^{IV} \rightarrow Fe_{a_3}^{III}$ ) and a proton is transferred to the oxo-complex forming a hydroxyl-ligand. The state of the tyrosin 288 is described as protonated and deprotonated in literature. This reaction step is again coupled to pumping a proton, and the slowest step with a reaction constant of  $\tau = 1$  to 3 ms.

The reaction of the cytochrome c oxidase can be summarized in the following equation:



The reaction pathways how the three protons are transferred to the tyrosine anion and the hydroxyl-ligands is still being discussed in literature. Mixing an oxygen rich buffer solution with the artificial  $R_4$  state of the cytochrome c oxidase using the flow-flash setup described in chapter 7.1 promised to give new insights into the described reaction mechanism. First steps towards this proposed experiment are described below.

### 7.3.1 Sample preparation

The sample was prepared as described in chapter 7.2.1 for the myoglobin samples. Adding  $Na_2S_2O_4$  to a final concentration of 29 mM resulted in the fully reduced form of cytochrome c oxidase ( $R_4$ ). Cytochrome c oxidase concentrations larger than 300  $\mu\text{M}$  lead to aggregation effects limiting the highest possible sample concentrations. For the pursued experiment, mixing such samples with a oxygen rich buffer would result in a protein concentration, which is less concentrated by a factor of 27 compared to the myoglobin concentration used for testing the flow-flash setup.

The samples were again measured in the UV/VIS range. The obtained spectra are shown in figure 7.8. From the shoulder at 421 nm in the spectrum of the CO bound  $R_4$  state (blue) it can be seen that a little percentage of the oxidized cytochrome c oxidase form was not reduced and CO bound.

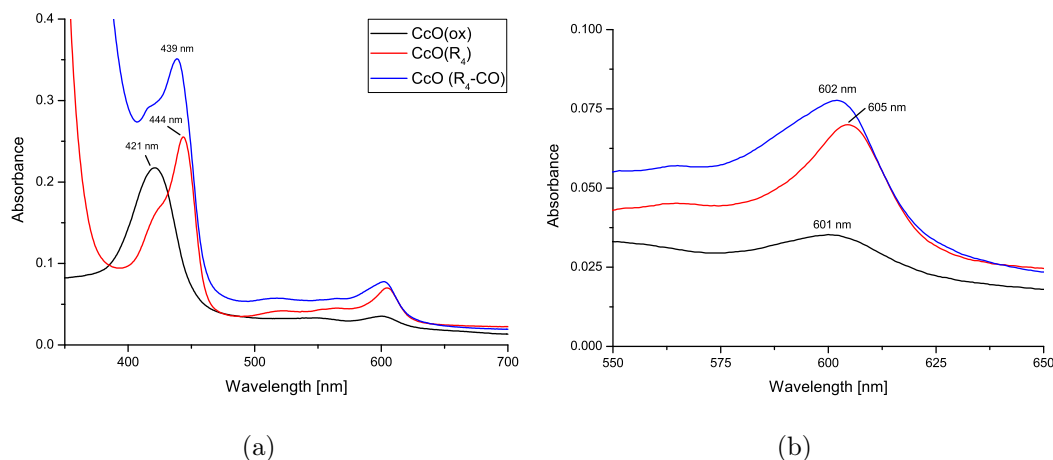


**Figure 7.8:** *UV/VIS spectra of the three states of cytochrome c oxidase. A blue shift of the Soret band and the  $\alpha$  band identifies the CO bound cytochrome c complex compared to the fully reduced form (R<sub>4</sub>) [67].*

### 7.3.2 Measurements

The sample was transferred into a BaF<sub>2</sub> cuvette with a path length of 25  $\mu\text{m}$  and measured using the beamcondenser for a first offline test. In analogy to the flow-flash experiment on myoglobin the CO complex of the R<sub>4</sub> state was excited by a laser flash (590 nm, 4 mJ  $\cdot$  cm<sup>-2</sup>) resulting in a negative difference band at 1964 cm<sup>-1</sup>, shown in figure 7.9, and a rebinding to the cytochrome c oxidase. In contrast to the measurements using the micro mixer a higher photon throughput was possible due to the missing aperture, giving a better S/N ratio as well as a higher path length was used.

Transferring the experiment into the micro mixer failed. Averaging the data from 22 experiments each containing 20 coadditions recorded on cytochrome c oxidase in flow inside the 10  $\mu\text{m}$  path length mixer led to a S/N ratio comparable to the one obtained in the stationary experiment. However, a signal from the CO excitation could not be recorded, most probably due to the smaller path length and a reduced sample concentration that had to be used because of the high viscosity of a 300  $\mu\text{M}$  cytochrome c oxidase solution which couldn't be pumped through the mixer any more.

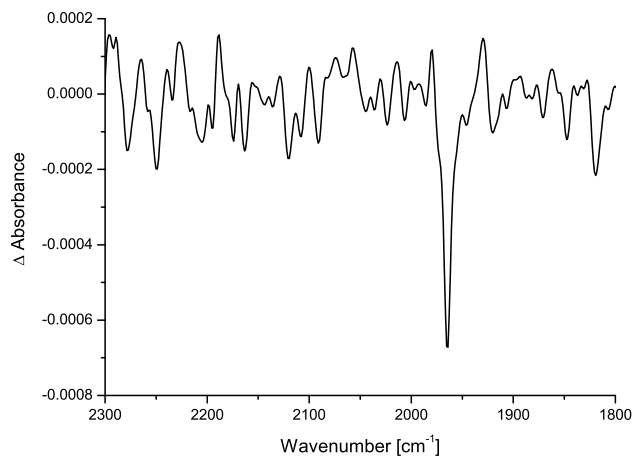


**Figure 7.9:** *Difference spectrum measured for the  $R_4$  state of cytochrome c oxidase using a static sample in a  $\text{BaF}_2$  cuvette with an optical path length of 25  $\mu\text{m}$  averaging 10 coadditions.*

Increasing the photon throughput while increasing the path length, however, could enable the proposed experiment in the future. One possible way would be to use an external cavity quantum cascade laser instead of the step-scan spectrometer, taking advantage of the higher spectral energy density of the laser. Increasing the path length of the mixer would result in a slower mixing time, which can be accepted since the measurements are taken at one spot only, which can be located at a point where the mixing process is already finished.



# Rapid scan TR-FTIR spectroscopy in a micro-fluidic system

---

The reactions, described in the following, have been measured in *continuous flow mode* as outlined in chapter 3.3 using the mixers of the new generation, described in chapter 4.2 by mixing two reagents under steady flow and following the advancing chemical reaction using the Bruker Hyperion 3000 microscope. By moving the measurement spot away from the mixing spot later reaction times are observed. Mixing induced measurements have been summarized in **Publication VIII**.

## 8.1 Experimental set-up

The mixing chip was mounted in its support holder, described in chapter 4.2.2, and screwed onto a metal plate, suitable for the use with the X,Y table of the Bruker Hyperion 3000 microscope. The two input connections were fed through PEEK capillaries to avoid pressure fluctuations due to stretching of the wall material of the tubings. The inner diameter of the tubings was 250  $\mu\text{m}$  and they were connected to Hamilton glass syringes of 500 or 1000  $\mu\text{L}$  volume. These syringes were mounted on a KDS100 syringe pump (KD Scientific Inc., MA, USA), which is capable of delivering even low volumes at constant flow rates.

The metal plate was then fixed on the X,Y stage by the provided clamps. Due to the stiffness of the PEEK tubings the plate was additionally fastened using two strips of adhesive tape. According to Nina Kaun this measure is not enough for holding the mixer in place [2, p.56], however, no deficiency has

been observed. One adversity observed was the fact that the mixing channel could never be arranged parallel to the X direction of the microscope. This fact was taken into account while calculating the measurement positions for the experiment by an introduced offset in Y direction after an appropriate number of measurement positions. Using this method the measurement spots were kept in the middle of the channel independent from the tilting of the mixer. The spacing of the measurement positions was chosen according to the selected aperture width of the microscope.

The height of the aperture was normally chosen to be 100  $\mu\text{m}$  considering the width of the mixing channel of 200  $\mu\text{m}$ , thus eliminating the areas on the side of the mixing channel where poor mixing occurred due to the laminar flow profile. The width of the aperture was also set to 100  $\mu\text{m}$  for S/N ratio considerations, giving a sufficient S/N ratio at  $100 \times 100 \mu\text{m}$  aperture size at 32 scans. Increasing the time resolution of the experiment was attained by changing the flow rate inside the mixing channel rather than by closing the width of the aperture.

In the following, three different chemical systems have been investigated in *continuous flow mode* using the new micro mixer design.

## 8.2 Formaldehyde sulfite clock reaction

The outstanding feature of clock reactions is the sudden appearance of a product some time after the initial mixing of reagents [68]. For the formaldehyde sulfite clock reaction such behaviour is observed in a closed batch reactor manifested by a slowly increasing pH value at the beginning, followed by a rapid increase. Conversely, a bistable behaviour oscillating between a low and a high pH state was reported for an open flow reactor [69]. Kovacs et al. summarized the formaldehyde sulfite clock reaction in the reaction scheme shown in table 8.1.

The rate determining step of the reaction can be found in the *dehydration of methylene glycol* – a dimer formed by formaldehyde in aqueous solution – releasing formaldehyde (step 1). The slow increase of the pH at the beginning of the reaction is due to an internal *sulfite - bisulfite buffer* (step 2) which supplies  $\text{HSO}_3^-$  and  $\text{H}^+$  which are consumed through reactions three and four.



**Table 8.1:** *Mechanism of the Formaldehyde sulfite clock reaction [69]*

reaction	rate constants ( $k_f$ , $k_r$ )	
$\text{CH}_2(\text{OH})_2 \rightleftharpoons \text{CH}_2\text{O} + \text{H}_2\text{O}$	$5.5 \times 10^{-3} \text{ s}^{-1}$ , $10 \text{ s}^{-1}$	(1)
$\text{HSO}_3^- \rightleftharpoons \text{SO}_3^{2-} + \text{H}^+$	$3.1 \times 10^3 \text{ s}^{-1}$ , $5 \times 10^{10} \text{ M}^{-1} \text{ s}^{-1}$	(2)
$\text{CH}_2\text{O} + \text{SO}_3^{2-} \longrightarrow \text{CH}_2(\text{O}^-)\text{SO}_3^-$	$5.4 \times 10^6 \text{ M}^{-1} \text{ s}^{-1}$	(3)
$\text{CH}_2(\text{O}^-)\text{SO}_3^- + \text{H}^+ \rightleftharpoons \text{CH}_2(\text{OH})\text{SO}_3^-$	$1 \times 10^9 \text{ M}^{-1} \text{ s}^{-1}$ , $2 \times 10^{-3} \text{ s}^{-1}$	(4)
$\text{H}_2\text{O} \rightleftharpoons \text{H}^+ + \text{OH}^-$	$1 \times 10^{-3} \text{ M}^{-1} \text{ s}^{-1}$ , $1 \times 10^{11} \text{ M}^{-1} \text{ s}^{-1}$	(5)
$\text{CH}_2\text{O} + \text{HSO}_3^- \longrightarrow \text{CH}_2(\text{OH})\text{SO}_3^-$	$4.5 \times 10^2 \text{ M}^{-1} \text{ s}^{-1}$	(6)
$\text{CH}_2(\text{OH})_2 + \text{SO}_3^{2-} \longrightarrow \text{CH}_2(\text{O}^-)\text{SO}_3^- + \text{H}_2\text{O}$	$2.5 \text{ M}^{-1} \text{ s}^{-1}$	(7)
$\text{CH}_2(\text{OH})_2 + \text{HSO}_3^- \longrightarrow \text{CH}_2(\text{OH})\text{SO}_3^- + \text{H}_2\text{O}$	$0.48 \text{ M}^{-1} \text{ s}^{-1}$	(8)

As soon as all  $\text{HSO}_3^-$  is consumed the pH of the reaction solution starts to increase rapidly. Reaction step 6 was added to the reaction scheme to explain the system's behaviour at low  $S^{IV}$  concentrations and reaction steps 7 and 8 together with reaction 1 are responsible for determining the computed induction time of the reaction. The proposed reaction mechanism however does not explain the observed pH oscillations in a flow reactor which would need some kind of a feedback process [69].

Measuring the reaction in our micro mixers allows for the direct observation of reaction species by following their progression over time. A typical data set recorded with the Bruker Hyperion 3000 microscope while mixing a 0.2 M aqueous solution of  $\text{Na}_2\text{SO}_3$  with a 0.2 M aqueous formaldehyde solution is

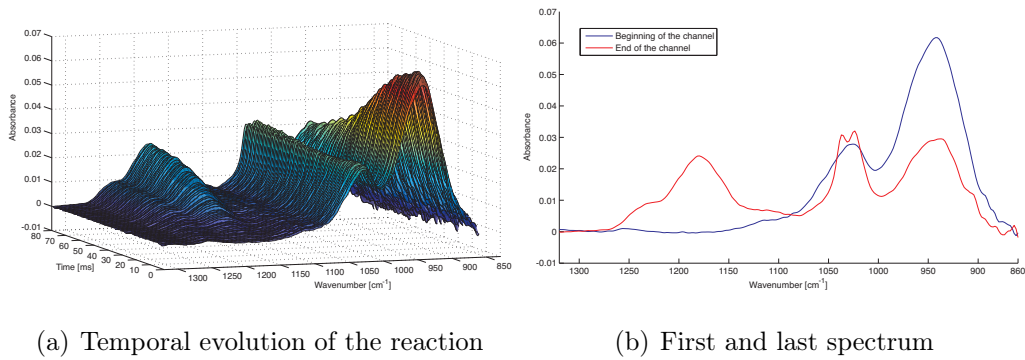


**Figure 8.1:** *Data set recorded for the formaldehyde sulfite clock reaction using an 8  $\mu\text{m}$  path length micro mixer at channel flow rate of  $10 \mu\text{L} \cdot \text{min}^{-1}$ .*

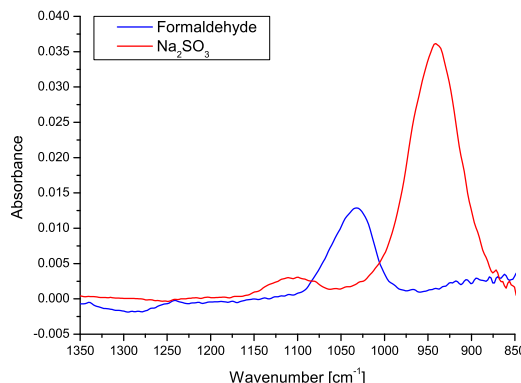


**Figure 8.2:** Reference spectra of pure  $\text{Na}_2\text{SO}_3$  and formaldehyde solutions measured inside an  $8\text{ }\mu\text{m}$  mixer showing the only observed bands in the mid-IR region located at  $941.8\text{ cm}^{-1}$  and  $1105\text{ cm}^{-1}$  for  $\text{Na}_2\text{SO}_3$  and at  $1031.8\text{ cm}^{-1}$  for formaldehyde.

plotted in figure 8.1(a) and figure 8.1(b) shows the first and last spectrum of the shown 3D plot pointing out the observed spectral changes.

Band assignments for the observed absorption bands are difficult due to the surprisingly complex chemistry of aqueous  $\text{SO}_2$  solutions [70]. Recorded reference spectra are shown in figure 8.2 showing an intensive band at  $941.8\text{ cm}^{-1}$  and a band of low intensity at  $1105\text{ cm}^{-1}$ . Investigations by Pichler et al. showed that with increasing concentrations of  $\text{HSO}_3^-$  a sharp absorption band at  $966\text{ cm}^{-1}$  rises which isn't observed for concentrations of  $0.5\text{ M}$  but very strong for  $\approx 3.6\text{ M}$  due to the  $\text{S}_2\text{O}_5^{2-}$  anion formed by the condensation reaction  $2\text{HSO}_3^- \rightleftharpoons \text{S}_2\text{O}_5^{2-} + \text{H}_2\text{O}$  [71]. Herlinge et al. assigned a broad band of strong intensity at  $961\text{ cm}^{-1}$  to the S–O stretching vibration of the  $\text{S}_2\text{O}_5^{2-}$  and  $\text{SO}_3^{2-}$  anions, a band at  $1022\text{ cm}^{-1}$  was assigned to the  $\text{HSO}_3^-$  species and a very strong band at  $1050\text{ cm}^{-1}$  also results from the  $\text{S}_2\text{O}_5^{2-}$  anion [72].

In figure 8.1(b) two absorption bands are observed for the first spectrum recorded inside the mixer. The stronger one observed at  $942\text{ cm}^{-1}$  comes close to the reported S–O vibration of  $\text{S}_2\text{O}_5^{2-}$  but wasn't observed by Pichler et al. for concentrations of  $0.2\text{ M}$  as used for our experiments. From the reaction progress shown in figure 8.1(a), however, it is apparent that the species contributing to this absorption are consumed during the reaction and are most likely a result from overlapping absorptions of different species. The

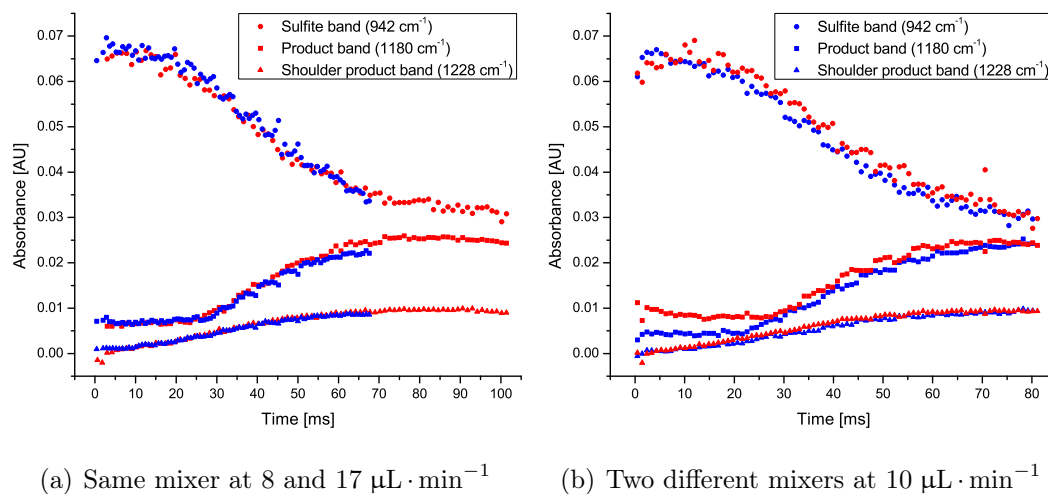


**Figure 8.3:** *Reproducibility tests for the formaldehyde sulfite clock reaction. (a) Using the same mixer on the same day at different flow rates gives very reproducible results. (b) Comparing two different mixers on different days using the same flow rates also gives reproducible results. However, slight deviations for the rising product band were observed.*

second observed band at 1025  $\text{cm}^{-1}$  is caused by the C–O stretching vibration of the methylene glycol form of formaldehyde overlapping with spectral features of  $\text{HSO}_3^-$ .

During the proceeding reaction a broad band at 1180  $\text{cm}^{-1}$  with a shoulder around 1228  $\text{cm}^{-1}$  rises, whereas the band located at 1025  $\text{cm}^{-1}$  splits into two bands located at 1024  $\text{cm}^{-1}$  (assigned to  $\text{HSO}_3^-$ ) and 1036  $\text{cm}^{-1}$ . Hinsmann et al. assigned the first one to the asymmetric  $\text{SO}_2$  stretching vibration [43], while Pichler et al. observed strongly overlapping bands of  $\text{HSO}_3^-$  and  $\text{S}_2\text{O}_5^{2-}$  from 1000 to 1300  $\text{cm}^{-1}$ .

The observed changes were evaluated by integration using the software package OPUS from Bruker Optics. A one point baseline correction was applied at 1320  $\text{cm}^{-1}$  to remove slight shifts in the baseline and the absorptions at the maximum of the bands were taken with reference to this baseline. For the evaluation of the shoulder of the product band the absorption was taken at a fixed wavenumber of 1226.75  $\text{cm}^{-1}$ . The obtained time traces for different mixers at different channel flow rates are plotted in figure 8.3.

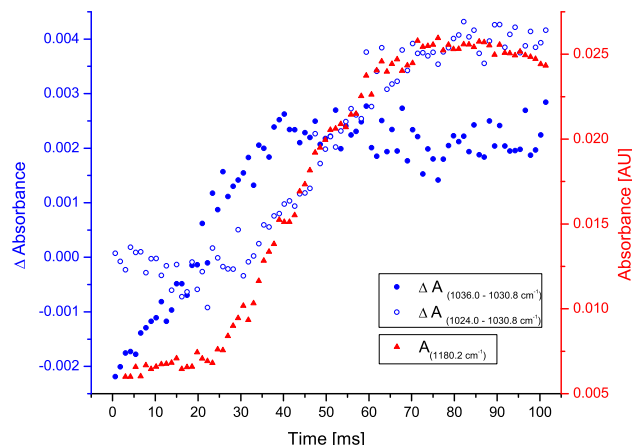


**Figure 8.4:** *Evaluation of the changes in the formaldehyde band by subtracting the minimum between the two emerging bands from their maxima (in blue). For comparison reasons the evolution of the product band is plotted in red.*

From figure 8.3 it can also be seen that the maximum of the product band stays at a constant level until approximately 25 ms before it starts rising, whereas the shoulder of the same band already starts to increase at the beginning of the mixing channel. From the sulfite band it seems that it exhibits an induction time similar to the product band maximum but starts to decrease at a slightly earlier reaction time. The observed reaction kinetics can't be fitted using a mono or bi-exponential fitting as it was possible for classical reaction kinetics as observed for the myoglobin experiments presented in chapter 7.2 underlining the complex reaction type of this kind of reaction which wasn't observed in earlier mixing experiments by Nina Kaun [73] and Peter Hinsmann [43].

The temporal evolution of the split in the band at  $1025\text{ cm}^{-1}$  was evaluated by subtracting the absorption of the minimum between the newly developing bands at  $1030.8\text{ cm}^{-1}$  from the absorption of the two emerging bands at  $1024\text{ cm}^{-1}$  and  $1036\text{ cm}^{-1}$ . The resulting kinetics show a surprising difference between the two difference signals, which can be seen in figure 8.4. While the band at  $1024\text{ cm}^{-1}$  exhibits the same sigmoid behaviour as the product band at  $1180\text{ cm}^{-1}$ , the band at  $1036\text{ cm}^{-1}$  starts to change immediately and exhibits a nearly exponential reaction kinetic.

From the presented data the characteristic behaviour of a clock reaction – the delayed starting of the reaction after an induction time – could be confirmed. However, it is difficult from the measured IR spectra to conclude on single sulphur species of the complex reaction due to strongly overlapping bands. From the kinetic evaluation presented in figure 8.3 and 8.4 three different species can be identified. The kinetics of the band at  $1024\text{ cm}^{-1}$  can possibly be linked to the evolution of the product band at  $1180\text{ cm}^{-1}$ . The difference in the behaviour for the band at  $1036\text{ cm}^{-1}$  suggests another chemical species, but can't be properly assigned. The induction times described by Kovacs et al. range up to 30 s, compared to observed induction times on the millisecond time scale for the micro mixer experiments representing a huge difference for a yet unknown reason.

The oscillating behaviour in a flow reactor, which the micro mixer represents, wasn't observed at the chosen experimental conditions or the time frame of the experiment wasn't long enough. However, it is not possible to operate the micro mixer at flow rates low enough to extend the observation window into the time scale of several seconds as reported by Kovacs et al [69].

### 8.3 H/D exchange on carbohydrates

Aqueous solutions of small carbohydrates are intensively studied in literature [74–77] not only because of their important role in food science. One outstanding sugar is trehalose, a disaccharide linking two glucose units with an  $\alpha(1 \rightarrow 1)\alpha$ -glucoside bond, making trehalose unique under all naturally occurring disaccharides [78]. Since both anomeric carbon atoms are participating on the glucosidic linkage trehalose is a non-reducing sugar.

Trehalose was found to be a highly efficient bioprotector for living organisms serving as a substitute for water upon dehydration [79]. It was also found to stabilize liposomes during freeze-drying [80]. Over the years several different hypotheses have been published trying to explain those unique properties of trehalose.

Green et al. reported that the glass transition temperature of different sugars [81] coincides well with their ability to prevent dehydration-induced

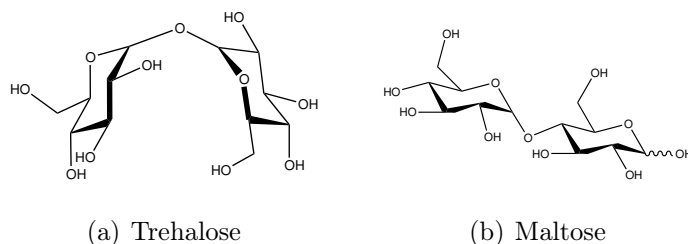


**Figure 8.5:** *Due to its unique linkage between the subunits trehalose can form a stable clam shell formation.*

fusion between liposomal membranes as found by Crowe et al. [82], with trehalose being the most effective sugar. Branca et al. investigated the O–H stretching region of water in the presence of different sugars finding a more marked destructuring effect on the H<sub>2</sub>O network for trehalose than other sugars [83–85]. This theory is supported by molecular dynamics simulations attributing trehalose that it reduces the size of water clusters more efficiently than sucrose or maltose [86]. Additional measurements using inelastic neutron scattering, Raman and IR spectroscopy support a stronger hydrogen-bond interaction between trehalose and water than for sucrose [87].

More recent neutron diffraction experiments, however, show exactly the opposite: A very limited number of sites on the trehalose molecule that can interact with water and a surprisingly small influence on the water network [88]. Again molecular dynamics simulations back up these findings stating that there is little special about trehalose from the view point of water dynamics [89].

It seems more likely that the cryoprotection ability of trehalose is a result of the direct interaction of it with membranes. Albertorio et al. attribute this feature to the  $\alpha(1 \rightarrow 1)\alpha$  linkage of trehalose leading to a stable clam shell formation, as can be seen in figure 8.5 where both glucopyranose rings can form hydrogen bonds with surrounding lipid molecules stabilizing the membrane upon drying [78].

Differences in the hydrogen bond network of different sugars should influence the proton exchange between OH groups of the sugar and surrounding water molecules. Therefore, mixing different sugar solutions with D<sub>2</sub>O should give different exchange kinetics for different sugars. Conducting such an experiment

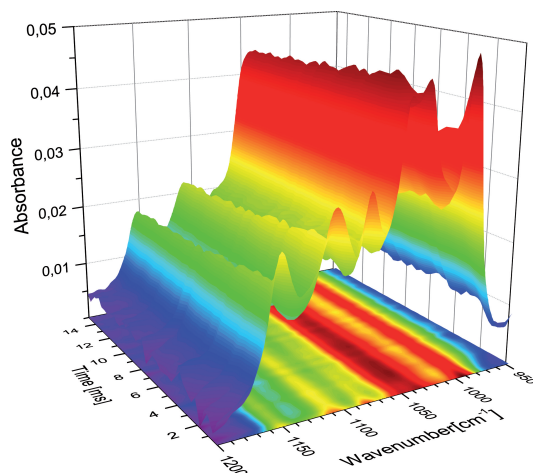


**Figure 8.6:** Measurement data showing the changes on the spectrum of trehalose upon mixing with  $D_2O$ . The flow rate was set to  $12 \mu\text{L} \cdot \text{min}^{-1}$  for each syringe.

in a microfluidic mixer consists of two measurement runs. First, only  $H_2O$  is mixed with  $D_2O$  for the background measurement and afterwards the aqueous sugar solution is mixed with  $D_2O$  for the sample measurement. This procedure, however, leads inevitably to spectral changes in the region of water absorption due to a displacement of water molecules by the sugar molecules, which doesn't overlap with the sugar absorptions observed in the spectral region ranging from  $1200$  to  $900 \text{ cm}^{-1}$ . A typical data set is shown in figure 8.6 showing the H/D exchange on trehalose.

To compare the H/D exchange rates the same measurements as for trehalose were recorded for maltose, a disaccharide formed by two  $\alpha(1 \rightarrow 4)$  linked glucose units. Maltose is found to be the second most effective sugar for bioprotection after trehalose.

Extracted raw spectra for both sugars, where both experiments were measured at a mixing channel flow rate of  $24 \mu\text{L} \cdot \text{min}^{-1}$ , are plotted in figure 8.7. Band assignments for the observed absorptions are summarized in table 8.2. The most prominent changing bands for trehalose are at  $1082 \text{ cm}^{-1}$  and  $995 \text{ cm}^{-1}$ . For maltose the band at  $1078 \text{ cm}^{-1}$  and the shoulder at  $996 \text{ cm}^{-1}$  are changing. As can be seen from the band assignment table, the band at  $995 \text{ cm}^{-1}$  is assigned to the glycosidic linkage by Kanou et al. [90] and

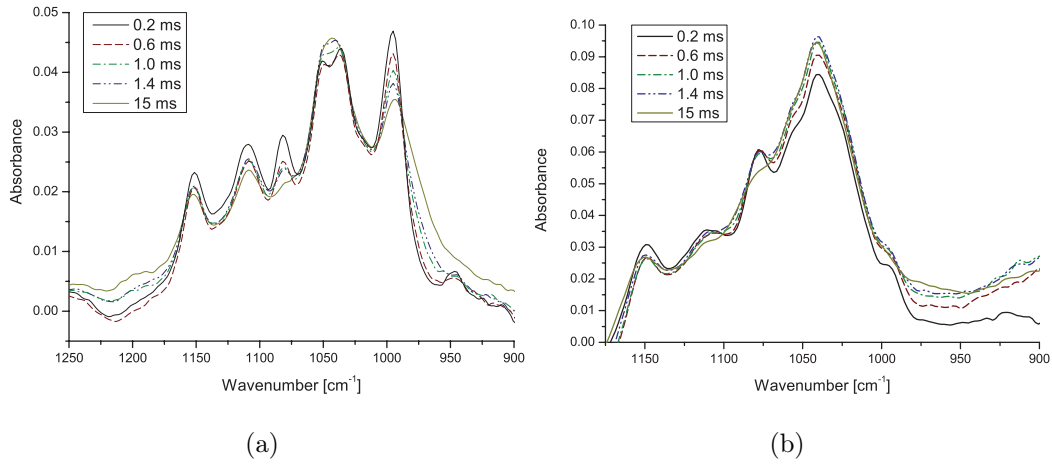


**Figure 8.7:** Extracted spectra of the  $H/D$  exchange reaction of (a) trehalose and (b) maltose of the first four measurement position inside the channel and after the exchange is completed at 15 ms.

Kačuráková et al. who assigned this vibration to a bending vibration of COH [77].

**Table 8.2:** Band assignments for the observed IR bands in the fingerprint region for Trehalose and Maltose. (sh) marks shoulders and \* bands used for kinetic analysis.

Trehalose	Maltose	Band Assignment [77]	Band Assignment [90]
946 $\text{cm}^{-1}$		Ring	
995 $\text{cm}^{-1}$ *	994 $\text{cm}^{-1}$ (sh)	$\delta(\text{COH})$ , $\nu(\text{C}-\text{O})$	glycosidic linkage
1036 $\text{cm}^{-1}$	1027 $\text{cm}^{-1}$ (sh)	$\delta(\text{COH})$ , $\nu(\text{C}-\text{O})$ , $\nu(\text{C}-\text{C})$	
	1027 $\text{cm}^{-1}$ (sh)		C-O-H
1036 $\text{cm}^{-1}$	1040 $\text{cm}^{-1}$		C-4-OH
	1040 $\text{cm}^{-1}$	unknown	
1050 $\text{cm}^{-1}$	1055 $\text{cm}^{-1}$ (sh)		$\alpha-D\text{-Glc}$
1050 $\text{cm}^{-1}$		$\delta(\text{COH})$ , $\nu(\text{C}-\text{O})$ , $\nu(\text{C}-\text{C})$	
1081 $\text{cm}^{-1}$ *	1078 $\text{cm}^{-1}$ *	$\delta(\text{COH})$ , $\nu(\text{C}-\text{O})$ , $\nu(\text{C}-\text{C})$	C-1-H
1109 $\text{cm}^{-1}$	1111 $\text{cm}^{-1}$	$\nu(\text{C}-\text{O})$ , ring	CO ring, C-4-O, C-6-O
1151 $\text{cm}^{-1}$	1149 $\text{cm}^{-1}$	$\nu(\text{C}-\text{O})$	pyranose ring



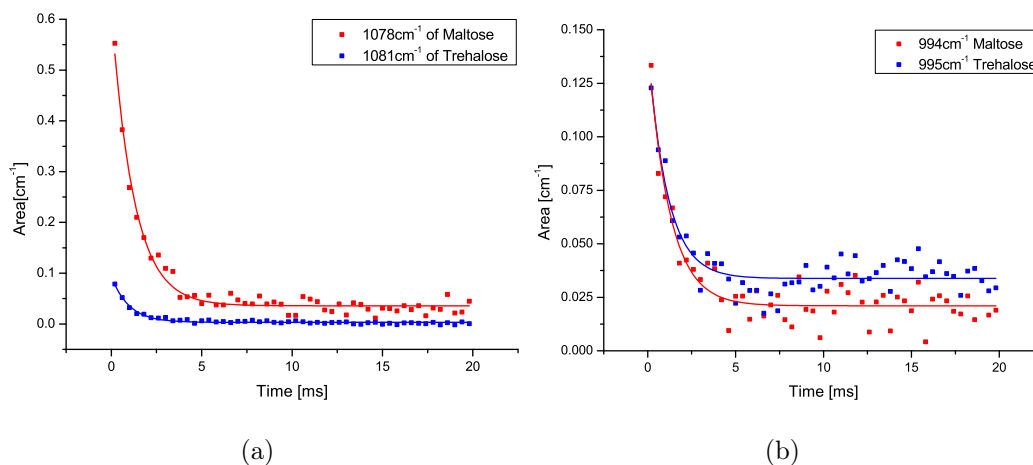


**Figure 8.8:** Time traces evaluated by band integration. (a) Absorption band around  $1080\text{ cm}^{-1}$  resulting in time constants  $\tau_1 = 0.97\text{ ms}$  for trehalose and  $\tau_1 = 1.24\text{ ms}$  for maltose. (b) Absorption band around  $995\text{ cm}^{-1}$  resulting in time constants of  $\tau_1 = 1.12\text{ ms}$  for trehalose and  $\tau_1 = 1.22\text{ ms}$  for maltose.  $R^2$  of fits:  $1080\text{ cm}^{-1}$ : Trehalose 0.97, Maltose 0.98;  $995\text{ cm}^{-1}$ : Trehalose 0.86, Maltose 0.87.

This overlap in bands seems to match with the observations for the H/D exchange reaction experiments since only the hydroxyl groups of the sugars can exchange the hydrogen atom with deuterium, whereas the glycosidic bond shouldn't be effected by an H/D exchange. Further, the band for trehalose as well as the shoulder for maltose show changes but do not disappear completely after the H/D exchange is finished, indicating an overlap in bands.

The second strongly changing absorption band for both sugars was assigned to a C–1–H vibration by Kačuráková et al., which again shouldn't be effected by the H/D exchange, with contributions from a bending vibration of COH. In fact, while C–H  $\rightarrow$  C–D labelling is widely used in carbohydrate research, this requires harsh conditions, such as refluxing the sugar solution with a catalyst or applying microwave-assisted techniques, to complete [91].

For evaluating the change of the bands at  $995\text{ cm}^{-1}$  and  $1080\text{ cm}^{-1}$  the spectral data set was Min/Max normalized in the spectral region between  $1180\text{ cm}^{-1}$  and  $980\text{ cm}^{-1}$  using the Bruker software OPUS and integrated afterwards.

The obtained time traces are plotted in figure 8.8 and show first order exponential decays for both sugars and both evaluated bands. From the time traces it can be seen that the H/D exchanges is finished after approximately 5 ms and the observed time constants are on the magnitude of 1 ms for all time traces. These decay times are on the same time scale as the evaluated mixing time of the micro fluidic devices, shown in chapter 4.2.3.1. The observed kinetics therefore are strongly overlapping with the mixing process and do not allow any conclusion on differences in the H-bonding network of the different sugars.

However, following H/D exchange reactions in other chemical environments may assist in band assignments of overlapping bands or exhibiting slower kinetics that can be separated from the mixing process.

## 8.4 Protein folding reactions

Protein folding investigation is a wide field in modern biochemistry with over 7000 hits in *Scopus* limiting the search to *reviews* only<sup>1</sup> studying conformational changes of proteins due to external influences. One method combined with various detection techniques is rapidly mixing [92] the protein under investigation with a second liquid [93] inducing the changes. Using IR spectroscopy as the detection principle gives access to the high information content of infrared spectra and is a valuable tool for investigating protein structure and folding [31].

For protein folding measurements in the *micro fluidic mixer* the smallest ubiquitous protein in nature was chosen: *ubiquitin*. With its 76 residues it forms a very stable native state and is therefore often used in research labs. Ubiquitin is stable from pH 1.2 to 8.5 and from 23 to 80 °C [94]. Despite from the native state, ubiquitin is known to exhibit a partially unfolded state called A-state in a mixture of water and methanol at low pH [95]. More recently it was discovered that in aqueous solution the native and A-state coexist but the native state is strongly favoured [96].

---

<sup>1</sup>Search for "Protein folding" on <http://www.scopus.com>, July 2012

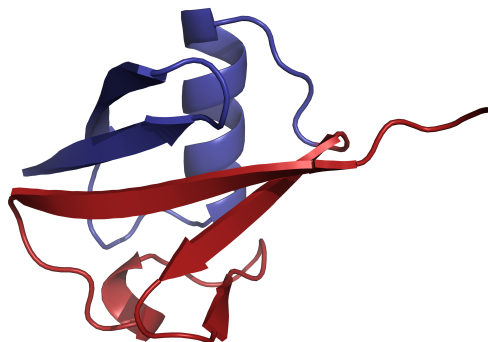
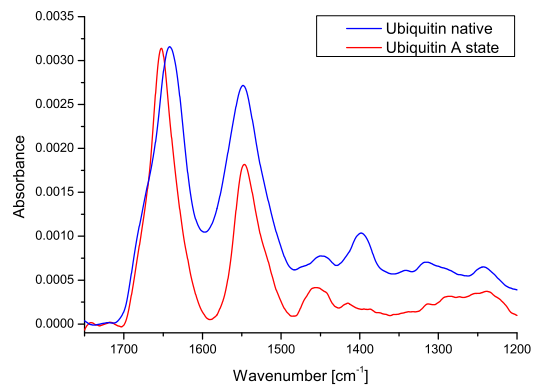


**Figure 8.9:** *Three dimensional structure of ubiquitin, the smallest naturally occurring protein. Data taken from [97]*

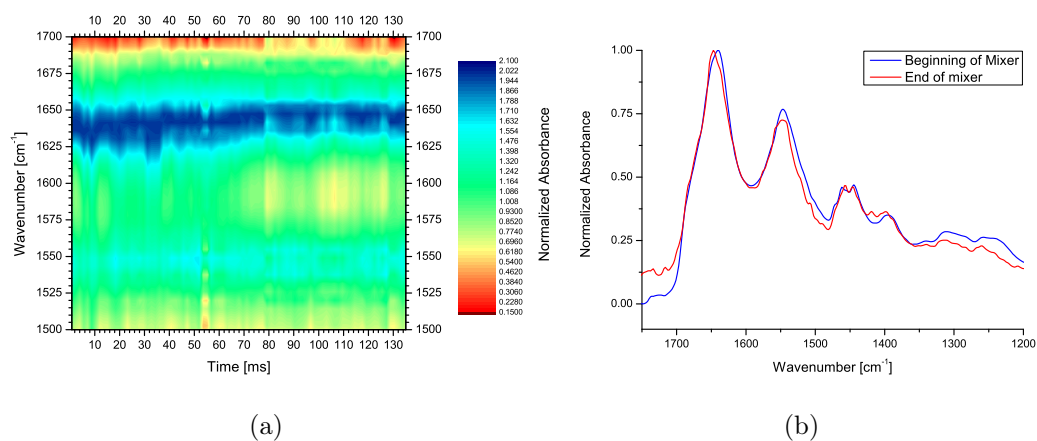
According to Brutscher et al. the change in protein structure from the native to the A-state mainly causes the C-terminal part (residues 39-72, marked in red in figure 8.9) of the protein to change from a  $\beta$ -sheet to a predominantly  $\alpha$ -helical structure. The N-terminal (blue) with its  $\beta$ -sheet and central  $\alpha$ -helix remain native-like [98]. Those changes in the secondary structure can be readily monitored by the Amide I band around  $1650\text{ cm}^{-1}$ , which arises from the C=O stretching vibration with minor contributions from the out-of-phase CN stretching vibrations, CCN deformation and NH in-plane bending modes of the amide bonds of the protein backbone [31].

Figure 8.10 shows *offline measurements* of acidified aqueous *ubiquitin from bovine erythrocytes* in its native state as well as the A-state formed by dissolving it in a mixture of 60 : 40 % methanol :  $\text{H}_2\text{O}$ . As expected a blue shift in the Amide I band from  $1642\text{ cm}^{-1}$  to  $1652\text{ cm}^{-1}$  occurs due to increasing  $\beta$ -sheet content in the A-state [31].

For the mixing experiments an acidified 6 mM ubiquitin solution was mixed with pure methanol, which was also adjusted to pH 2 using HCl. The flow rate was set to  $3\text{ }\mu\text{L} \cdot \text{min}^{-1}$  for each syringe resulting in a measurement window of 135 ms at a time resolution of 1.6 ms.



**Figure 8.10:** ATR reference spectra at pH 2 of the native and the A state of ubiquitin formed in a mixture of 60 : 40 % methanol :  $H_2O$  showing a shift of the Amide I band from  $1642\text{ cm}^{-1}$  to  $1652\text{ cm}^{-1}$  for the A state.



**Figure 8.11:** Measurement results of mixing a 6 mM aqueous ubiquitin solution with pure methanol at a channel flow rate of  $6\text{ }\mu\text{L} \cdot \text{min}^{-1}$ . (a) Spectral changes of the Amide I and II region over time (b) First and last spectrum recorded inside the micro mixer showing a band shift of the Amide I band from  $1640\text{ cm}^{-1}$  to  $1647\text{ cm}^{-1}$ .

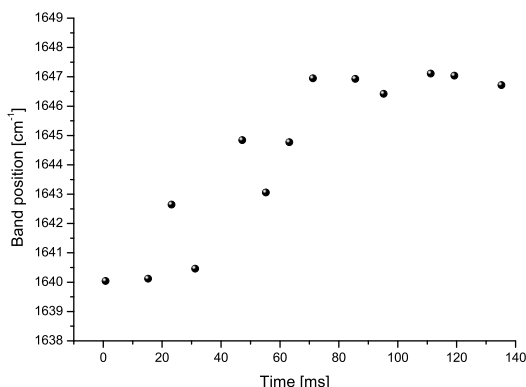


**Figure 8.12:** *Band positions of the Amide I band of manually selected spectra with little water vapour interferences against time showing the trend in the band position towards higher wavenumbers.*

The data set obtained from the mixing experiment, shown in figure 8.11, had to be corrected for the displacement of water molecules due to the high concentration of ubiquitin in the sample spectra compared to the background measurements. This compensation was achieved by manually adding a spectrum of water to each spectrum recorded along the mixing channel minimizing the negative absorption of the combination vibration of water around  $2100\text{ cm}^{-1}$ . Afterwards all spectra were normalized to the height of the Amide I band.

For the *mixing experiment* a blue shift in the Amide I band was observed too, shifting the band maximum from  $1640\text{ cm}^{-1}$  to  $1647\text{ cm}^{-1}$ , as can be seen from figure 8.11(b). A kinetic evaluation of the data set couldn't be performed due to strong water vapour interferences, seen in figure 8.11(a). This disturbance to single spectra along the mixing channel was inevitable due to the open beam-path of the Hyperion 3000 microscope at that time. Figure 8.12 summarizes the observed band positions by plotting manually selected spectra, showing only little water vapour disturbances, versus time.

The presented measurement data prove that it is possible to follow protein changes using our micro mixer. However, absolutely stable conditions of the used FTIR microscope are a prerequisite for successful measurements. A plexiglass housing, which was installed in the mean time around the optics

of the Bruker Hyperion 3000 microscope, allows already for more stable measurements by purging the whole optics with dry air. The limited supply of mixers limited the number of possible experiments (see chapter 4.2.4 for a description of challenges while using the micro mixers), leaving room for future investigations.

# Conclusion & Outlook

---

Time resolved mid-FTIR spectroscopy is a versatile technique to elucidate chemical reactions due to its content rich spectra. Over the years several techniques have been established and commercialized, of which *step scan technology* and *rapid scanning* are the most prominent ones. However, the step scan technique is usually limited to *cycle reactions* and can be extended to classical chemical reactions only by applying different approaches. Still, the system under investigation needs to be precisely repeatable after being started by an external trigger to completely record all necessary time traces.

Chemical reactions that can't be inhibited therefore can't be studied by the step scan technology. For such reactions, starting upon mixing of the reagents, microfluidic mixers can be used. In this thesis a new micro mixer design was tested and applied to several chemical reactions, such as the *formaldehyde sulfite clock reaction*, *H/D exchange on carbohydrates* and *protein foldings*. With its *optimized geometry* drawbacks of previous mixer designs concerning *mixing time* and *spatial homogeneity* have been overcome, resulting in faster mixing times compared to the last design used by Nina Kaun [2]. Additionally, the connection between the micro mixer and the macroscopic world was enhanced reducing the dead volume of the support holder and placing particle filters directly at the mixer inlets. Therefore, difficulties with dirt particles disturbing the laminar flow inside the mixer, which would render the mixer useless, could be reduced. Nonetheless, working with the mixers poses challenges taxing the user's patience. Especially the high pressures resulting from the usual flow rates needed can cause leakages. In combination with the brittle materials used breaking the mixer can easily occur trying to tighten the clamps responsible for sealing.

In addition to the classical approach of time resolved spectroscopy using mixers, an external focusing unit was used to couple micro mixers to a step scan FTIR spectrometer. This allowed to carry out step scan measurements on chemical systems not stable enough to be mixed off-line prior to the experiment by mixing the reagents directly before triggering the reaction. Measurements on *carboxy-myoglobin* using this system resulted in data being in good agreement with previously published literature.

Besides applying micro mixers fast scanning MOEMS spectrometers were tested allowing up to 1000 scans per second, which, however, were not suitable for kinetic measurements in their present early development stage.

**Future developments** of micro mixers should focus on further improving the *mixing efficiencies*, and no less important on *possible ways to clean the mixers*. One way to achieve easier cleaning could be the possibility to open the mixer itself and use solvents in combination with an ultrasonic bath. Flushing the mixer using the described ATLAS system helped to keep the mixers clean, but failed to dissolve residues after they had been introduced into the mixing channel.

Further developments could also focus on temperature stabilizing the mixer and its holder, since reaction kinetics of all (bio-)chemical reactions are highly temperature dependent. Accurate temperature measurements would need to be conducted right inside the mixing channel but should not interfere with the probing IR beam.

The emerging field of *quantum cascade lasers* and especially external cavity lasers will be able to overcome the need for small path lengths of 8  $\mu\text{m}$  for measurements in aqueous solutions due to their high energy density. Combining them with the 50  $\mu\text{m}$  micro mixer design briefly tested in this thesis might lead to successful measurements on *cytochrome c oxidase* in the near future.



# Bibliography

- [1] Peter Hinsmann. *Novel microfluidic chips with Fourier transform infrared spectroscopic detection for reaction and separation monitoring in miniaturised analysis systems*. PhD thesis, Vienna University of Technology, Vienna, 2002.
- [2] Nina Kaun. *New Strategies for Time Resolved Infrared Spectroscopy of Chemical Reactions in Solution*. PhD thesis, Vienna University of Technology, May 2006.
- [3] P R Griffiths. Introduction to Vibrational Spectroscopy. In *Handbook of Vibrational Spectroscopy*, pages 33–43. Wiley-VCH Verlag GmbH & Co. KGaA, Weinheim, 2002.
- [4] J E Bertie. Optical Constants. In *Handbook of Vibrational Spectroscopy*, pages 88–100. Wiley-VCH Verlag GmbH & Co. KGaA, Weinheim, 2002.
- [5] J E Bertie and Z Lan. Infrared Intensities of Liquids XX: The Intensity of the OH Stretching Band of Liquid Water Revisited, and the Best Current Values of the Optical Constants of  $H_2O$  (l) at 25° C between 15,000 and  $1\text{ cm}^{-1}$ . *Applied Spectroscopy*, 50(8):1047–1057, 1996.
- [6] P R Griffiths and J A de Haseth. *Fourier Transform Infrared Spectrometry*. WILEY-INTERSCIENCE, New York, 2 edition, April 2007.
- [7] G D Smith and R A Palmer. Fast Time-resolved Mid-infrared Spectroscopy Using an Interferometer. In *Handbook of Vibrational Spectroscopy*, pages 625–640. Wiley-VCH Verlag GmbH & Co. KGaA, Weinheim, 2002.
- [8] Peter R Griffiths, B L Hirsche, and C J Manning. Ultra-rapid-scanning Fourier transform infrared spectrometry. *Vibrational Spectroscopy*, 19(1):165–176, January 1999.
- [9] A Kenda, C Drabe, H Schenk, A Frank, M Lenzhofer, and W Scherf. Application of a micromachined translatory actuator to an optical FTIR spectrometer. *Proceedings of SPIE*, 6186:618609, 2006.

- [10] T Sandner, Cn Drabe, H Schenk, A Kenda, and W Scherf. Translatory MEMS actuators for optical path length modulation in miniaturized Fourier-transform infrared spectrometers. *Journal of Micro/Nanolithography, MEMS, and MOEMS*, 7(2):021006, 2008.
- [11] M Kraft, A Kenda, T Sandner, and H Schenk. MEMS-based compact FT-spectrometers - a platform for spectroscopic mid-infrared sensors. *Sensors 2008, IEEE*, pages 130 – 133, July 2008.
- [12] A Tortschanoff, A Kenda, M Kraft, T Sandner, H Schenk, and W Scherf. Improved MOEMS based ultra rapid Fourier transform infrared spectrometer. *Proceedings of SPIE*, 7319:73190I, 2009.
- [13] A Kenda, S Lüttjohann, T Sandner, M Kraft, A Tortschanoff, and A Simon. A compact and portable IR analyzer: progress of a MOEMS FT-IR system for mid-IR sensing. *Proceedings of SPIE*, 8032:80320O, 2011.
- [14] M Kraft, A Kenda, A Frank, W Scherf, A Heberer, T Sandner, H Schenk, and F Zimmer. Single-detector micro-electro-mechanical scanning grating spectrometer. *Analytical and Bioanalytical Chemistry*, 386(5):1259–1266, 2006.
- [15] H Schenk, P Dürr, T Haase, D Kunze, U Sobe, H Lakner, and H Kück. Large deflection micromechanical scanning mirrors for linear scans and pattern generation. *IEEE Journal of selected topics in quantum electronics*, 6:715–722, January 2000.
- [16] M Elwenspoek and H V Jansen. *Silicon Micromachining*. Cambridge University Press, August 2004., August 2004.
- [17] M Czerny and A F Turner. Über den Astigmatismus bei Spiegelspektrometern. *Zeitschrift für Physik*, 61(11-12):792–797, November 1930.
- [18] A B Shafer, L R Megill, and L A Droppleman. Optimization of Czerny-Turner Spectrometer. *J Opt Soc Am*, 54(7):879–887, 1964.

- 
- [19] A Kenda, M Kraft, C Wagner, B Lendl, and A Wolter. MEMS-based spectrometric sensor for the measurement of dissolved  $CO_2$ . *Sensors, 2008 IEEE*, pages 724–727, 2008.
- [20] T Nakano, T Yokoyama, and H Toriumi. One- and Two-Dimensional Infrared Time-Resolved Spectroscopy Using a Step-Scan FT-IR Spectrometer: Application to the Study of Liquid Crystal Reorientation Dynamics. *Applied Spectroscopy*, 47(9):1354–1366, September 1993.
- [21] H Sakai and R Murphy. Improvements in time resolved Fourier spectroscopy. *Applied Optics*, 17(9):1342–1346, January 1978.
- [22] W Uhmann, A Becker, C Taran, and F Siebert. Time-Resolved FT-IR Absorption-Spectroscopy Using a Step-Scan Interferometer. *Applied Spectroscopy*, 45(3):390–397, 1991.
- [23] C Rödig and F Siebert. Errors and artifacts in time-resolved step-scan FT-IR spectroscopy. *Applied Spectroscopy*, 53(8), 1999.
- [24] R Rammelsberg, S Boulas, H Chorongiewski, and K Gerwert. Set-up for time-resolved step-scan FTIR spectroscopy of noncyclic reactions. *Vibrational Spectroscopy*, January 1999.
- [25] E Kauffmann, H Frei, and R A Mathies. Nanosecond time-resolved step-scan FT-IR spectroscopy of the photochemical ring-opening of 1,3-cyclohexadiene. *Chemical Physics Letters*, 266(5-6):554–559, January 1997.
- [26] Q Cheng, M G Steinmetz, and V Jayaraman. Photolysis of  $\gamma$ -( $\alpha$ -carboxy-2-nitrobenzyl)-L-glutamic acid investigated in the microsecond time scale by time-resolved FTIR. *Journal of the American Chemical Society*, 124(26):7676–7677, January 2002.
- [27] A J Sommer. Mid-infrared Transmission Microscopy. In *Handbook of Vibrational Spectroscopy*, pages 1369–1385. Wiley-VCH Verlag GmbH & Co. KGaA, Weinheim, 2002.

- 
- [28] C M Snively and J L Koenig. Characterizing the Performance of a Fast FT-IR Imaging Spectrometer. *Applied Spectroscopy*, 53(2):170–177, February 1999.
- [29] P Lasch and D Naumann. Spatial resolution in infrared microspectroscopic imaging of tissues. *Biochimica et Biophysica Acta - Biomembranes*, 1758(7):814–829, January 2006.
- [30] Y Maréchal. The molecular structure of liquid water delivered by absorption spectroscopy in the whole IR region completed with thermodynamics data. *Journal of Molecular Structure*, 1004(1-3):146–155, 2011.
- [31] A Barth. Infrared spectroscopy of proteins. *Biochimica et Biophysica Acta (BBA) - Bioenergetics*, 1767(9):1073–1101, September 2007.
- [32] C Kötting, Y Suveyzdis, R Bojja, N Metzler-Nolte, and K Gerwert. Label-Free Screening of Drug–Protein Interactions by Time-Resolved Fourier Transform Infrared Spectroscopic Assays Exemplified by Ras Interactions. *Applied Spectroscopy*, 64(9):967–972, January 2010.
- [33] Z Y Zhou, N Tian, Y J Chen, S P Chen, and S G Sun. In situ rapid-scan time-resolved microscope FTIR spectroelectrochemistry: study of the dynamic processes of methanol oxidation on a nanostructured Pt electrode. *Journal of Electroanalytical Chemistry*, 573(1):111–119, 2004.
- [34] D C Grills, K W Huang, J T Muckerman, and E Fujita. Kinetic studies of the photoinduced formation of transition metal-dinitrogen complexes using time-resolved infrared and UV-VIS spectroscopy. In *Coordination Chemistry Reviews*, pages 1681–1695, 2006.
- [35] P Y Chen and R A Palmer. Ten-nanosecond step-scan FT-IR absorption difference time-resolved spectroscopy: Applications to excited states of transition metal complexes. In *Applied Spectroscopy*, pages 580–583, 1997.
- [36] M Brandstetter and B Lendl. Tunable mid-infrared lasers in physical chemosensors towards the detection of physiologically relevant parameters in biofluids. *Sensors and Actuators B: Chemical*, 2011.

- [37] D Lumpi, C Wagner, M Schöpf, E Horkel, G Ramer, B Lendl, and J Fröhlich. Fibre optic ATR-IR spectroscopy at cryogenic temperatures: in-line reaction monitoring on organolithium compounds. *Chemical Communications*, 48:2451–2453, 2012.
- [38] H Hartridge and F J W Roughton. A method of measuring the velocity of very rapid chemical reactions. *Proceedings of the Royal Society of London. Series A, Containing Papers of a Mathematical and Physical Character*, 104(726):376–394, 1923.
- [39] Q H Gibson and L Milnes. Apparatus for rapid and sensitive spectrophotometry. *Biochemical Journal*, 91(1):161, April 1964.
- [40] B C Dunn and E M Eyring. Stopped-flow rapid-scan Fourier transform infrared spectroscopy. *Applied Spectroscopy*, 53(3):292–296, 1999.
- [41] B C Dunn, J R Marda, and E M Eyring. Stopped-flow FT-IR spectroscopy of aqueous solutions using attenuated total reflectance. *Applied Spectroscopy*, 56(6):751–755, 2002.
- [42] M L Reback, C W Roske, T E Bitterwolf, P R Griffiths, and C J Manning. Stopped-Flow Ultra-Rapid-Scanning Fourier Transform Infrared Spectroscopy on the Millisecond Time Scale. *Applied Spectroscopy*, 64(8):907–911, 2010.
- [43] P Hinsmann, M Haberkorn, J Frank, P Svasek, M Harasek, and B Lendl. Time-Resolved FT-IR Spectroscopy of Chemical Reactions in Solution by Fast Diffusion-Based Mixing in a Micromachined Flow Cell. *Applied Spectroscopy*, 55(3):241–251, January 2001.
- [44] P Hinsmann, J Frank, P Svasek, M Harasek, and B Lendl. Design, simulation and application of a new micromixing device for time resolved infrared spectroscopy of chemical reactions in solution. *Lab on a Chip*, 1(1):16–21, January 2001.
- [45] A Rigler, C Wagner, P Svasek, A Jachimowicz, P Hudek, M Kraft, and M J Vellekoop. Improved lamination micromixer with wedge shaped

- inlet channels for IR spectroscopy. In *Proceedings EUROSENSORS XXII*, pages 187–190, July 2008.
- [46] W Buchegger, C Wagner, B Lendl, M Kraft, and M J Vellekoop. A highly uniform lamination micromixer with wedge shaped inlet channels for time resolved infrared spectroscopy. *Microfluidics And Nanofluidics*, 10(4):889–897, 2011.
- [47] W Buchegger, C Wagner, P Svasek, B Lendl, M Kraft, and M J Vellekoop. Fabrication and characterization of a vertical lamination micromixer for mid-IR spectroscopy. *Sensors and Actuators B: Chemical*, 159(1):336–341, November 2011.
- [48] Robert C Weast, editor. *Handbook of Chemistry and Physics*. CRC Press, Inc., 56 edition, 1975.
- [49] P Svasek, E Svasek, B Lendl, and M J Vellekoop. Fabrication of miniaturized fluidic devices using SU-8 based lithography and low temperature wafer bonding. In *Sensors and Actuators A: Physical*, pages 591–599, 2004.
- [50] N Kaun, S Kulka, J Frank, U Schade, M J Vellekoop, M Harasek, and B Lendl. Towards biochemical reaction monitoring using FT-IR synchrotron radiation. *The Analyst*, 131(4):489–494, January 2006.
- [51] E Kauffmann, N C Darnton, R H Austin, C Batt, and Klaus Gerwert. Lifetimes of intermediates in the  $\beta$ -sheet to  $\alpha$ -helix transition of  $\beta$ -lactoglobulin by using a diffusional IR mixer. *Proceedings of The National Academy of Sciences*, 98(12):6646–6649, 2001.
- [52] L M Tolbert and K M Solntsev. Excited-state proton transfer: From constrained systems to “super” photoacids to superfast proton transfer. *Accounts of Chemical Research*, 35(1):19–27, 2002.
- [53] M Rini, B-Z Magnes, E Pines, and E T J Nibbering. Real-Time Observation of Bimodal Proton Transfer in Acid-Base Pairs in Water. *Science*, 301(5631):349–352, July 2003.

- 
- [54] M Rini, D Pines, BZ Magnes, E Pines, and E T J Nibbering. Bimodal proton transfer in acid-base reactions in water. *Journal Of Chemical Physics*, 121(19):9593–9610, January 2004.
- [55] PL Geissler, C Dellago, D Chandler, J Hutter, and M Parrinello. Autoionization in liquid water. *Science*, 291(5511):2121–2124, January 2001.
- [56] Michael Haberkorn. *Development and implementation of novel interfaces for miniaturized analysis systems with vibrational spectroscopic detection*. PhD thesis, Vienna University of Technology, 2003.
- [57] Stephan Kulka. *Advances in automated flow systems for microfluidic analysis with mid-IR detection*. PhD thesis, Vienna University of Technology, 2005.
- [58] C Wagner, S Armenta, and B Lendl. Developing automated analytical methods for scientific environments using LabVIEW. *Talanta*, 80(3):1081–1087, January 2010.
- [59] H P Hersleth, T Uchida, Å K Røhr, T Teschner, V Schünemann, T Kitagawa, A X. Trautwein, C H Görbitz, and K K Andersson. Crystallographic and spectroscopic studies of peroxide-derived myoglobin compound II and occurrence of protonated FeIV-O. *Journal of Biological Chemistry*, 282(32):23372–23386, 2007.
- [60] K Chu, J Vojtechovský, B H McMahon, R M Sweet, J Berendzen, and I Schlichting. Structure of a ligand-binding intermediate in wild-type carbonmonoxy myoglobin. *Nature*, 403(6772):921–923, 2000.
- [61] A Ostermann, R Waschipky, F G Parak, and G U Nienhaus. Ligand binding and conformational motions in myoglobin. *Nature*, 404(6774):205–208, 2000.
- [62] J Kuriyan, S Wilz, M Karplus, and G A Petsko. X-ray structure and refinement of carbon-monooxy (Fe II)-myoglobin at 1.5 Å resolution. *Journal of Molecular Biology*, 192(1):133–154, 1986.

- [63] M Biesaga, K Pyrzynska, and M Trojanowicz. Porphyrins in analytical chemistry. A review. *Talanta*, 51(2):209–224, 2000.
- [64] A J Dixon, P Glyn, M A Healy, P M Hodges, T Jenkins, M Poliakoff, and J J Turner. Fast time-resolved i.r. spectroscopy of biological molecules in aqueous solution: the reaction kinetics of myoglobin with carbon monoxide. *Spectrochimica Acta Part A: Molecular and Biomolecular Spectroscopy*, 44(12):1309–1314, 1988.
- [65] Michael Schleege. *Funktionsstudie der Cytochrom c Oxidase mit Hilfe von stationärer Differenz- und zeitaufgelöster FT-IR-Spektroskopie*. PhD thesis, Shaker Verlag, May 2009.
- [66] M Svensson-Ek, J Abramson, and G Larsson. The X-ray Crystal Structures of Wild-type and EQ(I-286) Mutant Cytochrome c Oxidases from *Rhodobacter sphaeroides*. *Journal of Molecular Biology*, 2002.
- [67] D Heitbrink, H Sigurdson, C Bolwien, P Brzezinski, and J Heberle. Transient binding of CO to CuB in cytochrome c oxidase is dynamically linked to structural changes around a carboxyl group: A time-resolved step-scan fourier transform infrared investigation. *Biophysical journal*, 82(1):1–10, 2002.
- [68] P Warneck. The Formaldehyde-Sulfite Clock Reaction Revisited. *Journal Of Chemical Education*, 66(4):334–335, January 1989.
- [69] K Kovacs, R McIlwaine, K Gannon, A F Taylor, and S K Scott. Complex behavior in the formaldehyde - Sulfite reaction. *Journal of Physical Chemistry A*, 109(1):283–288, 2005.
- [70] Z Zhang and G E Ewing. Infrared spectroscopy of  $SO_2$  aqueous solutions. *Spectrochimica Acta Part a-Molecular and Biomolecular Spectroscopy*, 58(10):2105–2113, 2002.
- [71] A Pichler, G Fleissner, A Hallbrucker, and E Mayer. FT-IR spectroscopic monitoring of alkali metal disulfite and hydrogensulfite in freeze-



- concentrated and glassy aqueous solution. Implications for atmosphere chemistry. *Journal of Molecular Structure*, 408-409:521–525, June 1997.
- [72] A W Herlinge and T V Long. An Investigation of Structure of Disulfite Ion in Aqueous Solution Using Raman and Infrared Spectroscopies. *Inorganic Chemistry*, 8(12):2661–2665, 1969.
- [73] N Kaun, M J Vellekoop, and B Lendl. Time-Resolved Fourier Transform Infrared Spectroscopy of Chemical Reactions in Solution Using a Focal Plane Array Detector. *Applied Spectroscopy*, 60(11):1273–1278, January 2006.
- [74] S Magazu, F Migliardo, and M T F Telling. Structural and dynamical properties of water in sugar mixtures. *Food Chemistry*, 106(4):1460–1466, 2008.
- [75] A Gharsallaoui, B Roge, J Genotelle, and M Mathlouthi. Relationships between hydration number, water activity and density of aqueous sugar solutions. *Food Chemistry*, 106(4 SPEC. ISS.):1443–1453, 2008.
- [76] A Lerbret, P Bordat, F Affouard, Y Guinet, A Hédoux, L Paccou, D Prévost, and M Descamps. Influence of homologous disaccharides on the hydrogen-bond network of water: complementary Raman scattering experiments and molecular dynamics simulations. *Carbohydrate Research*, 340(5):881–887, April 2005.
- [77] M Kačuráková and M Mathlouthi. FTIR and laser-Raman spectra of oligosaccharides in water: Characterization of the glycosidic bond. *Carbohydrate Research*, 284(2):145–157, January 1996.
- [78] F Albertorio, Vanessa A Chapa, X Chen, A J Diaz, and P S Cremer. The  $\alpha, \alpha$ -(1  $\rightarrow$  1) Linkage of Trehalose Is Key to Anhydrobiotic Preservation. *Journal of the American Chemical Society*, 129(34):10567–10574, August 2007.
- [79] K-I Akao, Y Okubo, N Asakawa, Y Inoue, and M Sakurai. Infrared spectroscopic study on the properties of the anhydrous form II of trehalose.

- Implications for the functional mechanism of trehalose as a biostabilizer. *Carbohydrate Research*, 334(3):233–241, January 2001.
- [80] L M Crowe, D S Reid, and J H Crowe. Is trehalose special for preserving dry biomaterials? *Biophysical journal*, 71(4):2087–2093, 1996.
- [81] J L Green and C A Angell. Phase relations and vitrification in saccharide-water solutions and the trehalose anomaly. *The Journal of Physical Chemistry*, 93(8):2880–2882, 1989.
- [82] L M Crowe, J H Crowe, A Rudolph, C Womersley, and L Appel. Preservation of freeze-dried liposomes by trehalose. *Archives of Biochemistry and Biophysics*, 242(1):240–247, 1985.
- [83] C Branca, S Magazu, G Maisano, and P Migliardo. Anomalous cryoprotective effectiveness of trehalose: Raman scattering evidences. *Journal Of Chemical Physics*, 111(1):281–287, January 1999.
- [84] C Branca, S Magazu, G Maisano, and P Migliardo.  $\alpha, \alpha$ -Trehalose-Water Solutions. 3. Vibrational Dynamics Studies by Inelastic Light Scattering. *Journal of Physical Chemistry B*, 103(8):1347–1353, 1999.
- [85] C Branca, S Magazu, and F Migliardo. Experimental evidences of structural changes in trehalose/water mixtures. *Journal of Molecular Liquids*, 2003.
- [86] A Lerbret, P Bordat, F Affouard, M Descamps, and F Migliardo. How Homogeneous Are the Trehalose, Maltose, and Sucrose Water Solutions? An Insight from Molecular Dynamics Simulations. *Journal of Physical Chemistry B*, 109(21):11046–11057, June 2005.
- [87] C Branca, S Magazu, G Maisano, S M Bennington, and B Fåk. Vibrational studies on disaccharide/ $H_2O$  systems by inelastic neutron scattering, Raman, and IR spectroscopy. *Journal of Physical Chemistry B*, 107(6):1444–1451, 2003.

- [88] S E Pagnotta, S E McLain, A K Soper, F Bruni, and M A Ricci. Water and Trehalose: How Much Do They Interact with Each Other? *Journal of Physical Chemistry B*, 114(14):4904–4908, April 2010.
- [89] Ana Vila Verde and R Kramer Campen. Disaccharide Topology Induces Slowdown in Local Water Dynamics. *Journal of Physical Chemistry B*, 115:7069–7084, 2011.
- [90] M Kanou, K Nakanishi, A Hashimoto, and T Kameoka. Influences of monosaccharides and its glycosidic linkage on infrared spectral characteristics of disaccharides in aqueous solutions. *Applied Spectroscopy*, 59(7):885–892, 2005.
- [91] E A Cioffi, R H Bell, and B Le. Microwave-assisted C-H bond activation using a commercial microwave oven for rapid deuterium exchange labeling (C-H  $\rightarrow$  C-D) in carbohydrates. *Tetrahedron Asymmetry*, 16(2):471–475, January 2005.
- [92] H Roder, K Maki, and H Cheng. Early events in protein folding explored by rapid mixing methods. *Chemical Reviews*, 106(5):1836–1861, 2006.
- [93] R M Ionescu and C R Matthews. Folding under the influence. *Nature Structural Biology*, 6(4):304–306, 1999.
- [94] S E Jackson. Ubiquitin: a small protein folding paradigm. *Organic & Biomolecular Chemistry*, 4(10):1845–1853, 2006.
- [95] M M Harding, D H Williams, and D N Woolfson. Characterization of a Partially Denatured State of a Protein by 2-Dimensional Nmr - Reduction of the Hydrophobic Interactions in Ubiquitin. *Biochemistry*, 30(12):3120–3128, 1991.
- [96] H Shi, N A Pierson, S J Valentine, and D E Clemmer. Conformation types of ubiquitin  $[M + 8H]^{8+}$  ions from water:methanol solutions: Evidence for the N and A states in aqueous solution. *Journal of Physical Chemistry B*, 116(10):3344–3352, 2012.

- [97] S Vijay-Kumar, C E Bugg, and W J Cook. Structure of ubiquitin refined at 1.8 Å resolution. *Journal of Molecular Biology*, 194(3):531–544, April 1987.
  
- [98] B Brutscher, R Bruschweiler, and R R Ernst. Backbone dynamics and structural characterization of the partially folded A state of ubiquitin by H-1, C-13, and N-15 nuclear magnetic resonance spectroscopy. *Biochemistry*, 36(42):13043–13053, January 1997.

# Published scientific papers

---

## Publication I

W. Buchegger, C. Wagner, B. Lendl, M. Kraft, and M.J. Vellekoop,  
Microfluidics and Nanofluidics 10, 4, 889-897 (2011),  
DOI: 10.1007/s10404-010-0722-0.



# A highly uniform lamination micromixer with wedge shaped inlet channels for time resolved infrared spectroscopy

Wolfgang Buchegger · Christoph Wagner ·  
Bernhard Lendl · Martin Kraft · Michael J. Vellekoop

Received: 10 June 2010 / Accepted: 5 August 2010 / Published online: 4 November 2010  
© Springer-Verlag 2010

**Abstract** We present a horizontal multi-lamination micromixer with specially wedge shaped vertical fluid inlets for fast and highly uniform fluid mixing in the low millisecond range. The four-layer laminar flow is created by a fluidic distribution network, reducing the amount of fluid connectors to the macroscopic world to two. All the geometries of the channel inlets and the distribution network were optimized for low flow rates and hence for low sample consumption using CFD simulations. The device materials applied feature low absorption in the mid-infrared (wavelength 3–10  $\mu\text{m}$ ) allowing to use this device for time resolved infrared spectroscopy. The micromixer itself can be built by silicon micromachining techniques without the need of complicated fabrication steps. Due to a transparent calcium fluoride cover optical measurements are possible as well which were used to characterize the device. Mixing times in the range of 1 ms with optical color measurements of aqueous solutions and with time resolved infrared measurement of the proton exchange reaction of  $\text{H}_2\text{O}$  and  $\text{D}_2\text{O}$  are achieved.

**Electronic supplementary material** The online version of this article (doi:10.1007/s10404-010-0722-0) contains supplementary material, which is available to authorized users.

W. Buchegger (✉) · M. J. Vellekoop  
Institute of Sensor and Actuator Systems,  
Vienna University of Technology, Vienna, Austria  
e-mail: wolfgang.buchegger@tuwien.ac.at

C. Wagner · B. Lendl  
Institute of Chemical Technologies and Analytics,  
Vienna University of Technology, Vienna, Austria

M. Kraft  
Carinthian Tech Research AG, Villach, Austria

**Keywords** Microfluidic · Diffusion micromixer · Time resolved · Infrared spectroscopy

## 1 Introduction

Many advancements in the field of on-chip biological and biomedical analysis systems have been made in the last decades with the goal to decrease reagent consumption, lower processing time, increase throughput, lower the cost, introduce disposable platforms or to study new phenomena (Nguyen and Wereley 2002; Hardt et al. 2005). In biological or medical processes two or more reagents need to be mixed before a reaction can occur. The mixing must be fast and uniform at micrometer scale so that the reaction can fully develop and reaction dynamics can be studied.

In general, mixers can be divided into active and passive mixing principles. Active mixers need external energy or actuation and are, therefore, often more complex while passive mixers rely on diffusion or chaotic advection and are operated autonomically. A review summarizing the most common design approaches is given by Nguyen and Wu (2005), Mansur et al. (2008). A simple electromagnetically actuated micromixer was presented by Wen et al. (2009) with mixing times in the 1 s range. Designs utilizing acoustic waves achieved mixing times down to 7 ms (Ahmed et al. 2009; Johansson et al. 2009). Another active mixing principle with an actuated cantilever in the mixing channel was investigated by Williams et al. (2009) without stating actual mixing times. Mao et al. (2010) presented a chaotic bubble mixer with mixing times of 20 ms which uses monodisperse microbubbles for stirring. To overcome the need of an external energy source, which often leads to a complex device design, passive mixing principles are attractive. The probably most investigated passive mixing

principle is based on a T-shaped channel crossing, a so called T-mixer, with several channel variations. Mixing times in the 1 s range can be achieved with these designs in low Reynolds number flow regimes (Hossain et al. 2009). To reduce mixing time in T-mixers in the order of one magnitude, pillar structures (Chen et al. 2009) or herringbone structured walls (Park et al. 2010; Cortes-Quiroz et al. 2009) can be used, which introduce chaotic advection of the fluid. As many chemical and biochemical reaction times occur in the millisecond range, fast mixing at low flow rates, and thus small sample consumption, is desirable. Because the infrared (IR) absorption of aqueous solutions can be dominant compared to IR absorption changes caused by chemical reactions, the mixing channel height should not exceed 8–10  $\mu\text{m}$  and be constant along the measurement section. The reduced cross section area of the mixing channel combined with a low flow rate, results in very low Reynolds numbers ( $Re < 1$ ). This indicates strictly laminar flow conditions and mixing only occurs due to diffusion. Gambin et al. (2010) presented a design recently, which uses three dimensional flow focusing for fast mixing. However, this design with a focusing spot of about 5  $\mu\text{m}$  is not applicable for IR spectroscopy because a measuring spot of about 150  $\mu\text{m}$  in diameter is necessary to gain an acceptable signal to noise ratio. High aspect ratio laminar flow sheets were firstly used by Hinsmann et al. (2001a) for a stopped flow mixing device. The mixing time  $t$  of a diffusion based mixing system scales inversly proportional with the diffusion coefficient  $D$  and direct proportional with the square of the diffusion length  $d_{\text{diff}}$ :

$$t \propto \frac{d_{\text{diff}}^2}{D}. \quad (1)$$

A multilaminar flow design was presented by Kauffmann et al. (2001) and a similar design by Lipman et al. (2003) with mixing times of 50 ms. Figure 1a shows a laminar fluid structure with two layers (left) and four layers (right). In the right image the layers in the middle differ in thickness compared to the layers next to the channel wall. According to Eq. 1, the mixing time can be reduced by a factor of nine with this approach. A first design utilizing layers that differ in thickness was introduced by Kanai et al. (2002). Simulations show that with diffusion lengths of around 1  $\mu\text{m}$ , mixing times of 1 ms are possible assuming fluid properties of water. However, if a multilaminar flow structure is used the off-chip effort increases as for every layer a fluid pump is needed or complicated fabrication steps are necessary to cross over fluid channels.

## 2 Materials and methods

In our design presented here, different fluid layers were laminated in a horizontal way by four vertical channels

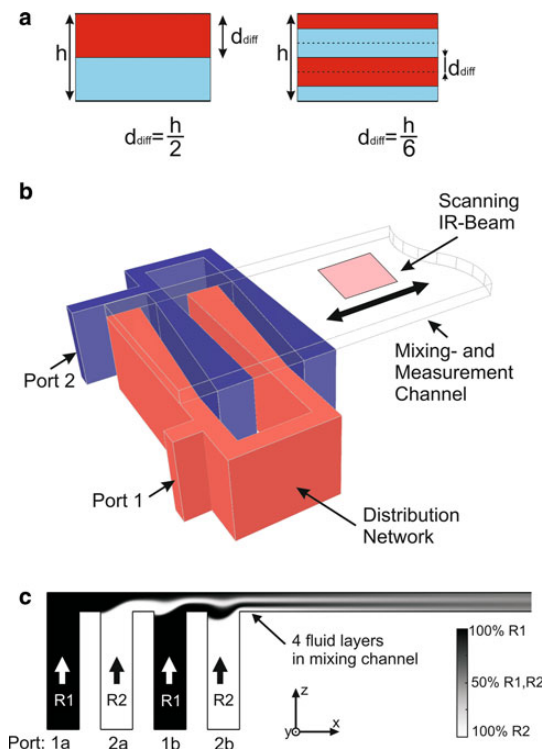


**Fig. 1** **a** Cross section of fluidic channel with two lamination layers left and four lamination layers right. By doubling the layers from two to four the diffusion length decreases by a factor of three, the diffusion time by a factor of nine. **b** Schematic of the micromixer, forming four lamination layers. Two different reagents are pumped into ports 1 and 2. The mixing channel itself serves as measurement area. By moving the scanning IR-beam along the channel a time resolved measurement is achieved. **c** Two dimensional flow simulation of the micromixer to determine the individual flow velocities of each channel inlet for optimizing the thickness of each fluid layer

which lead into a horizontal mixing channel. A schematic of the design is given in Fig. 1b which shows the filled fluid channels, the wedge shaped inlet channels, and the mixing channel (Rigler et al. 2008). In order to keep the fluidic setup as simple as possible, the inlet channels with the same reagent are fed from one side through a fluidic distribution network. The exterior fluid connectors are indicated by ports 1 and 2 for the two different reagents. In contrary to previously presented designs, this system can be supplied by one double-syringe pump. To achieve the shortest mixing time and low premixing, the number of lamination layers in combination with the channel dimensions and geometry were investigated by computational fluid dynamics (CFD) simulations with *Comsol Multiphysics*. Simulations showed that wedge shaped inlets yield much faster mixing than straight inlets. The difference in



mixing performance between this novel wedge design and the classical straight design is investigated with simulations and measurements in the following.

## 2.1 Simulations

In first simulations the feeding channels and the fluid distribution network were designed before a full three dimensional model was investigated. For fully simultaneous diffusion of all lamination layers their thickness was varied until unwanted effects like premixing were minimized. Different flow velocities of the fluid junctions are also comprised in the simulations. To generate an individual optimum for each layer thickness, a fluid distribution network utilizes the pressure drop along a microchannel to feed the inlet channels with different fluid velocities. These velocities were predetermined by a two dimensional simulation of the micromixer shown in Fig. 1c. In this simulation port 1 was modeled with a reagent concentration  $R1$  of  $1 \text{ mol/m}^3$  and port 2 with a reagent concentration  $R2$  of  $0 \text{ mol/m}^3$ . The diffusion coefficient was set to  $D = 5 \cdot 10^{-10} \text{ m}^2/\text{s}$  to suppress mixing and clearly show the different fluid layers. In addition, a flow rate of  $30 \text{ } \mu\text{l/min}$  was chosen, which is the maximum flow rate used with this micromixer. The resulting values of the relative flow velocities in the inlet channels are given in Table 1. These were used to design the fluidic distribution network according to Eq. 2 which gives the pressure drop ( $\frac{dp}{dx}$ ) depending on the change in flow rate  $\dot{Q}$  in rectangular channels ( $b$  = channel width,  $h$  = channel height and  $h < b$ ), where  $\eta$  means the dynamic viscosity (Nguyen and Wereley 2002).

$$\dot{Q} = \frac{4bh^3}{3\eta} \left( -\frac{dp}{dx} \right) \left[ 1 - \frac{192b}{\pi^5 h} \sum_{i=1,2,3,\dots}^{\infty} \frac{\tanh\left(\frac{ih\pi}{2b}\right)}{i^5} \right] \quad (2)$$

The cross section of the concentration profile of a three dimensional micromixer design is shown in Fig. 2. The channel width was set to  $b = 200 \text{ } \mu\text{m}$  so if the measurement spot of the IR-spectrometer is placed in the middle there will be an edge of  $25 \text{ } \mu\text{m}$  on each side. These areas are excluded from the measurement to cancel time differences occurring at the border fluid layers due to the parabolic velocity profile caused by the pressure driven flow. To gain a lower off-chip complexity, each inlet is fed from

one side. A certain pressure drop occurs between the injecting and the far side of the channel inlet. This causes an inhomogeneous velocity and pressure distribution and hence non-uniform layers of fluid, as depicted in Fig. 2, profile A. Therefore, fast mixing of the reagents is inhibited. The cross sections in Fig. 2 show the four fluid layers in the mixing channel right after they are formed (profile A) and  $50 \text{ } \mu\text{m}$  after the layers were formed (profile B). The distance between profile A and B equals  $2.5 \text{ ms}$  with the used flow rates. Proper mixing is only occurring in the middle areas and the lamination structure in Fig. 2 profile A shows a kind of a zigzag shape. This limits the time resolution of the mixing chip because dynamic measurements can only be recorded of chemical reactions slower than the mixing procedure. To reduce the mixing time and form uniform fluid layers, the contact surface is increased by using a special geometry for the lamination inlets. The inlet broadens to a wedge shape at the far end of the feeding, resulting in a constant pressure distribution and hence uniform fluid layers.

An integration of the z-component of the fluid velocity over the channel width (y-component) gives information about the amount of fluid  $Q'$  added into the channel corresponding to Eq. 3

$$Q'(y) = \int v_z(x, y) dx. \quad (3)$$

The result of this integration is plotted on the y-axis, see Fig. 3a. In the two dimensional plot the x-axis shows the channel width  $b$  with the measurement region from  $25$  to  $175 \text{ } \mu\text{m}$ . If the quantity  $Q'$  is constant over the width of the mixing channel, uniform fluid layers are formed. The optimum geometry is found by comparing the variation of  $Q'$  in the measurement area:

$$\Delta Q = \int_{25 \text{ } \mu\text{m}}^{175 \text{ } \mu\text{m}} \frac{|Q'(y) - \overline{Q'(y)}|}{\overline{Q'(y)}} dy. \quad (4)$$

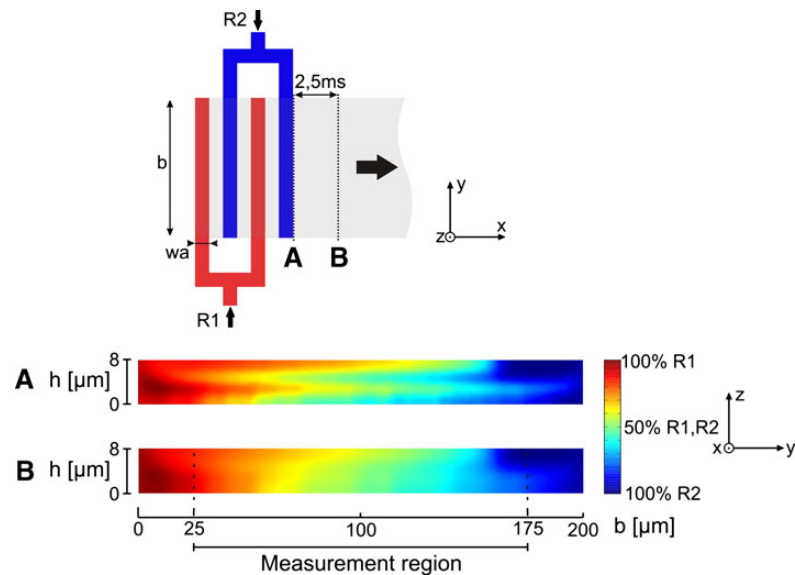
A graphical illustration of  $\Delta Q$  is given in Fig. 3b. The best results can be achieved with a wedged inlet channel opening from  $w_b = 10 \text{ } \mu\text{m}$  to  $w_e = 22 \text{ } \mu\text{m}$ . As a result, the pressure and hence the flow velocity variations are below 3% of their mean value. The geometry of this optimized wedge shape is strongly depending on the depth of the feeding channel ( $200 \text{ } \mu\text{m}$  in this design), the inlet channel width ( $w_e = 10 \text{ } \mu\text{m}$ ), the mixing channel height ( $h = 8 \text{ } \mu\text{m}$ ) and the flow velocity if varied in a wide range.

The simulation of Fig. 2 was repeated with the calculated wedge shape of  $w_b = 10 \text{ } \mu\text{m}$  and  $w_e = 22 \text{ } \mu\text{m}$ . A top view of the schematic and the corresponding concentration profile at the same times as in Fig. 2 are given in Fig. 4. In contrary to the straight shaped micromixer, profile A shows uniform lamination layers. Due to this precondition, the

**Table 1** Simulation result of normalized flow rates for the optimal non-uniform lamination layers

Lamination inlet	Normalized flow rates
Port 1a	0.18
Port 1b	0.32
Port 2a	0.375
Port 2b	0.125

**Fig. 2** Two dimensional concentration profile of the straight micromixer at the point where the four fluid layers are formed and 2.5 ms further down the mixing channel. The reagents in channels 1 and 2 are dark colored. Proper mixing of the reagents is occurring in the bright region



mixing performance in profile B yields far better results. The region of  $\pm 10\%$  of ideal mixing concentration ranges over a total width of  $160 \mu\text{m}$  in a channel of  $200 \mu\text{m}$  width, which perfectly suits the IR measurement region of  $150 \times 150 \mu\text{m}^2$ .

A simulation of the mixing performance at a flow rate of  $30 \mu\text{l}/\text{min}$  and with four different diffusion coefficients is given in Fig. 5. The diffusion coefficients model different solutions, for instance,  $D = 2 \cdot 10^{-9} \text{ m}^2/\text{s}$  models the diffusion coefficient of aqueous solutions (Crowell and Bartels 1996) whereas  $D = 5 \cdot 10^{-10} \text{ m}^2/\text{s}$  models the diffusion of large biomolecules in aqueous solutions (e.g., proteins) which diffuse much slower. However, after a distance of  $x_{90} = 200 \mu\text{m}$  in the channel, a mixing quality of 90% is reached for a diffusion coefficient of  $D = 2 \cdot 10^{-9} \text{ m}^2/\text{s}$  which corresponds to a mixing time of  $t_{90} = 0.64 \text{ ms}$ .

## 2.2 Fabrication

The micromixer was fabricated according to the process depicted in Fig. 6 by silicon micromachining techniques on a silicon (Si) wafer ( $360 \mu\text{m}$  thick, double-side polished, silicon-nitride covered,  $\langle 100 \rangle$  lattice orientation) and a calcium fluoride ( $\text{CaF}_2$ ) wafer ( $1 \text{ mm}$  thick, Korth Kristalle GmbH, Altenholz, GER). Both wafers have a diameter of  $100 \text{ mm}$ . The fluid inlets and the distribution network were processed on the silicon wafer. The photoresist AZ6612 and the resist developer AZ826 used for these steps were purchased from AZ Electronic Materials (Branchenburg, NJ, USA). The mixing channel was structured in WL-5150,

a photopatternable spin-on silicone (Dow Corning Corporation, Midland, MI, USA), on the  $\text{CaF}_2$  wafer. To utilize this device for IR spectroscopy, it was necessary to use materials with low absorption in the mid IR region ( $3\text{--}10 \mu\text{m}$ ). Silicon and calcium fluoride suit these requirements and  $\text{CaF}_2$  is also transparent in the visible region so that this microchip can also be used for optical measurements with a light microscope. For more details about the IR absorption of materials and the setup of the IR spectrometer see Hinsmann et al (2001). Other cleanroom chemicals used for processing steps were alkali hydroxide etchant-KOH, propylene glycol monomethyl ether acetate-PGMEA and for cleansing ethanol, acetone, and isopropyl alcohol (Sigma Aldrich, St. Louis, MO, USA).

In the first step, the Si wafer was spin coated with a positive photoresist (Fig. 6a). A photomask was used to pattern the inlet holes for the fluid connections. Silicon nitride ( $\text{Si}_3\text{N}_4$ ) was partly removed by plasma etching, acting as etch mask for wet-etching. The inlet holes were wet-etched using KOH to form pyramidal grooves (Fig. 6b). To form the fluidic distribution network, a deep reactive ion etching (DRIE) process was applied on the other side of the silicon wafer after the inlet distribution structure was patterned by photolithography (Fig. 6c). For this process step precise backside alignment with a double-side mask-aligner was necessary to join the KOH etched grooves with the DRIE trenches. The fabrication was then continued by spincoating a calcium fluoride wafer with WL-5150 (Fig. 6d). This layer was soft baked before patterning of the mixing channel by UV-exposure. After a post-exposure bake, the desired pattern was developed

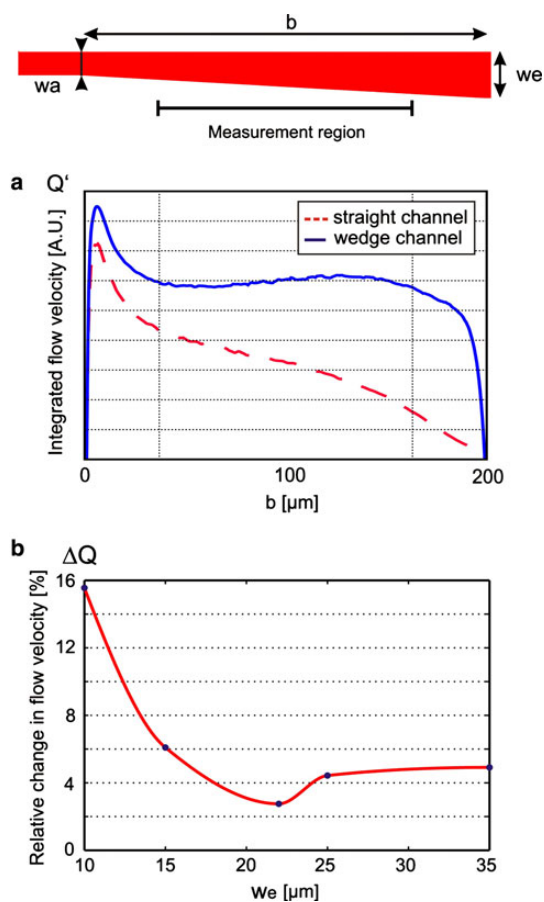


**Fig. 3** **a** Integrated flow velocity  $Q'$  over the x-component of the inlet wedge. The homogeneity of  $Q'$  in the measurement area is crucial for uniform fluid layers. **b** The y-axis shows  $\Delta Q$ , the relative change of the integrated flow velocity while the x-axis shows different values of  $w_e$  ( $w_a$  was fixed to 10 μm). The minimum of this plot defines the optimal wedge geometry for homogeneous fluid layers

(Fig. 6e). WL-5150 is an elastic material (bulk elongation 37.6 %) which allows bonding of silicon and calcium fluoride despite their highly different thermal expansion coefficients ( $\alpha_{Si} = 2 \cdot 10^{-6} 1/K$  and  $\alpha_{CaF_2} = 18.85 \cdot 10^{-6} 1/K$ ). The cold bonding procedure was applied for several hours at room temperature (Fig. 6f). The fully processed 100 mm wafer contains 40 devices ( $6 \times 17 \text{ mm}^2$ ). To connect the microfluidic chip to a commercial syringe pump from KD Scientific Inc (Holliston, MA, USA), a custom holder was designed. To provide excellent chemical resistance combined with mechanical strength polyetheretherketon (PEEK), a partly crystalline plastic was chosen as material for the holder. The custom device holder with an integrated micromixer

is shown in Fig. 6. A window opening in the custom holder underneath the mixing channel enables measurements with a FTIR brightfield microscope.

## 2.3 Experimental results and discussion

### 2.3.1 Color experiment

A suitable reaction of two reagents was chosen to verify the simulation results. It is not possible to use a dyed and a colorless liquid to distinguish between a layered and a mixed system without a confocal microscope as the mixing principle relies on vertical diffusion and the mixing process is observed from top. As the mixing channel is only 8 μm high, a simple pH indicator was also not satisfactory because the color intensity was not sufficient. Therefore, we applied a very strong color reaction. Tests showed that the reaction of colorless thiocyanate ( $\text{SCN}^-$ ) and slightly yellowish iron(III) ( $\text{Fe}^{3+}$ ) solution forms a deep red complex of adequate color intensity ( $\text{Fe}^{3+} + \text{SCN}^- \rightarrow [\text{FeSCN}]^{2+}$ ). For the following experiments 1.1 mol potassium thiocyanate KSCN and 0.1 mol iron(III) chloride  $\text{FeCl}_3$  solutions were used. To get comparable results, the mixing quality  $M_Q$  was defined according to Eq. 5.

$$M_Q = \frac{I_m - I_{\text{back}}}{I_{\text{cm}} - I_{\text{back}}} \quad (5)$$

To cancel the coloration intensity of the background image  $I_{\text{back}}$ , it is subtracted from the coloration intensities of the mixing experiment  $I_m$  and the completely mixed coloration value  $I_{\text{cm}}$ . In the experiment the micromixer was flushed solely with iron(III) solution and a premixed complex solution to get the respective color intensity values. For the experiment two micromixers, one with a wedge shaped inlet channel design and another one with a straight inlet channel design, was used. The mixers were driven by a dual syringe pump to gain stable and even flow rates ranging from 1 up to 30 μl/min in the mixing channel. Images were taken during the experiments with a digital camera applied to a microscope. The mixing times were calculated from the intensity values of a greyscale bitmap image by processing it with *Matlab* software.

The experimental result for the two different designs is shown in Figs. 7 and 8. An exponential curve fitting was applied for both measurements and the distance and time values at 90% mixing quality is calculated ( $x_{90}$  and  $t_{90}$ ). In addition, a *R*-square value is given, showing the quality of the curve fitting, where one corresponds to a perfect fit. The resulting mixing time for the wedge shaped design of  $t_{90w} = 0.9 \text{ ms}$  is in good agreement to the simulation results. The slightly faster result from the simulation could lead from a difference of the actual diffusion coefficient of

**Fig. 4** Two dimensional concentration profile of the optimized wedge shaped micromixer at the point where the four fluid layers are formed and 2.5 ms further down the mixing channel. The reagents in channels 1 and 2 are dark colored. Proper mixing of the reagents is occurring in the bright region

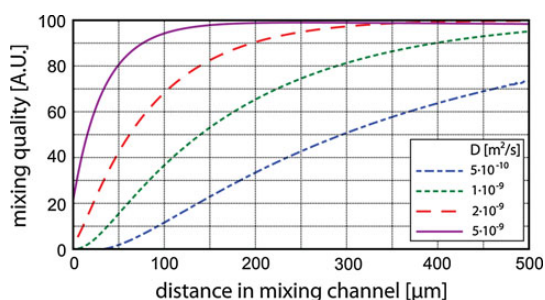
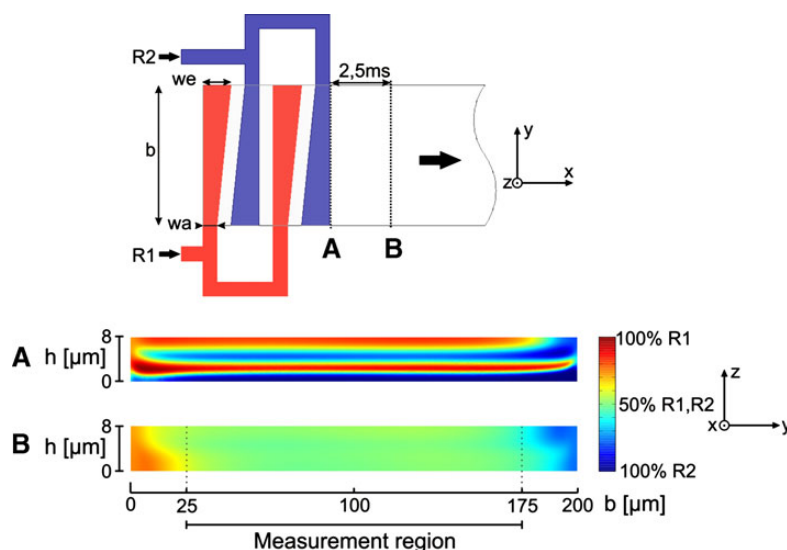


**Fig. 5** Simulation result of the mixing performance with a flow rate of 30  $\mu\text{l}/\text{min}$  in the mixing channel and different diffusion coefficients. The diffusion coefficient of  $D = 2 \cdot 10^{-9} \text{ m}^2/\text{s}$  represents the diffusion of water molecules

the used reagents compared to the one used in the simulation model. A significant result is the improvement of mixing time of the wedge shaped design compared to the straight channel design in Fig. 8. The distance at which 90% mixing quality is reached for the straight channel design is not visible in Fig. 8, but was calculated from the exponential fit to be  $x_{90s} = 1200 \mu\text{m}$ . This corresponds to a mixing time of  $t_{90s} = 3.8 \text{ ms}$  which is a factor four slower compared to the optimized wedge design. Consequently, the wedge design leads to a higher time resolution when analyzing kinetics of fast chemical reactions (e.g., Jung et al. 2008).

### 2.3.2 IR experiment

This micromixer uses the mixing chamber of a diffusion mixer as measurement region for time resolved

measurements. Measuring close to the beginning of the mixing channel corresponds to shorter reaction times than when moving further down the channel in the flow direction. In the IR experiment the proton exchange reaction of  $\text{H}_2\text{O}$  and  $\text{D}_2\text{O}$  forming 2 HDO is investigated. This is a well-known reaction, which is commonly used for characterizing microfluidic devices used in IR spectroscopy (e.g., Chan et al. 2009). Further, this reaction occurs between small water molecules which mix faster than larger biomolecules. If the measurement of the mixing procedure of such a fast reaction can be shown, it is obvious that other bioreactions, which are normally slower, can be measured with the device. The infrared measurements were carried out in transmission mode on a Hyperion 3000 microscope [Bruker Optics (Ettlingen, GER)], which was equipped with two 15-fold Cassegrain objectives. A mercury cadmium telluride (MCT) detector (Infrared Associates (Stuart, FL, USA)) with an element size of  $250 \times 250 \mu\text{m}^2$  was used. A picture of the optical beam path of the microscope is depicted in Fig. 1 ESM. The micromixing device was mounted in a custom chip holder and clamped onto the automated XY stage of the microscope. The two reagents were pumped through the mixer by a kdS 100 syringe pump (KD Scientific Inc (Holliston MA, USA)), which was equipped with two 500  $\mu\text{l}$  syringes at a pumping speed of 15  $\mu\text{l}/\text{min}$  per syringe resulting in a flow velocity of 31  $\text{cm}/\text{s}$  in the mixing channel. The optical aperture of the microscope was limited to 150  $\mu\text{m}$  width. The first measurement spot was positioned 75  $\mu\text{m}$  downstream from the last outlet channel. By moving the mixer, placed on a XY stage, the measurement spots were equally spaced 150  $\mu\text{m}$  apart. This resulted in a time resolution of

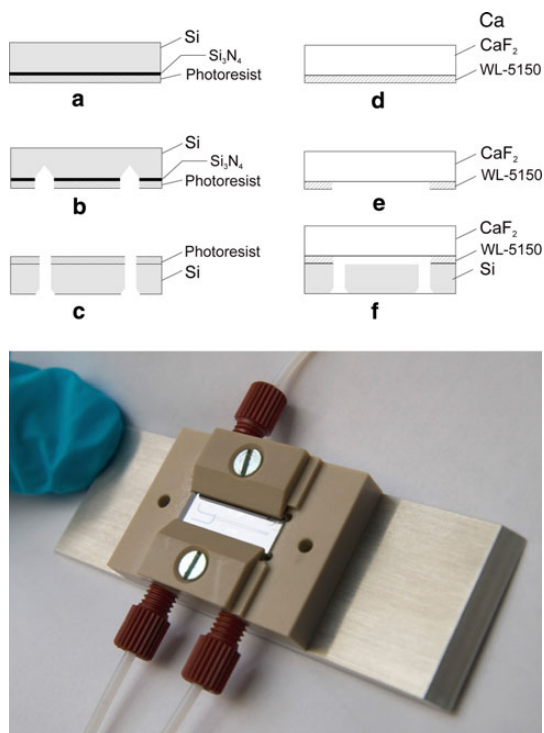


**Fig. 6** Top fabrication procedure of the micromixer: **a** spin coating of positive photoresist on Si wafer, **b** KOH etching of the inlet holes after a photolithographic step and plasma etching of the  $\text{Si}_3\text{N}_4$  layer, **c** spin coating of the other side and DRIE etching of the inlet channels, **d** spin coating of the  $\text{CaF}_2$  wafer with a photopatternable silicone, **e** photo-patterning of the mixing channel, **f** bonding of the  $\text{CaF}_2$  and the Si wafer. Bottom image of the custom built chip holder and a mounted micromixer, which enables using standard fittings as fluid connectors

0.48 ms between two spectra. At each measurement spot 32 co-additions at a spectral resolution of  $4\text{ cm}^{-1}$  were recorded. The diffusion coefficients of  $\text{D}_2\text{O}$  and  $\text{H}_2\text{O}$  are found in Crowell and Bartels (1996), which lead to calculated mixing times of about 1 ms as outlined in Sec. 2.1.  $\text{D}_2\text{O}$  was purchased from Sigma Aldrich (St. Louis, MO, USA) whereas deionized  $\text{H}_2\text{O}$  was taken from the lab. Each experiment consisted of two separate measurements. First, both syringes were filled with water and background measurements along the mixing channel were recorded. This procedure was necessary due to slight inhomogeneities in the transmission behavior along the mixing channel. Afterwards, one syringe was replaced with a syringe filled with  $\text{D}_2\text{O}$  and the experiment was repeated while mixing  $\text{D}_2\text{O}$  and  $\text{H}_2\text{O}$ . After both measurements were recorded, the absorbance spectrum was calculated with *OPUS* and plotted with *Origin*, Fig. 9. The dataset shows the deformation vibrations of  $\text{H}_2\text{O}$  ( $1640\text{ cm}^{-1}$ ),  $\text{HDO}$  ( $1456\text{ cm}^{-1}$ ) and

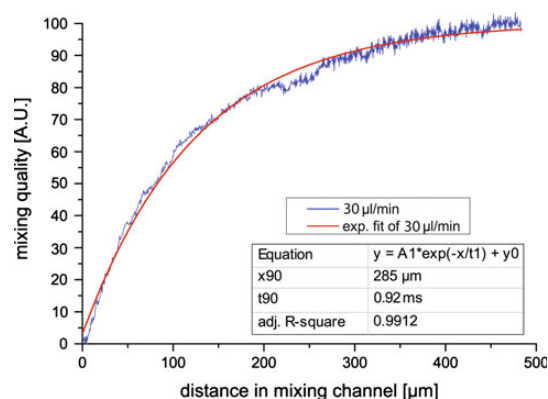


**Fig. 7** Recorded measurement result with the optimized wedge shaped design. The mixing quality was averaged over the channel width. The mixing time was calculated with MATLAB after an exponential fit was applied. Measurements along the mixing channel (x-axis) correspond to a reaction time defined by the flow velocity

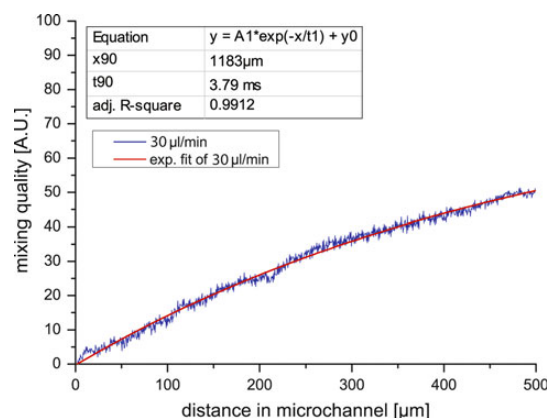


**Fig. 8** Recorded measurement result with the straight shaped design. The mixing quality was averaged over the channel width. The mixing time was calculated with MATLAB after an exponential fit was applied. Measurements along the mixing channel (x-axis) correspond to a reaction time defined by the flow velocity

$\text{D}_2\text{O}$  ( $1212\text{ cm}^{-1}$ ), measured along the mixing channel. The  $\text{H}_2\text{O}$  band appears negative due to the fact that  $\text{H}_2\text{O}$  served as the background of the measurement (Fig. 9a). The integrated band area of the  $\text{HDO}$  and  $\text{H}_2\text{O}$  bands, including mono-exponential fits to the data, are presented in Fig. 9b.

### 3 Conclusion

The microfluidic device presented is the first highly uniform multilamination mixer utilizing wedge shaped inlet channels, which can be applied for very fast time resolved



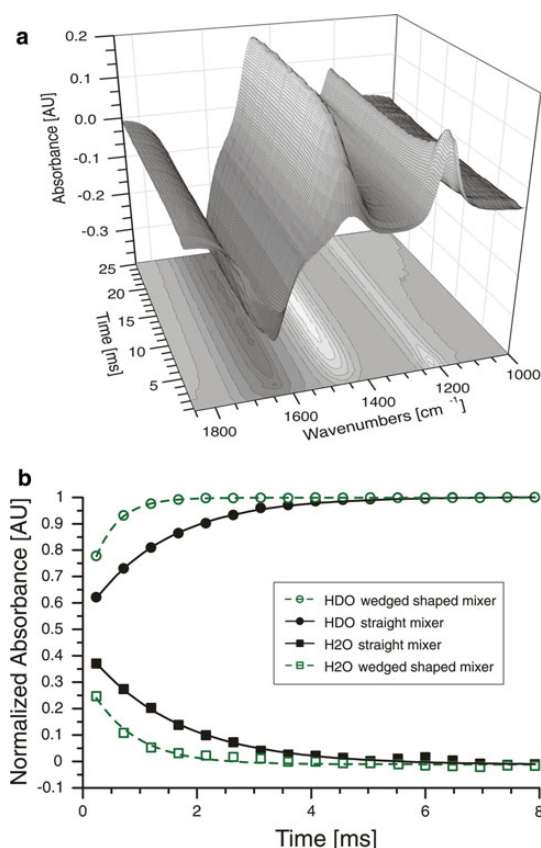


**Fig. 9** **a** This dataset shows the deformation vibrations of  $\text{H}_2\text{O}$  ( $1640\text{ cm}^{-1}$ ),  $\text{HDO}$  ( $1456\text{ cm}^{-1}$ ) and  $\text{D}_2\text{O}$  ( $1212\text{ cm}^{-1}$ ) measured along the mixing channel. The  $\text{H}_2\text{O}$  band appears negative due to the fact that  $\text{H}_2\text{O}$  served as the background for the measurement, **b** shows the integrated band area of the  $\text{HDO}$  and  $\text{H}_2\text{O}$  bands including mono-exponential fits to the data, resulting in reaction time constants of  $\text{H}_2\text{O}$  1.4 ms for the straight shaped mixer and 0.4 ms for the wedge shaped mixer

optical and infrared measurements. Simulated mixing times of around 1 ms could be confirmed through optical and infrared spectroscopic methods. Due to the optimized wedge shaped inlet channel, this design is applicable for very low flow rates down to  $1\text{ }\mu\text{l/min}$  and hence reduces costly reagent consumption to a minimum. Further, this device is applicable for IR spectroscopy to analyze the so far unclear kinetics of chemical reactions. The fabrication procedure of this device is simple and time efficient as the channel structures are processed on a silicon wafer by standard micromachining techniques. An easy device upgrade for mixing more than two reagents is possible by simply adding further lamination layers. In the same way, a two stage mixer can be realized where first two reacting

fluids are mixed and monitored before a third reagent is added (e.g., to quench the chemical reaction). The easy setup and handling with the custom holder and standard fluid connectors make this device an attractive tool for studying chemical reaction kinetics. In further experiments, this micromixer could also be used for determining diffusion coefficients of different fluids.

**Acknowledgments** For the sensor fabrication and technical support we thank E. Svasek and P. Svasek (ISAS Technology Lab and ZMNS, Center of Micro- and Nanostructures, Vienna University of Technology) and P. Hudek at the Vorarlberg University of Applied Sciences. For financial support we gratefully acknowledge the COMET Competence Center Program of the Austrian Government.

## References

- Ahmed D, Mao X, Shi J, Juluri BK, Huang TJ (2009) A millisecond micromixer via single-bubble-based acoustic streaming. *Lab Chip* 9(18):2738–2741
- Chan KLA, Gulati S, Edel JB, de Mello AJ, Kazarian SG (2009) Chemical imaging of microfluidic flows using atr-ftir spectroscopy. *Lab Chip* 9(20):2909–2913
- Chen L, Wang G, Lim C, Seong GH, Choo J, Lee EK, Kang SH, Song JM (2009) Evaluation of passive mixing behaviors in a pillar obstruction poly(dimethylsiloxane) microfluidic mixer using fluorescence microscopy. *Microfluid Nanofluid* 7(2):267–273
- Cortes-Quiroz CA, Zangeneh M, Goto A (2009) On multi-objective optimization of geometry of staggered herringbone micromixer. *Microfluid Nanofluid* 7(1):29–43
- Crowell R, Bartels DM (1996)  $\text{H}_2\text{O}/\text{D}_2\text{O}$  Isotope effect in geminate recombination of hydrated electron. *J Phys Chem* 100:17713–17715
- Gambin Y, Simonnet C, VanDelinder V, Deniz A, Groisman A (2010) Ultrafast microfluidic mixer with three-dimensional flow focusing for studies of biochemical kinetics. *Lab Chip* 272(23):5962–5970
- Hardt S, Drese KS, Hessel V, Schnfeld F (2005) Passive micromixers for applications in the microreactor and TAS fields. *Microfluidics Nanofluidics* 1(2):108–118
- Hinsmann P, Frank J, Svasek P, Harasek M, Lendl B (2001) Design, simulation and application of a new micromixing device for time resolved infrared spectroscopy of chemical reactions in solution. *Lab Chip* 1(1):16–21
- Hinsmann P, Haberkorn M, Frank J, Svasek P, Harasek M, Lendl B (2001) Time-resolved FT-IR spectroscopy of chemical reactions in solution by fast diffusion-based mixing in a micromachined flow cell. *Appl Spectrosc* 55(3):241–251
- Hossain S, Ansari MA, Kim KY (2009) Evaluation of the mixing performance of three passive micromixers. *Chem Eng J* 150(2–3):492–501
- Johansson L, Johansson S, Nikolajeff F, Thorslund S (2009) Effective mixing of laminar flows at a density interface by an integrated ultrasonic transducer. *Lab Chip* 9(2):297–304
- Jung SY, Liu Y, Collier CP (2008) Fast mixing and reaction initiation control of single-enzyme kinetics in confined volumes. *Langmuir* 24(9):4439–4442
- Kanai M, Uchida D, Sugiura S, Sato H, Mori Y, Sakamoto K, Nakanishi H, Shoji S (2002) Optimal design of the micromixer using nonhomogeneous multilayer laminar flow. In: *Proc. Micro-TAS*, vol 1, pp 73–75

- Kauffmann E, Darnton N, Austin R, Batt C, Gerwert K (2001) Lifetimes of intermediates in the beta-sheet to alpha-helix transition of beta-lactoglobulin by using a diffusional ir mixer. *Proc Natl Acad Sci USA* 98(12):6646–6649
- Lipman E, Schuler B, Bakajin O, Eaton W (2003) Single-molecule measurement of protein folding kinetics. *Science* 301(5637):1233–1235
- Mansur EA, Ye M, Wang Y, Dai Y (2008) A state-of-the-art review of mixing in microfluidic mixers. *Chinese J Chem Eng* 16(4):503–516
- Mao X, Juluri BK, Lapsley MI, Stratton ZS, Huang TJ (2010) Milliseconds microfluidic chaotic bubble mixer. *Microfluid Nanofluid* 8(1):139–144
- Nguyen N, Wu Z (2005) Micromixers—a review. *J Micromech Microeng* 15(2):R1–R16
- Nguyen NT, Wereley ST (2002) *Fundamentals and Applications of Microfluidics*. MEMS Series, Artech House
- Park JM, Seo KD, Kwon TH (2010) A chaotic micromixer using obstruction-pairs. *J Micromech Microeng* 20(1):015023 (11 pp)
- Rigler A, Wagner C, Svasek P, Jachimowicz A, Hudek P, Kraft M, Vellekoop M (2008) Improved lamination micromixer with wedge shaped inlet channels for IR spectroscopy. In: *Proceedings of 22nd international eurosensors conference*
- Wen CY, Yeh CP, Tsai CH, Fu LM (2009) Rapid magnetic microfluidic mixer utilizing AC electromagnetic field. *Electrophoresis* 30(24, Sp. Iss. SI):4179–4186
- Williams AM, Griffiths DJ, Vlachos PP (2009) Laminar mixing using oscillating cantilevered ionic polymer actuators. *Sensor Actuat A Phys* 153(1):105–113





## Publication II

W. Buchegger, C. Wagner, P. Svasek, B. Lendl, M. Kraft, and M.J. Vellekoop, Sensors and Actuators B: Chemical 159, 1, 336-341 (2011), DOI: 10.1016/j.snb.2011.06.083.





## Fabrication and characterization of a vertical lamination micromixer for mid-IR spectroscopy

Wolfgang Buchegger<sup>a,\*</sup>, Christoph Wagner<sup>b</sup>, Peter Svasek<sup>a</sup>, Bernhard Lendl<sup>b</sup>, Martin Kraft<sup>c</sup>, Michael J. Vellekoop<sup>a</sup>

<sup>a</sup> Institute of Sensor and Actuator Systems, Vienna University of Technology, Gusshausstrasse 27–29, 1040, Vienna, Austria

<sup>b</sup> Institute of Chemical Technologies and Analytics, Vienna University of Technology, Austria

<sup>c</sup> Carinthian Tech Research AG, Villach, Austria

### ARTICLE INFO

#### Article history:

Received 13 May 2011

Received in revised form 27 June 2011

Accepted 30 June 2011

Available online 7 July 2011

#### Keywords:

Micromixer

Passive mixing

Lamination mixer

Mid-IR spectroscopy

Microfabrication

### ABSTRACT

A multilamination micromixer for time resolved infrared spectroscopy, optimized by fluid simulations is characterized by fluidic means for different flow rates. The mixer is fabricated with silicon micromachining techniques. Using four instead of two lamination layers yields a reduction of the diffusion length and decreases mixing time significantly. Measurement results show the ultrafast mixing performance of this micromixer (<1 ms for aqueous solutions) with high uniformity. An infrared measurement (mid-IR spectral range, 3–10  $\mu\text{m}$ ) proves the applicability of the device to monitor fast (bio)chemical reactions. The mixer operates in a high dynamic range enabling the investigation of a variety of chemical reaction kinetics in the time range of 10–300 ms. A high yield in fabrication is achieved due to well controlled processes. Easy chip handling and higher pressure durability is provided by a dedicated custom chip holder.

© 2011 Elsevier B.V. All rights reserved.

### 1. Introduction

The use of micromixers in time resolved mid-infrared (mid-IR) spectroscopy is an effective method to investigate the kinetics of (bio)chemical reactions including interaction processes [1–4]. In contrary to other detection techniques like optical or fluorescence-based methods the reaction under investigation does not have to be labeled for the measurement. Hence, the applicability of this technique is broadened because of the limited availability and selectivity of suitable labels. To study such reaction kinetics the mixing of reagents has to be completed before a reaction evolves. Therefore, mixing time is crucial for investigating fast chemical reactions. To limit the amount of – often costly – reagents, low flow rates are preferred. Recent developments of micromixers together with variety of different design approaches can be found in Refs. [5,6]. The resulting small dimension of the channel and the low flow rates cause a strictly laminar flow regime (Reynolds number < 1), which inhibits fast mixing. To support mixing, active principles can be applied. Designs utilizing acoustic waves were published in Refs. [7,8]. A mixer using mono disperse micro-bubbles for mixing was presented in Ref. [9]. The mixing design shown in Ref. [10] utilized a magnetic actuated stir bar. Most of the active mixing designs require active transducers in the mixing channel, e.g. electrodes,

beams, bubbles which would disturb the IR measurement. Hence, passive mixing principles, reported in Ref. [11], are preferred. A typical design is the T-mixer, which simply employs a junction of two channels into a perpendicular channel. Design variations with pillar structures [12] or herringbone structured walls [13] improve the mixing quality. In the visible spectrum a stopped-flow approach together with external trigger methods can be used to study chemical reactions [14]. Nevertheless, these techniques are subject to a certain limitation in the mid-IR spectral region. Due to excessive infrared absorption by aqueous media [15], a channel height of 10  $\mu\text{m}$  should not be exceeded. The resulting small cross-section of the mixing channel yields high pressure gradients in the mixing device resulting from stopping flow abruptly in the channels. Therefore, a continuous flow mixing device is highly attractive to avoid this problem. A diffusional flow cell for investigating chemical reactions operated in a stopped flow principle was presented in Ref. [16]. Alternate vertical fluid layers of two reagents were created and mixing times in the 200 ms time range were achieved. Lamination of two fluid layers was proposed in Ref. [1] allowing to increase mixing speed by a factor of 2. To further improve mixing and reduce mixing times multilayered diffusional mixers were introduced. A one sided fed horizontal diffusional micromixer with one inlet for each of the three layers was reported with mixing times in the order of 50 ms by Ref. [17]. Time resolved Fourier transform infrared (FTIR) measurements with a lamination micromixer with two inlets, using two horizontal fluid layers in a 10  $\mu\text{m}$  deep channel were presented by Ref. [18].

\* Corresponding author. Tel.: +43 1 58801 76690; fax: +43 1 58801 36699.  
E-mail address: [wolfgang.buchegger@tuwien.ac.at](mailto:wolfgang.buchegger@tuwien.ac.at) (W. Buchegger).

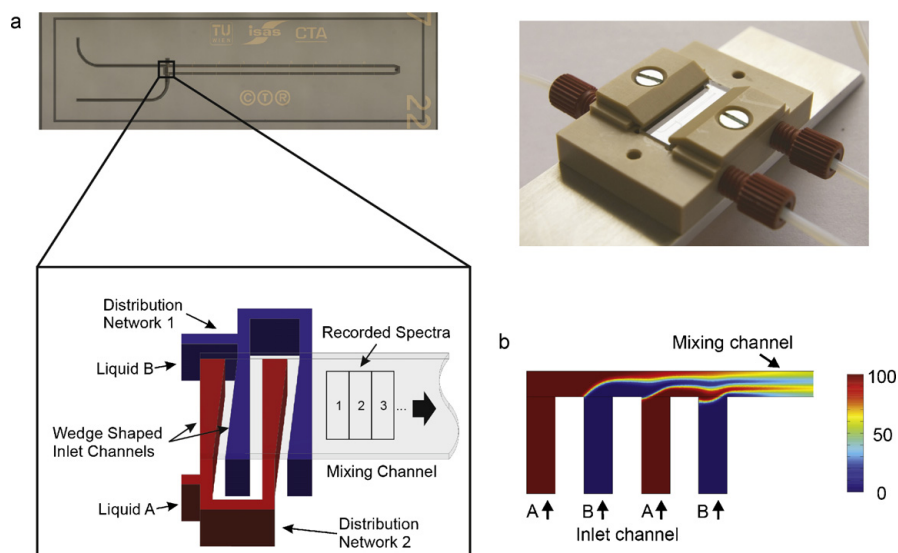


**Fig. 1.** (a) Photograph of the micromixer and the chip holder with detailed section of distribution network, wedged inlets and mixing channel which also serves as measurement area, (b) simulation result of a side view of the mixing channel with individual fluid layers.

In our continuous flow approach, the mixing channel also serves as measurement area. Wedge shaped inlet channels yield a highly uniform mixing of reagents. The chemical reaction can then be followed by recording IR spectra along the mixing channel (1,2,3...  $n$ ), see Fig. 1(a). The time resolution of the experiment is determined by the spotsize of the lightbeam ( $150\ \mu\text{m} \times 150\ \mu\text{m}$ ) and the flow rate of the liquids inside the measurement channel, allowing to average at each measurement position in any desired order. A smaller spotsize or faster pumping gives higher time resolutions. In this contribution the fabrication and flow characterization of our micromixer designed for fast mixing of aqueous solutions is presented. A bio-chemical model reaction investigated by infrared microscopy serves as an illustration for the broad applicability of this device. The improved mixer design generates four laminated fluid layers out of two fluid feeds by a distribution network shown in Fig. 1(a). Straight, rectangular inlet channels would generate a non-uniform flow distribution across the channel [19]. Therefore, wedge shaped inlet channels are used to compensate this interaction and achieve a uniform pressure and concentration profile of both liquids across the channel width. The mixing time is proportional to the square of the diffusion lengths in the channel ( $t_{\text{mix}} \sim l_{\text{diff}}^2$ ) [20]. The fluid layers have different thicknesses, taking into account that diffusion occurs on both sides on the inner layers. In this way the mixing time can be reduced by a factor of 9 compared to a two layer system. A transparent cover of calcium fluoride ( $\text{CaF}_2$ ) enables the optical characterization and eases the handling and positioning of the mixing device for the infrared analysis. The fluid support for the chip is provided by a custom holder which allows the use of standard 1/4 in. fluid connectors. These two exterior fluid feeds are driven by syringe pumps. Flow rates ranging from  $2\ \mu\text{l}/\text{min}$  up to  $30\ \mu\text{l}/\text{min}$  were investigated experimentally.

## 2. Simulation

Simulations were carried out with COMSOL Multiphysics 3.5a using the Incompressible Navier – Stokes and the Convection and Diffusion Model. Three different diffusion constants were assumed

in the simulations, where a concentration of  $50\ \mu\text{mol}/\text{l}$  is mixed with  $0\ \mu\text{mol}/\text{l}$ . Further, properties of the reagents were assumed to be similar to water. To optimize the channel geometry and the fluid distribution network, CFD (computational fluid dynamic) simulations were used. The fluid distribution network forms four horizontal fluid layers out of two fluid feeds connected to the macro world. A two dimensional simulation result of a side view of the micromixer is depicted in Fig. 1(b). For this simulation a diffusion coefficient of water  $D_{\text{H}_2\text{O}} = 2 \times 10^{-9}\ \text{m}^2/\text{s}$  and a flow rate of  $20\ \mu\text{l}/\text{min}$  was used to show the individual fluid layers. Mixing of the reagents is achieved after a very short distance in the mixing channel consequently the following chemical reaction can be investigated thereafter by IR spectroscopy. Simulation results were also applied to find an optimized inlet wedge shape for a homogeneous sample distribution over the channel width [20]. The calculated Reynolds number (1) representing the ratio between momentum and viscous friction lies in the range of  $Re = 0.5$  for a flow velocity of  $v = 0.2\ \text{m}/\text{s}$ . The Peclet number (2) giving the ratio between the mass transport due to convection divided by that of diffusion with values  $Pe \leq 80$  shows that mixing is diffusion dominated, see Ref. [6]. In the calculation the hydraulic diameter  $D_H \approx 15\ \mu\text{m}$  is about one order of magnitude higher than the mixing path length  $L$  due to the multilaminar mixing approach  $D_H/L \approx 10$ . Therefore, according to Fick's law (3) a mixing time of  $t \approx 0.64\ \text{ms}$  can be estimated.

$$Re = \frac{\rho v D_H}{\mu} \quad (1)$$

$$Pe = \frac{Lv}{D} \quad (2)$$

$$t = \frac{L^2}{2D} \quad (3)$$

Further, three different fluids were modelled and investigated by simulations. A liquid of large and slow diffusing molecules is represented by  $D = 1 \times 10^{-9}\ \text{m}^2/\text{s}$ . A diffusion coefficient of  $D_{\text{H}_2\text{O}} = 2 \times 10^{-9}\ \text{m}^2/\text{s}$  represents aqueous and  $D = 5 \times 10^{-9}\ \text{m}^2/\text{s}$  very fast diffusing solutions of small molecules. A mixing time was calculated at a distance of 90 % mixing and plotted over the designed

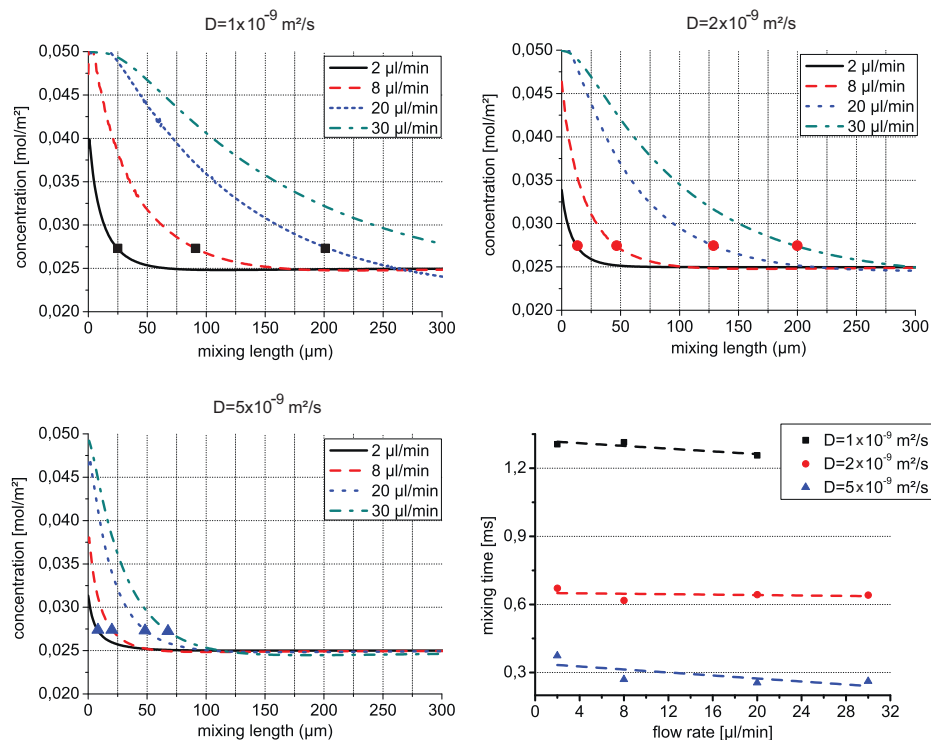


Fig. 2. Simulation of the concentration along the mixing channel when mixing a 50 μmol/l solution with a 0 mol/l solution, 90% mixture is marked. The graph shows the mixing behavior of liquids with three different diffusion constants and the calculated mixing times at the bottom right.

range of flow rates, see Fig. 2. All modelled fluids mix in the low millisecond time regime. The graph shows an almost constant mixing time for increasing flow rates of the same diffusion constant which means that there is no performance loss in a wide range of flow rates. A small distortion at very low flow rates is recognizable but can be explained by premixing of the reagents. A mixing time of  $t_{\text{mix}} = 0.7$  ms for aqueous solutions and  $t_{\text{mix}} = 0.29$  ms for small organic molecules, were determined by simulation results.

### 3. Fabrication

The micromixer was fabricated using standard micromachining techniques on a silicon wafer (350 μm thick, (100) lattice orientation) and a calcium fluoride (CaF<sub>2</sub>) wafer (1 mm thick, Korth Kristalle GmbH, GER). Both wafers have a diameter of 100 mm. Fig. 3 shows the fabrication procedure schematically. A double-side polished silicon (Si) wafer covered with a silicon oxide (SiO<sub>2</sub>) and silicon nitride (Si<sub>3</sub>N<sub>4</sub>) layer was spin coated with a protective layer of positive photoresist AZ1512 on the bottom side before removing the SiO<sub>2</sub> and Si<sub>3</sub>N<sub>4</sub> layer on top by plasma etching (a). A layer of positive resist AZ6624 was spin coated onto the bottom side of the wafer followed by a photolithographic step with developer AZ826 to pattern the inlet holes for the fluid inlets. SiO<sub>2</sub> and Si<sub>3</sub>N<sub>4</sub> were partly removed by reactive ion etching (RIE). This pattern was then used as an etch mask for an alkali hydroxide etchant – KOH etch process of the pyramidal inlet grooves from the bottom with a depth of 150 μm (b). Then the top side of the Si wafer was spin coated with AZ624 and patterned by lithography after a

backside alignment step (c). The structure of the distribution network was established by deep reactive ion etching (DRIE) (d). Etch tests showed that after applying 340 “Bosch-Process” steps an etch depth of 200 μm with an aspect ratio of 1:20 could be achieved. A final cleaning step with O<sub>2</sub> plasma from both sides was applied to

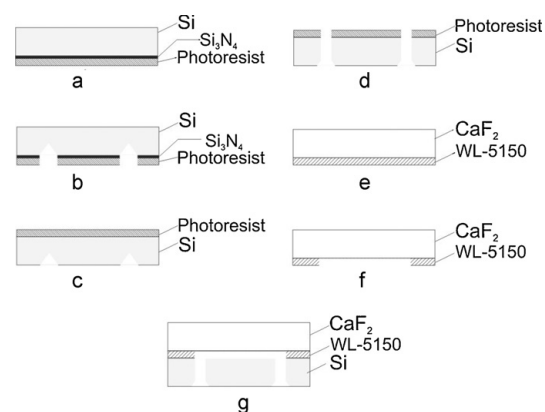


Fig. 3. Fabrication process of the mixer: (a) spin coating of the lower side of a Si wafer, (b) KOH etching of the inlet holes, (c) spin coating of the upper side, (d) DRIE etching of the inlet channels, (e) spin coating the CaF<sub>2</sub> wafer with silicone, (f) photo-pattern of the mixing channel, (g) bonding of the CaF<sub>2</sub> and the Si wafer.

remove the remaining photoresist. The fabrication continued with a 1 mm thick  $\text{CaF}_2$  wafer. The mixing channel itself was realized in a photosensitive silicone (WL-5150, Dow Corning, USA). To achieve a layer thickness of 8  $\mu\text{m}$ , the silicone was diluted in a ratio of 16:1 of WL5150:Mesitylen and spin coated onto the  $\text{CaF}_2$  wafer (e). The wafer was then soft baked before UV-exposure. This occurred with a proximity lithographic step as the mask would stick to the silicone layer on the wafer. After a post-exposure bake, the desired pattern was developed with Mesitylen (f). The two wafers were then aligned on top of each other without contact as the WL5150 structure would immediately stick to the silicon wafer. Taking into account the different thermal expansion coefficients of calcium fluoride and silicon (factor 9), the two wafers were finally cold bonded for 4 h (g). Other cleanroom chemicals used for processing were propylene glycol monomethyl ether acetate (PGMEA) and for cleansing ethanol, acetone, isopropyl alcohol (Sigma Aldrich, USA). On a fully processed 100 mm wafer 40 devices ( $6\text{ mm} \times 17\text{ mm}$ ) are fabricated. A custom holder was designed to connect the fluid inlets to polytetrafluoroethylene (PTFE) tubings. To provide chemical resistance and mechanical strength the holder was fabricated in polyetheretherketon (PEEK). For the fluid support a commercial syringe pump was used (Fusion200, Chemyx Inc., USA).

Fig. 4 shows scanning electron microscopic (SEM) images from the silicon part of the mixer. As preparation the mixer was cut in half lengthwise with a wafer saw. This enables to observe the deep etched grooves fabricated by DRIE. Due to the inhibited gas exchange in the narrow regions the grooves with a high aspect ratio normally etch much slower than broader areas. In our design the wedge shaped inlet channels form such a structure. However, in our case there is only a small difference in etch depth between the wide and the narrow region as shown in Fig. 4(a) due to a well controlled process. Although, aspect ratios as high as 1:20 are fabricated a high yield of almost 100% can be achieved on a wafer. In Fig. 4(b) a part of the distribution network, which generates the individual fluid layers by splitting up the fluid stream, is depicted. Simulations showed that the splitting ratio of the fluid stream in this section has a great influence on the mixing behavior of the fluids so that straight channel walls and narrow tolerances are required. In the picture the etching cycles with about 1  $\mu\text{m}$  in depth are indicated by the bright horizontal lines, see Fig. 4(b). The deep etched groove shows a very smooth channel wall and low roughness which leads to a well controlled fluid handling.

#### 4. Experimental

##### 4.1. Optical characterization

To determine the mixing performance two transparent liquids forming a strongly colored reaction product when mixed were used. This is necessary since, as the mixer is observed from the top and the liquids are mixed vertically, it is not possible to use a simple dye to distinguish between the established fluid layers and a mixed solution. The model reaction of iron (III) ( $0.1\text{ mol/l Fe}(\text{NO}_3)_3$  solution, which is slightly yellow), and a colorless rhodanide ( $1.1\text{ mol/l KSCN}$ ) solution were used. When mixed, these two reagents form a bright red complex that can be measured optically with a standard light microscope. A standard double-syringe pump with 1 ml syringes provided the solutions at different flow rates. The liquids are assumed to have a diffusion coefficient of  $D = 2 \times 10^{-9}\text{ m}^2/\text{s}$ . To compare the experimental results with the CFD simulations the flow rates of 2, 8, 20 and  $30\text{ }\mu\text{l}/\text{min}$  were used. Results showing a very uniform mixing across the channel width are depicted in Fig. 5. A marker indicates the calculated 90 % mixture from simulations which matches the results of the experiment very well if compared to Fig. 2. All marked distances match a mixing time of about  $t_{\text{mix}} = 1\text{ ms}$ .

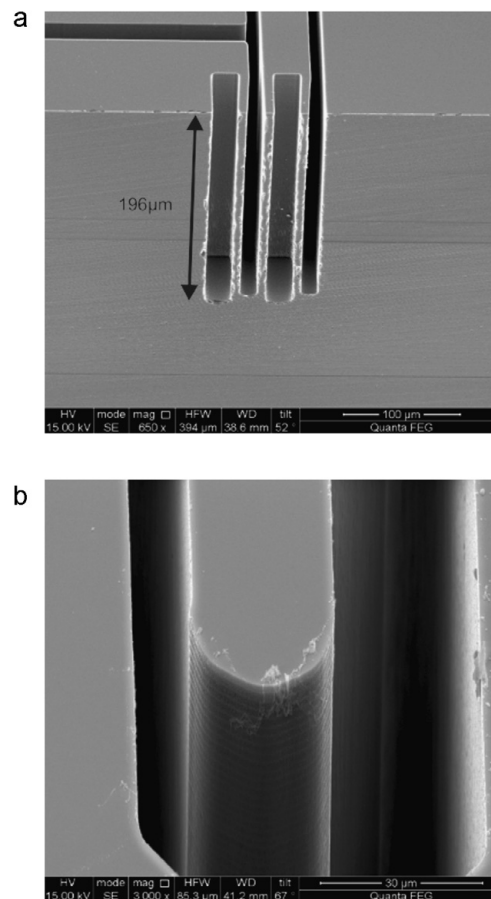


Fig. 4. Scanning electron microscopic image of the silicon part of the micromixer of (a) a lengthcut of the micromixer with the wedge shape inlets and (b) a part of the distribution network. High aspect ratio grooves with aspect ratios as high as 1:20 are fabricated by deep reactive ion etching. The well controlled fabrication yields very smooth and vertical sidewalls with a uniform depth.

##### 4.2. Infrared measurements

With the mixer the rapid hydrogen deuterium (H/D) exchange reactions of carbohydrates in aqueous solutions were studied. Fig. 6 shows the H/D exchange reaction of the OH groups of an aqueous ( $\text{H}_2\text{O}$ )  $0.2\text{ mol/l}$  trehalose solution upon mixing with  $\text{D}_2\text{O}$ . The fast H/D exchange between  $\text{H}_2\text{O}$  and  $\text{D}_2\text{O}$  was taken as the background measurement ( $I_0$ ) prior to recording the reaction of trehalose solution with  $\text{D}_2\text{O}$ . After applying Beer's law (4) the absorption spectra shown in Fig. 6 are obtained and plotted without any further data treatment.

$$A = \log \left( \frac{I_0}{I} \right) \quad (4)$$

Measurements were taken on a Bruker Hyperion 3000 microscope attached to a Bruker Tensor mid-IR Fourier transform spectrometer applying a rectangular aperture of  $180\text{ }\mu\text{m} \times 100\text{ }\mu\text{m}$  averaging 32 scans at each measurement position to improve the S/N ratio. The flow rate in the mixing channel amounts to  $24\text{ }\mu\text{l}/\text{min}$ . According to Ref. [21] the changing bands observed at  $1082\text{ cm}^{-1}$ ,

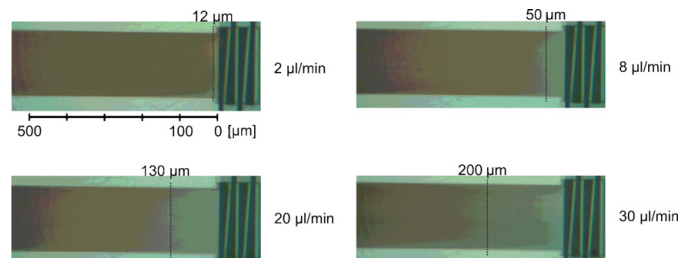


**Fig. 5.** Mixing experiments of  $\text{Fe}^{3+}$  and  $\text{SCN}^-$  ( $D = 2 \times 10^{-9} \text{ m}^2/\text{s}$ ) with the optimized wedge geometry. The result of 90% mixture of the simulations ( $t_{\text{mix}} = 0.7 \text{ ms}$ ) is marked and the distance from the inlet is given. Mixing times resulting from measurements are in good agreement to the simulated values.

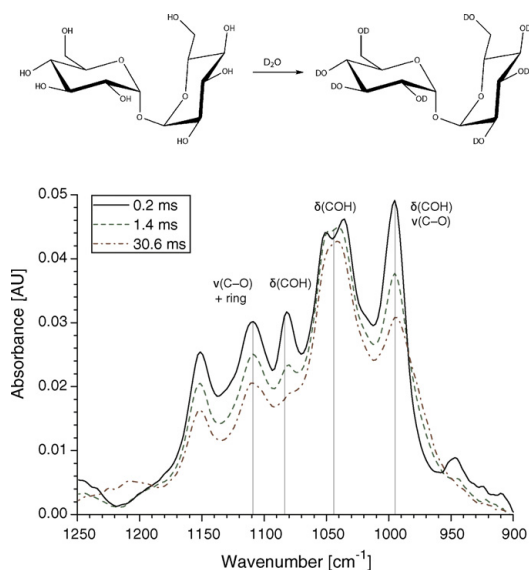


**Fig. 6.** Time resolved FTIR measurement of trehalose with  $\text{D}_2\text{O}$  at a total flow rate of  $24 \mu\text{l}/\text{min}$  in the mixing channel. Three different spectra at specific times along the mixing channel are plotted, showing the decrease of OH bands during the exchange to OD.

$995 \text{ cm}^{-1}$  and in the region around  $1042 \text{ cm}^{-1}$  can be assigned to the COH bending vibrations ( $\delta(\text{COH})$ ) of the different OH groups. The band at  $1109 \text{ cm}^{-1}$  is a combination of the CO stretching ( $\nu(\text{C-O})$ ) and a ring vibration. The clear difference in the absorption spectra between  $t = 0.2 \text{ ms}$  and  $t = 1.4 \text{ ms}$  show the suitability of this micromixer for the investigation of fast (bio)chemical reactions by mid-IR spectroscopy in the low millisecond time range. Most significant changes take place until a reaction time of about  $t = 4 \text{ ms}$ . The measurement indicates that the equilibrium state of the reaction is almost reached after  $t = 30.6 \text{ ms}$ .

## 5. Conclusions

The presented passive micromixer can be applied for time resolved optical and infrared measurements of various (bio)chemical reactions. Optical measurements show that the optimized inlet wedge shape of this design yields fast mixing times of around  $1 \text{ ms}$  for aqueous solutions at very low flow rates down to  $1 \mu\text{l}/\text{min}$ . Hence, costly reagent consumption is reduced to a minimum. Further, this device is applicable for time resolved mid-IR

spectroscopy because of the selected materials of this micromixer. The IR measurement of the H/D exchange occurring in trehalose upon mixing of an aqueous ( $\text{H}_2\text{O}$ ) trehalose solution with heavy water ( $\text{D}_2\text{O}$ ) shows the ability of the system to monitor fast (bio)chemical reactions with high S/N ratio. The fabrication procedure of this device is simple and time efficient as the channel structures are generated in silicon by micromachining techniques. Further, this technology enables the easy integration of other sensing elements (e.g. temperature, flow rate, etc.). The easy setup and handling with the custom chip holder and standard fluid connectors make this device an attractive tool for studying chemical reaction kinetics.

## Acknowledgments

For the sensor fabrication and the technical support we thank E. Svasek (ISAS Technology Lab and ZMNS, Center of Micro- and Nanostructures, Vienna University of Technology). For the scanning electron microscope images we thank FEI Europe and A. Bittner (ISAS Technology Lab and ZMNS, Center of Micro- and Nanostructures, Vienna University of Technology). For financial support we gratefully acknowledge the COMET Competence Center Program of the Austrian Government.

## Appendix A. Supplementary Data

Supplementary data associated with this article can be found, in the online version, at doi:10.1016/j.snb.2011.06.083.

## References

- [1] P. Hinsmann, J. Frank, P. Svasek, M. Harasek, B. Lendl, Design, simulation and application of a new micromixing device for time resolved infrared spectroscopy of chemical reactions in solution, *Lab Chip* 1 (1) (2001) 16–21.
- [2] N. Kaun, M.J. Vellekoop, B. Lendl, Time-resolved fourier transform infrared spectroscopy of chemical reactions in solution using a focal plane array detector, *Appl. Spectrosc.* 60 (11) (2006) 1273–1278.
- [3] H.M. Al-Hashimi, N.G. Walter, RNA dynamics: it is about time, *Curr. Opin. Struct. Biol.* 18 (3) (2008) 321–329 (Nucleic acids/Sequences and topology).
- [4] C. Koetting, Y. Suveyzdis, R.S. Bojja, N. Metzler-Nolte, K. Gerwert, Label-free screening of drug–protein interactions by time-resolved Fourier transform infrared spectroscopic assays exemplified by RAS interactions, *Appl. Spectrosc.* 64 (9) (2010) 967–972.
- [5] E.A. Mansur, M. Ye, Y. Wang, Y. Dai, A state-of-the-art review of mixing in microfluidic mixers, *Chin. J. Chem. Eng.* 16 (4) (2008) 503–516.
- [6] N. Nguyen, Z. Wu, Micromixers—a review, *J. Micromech. Microeng.* 15 (2) (2005) R1–R16.
- [7] D. Ahmed, X. Mao, J. Shi, B.K. Juluri, T.J. Huang, A millisecond micromixer via single-bubble-based acoustic streaming, *Lab Chip* 9 (18) (2009) 2738–2741.
- [8] L. Johansson, S. Johansson, F. Nikolajeff, S. Thorslund, Effective mixing of laminar flows at a density interface by an integrated ultrasonic transducer, *Lab Chip* 9 (2009) 297–304.
- [9] X. Mao, B.K. Juluri, M.I. Lapsley, Z.S. Stratton, T.J. Huang, Milliseconds microfluidic chaotic bubble mixer, *Microfluid. Nanofluid.* 8 (1) (2010) 139–144.

- [10] K.S. Ryu, K. Shaikh, E. Goluch, Z. Fan, C. Liu, Micro magnetic stir-bar mixer integrated with parylene microfluidic channels, *Lab Chip* 4 (6) (2004) 608–613.
- [11] S. Hardt, K.S. Drese, V. Hessel, F. Schnfeld, Passive micromixers for applications in the microreactor and TAS fields, *Microfluid. Nanofluid.* 1 (2) (2005) 108–118.
- [12] L. Chen, G. Wang, C. Lim, G.H. Seong, J. Choo, E.K. Lee, et al., Evaluation of passive mixing behaviors in a pillar obstruction poly(dimethylsiloxane) microfluidic mixer using fluorescence microscopy, *Microfluid. Nanofluid.* 7 (2) (2009) 267–273.
- [13] J.M. Park, K.D. Seo, T.H. Kwon, A chaotic micromixer using obstruction-pairs, *J. Micromechan. Microeng.* 20 (1) (2010) 015023–015111.
- [14] B.J. Burke, F.E. Regnier, Stopped-flow enzyme assays on a chip using a micro-fabricated mixer, *Anal. Chem.* 75 (8) (2003) 1786–1791.
- [15] J.K. Koenig, D.L. Tabb, Analytical applications of FT-IR to molecular and biological systems, in: *Proc of the NATO Advanced Study Institute*, D. Reidl, 1980, pp. 241–255.
- [16] P. Hinsmann, M. Haberkorn, J. Frank, P. Svasek, M. Harasek, B. Lendl, Time-resolved FT-IR spectroscopy of chemical reactions in solution by fast diffusion-based mixing in a micromachined flow cell, *Appl. Spectrosc.* 55 (3) (2001) 241–251.
- [17] E. Lipman, B. Schuler, O. Bakajin, W. Eaton, Single-molecule measurement of protein folding kinetics, *Science* 301 (5637) (2003) 1233–1235.
- [18] M. Schlegler, C. Wagner, M.J. Vellekoop, B. Lendl, J. Heberle, Time-resolved flow-flash FT-IR difference spectroscopy: the kinetics of CO photodissociation from myoglobin revisited, *Anal. Bioanal. Chem.* 394 (7) (2009) 1869–1877.
- [19] A. Rigler, C. Wagner, P. Svasek, A. Jachimowicz, P. Hudek, M. Kraft, et al., Improved lamination micromixer with wedge shaped inlet channels for IR spectroscopy, in: *Proceedings of 22nd International Eurosensors Conference*, 2008, pp. 577–580.
- [20] W. Buchegger, C. Wagner, B. Lendl, M. Kraft, M.J. Vellekoop, A highly uniform lamination micromixer with wedge shaped inlet channels for time resolved infrared spectroscopy, *Microfluid. Nanofluid.* 10 (4) (2010) 889–897 (online available).
- [21] M. Kacurkov, M. Mathlouthi, FTIR and laser-Raman spectra of oligosaccharides in water: characterization of the glycosidic bond, *Carbohydrate Res.* 284 (2) (1996) 145–157.

## Biographies

**Wolfgang Buchegger** was born in Austria, in 1983. In June 2009, he received his master degree in electrical engineering at the Vienna University of Technology. In the same year he joined the Institute of Sensors and Actuator Systems at the Vienna University of Technology, Austria, where he is pursuing the Ph.D. degree. His main research activity concerns the development of novel microfluidic devices in the field of microfluidic sensors.

**Christoph Wagner** was born in Austria, in 1981. In June 2007, he received his master degree in technical chemistry at the Vienna University of Technology. He continued his work at the Institute of Chemical Technologies and Analytics in the field of time resolved FTIR measurements. His interests lie in field of step scan spectroscopy and the application of microfluidic mixers for TR-FTIR measurements.

**Peter Svasek** was born in Vienna, Austria, 1951. He received the Diploma in electronic engineering from HTL, Vienna, in 1977. From 1977 to 1984, he worked in the field of industrial electronics. Since 1984, he has been with the Institute of Sensor and Actuator Systems, Vienna University of Technology. The main topics of his work are instrumentation for miniaturized electrochemical sensors and biosensors, thin-film technology, microfluidics, and low-temperature wafer bonding.

**Bernhard Lendl** was born in Salzburg, Austria in 1968. He received the M.Sc. degree in 1993 and the Ph.D. in 1996 both from the Vienna University of Technology and both in analytical chemistry. Since 2001 he is Associated Professor for Analytical Chemistry at the Institute of Chemical Technologies and Analytics of the Vienna University of Technology. From September 2003 through August 2004 he was guest professor at the Institute of Analytical Chemistry at the University of Córdoba, Spain. His research interests include Infrared and Raman spectroscopy and their application in analytical chemistry. He is current member of the editorial boards of the journals *Applied Spectroscopy* and *Vibrational Spectroscopy* and author of more than 140 scientific papers. In 2008 he founded QuantaRed Technologies which develops chemical analyzers based on mid-IR Quantum Cascade Lasers.

**Martin Kraft** was born in Vienna, Austria, in 1972. He holds an M.Sc. in analytical chemistry (1997) and a Ph.D. in technical chemistry from the Vienna University of Technology, Austria. Following a research stay at the University of Cambridge, UK in 1996, in 1997 he joined the working group for Vibrational Spectroscopy (Prof. R. Kellner) at the Institute of Analytical Chemistry as a research assistant. After finishing his Ph.D. in 2001, he joined CTR Carinthian Tech Research, a non-university research company and COMET K1 Competence Centre for advanced sensor technologies in Villach, Austria. There, he serves in a dual role as Intellectual Property manager and Funding Applications coordinator and key researcher for spectroscopic sensors and optical systems. Since 2004, he also engages himself as industrial part-time lecturer for chemistry and for intellectual property rights at the Carinthian University of Applied Sciences. Current research interests include Spectral Imaging, MEMS-based spectroscopic analyzers and combined process simulation and validation approaches. He authored or co-authored more than 50 patents and publications in peer reviewed journals and international conferences.

**Michael J. Vellekoop** was born in Amsterdam, the Netherlands. He received the B.Sc. degree in physics in 1982 and the Ph.D. degree in electrical engineering in 1994. From 1982 to 1984 he was an officer in the Dutch Royal Navy and in 1984 he joined the Delft University of Technology as a research assistant. In 1988 he co-founded Xensor Integration B.V. where he was managing director until 1996. In that year he initiated a new research group at the DIMES Electronic Instrumentation Laboratory of the Delft University of Technology, where in 1997 he became an associated professor. Since 2001 he is a full professor of Industrial Sensor Systems at the Institute of Sensor and Actuator Systems of the Vienna University of Technology, Austria. In 2002 he became head of this institute. Prof. Vellekoop was elected as a corresponding and full member of the Austrian Academy of Sciences in 2005 and 2007, respectively. He received the Eurosensors Fellow Award in 2005 and the IEEE Sensors Council Meritorious Service Award in 2010. In 2004 he was the general chair of the IEEE Sensors Conference in Vienna and in 2010 the TPC chair of Eurosensors XXIV in Linz, Austria. Since 2005 he has been a Senior Editor of the *IEEE Sensors Journal*. He authored or co-authored 220 publications in peer reviewed Journals and International Conferences. Keywords of research are physical chemosensors, biochips, microfluidics & optofluidics, sensor systems, and technology.



## Publication III

C. Wagner, S. Armenta, and B. Lendl, *Talanta* 80, 3, 1081-1087 (2010), DOI: 10.1016/j.talanta.2009.08.018.





## Developing automated analytical methods for scientific environments using LabVIEW

Christoph Wagner, Sergio Armenta, Bernhard Lendl\*

*Institute of Chemical Technologies and Analytics, Vienna University of Technology, Getreidemarkt 9/164 AC, A-1060 Vienna, Austria*

### ARTICLE INFO

#### Article history:

Received 15 May 2009  
Received in revised form 4 August 2009  
Accepted 17 August 2009  
Available online 22 August 2009

#### Keywords:

Capillary electrophoresis  
Infrared spectroscopy  
Sequential injection analysis  
LabVIEW programming  
Automated analytical methods  
Enzyme inhibition

### ABSTRACT

The development of new analytical techniques often requires the building of specially designed devices, each requiring its own dedicated control software. Especially in the research and development phase, LabVIEW has proven to be one highly useful tool for developing this software. Yet, it is still common practice to develop individual solutions for different instruments. In contrast to this, we present here a single LabVIEW-based program that can be directly applied to various analytical tasks without having to change the program code. Driven by a set of simple script commands, it can control a whole range of instruments, from valves and pumps to full-scale spectrometers. Fluid sample (pre-)treatment and separation procedures can thus be flexibly coupled to a wide range of analytical detection methods. Here, the capabilities of the program have been demonstrated by using it for the control of both a sequential injection analysis – capillary electrophoresis (SIA-CE) system with UV detection, and an analytical setup for studying the inhibition of enzymatic reactions using a SIA system with FTIR detection.

© 2009 Elsevier B.V. All rights reserved.

### 1. Introduction

Current trends in analytical chemistry clearly aim at developing fully automated, integrated analytical solutions, comprising necessary sample (pre-)treatment, the actual analyte detection, and data processing. Hence, nowadays, practically all newly developed analytical methods involve computers for system control and/or data recording. Yet, in research and development the configurations of the experimental set-ups change frequently, making it necessary to adapt not only the analytical system itself, but also very often the software. In this context, the possibility of flexible control software for the automation of an experimental set-up and the corresponding data analysis would be of great practical value. Such a software platform would allow quick adaptation of experimental set-ups to new findings and ideas, thus focusing on the evaluation of new approaches and characterisation of their analytical performance, rather than re-writing software.

LabVIEW, by National Instruments, is widely used as a control software development tool in both academic and industrial R&D. This software allows programming of virtual instruments (VIs), combining electronics with computer resources to control instruments and collect sets of data [1–3]. In contrast to C++ or Visual Basic for example, LabVIEW is a graphical programming language

enabling the creation of high quality programs within short time periods. Typically, different (sub-)VIs, each fulfilling its own specific duties, are placed on a programming diagram and wired together. These virtual wires directly visualise the program and all data flows while writing the program, making it easier to interpret programs compiled by someone else and adjust them to specific needs. Furthermore, it also helps by keeping a sustainable knowledge base, allowing the handing over of software responsibility from one employee/student to another. Using controls and indicators from a large set of predefined elements, a user-friendly graphical user interface (GUI, called a panel) can easily be designed [4]. A final practical advantage of LabVIEW is that a parallelisation of code execution can easily be achieved, something that can be of great advantage, e.g. for decoupling data acquisition and data processing and evaluation.

A variety of previously published papers describe such LabVIEW-based programs aiming towards the automation of specific analytical systems fulfilling a particular task, including developing a new flow injection analysis (FIA) method by replacing the mixing coil with a continuously variable volume reactor [5], measuring picomolar concentrations of silver in seawater [6], monitoring particle/water interactions [7], determining morphine by a sequential injection analysis (SIA) system [8] or coupling such a system to a combined electro-generated chemiluminescence and amperometric detection [9]. Altogether, applications range from automating sample pre-treatment using a FIA system over auto-sampling devices to the possibility of combining versatile liquid handling with different kinds of detectors, like SIA with capillary

\* Corresponding author.

E-mail address: [blendl@mail.tuwien.ac.at](mailto:blendl@mail.tuwien.ac.at) (B. Lendl).

URL: <http://www.cta.tuwien.ac.at/cavs> (B. Lendl).

electrophoreses (CE) separation [10,11]. Irrespective of the actual analytical detection principle, a common denominator of these and many other analytical systems is the need to precisely handle fluids, very often different types of liquids. Still, each of these VIs is highly specialized and not very well suited to rapid adaptation for new systems and requirements.

This circumstance was the motivation behind the development described here. The goal was to develop a VI that allows the experimentalist to flexibly combine different laboratory equipment into new setups, without having to rewrite the control software. As outlined above, this requires combining fluid handling systems based, for example, on one of the various embodiments of flow injection, with different types of analytical detectors, and eventually some sort of analyte separation. A detailed analysis of these methods show that, while diverse and complex in overall operation, the active hardware core elements are essentially just a few pumps and valves. The resulting solution thus focused on designing a system that can flexibly control different such devices, irrespective of their specific combination or function in the analytical set-up. These functions are supplemented by a number of interfaces to optical detectors and auxiliary instruments, such as high-voltage supplies for CE separation.

The possibilities of the resulting control platform are demonstrated by successfully applying the identical control software to two widely different analytical devices, (i) a fully automated SIA-CE-UV system and (ii) label-free inhibition monitoring of an enzyme using a second SIA system coupled to an FTIR spectrometer. While the first analytical set-up includes capillary conditioning, sample preparation and analyte detection using a UV detector, the second example application requires rapid mixing of an enzyme solution with an inhibitor/substrate solution, transfer of the mixture into an IR measurement cell before the reaction of the enzyme with the substrate starts, and monitoring of minute spectral features changes over time.

## 2. Experimental

### 2.1. System components

In its present form, the program supports Vici's selection- and injection valves (Vici AG, Switzerland), Cavo's XP3000 and XL3000 syringe pumps and Smart Valves XL (Cavro Scientific Instruments, Sunnyvale, CA, USA), the kDS200 syringe pump (KD Scientific, Holliston, MA, USA) and Gilson's Miniplus peristaltic pump series (Gilson Inc., Middleton, WI, USA). For data acquisition, interfaces to both a UV detector (Dionex, Sunnyvale, CA, USA) and Bruker's FT-IR spectrometers (Bruker Optics GmbH, Ettlingen, Germany) have been implemented, together with a control device for a Spellman CZE 1000R high voltage power supply (Spellman, NY, USA).

The valves, the syringe pumps and the UV detector were interfaced to the PC running the LabVIEW VI using standard RS232 data connections, both for sending commands and receiving confirmation or error responses, which in turn allow the program to react to such events immediately. It is worth noting here that one RS232 interface can control up to nine different Vici valves.

The Gilson pump and the high voltage supply were connected via a cDAQ system from National Instruments using application specific protocols. For the Gilson pump this comprised two TTL signals, switching between the ON/OFF state and selecting the rotation direction, respectively, and a speed control in form of a continuously variable 0–5 V signal, corresponding to 0–100% of the maximum speed, as manually entered on the pump's control panel. The high voltage power supply was similarly controlled by a continuously variable 0–10 V input voltage signal, here corresponding to 0–30 kV output voltage.

**Table 1**  
Typical example commands for sequence programming.

Command	Effect
PPn	Pick up <i>n</i> steps with the Cavo pump and do not wait to finish
PDWn	Dispense <i>n</i> steps with the Cavo pump and stay further program execution until it finishes
GOm k	Switch the Vici valve with ID <i>n</i> to port <i>k</i> , choosing the fastest way (clockwise or counter-clockwise)
OSn k	Start an IR measurement, where <i>n</i> is the number of spectra to be recorded and <i>k</i> the time between two spectra acquisitions in seconds
UVn k	Start an UV measurement, where <i>n</i> is the sampling rate in microseconds and <i>k</i> the total measurement time in minutes
HVn k	Apply <i>n</i> Volts in <i>k</i> seconds, using the Spellman high voltage power supply
SM	Stop running UV or IR measurements as soon as the Cavo syringe pump stops moving
WAn	Wait for <i>n</i> milliseconds
LOOPn END LOOP	Repeat the sequence between LOOP and END LOOP for <i>n</i> times

The Bruker spectrometers were controlled over a network connection through interaction with an OPC (OLE for Process Control) server, which is part of the "Process" package of the OPUS software. Due to the complexity of an IR measurement and to limitations in the OPC software itself, in its present development state the LabVIEW program is only capable of starting background and sample data acquisition; all setup parameters, such as optical resolution, number of scans as well as data post processing, have to be defined in a process control script in OPUS. Another restriction to the IR measurements is the fact that the "Process" package does not support rapid scanning or step-scan measurements yet.

Altogether, a large number of different system components can be integrated and controlled by the VI developed here, allowing the realisation of practically any relevant liquid sample pre-treatment. Furthermore, the modular approach of LabVIEW allows easy incorporation of sub-VIs for almost any other hardware component that can be controlled by LabVIEW.

### 2.2. The program

Since the program has been designed to control a variety of different hardware modules at once, and to keep the graphical user interface (GUI) as simple as possible (Fig. 1), all the commands controlling the hardware are entered in a text box (refer to Table 1 for command code examples out of more than 40 available commands). Every command is written on a separate line. This list of commands is then taken by the program code and executed from top to bottom. This approach keeps the graphical user interface simple and each of the sequences can be stored as plain text files for archiving. While running a sequence, all upcoming commands are displayed in a second text box in order to see the actual execution state of the sequence. The hardware setup parameters, including COM ports, channel numbers for the analogue outputs or the host-name of the computer running OPUS, can be entered in a separate setup area. The outputs of the UV detector and/or the IR spectrometer are displayed in two different tabs to save room on the GUI. A third tab holds all the error displays.

The internal design of the program code consists mainly of five parallel loops. The first loop, the master loop, executes the sequence entered by the user. When a command to move the plunger of the Cavo syringe pump is executed, a second loop is triggered by the master-loop, sending a notifier message to monitor the plunger movement. This can be done in parallel to the script execution, enabling data acquisition in the meantime, or the sequence can wait for the pump to finish its movement, which can be useful e.g.

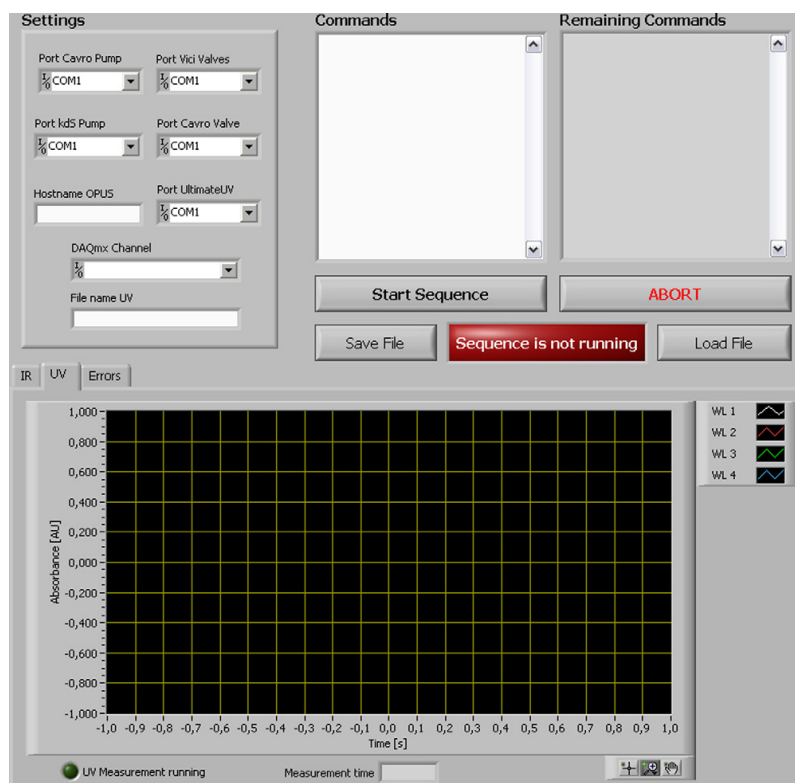


**Fig. 1.** Graphical user interface showing three different sections: in the upper row on the left is the communication port selector, on the right the interfaces for entering commands and surveying the sequence execution; in the lower row, a display with three tabs displays the data output of the UV and the IR detectors, and error messages, respectively.

during cleaning steps. The third loop polls an Abort button, so the user can terminate the script execution if an error occurs that is not recognized by the program itself. As soon as an error occurs or the Abort button is pressed, the program tries to shutdown any attached pump and the high voltage power supply. In addition, it switches to the error tab and displays a comprehensive error message. The two remaining loops handle IR and UV data acquisition. These two measurement loops are also triggered by the master-loop by a notifier message. The measurement loops will send back a notifier message to the main loop as soon as the measurement begins. This approach ensures that the entered sequence is kept in the event of any delay.

### 3. Results and discussion

#### 3.1. Application I: sequential injection analysis – capillary electrophoresis with UV detection

Sequential injection analysis (SIA) is a viable tool to automate sample pre-treatment steps like pre-concentration and/or purification, applying chemical reactions and diluting samples. Capillary electrophoresis (CE) is a highly effective separation technique separating molecules by their charge to size ratio. Coupling SIA with CE has been successfully demonstrated in literature combining the advantages of both techniques making it even easier to apply conditioning or cleaning steps to the separation capillary. However, the main problem associated with this coupling arises from the discon-

tinuous sample introduction mode of CE, where the system needs to be decoupled and coupled before and after the application of the separation voltage. This usually requires specially designed interfaces [11]. One of the first coupling systems by Arce et al. used a programmable arm to connect a FIA system to an at-line commercial CE analyzer [12]. Zacharis et al. used a special micro valve with a very low port-to-port volume and a CE capillary as a kind of injection loop [13] to couple the SIA system to the CE separation part. Wu et al. utilized a Lab-on-Valve approach for this purpose [14]. Both ways share the need for special equipment for the coupling process and the introduction of the electrodes needed to apply the separation voltage. Another approach by Kulka et al. used T-connection pieces connecting the capillary and the electrodes to the SIA system [10]. This manifold suffers from the fact that using capillaries with bigger inner diameters than 50  $\mu\text{m}$ , as used by Kulka et al., can be problematic as the valve used to close the system for cleaning purposes creates some backpressure, even in the opened position. This results in the sample already being injected into the capillary while pumping it through the T-piece.

In the presented work the capillary is connected directly to an inexpensive valve, making special valves unnecessary, and overcoming pressure problems with capillaries.

#### 3.1.1. Material and methods

**3.1.1.1. Instrumentation.** The manifold shown in Fig. 2 used a Cavo XP 3000 (Cavo Scientific Instruments, Sunnyvale, CA, USA) pump equipped with a 2500  $\mu\text{l}$  syringe, a Valco (Valco Instruments Co.

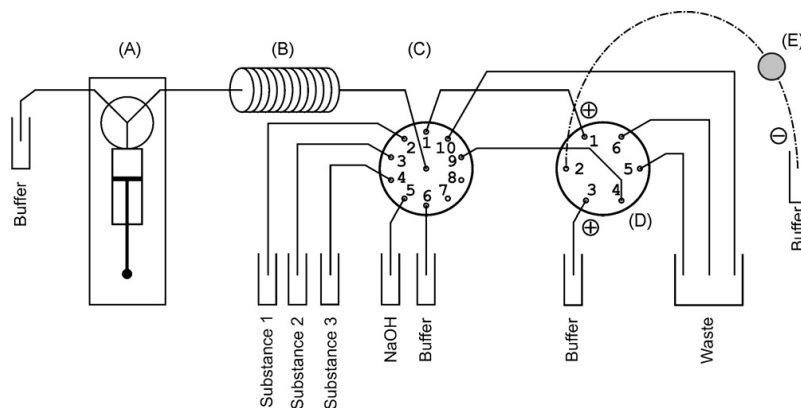


**Fig. 2.** Schematic view of the SIA-CE-UV manifold. (A) Cavity syringe pump; (B) 500 µl Teflon holding coil; (C) Vici selection valve; (D) Vici injection valve; (E) Capillary (100 µm ID) with UV detection window (not shown): Spellman high voltage power supply to apply 15 kV between the buffer reservoir and either Port 1 or Port 3.

Inc, Houston, TX, USA) six-port injection valve and a Valco ten-port selection valve. The HV system was a Spellman CZE 1000R (Spellman, New York, USA), capable of delivering up to 30 kV and 300 µA. Two metal tubings, each of the length of 2 cm, were connected to ports 1 and 3 of the injection valve and served as connections for the ground electrodes. The negative potential was applied by using a platinum wire (0.5 mm OD, ÖGÜSSA, Austria) placed inside a glass vial. The capillary (Polymicro Technologies LLC, Phoenix, AZ, USA) had an ID of 100 µm, an OD of 350 µm, a total length of 60 cm and was covered by a Teflon tubing (1.588 mm OD) on the end connected to the injection valve. UV detection was achieved with a fiber optic Ultimate UV-Vis detector (Dionex, Sunnyvale, CA, USA) at 50 cm capillary length.

**3.1.1.2. Procedure.** A new capillary was first initialized by flushing it with 0.10 M sodium hydroxide and BGE buffer solutions using an automated sequence. By placing the injection valve in position B (ports 1–2, 3–4 and 5–6 connected), the syringe pump pressurized the whole SIA-CE system, forcing the solutions to flow through the capillary. Before each separation run the capillary was flushed, applying the same procedure with BGE buffer only. As the electrophoresis process alters the running buffer pH by electrolysis and subsequently changes the electro-osmotic flow (EOF), the separation buffer was renewed before every run by pumping buffer through port 9 of the selection valve.

The separation background electrolyte consisted of 100 mM phosphate buffer at pH 6.8. The UV detector was set to 241, 270 and 294 nm, corresponding to the absorption maxima of the three analytes, the applied voltage used for electrophoretic separation was 15 kV and samples were introduced into the capillary in the electrokinetic injection mode. The samples were prepared on the fly by aspirating small volumes of pyridine-2-aldoxime methochloride, thiamine and 1,10-phenanthroline (3500 mg L<sup>-1</sup> each) in a sequential order, repeating the sequence 10 times, into the holding coil. By varying the aspirated volume of each of the substances, different sample concentrations could be produced. In the electrokinetic injection mode, the sample flowed from the selection valve to port 1 of the injection valve, which was in position A (ports 1–6, 2–3 and 4–5 connected). Then, the injection valve changed to position B following counter clockwise rotation and the high voltage power supply applied a constant potential of 15 kV for 10 s. Finally, the 2-way valve switched back to position A by clockwise rotation connecting the capillary with the buffer reservoir at position 3 of the valve and the electrophoretic separation was initiated by applying 15 kV.

### 3.1.2. Results

The analytical performance of the SIA-CE-UV automated system was evaluated by considering the linearity, linear range, limit of detection (LOD), limit of quantification (LOQ) and precision expressed as relative standard deviation (RSD).

An electropherogram obtained is shown in Fig. 3. The linear relationships deduced between absorbance and drug concentration are summarized in Table 2. The LOD and LOQ were calculated as 3 and 10 times, respectively, the standard deviation of the intercept of the calibration line divided by the slope of the curve. The intra-day precision of the method was evaluated using the results obtained for five independent runs of 500 mg L<sup>-1</sup> pyridine-2-aldoxime methochloride, 1000 mg L<sup>-1</sup> thiamine and 500 mg L<sup>-1</sup> 1,10-phenanthroline standards mixture and the results were expressed as RSD. The linearity was tested using a pure error lack of fit test with simple regression, which was not significant at the 5% level.

### 3.2. Application II: SIA-FTIR coupling for enzymatic reaction monitoring

To demonstrate the suitability of the developed LabVIEW program for the automated control of analytical instrumentation in process monitoring and analysis of evolving systems, an enzy-

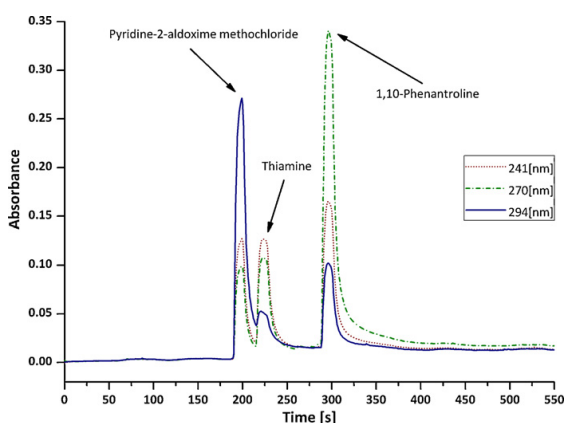


**Fig. 3.** Electrophoretic separation of pyridine-2-aldoxime methochloride, thiamine and 1,10-phenanthroline using a capillary with an internal diameter of 100 µm by applying 15 kV potential. See the text for further details.

**Table 2**

Analytical features of the SIA-CE-UV automated procedure for the determination of pyridine-2-aldoxime methochloride, thiamine and 1,10-phenantroline.

	Pyridine-2-aldoxime methochloride	Thiamine	1,10-Phenantroline
Wavelength (nm)	294	241	270
Migration time (s)	201	227	303
Regression equation			
Slope	0.00628 ± 0.00016	0.00261 ± 0.00005	0.0175 ± 0.0006
Intercept	−0.12 ± 0.11	−0.10 ± 0.08	−0.4 ± 0.4
Linearity ( $R^2$ )	0.997	0.998	0.996
Linear range ( $\text{mg L}^{-1}$ )	52–1273	90–2722	66–1273
LOD ( $\text{mg L}^{-1}$ ) <sup>a</sup>	52	90	66
LOQ ( $\text{mg L}^{-1}$ )	174	299	220
RSD area (%) <sup>b</sup>	5.0	5.1	4.2
RSD migration time (%)	3.4	3.3	4.5

<sup>a</sup> LOD and LOQ established as 3 and 10 times, respectively, the standard deviation of the intercept of the calibration curve divided by the slope of the calibration line.<sup>b</sup> Relative standard deviation value of five independent runs of 500  $\text{mg L}^{-1}$  pyridine-2-aldoxime methochloride, 1000  $\text{mg L}^{-1}$  thiamine and 500  $\text{mg L}^{-1}$  1,10-phenantroline standards mixture.

matic reaction, the dephosphorylation of fructose 1,6-bisphosphate (F16BP) to fructose 6-phosphate (F6P) and inorganic phosphate in the presence of divalent cations, such as  $\text{Mg}^{2+}$ , and its inhibition by adenosine 5'-monophosphate (AMP) was selected as a case study. In this way, the use of infrared spectroscopy allows the direct monitoring of enzymatic activity because of the specific absorption bands in the middle infrared spectral range providing molecular specific information on the substrate and reaction products.

The most critical step of reaction process monitoring, especially of enzymatic systems, is the accurate control of the process starting point. It is absolutely necessary to use of a fully automated system to define the starting point of the reaction, thus avoiding human error and thereby increasing the quality of the obtained analytical data. This problem has been overcome by using a SIA system coupled to a FTIR spectrometer both controlled by the developed LabVIEW program.

### 3.2.1. Material and methods

**3.2.1.1. Instrumentation.** Enzymatic experiments were carried out on an Equinox 55 FTIR spectrometer (Bruker Optics GmbH, Karlsruhe, Germany) equipped with a narrow band mercury cadmium telluride (MCT) detector. Spectra were recorded by co-adding 128 scans at a resolution of  $4 \text{ cm}^{-1}$  and a scanner velocity of 100 kHz HeNe frequency.

The IR cell consisted of a temperature-controlled aluminium flow cell [15] with  $\text{CaF}_2$  windows (thickness 2 mm) separated by a polyethylene spacer of 25  $\mu\text{m}$ , thus establishing a constant IR path length.

The SI manifold (Fig. 4) was set up with a Cavo XP 3000 syringe pump (Cavo Scientific Instruments, Sunnyvale, CA, USA; syringe size 5000  $\mu\text{L}$ ) and a Valco (Valco Instruments Co. Inc, Houston, TX, USA) 10 port selection valve. A 1.5 mL safe-lock Eppendorf tube placed in a TTS2 minishaker (IKA Works Inc., Wilmington, NC, USA) was used as a mixing chamber to ensure a complete and homogeneous mixing prior to measurement.

**3.2.1.2. Procedure.** Different and accurately measured volumes of F16BP, AMP and working buffer were aspirated sequentially into the holding coil, and delivered into the mixing chamber obtaining a final volume of 250  $\mu\text{L}$ . After that, FBPase solution was added and homogenized by shaking. The mixture was injected into the carrier stream and the flow was stopped at a fixed time, with the bulk of sample in the flow cell. FTIR spectra were recorded for 15 min at equal time intervals of 30 s to monitor the course of the reaction taking place using the spectrum of the cell filled with working buffer as background.

Using FTIR difference spectroscopy enabled the monitoring of the progress of the enzyme catalyzed reaction even though enor-

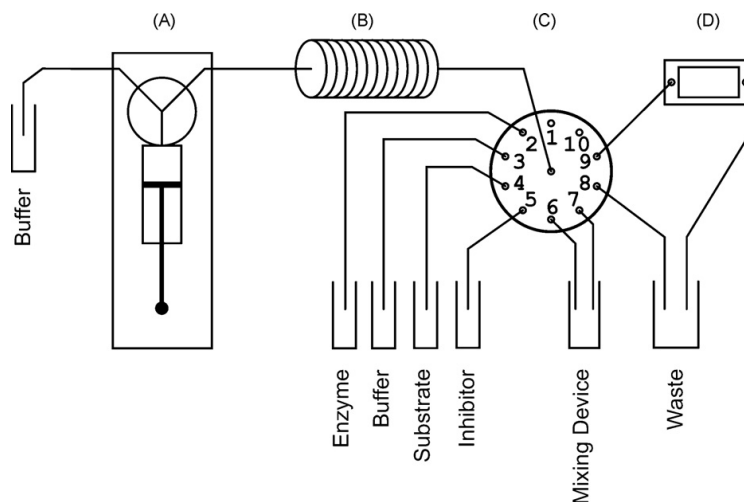


**Fig. 4.** Schematic view of the SIA-IR manifold for measuring enzymatic reactions. (A) Cavo syringe pump; (B) Teflon holding coil (500  $\mu\text{L}$ ); (C) Vici selection valve; (D) IR flow cell 25  $\mu\text{m}$  path length.



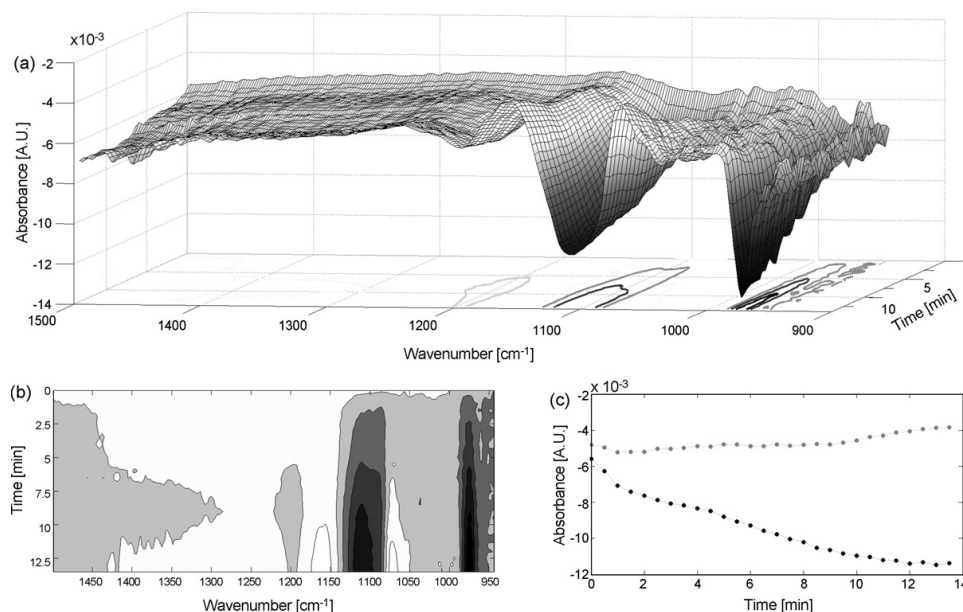


**Fig. 5.** FTIR difference spectra of the dephosphorylation of F16BP to F6P and phosphate in the presence of FB Pase (a) three dimensional view, (b) projection on the space defined by the time and wavenumbers and (c) absorbance values of the selected wavenumbers (1109 and 1156  $\text{cm}^{-1}$ ) in the difference spectrum used for data evaluation.

mous similarities between the products and the substrate infrared spectra exist. Difference spectra, containing the spectral fingerprint of the reaction under investigation, were obtained by subtracting the first spectrum from the whole dataset, as it can be seen in Fig. 5. The absorbance difference between two selected wavenumbers (1109 and 1156  $\text{cm}^{-1}$ ), a maximum and a minimum, in the difference spectrum were used for data evaluation. The concentration of hydrolyzed F16BP was obtained by interpolation of those difference values in a calibration curve obtained from synthetic mixtures of substrate and products with the same data treatment.

### 3.2.2. Results

FTIR spectroscopy has been demonstrated to be an appropriate technique for the rapid investigation of enzymatic reactions [16,17] as the recording of a spectrum takes only a few seconds and is able to monitor the reaction of interest directly, in real-time. The starting point of the reaction can be accurately controlled and reproduced by using the automated SIA system for sample preparation and introduction into the FTIR cell. Thus, from the mixing of the enzyme with the substrate and buffer into the mixing chamber to the recording of the first spectrum only a few seconds (15 s approximately) passed, obtaining a highly reproducible starting point.

The Michaelis–Menten constant ( $K_M$ ) can be determined in conditions of zero order kinetics with respect to the substrate. The  $K_M$  value was calculated from the Lineweaver–Burk graph, plotting the reciprocal of initial velocity against the reciprocal of substrate concentration.  $K_M$  was found to be 14.1  $\text{g L}^{-1}$ .

Moreover, the inhibitor activity of AMP on the enzymatic dephosphorylation of F16BP at different inhibitor concentrations was evaluated. Kinetic studies demonstrate the capability of the methodology for label free monitoring of enzyme inhibition. The presence of increasing concentrations of the inhibitor AMP (0, 7.5 and 15  $\mu\text{M}$ ) reduces the maximum rate of the reaction without changing the apparent binding affinity of the catalyst for the substrate (Michaelis–Menten constant  $K_M^{\text{APP}}$ ). The obtained  $K_M^{\text{APP}}$

values were determined to be 12.5 and 12.2  $\text{g L}^{-1}$ , for 7.5 and 15  $\mu\text{M}$  AMP, respectively. The results obtained were published in detail separately [18].

## 4. Conclusion and outlook

The developed LabVIEW program has been shown to be suitable for controlling various different liquid handling systems and coupling them to different analytical measurement techniques. The next steps will focus on expanding the program to work with other hardware, such as quantum cascade lasers or oscilloscopes. In essence, any hardware with LabVIEW drivers, or defined control interfaces reacting to specific input signals, could be incorporated into the program. Setting up an archive of relevant sub-VIs representing different hardware functionalities is another future step of this development. These VIs can be directly placed and wired in the program's case structure, executing corresponding hardware functionalities triggered by a command in a scripted sequence. This makes it easy even for inexperienced programmers to add new functionalities to the LabVIEW program.

If you are interested in using this program please do not hesitate to contact the authors by email.

## Acknowledgement

C. Wagner gratefully acknowledges the financial support by Carinthian Tech Research AG and the COMET Competence Centre Programme of the Austrian Government.

S. Armenta acknowledges the financial support provided by the Ministerio de Educación y Ciencia (Ref. EX2007-1257).

## References

- [1] R.A. Aspey, I.S. McDermid, T. Leblanc, J.W. Howe, T.D. Walsh, Rev. Sci. Instrum. 79 (2008) 094502.
- [2] J. Fernandez de Canete, P. Del Saz Orozco, S. Gonzalez-Perez, Int. J. Comput. Inf. Syst. Sci. Eng. 4 (2007) 222–225.



- [3] Z. Stevic, Z. Andjelkovic, D. Antic, *Sensors* 8 (2008) 1819–1831.
- [4] A. Krauss, U. Weimar, W. Gopel, *Trends Analyt. Chem.* 18 (1999) 312–318.
- [5] L.L. Lipe, S.M. Purinton, E. Mederios, C.C. Harrell, C. Efta, M. Murray, M. Wood, R.B. Portier, S.J. Chalk, *Anal. Chim. Acta* 455 (2002) 287–304.
- [6] J.L. Barriada, J.B. Truscott, E.P. Achterberg, *J. Autom. Methods Manag. Chem.* 25 (2003) 93–100.
- [7] M.J.M. Séguret, S.J. Ussher, P.J. Worsfold, M. Nimmo, J.W. Wood, *Instrum. Sci. Technol.* 36 (2008) 18–31.
- [8] C.E. Lenehan, N.W. Barnett, S.W. Lewis, *J. Autom. Methods Manag. Chem.* 24 (2002) 99–103.
- [9] A. Economou, M. Nika, *J. Autom. Methods Manag. Chem.* (2006) 1–9.
- [10] S. Kulka, G. Quintás, B. Lendl, *Analyst* 131 (2006) 739–744.
- [11] G.A. Theodoridis, C.K. Zacharis, A.N. Voulgaropoulos, *J. Biochem. Biophys. Methods* 70 (2007) 243–252.
- [12] L. Arce, A. Rios, M. Valcárcel, *Fresenius, J. Anal. Chem.* 360 (1998) 697–701.
- [13] C.K. Zacharis, F.W.A. Tempels, G.A. Theodoridis, A.N. Voulgaropoulos, W.J.M. Underberg, G.W. Somsen, G.J. de Jong, *J. Chromatogr. A* 1132 (2006) 297–303.
- [14] C. Wu, L. Scampavia, J. Ruzicka, *Analyst* 128 (2003) 1123–1130.
- [15] S. Armenta, W. Tomischko, B. Lendl, *Appl. Spectrosc.* 62 (2008) 1322–1325.
- [16] M. Haberkorn, P. Hinsmann, B. Lendl, *Analyst* 127 (2002) 109–113.
- [17] R. Pacheco, M.L.M. Serralheiro, A. Karmali, P.I. Haris, *Anal. Biochem.* 322 (2003) 208–214.
- [18] M. López-Sánchez, M. Ayora-Cañada, A. Molina-Díaz, M. Siam, W. Huber, G. Quintás, S. Armenta, B. Lendl, *Anal. Bioanal. Chem.* 394 (2009) 2137–2144.



## Publication IV

C. Wagner, A. Genner, G. Ramer, and B. Lendl, Chapter in LabVIEW - Modeling, Programming and Simulations, E.B. de Asmundis, Ed. (INTECH, Rijeka, 2011), 3-20, ISBN 978-953-307-521-1, DOI: 10.5772/14110.



# Advanced Total Lab Automation System (ATLAS)

Christoph Wagner, Andreas Genner, Georg Ramer and Bernhard Lendl  
*Vienna University of Technology  
Austria*

## 1. Introduction

In modern analytical chemistry not only do new measurement principles have to be investigated but newly found techniques also need to be developed into integrated and more and more automated analytical solutions. Exploring new techniques in research and development (R&D) environments mostly means designing different setups incorporating a huge variety of different equipment. Whether this hardware is a pump, a valve or more complex elements such as oscilloscopes, lasers or detectors, in one way or another they can be controlled by a computer or the acquired data is digitized and evaluated afterwards. Those setups, however, change frequently in R&D labs to evaluate new ideas or to improve a current setup. Inevitably whenever the setup changes, the software controlling it will also need adaptation. An ideal software platform, therefore, would reduce the time needed for making those changes to a minimum, giving the researcher the possibility to focus on the evaluation of new approaches and the characterization of new techniques. Especially for small startup companies it might also be of great interest that the needed software packages can be maintained and adopted by the scientist himself instead of the need to outsource it to a software company. This would not only reduce the cycle time from a new idea to the first prototype but also has the potential to decrease the associated costs.

One programming language ideally suited for such a software environment is LabVIEW from National Instruments. Due to its graphical programming language all data flow is visualized directly in the source code. This fact makes it easier to read and understand a given program, especially for beginners without programming experience in classical programming languages, such as C++ or Visual Basic. Another point where LabVIEW outperforms other programming languages is its rich library of Graphical User Interface (GUI) elements, for example XY graphs are predefined as well as 3D graphs. Another advantage of LabVIEW is the very simple way to create parallel running tasks. In combination with LabVIEW's queues, which represent a "first in - first out" buffer system, separating the readout of data and its evaluation can be separated easily. Using National Instruments hardware for the data readout brings easy integration for the software developer. Secondly interfaces for RS-232, GPIB, USB etc. are also provided for communicating with third party hardware.

All these advantages make LabVIEW a good choice for developing software in R&D laboratories. Generally speaking, laboratories focus on the development of software for their

current experimental setup ending up with a LabVIEW program built for this specialized task. Dominguez et al. designed a LabVIEW program to control a Sequential Injection Analysis (SIA) system (Dominguez et al., 2010) which consisted of a valve and a peristaltic pump. Jitmanee et al. used a more complex liquid handling system consisting of three valves and three pumps to automatically prepare samples for Inductive Coupled Plasma Mass Spectrometry (ICP-MS) measurements (Jitmanee et al., 2007). Barzin et al. proposed a spectrophotometric method for pH measurements in miniaturized systems where LabVIEW handles data acquisition from a flowmeter and a spectrometer and is linked to a Matlab feedback loop to calculate the appropriate flow rate which is sent to a syringe pump afterwards via LabVIEW (Barzin et al., 2010). In all these examples the program is limited to control the hardware it was designed for. In the first two examples automation tasks are carried out whereas in the latter one a complex control feedback loop is realized. When we started working with LabVIEW we wanted to create a software platform, which gives the operator the freedom to combine different hardware elements in any imaginable way without the need to make changes to the program code. Only adding new hardware to the software platform should require software changes, which would be easier using LabVIEW than any other programming language.

First we created a program that allowed the combination of valves, pumps and an high voltage supply for the sample preparation with an UV detector and infrared spectrometers from Bruker Optics to build different setups including SIA (Růzicka, 1992) and flow injection analysis (FIA) (Růzicka, 1981) systems as well as capillary electrophoreses systems (Wagner et al., 2010). To address all necessary components in a simple way we decided to use a scripting language containing commands representing tasks including switching a valve, applying voltages or starting measurements. The script was written manually and afterwards started sending commands to the connected hardware consecutively. This system allowed the easy combination of the integrated hardware into different analytical systems. However, after adding support for additional hardware and the need for more complex commands the GUI became too crowded with elements and writing the scripts became more and more difficult due to the number of available commands.

Our first program allowed the scientist to combine all integrated components with ease but adding new hardware components to the program became more and more sophisticated due to the growing source code. Therefore, we decided to create a new platform based on a client server approach, where every hardware component is controlled by a dedicated client which can be controlled remotely by a server application. A schematic of this software platform can be seen in figure 1. Each of the clients can be run in three different modes. The *local mode* directly interacts with the connected hardware upon user input, the *programming mode* sends commands to the server application and in the *server mode* the clients receive commands from the server and execute them on their hardware. In that manner adding new hardware is done by adding client specific program code to a provided client template, containing all necessary code to handle the communication with the server. Additionally the user doesn't need to remember client specific commands because the programming of a sequence can be done with the GUI of each client.

In the following we will describe our *Advanced Total Laboratory Automation System* (ATLAS), including a list of existing clients as well as two examples of experimental setups controlled by ATLAS.

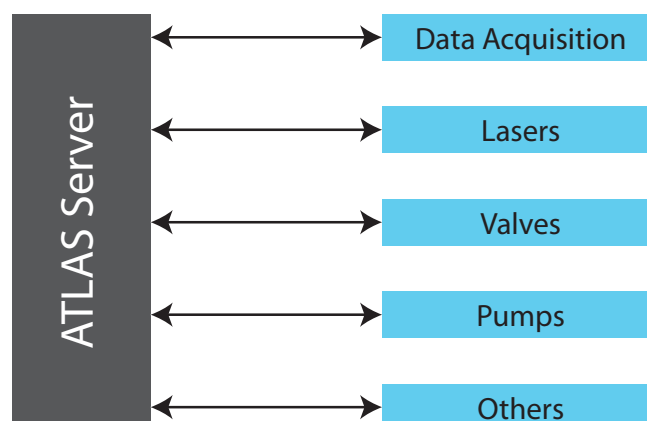


Fig. 1. Schematic of our *Advanced Total Laboratory Automation System* (ATLAS). Each hardware component is controlled by a dedicated client program which can communicate with the ATLAS server to be remote controlled.

## 2. The ATLAS platform

The ATLAS platform consists of one *server* application and numerous *client* applications. Each client controls connected hardware such as a pump, valves or a spectrometer. The *server* is used to remote control connected *clients* by sending script commands over a TCP/IP connection to the *clients*. Each *client* can be used in a *local* mode, as well, to control connected hardware directly. The *server* application was designed so that adding new *clients* can be done without modifying the *server* application.

### 2.1 Client server communication

#### 2.1.1 Simple TCP/IP Messaging (STM)

The ATLAS software is based on the *Simple Messaging Reference Library* (STM)<sup>1</sup> maintained by National Instruments, which contains a set of VIs for developing server/client-based applications. Beside the *TCP Connection Manager VI*, which handles connection informations, the library contains also VIs for transporting data over TCP/IP connections.

First of all, a server, handling several clients, requires a *New Connection Monitor*<sup>2</sup>, which creates a listener on a certain port (e.g. 8080) and waits until a client tries to establish a TCP network connection. In the next step the server defines meta data, which basically define data channels for data transportation. All information concerning a certain client connection is stored using the *TCP Connection Manager VI*, which represents a Functional Global Variable (FGV). All further communication between the server and the connected clients is handled in a separate loop, called the server loop, by accessing this FGV.

The *TCP Connection Manager VI* offers also the functionality for listing all established connections. The resulting output is an array of connection-IDs which has to be indexed for sending or receiving data to a specific client. If the communication to a client breaks down due to hardware- (e.g. network cable is unplugged), or software problems (e.g. client program crashes) it is necessary to remove the connection information of this client from the

<sup>1</sup> <http://zone.ni.com/devzone/cda/tut/p/id/4095>

<sup>2</sup> <http://zone.ni.com/devzone/cda/tut/p/id/3055>

FGV. Otherwise the server may try to send data to an unreachable client which would lead to a timeout. All data between the server and the clients is transported by using the *STM Write Message* and *STM Read Message VIs*. Beside the string that has to be sent, a cluster, containing timeout settings, can be attached to the *STM Write Message VI*. At first, the meta data index, containing the data channel names is obtained, flattened to a string and concatenated with the data to send. In the next step the byte length of this data string is calculated and attached to the beginning of the string. Finally, the complete string is written to the TCP connection. The receiving program utilizes the *STM Read Message VI* to read the first four bytes of the transported string. These four bytes are converted to an integer representing the length of the remaining data string. In a second step this value is taken to read the residual data. Finally, the transported string can be accessed for further processing.

### 2.1.2 Communication principle

The communication between the server and the connected clients is controlled by the server only. This means that the server sends commands to the clients, which reply to the server afterwards (for a typical communication sequence see figure 2). Every 50 ms the server queries the status of the connected clients by sending the command *status*. Receiving the status request for the first time after establishing the connection to the server a client replies with *cmd:ID* identifying itself with its *client identifier*, where ID consists of two device depending alphanumerical characters. Upon the reception of a *cmd:ID* string the server stores the new client and the according STM connection ID. This data is accessed by the server to send client specific commands only to the according client in any further communication.

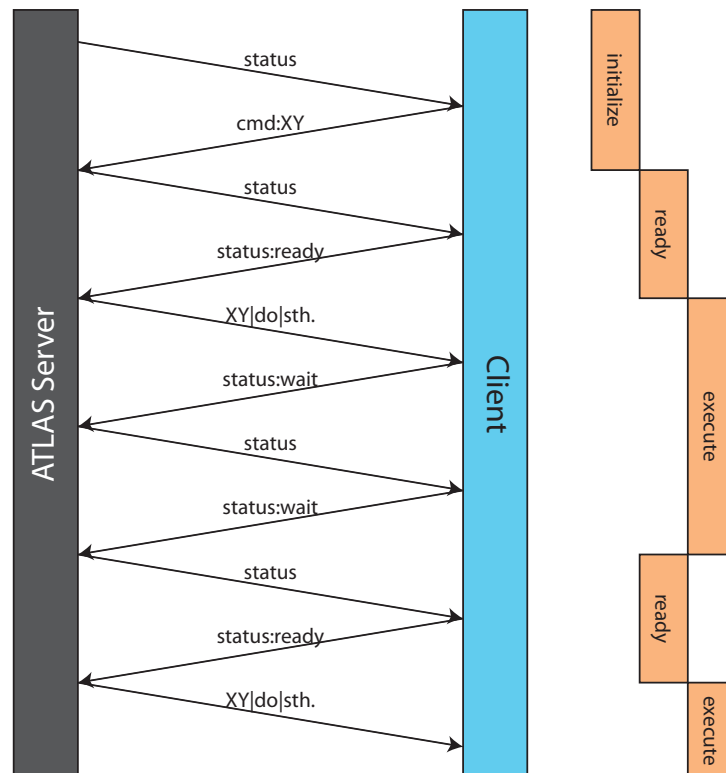


Fig. 2. Simplified communication scheme between the ATLAS server and one client.



Receiving further status queries from the server clients respond with either *status:ready*, *status:wait* or *status:error*. *status:ready* means that the client is ready to accept instructions from the server and that both, software and hardware, are working correctly. *status:wait* will be sent if the client is executing a command, such as measuring a voltage or recording a spectrum. In the case that a hardware failure occurred or an invalid command was sent to the client, it will respond with *status:error*.

After the user starts the execution of the sequence by clicking the corresponding button, the server checks whether all required clients are connected. If so, it will run the command interpreter, described in section 2.2.2. Afterwards the server begins distributing commands to the correct clients. After a command was sent the server goes on with polling the status of the connected clients. The addressed client starts executing the received command and answers *status:wait* to the server. The server will continue the execution of the script as soon as its status requests are answered with *status:ready* instead of *status:wait*.

In case a device failure occurs (e.g.: a tubing is plugged, a device becomes disconnected) or an invalid command was sent, the client controlling the according device will answer the status request from the server with *status:error*. As a result the server terminates the running sequence and executes the alias-command *AL|error*. As explained later in section 2.2.2 the server notifies all connected clients of the error event. The clients will execute a special protocol that contains commands for such an error case. Usually it is sufficient to abort the experiment, but some devices have to be shut down in a special way to avoid further problems.

## 2.2 Server application

### 2.2.1 Description

The central part of ATLAS server is a timed loop structure, further referred to as *server loop*, and can be seen in the middle of the plotted code in figure 3. As already mentioned in section 2.1.1 the *TCP Connection Manager VI* is used to list all connections established to clients. The resulting array of connection IDs of connected clients is treated in a for-loop structure. In this for-loop the server requests status information from the currently addressed client. It can respond with one of the following strings which is evaluated by the server in a case structure:

- *cmd:ID*: The client-ID is added to the list of *available client commands*.
- *programming*: The received string is added to the *commands\_list*.
- *status:ready*: In that case the corresponding LED in the *available client commands*-list turns green.
- *status:wait*: A variable is set to prevent sending the next command. In addition, the LED next to the client-ID turns red, indicating that the client is currently executing a task.
- *status:error*: The command queue is flushed and therefore the command *AL|error* is interpreted. As the software should also display an error message, the client-ID is inserted into a queue. Outside of the communication loop is a while loop which is only used for displaying error messages. This makes it possible, to go on with sending the error information immediately to all clients instead of waiting for an user interaction.

If a time-out occurs while the server awaits the answer from the client because the connection was interrupted, the *TCP Check Connection VI* removes the connection from the *Connection Manager VI* and the client-ID is removed from the list of *available clients*. This client list is displayed on the GUI to visualize the status of the connected clients. Finally, the received string from the client is logged together with a timestamp for debugging purposes.



This procedure is repeated in the for-loop for each client and after each client responds *status:ready* the server takes the next available command from the script. The corresponding client is identified by its client ID and the command is sent over the corresponding TCP connection. In addition the timestamp and the sent string are logged and the progress of the script execution is visualized.

User input such as loading, saving, starting and canceling of sequences, as well as saving the server-send-log, is treated by an additional event handler structure. Whenever a script is executed the server automatically saves the script sequence to be able to connect recorded measurement data unambiguously with the used sequence.

### 2.2.2 Additional server features

Before the ATLAS server starts distributing the commands to the corresponding clients, the sequence has to pass an interpreter. It enables three useful features which are a for-loop, a mathematical formula solver and the use of aliases. Moreover, the software supports the usage of comments, which have to start with a hash key. These features can be used to program complex script sequences and are summarized in table 1.

feature	code	result
comment	#this is a comment	
loop	loop(\$i=5 9 1) WA \$i sec loop_end	WA 5 sec WA 6 sec WA 7 sec WA 8 sec WA 9 sec
mathematics	loop(\$i=0 2 1) WA (5^\$i+2^2-exp(0.5)+sin(1.5)) loop_end	WA 4.349 sec WA 8.349 sec WA 28.349 sec
alias	AL name sample_001	AA name sample_001 AB name sample_001 AC name sample_001 AD name sample_001

Table 1. Examples for the script-interpreter features. It is able to handle loops, formulas and aliases.

#### 2.2.2.1 Loop constructions in the script sequence

Often a part of a sequence has to be executed many times. For example, a scientist wants to measure a large number of liquid samples by using valves and pumps. One way to solve this problem is to enter every line of the sequence manually, which means that every change of the valve-position and every operation of the pump has to be written down in the sequence. As this way is inefficient and hard to adopt to further experiments, the ATLAS server implements a function that is similar to a for-loop in conventional programming. In C++, for example, a for-loop begins with `for(int i=5; i<13; i++){` and ends with `}` whereas the repeated code is located between the braces. Scientists, who want to use such a function in their ATLAS sequence, have to write the repeated section between the lines `loop($i=5|13|1)` and `loop_end`. The opening bracket is followed by `$`, a variable name, `=` and the starting point for the variable. The next number is the last variable value and the third number represents the increment. Nested loops are also allowed whereas different variable names have to be used.

### 2.2.2.2 Solving mathematic formulas

It is important to mention that the loop-feature only allows for a constant increment. To overcome this limitation the ATLAS server can solve formulas based on *NI\_Gmath.lvlib:Eval Formula String.vi*<sup>3</sup>. The mathematical expressions are defined by writing them between brackets and the result will have a precision of 3 digits after the decimal separator. As the loop-function is interpreted before any formula is solved, it is also possible to use loop-variables in these mathematical expressions.

### 2.2.2.3 Aliases

Another feature in the ATLAS scripting language are aliases. These are abbreviations for longer program sequences which are used frequently. For example, a cleaning procedure in a liquid handling system, consisting of many single instructions, can be saved in the file <ATLAS directory>\Server\alias\cleaning.txt. After that the cleaning procedure is inserted in the script sequence by using the command `AL|cleaning.txt`, which shortens the script sequence and makes it easier to comprehend the whole sequence.

Aside from custom built aliases, the ATLAS server can access the aliases `AL|name|measurement_name` and `AL|error`. Their special characteristics are that the server replaces the alias-indicator `AL` by all available client-identifiers. Using `AL|name|measurement_name` will distribute a measurement filename to all connected clients which will save their measurement data by this name. `AL|error` is used to distribute the information, that an error has occurred, to all connected clients immediately.

## 2.3 Client applications

Each client can be operated in 3 different modes: The *server* mode, the *programming* mode and the *local* mode. If a client is switched to the *server* mode, it tries to connect to the ATLAS server over TCP/IP and after the connection has been established the device can be remote controlled by the server. The *programming* mode offers a comfortable way to create a script sequence on the server since every user event will be sent to the ATLAS server as the according script command instead of executing it. In *local* mode the connected device is controlled directly and user input is executed immediately.

The code structure is based on a state-machine<sup>4</sup> and a simplified scheme of the state-machine used is shown in figure 4. It consists of three states called *init*, *state changed* and *running*. The *init* state is used for initializing the user interface, setting constants, configuring a RS-232 connection etc. The *state changed* state is called if the user changes the client mode. Depending on the selected mode the network connection to the ATLAS server is established. If the connection initialization fails, the client automatically switches back to the *local* mode. All other functionality of the client is located in the *running* case of the state-machine.

The *running* state contains code elements for communicating with the ATLAS server, handling user inputs and controlling the connected device. An overview of the code can be found in figure 5. To simplify the block diagram all client specific hardware functionalities have been removed. The code inside the *running* state is based on a *producer consumer architecture*<sup>5</sup> consisting of three loops in our case. The first loop contains an event handler for user interactions whereas a second loop receives script commands from the ATLAS server

<sup>3</sup> [http://zone.ni.com/reference/en-XX/help/371361G-01/gmath/advanced\\_formula\\_vis/](http://zone.ni.com/reference/en-XX/help/371361G-01/gmath/advanced_formula_vis/)

<sup>4</sup> <http://zone.ni.com/devzone/cda/tut/p/id/2926>

<sup>5</sup> <http://zone.ni.com/devzone/cda/tut/p/id/3023>

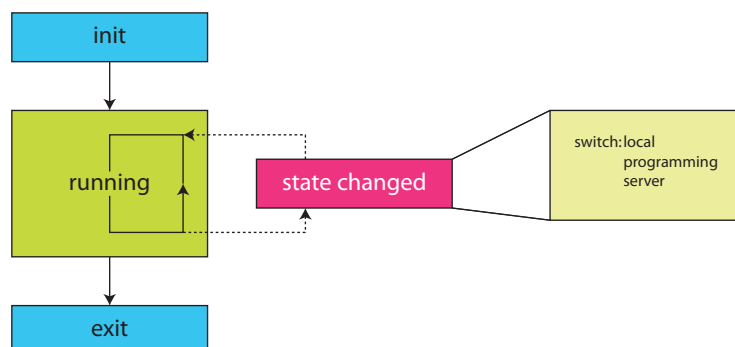


Fig. 4. Scheme of the client's architecture, which consists of a state-machine. It enables the software to switch between the different operating modes "client", "server" and local".

in *server* mode and passes them on to the third loop functioning as the consumer loop. In *programming* mode, however, the second loop is used to send script commands to the ATLAS server upon user interaction. The consumer loop interprets the script commands and translates them into hardware interactions. The exchange of commands between these three loops is realized by a queue (referred to as command queue) code structure. A second queue (referred to as status queue), which can also be seen in figure 5 is used to transport the status of the client from the consumer loop to the server loop and on to the ATLAS server if the client is in *server* mode. The differences in program execution for the three different states are explained in further detail below.

- **local** mode: The communication between the server and the client is deactivated. User interaction on the front panel triggers the event handler which assembles a script command, representing the user input from the GUI, and adds this script command to the command queue triggering the consumer loop execution.
- **programming** mode: The server loop is used to send script commands received via the command queue to the ATLAS server after receiving a status request from the server. The consumer loop, however, does not pass on any command to the connected hardware.
- **server** mode: The server loop is used to receive script commands from the ATLAS server and adds them to the command queue. The event handler structure, however, can still add commands to the command queue on user input to enable the user to interrupt automated script execution. The server loop is also used to reply to status requests from the ATLAS server according to the current state of the client, which is transported over the status queue as described above.

### 2.3.1 Available clients

At the moment 16 different clients are available and listed below. The list contains the client identifiers and a short description of the client functionality.

AC: Self-developed 230V AC power socket.

The AC client can switch a power socket and is connected to the PC via a RS-232-port.

BC: Self-developed Boxcar-Integrator.

This client reads the data, whereas the gating- and trigger-delay have to be set manually at the device.

BP: Beep client.

If the ATLAS server has to alert the user, the BP client can be used. It produces an audible tone with a certain frequency for 100 ms and is already included in the ATLAS server.

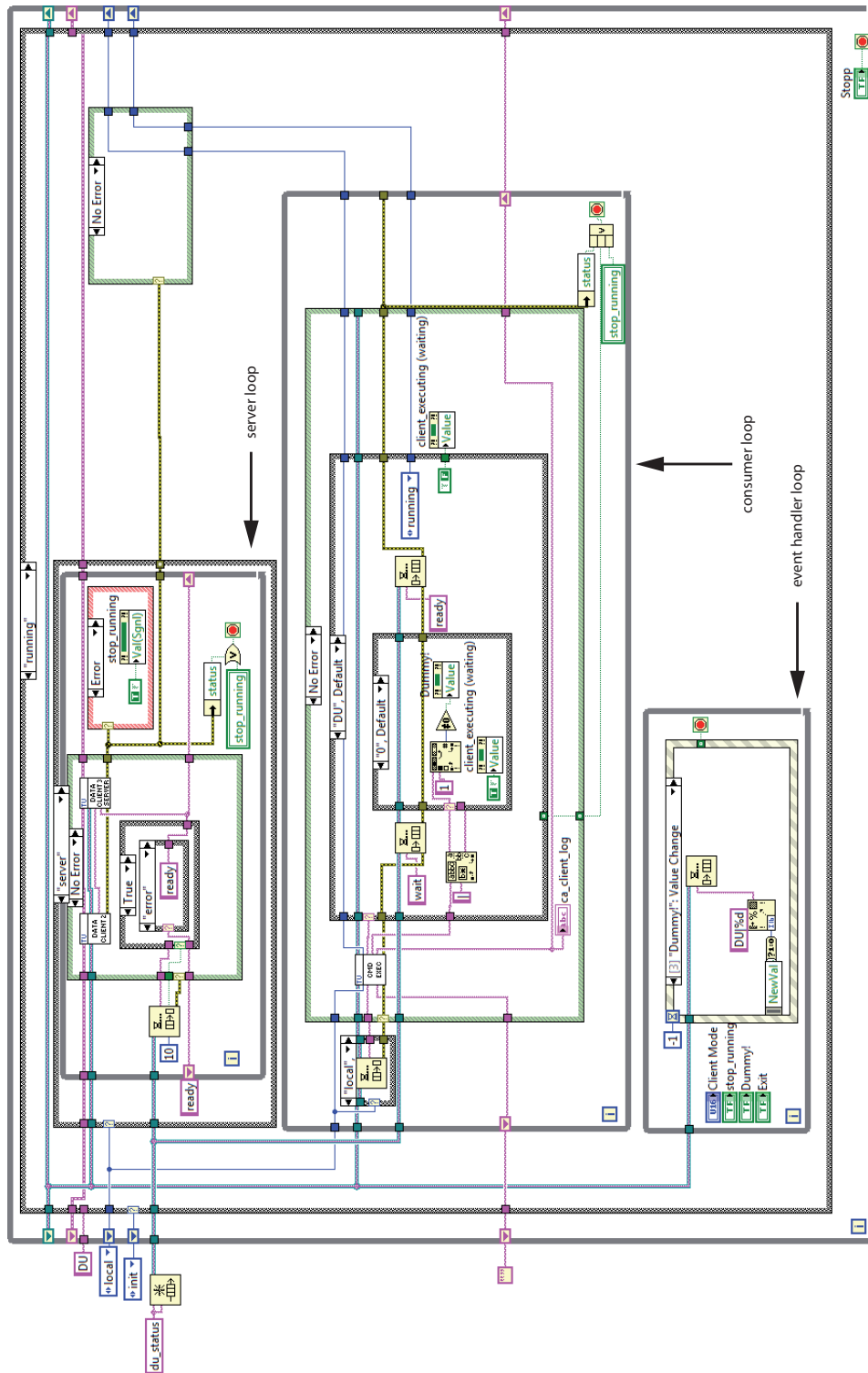


Fig. 5. Block diagram of a simplified ATLAS client, showing the *running* state. See the text for further information.

- CA: Syringe pumps by Cavo Scientific Instruments (Sunnyvale, CA, USA).  
Liquids can be aspirated and dispensed from two liquid connections at different speeds. The ramping up and down to the programmed speed can also be programmed.
- DB: A digital board from TVE Elektronische Systeme GmbH (Vienna, Austria).  
This board is a combination of a 16-bit-AD converter for a thermoelectrical cooled infrared detector. The integrated CPU supports features such as trigger delay, internal averaging and base line correction and is connected to the PC via USB.
- DI: Micro dispenser from Picology AB (Sweden).  
The piezo-element of the dispenser is controlled by burst signals from an Agilent 33120A function generator. The size of the dispensed drops and the number of drops per second can be adjusted.
- DL: External Cavity Quantum Cascade Laser from Daylight Solutions Inc. (CA, USA).  
The wavenumber and the intensity of the emitted light can be set among other laser parameters. The DL client also supports a scanning mode, where the emission wavenumber of the laser is tuned automatically.
- GI: Miniplus 3 peristaltic pump from Gilson Inc. (Middleton, WI, USA).  
The speed as well as the pumping direction can be controlled.
- HV: CZE 1000R high voltage supply from Spellman (NY, USA).  
It is supported via an DAC module from National Instruments. The output voltage of the module is transformed into high voltage output (10 V equal 30 kV).
- LC: Waverunner 64-Xi oscilloscope from LeCroy Corp. (NY, USA).  
Only the most important features such as setting V/div, timebase and trigger-parameters are implemented. Single pulses can be read and stored.
- OP: FTIR spectrometers from Bruker Optik GmbH (Ettlingen, Germany).  
This client connects to OPUS over a DDE connection and can trigger measurements utilizing predefined experiment files. Single and repeated measurements are supported.
- TE: TDS 220 oscilloscope by Tektronix (OR, USA).  
Only the most important features such as setting V/div, timebase and trigger-parameters are implemented. Single pulses can be read and stored.
- UV: Capillary UV-Detector from Dionex (Sunnyvale, CA, USA).  
The client allows to set four wavelengths for absorption measurements. It can autozero the absorbance values and record the absorbance over time.
- VI: Valves from Vici AG (Switzerland).  
Injection and selection valves are supported by this client.
- WA: Wait client  
The wait client allows a delay of the execution of the next command by a defined time period. It is also included in the ATLAS server as the BP client.
- XY: Custom-built XY stage.  
The XY stage is operated by a Trinamic TMC610 stepper motor control, which is controlled by the XY client. This client allows the user to move the stage for a certain distance by a predefined speed.

### 3. Sample applications

#### 3.1 Example I: Quantification of lactate in aqueous solution using an External Cavity Quantum Cascade Laser

In clinical diagnostics numerous parameters, such as glucose, phosphate and lactate in blood have to be measured with high precision and accuracy in short time intervals. One

measurement principle suitable for such requirements is infrared spectroscopy. Using classical Fourier transform infrared spectrometry (Griffiths & Haseth, 2007) two approaches can be chosen. Measuring the solution in transmission requires low path lengths typically below 25  $\mu\text{m}$  in the spectral region of 1000 – 1250  $\text{cm}^{-1}$  due to the high absorbance of water in the region of interest. The measurement cell can suffer from bio-fouling on the window materials when biological samples are measured. Additionally, particles in the sample solution can cause cell-clogging in such small path lengths. The second suitable measurement method overcoming the clogging problem is attenuated total reflection (ATR). Using the ATR technique the light doesn't transmit through the sample solution but is coupled into an IR transparent crystal (e.g. Germanium). At the surface between the crystal and the sample total reflection of the light occurs and the evanescent field of the propagating light is reaching into the sample. This evanescent field interacts with the sample and is absorbed by the target molecules. Applying the ATR technique allows the use of flow cells on top of the crystal with bigger dimensions since the light doesn't need to penetrate the whole sample thickness. This advantage comes with the tradeoff that the penetration depth of the light into the sample is small compared to the transmission measurement. Therefore, one must expect higher limits of detection and less sensitivity according to Lambert Beer's law (1). Additionally bio fouling on the crystal surface is an even bigger issue due to the low penetration depth.

$$A(\text{cm}^{-1}) = -\log\left(\frac{I(\text{cm}^{-1})}{I_0(\text{cm}^{-1})}\right) = \varepsilon \cdot c \cdot l \quad (1)$$

In this formula  $I_0$  denotes the measured intensity of the light reaching the detector without sample whereas  $I$  gives the intensity after the light was absorbed by the sample.  $\varepsilon[\text{L}/\text{cm}]$  is the molar absorption coefficient at a given wavenumber.  $c[\text{mol}/\text{L}]$  denotes the concentration of the analyte and  $l[\text{cm}]$  gives the path length of the measurement cell.

Increasing the optical path length of the measurement cell would solve both drawbacks, described above, at the same time. Larger cell dimensions would make the cleaning of the cell easier, accompanied by better sensitivity because of the increased interaction length. Replacing the IR spectrometer with a Quantum Cascade Laser (QCL) (Faist et al., 1994) enables the penetration of higher path lengths at one wavenumber due to the higher energy output of the laser compared to the light source of an IR spectrometer. Applying an External Cavity Quantum Cascade Laser (EC-QCL), which can shift its emission wavenumber over a range of 200  $\text{cm}^{-1}$  gives a spectrum instead of a single absorbance value at a given wavenumber.

Using an EC-QCL enabled us to use an optical path length of 130  $\mu\text{m}$  for the measurement of physiological relevant compounds in Ringer solution. Using ATLAS we realized an experimental setup for the measurement of liquid samples and tested it on lactate samples in Ringer solution.

### 3.1.1 Experiment

For our studies we combined an EC-QCL (tuning range: 1030 – 1230  $\text{cm}^{-1}$ ) from Daylight Solutions Inc. with a thermoelectrically cooled Mercury Cadmium Telluride (MCT) detector and a Sequential Injection Analysis (SIA) system for sample preparation (Brandstetter et al., 2010). The detector signal was digitized by a specially designed analogue to digital



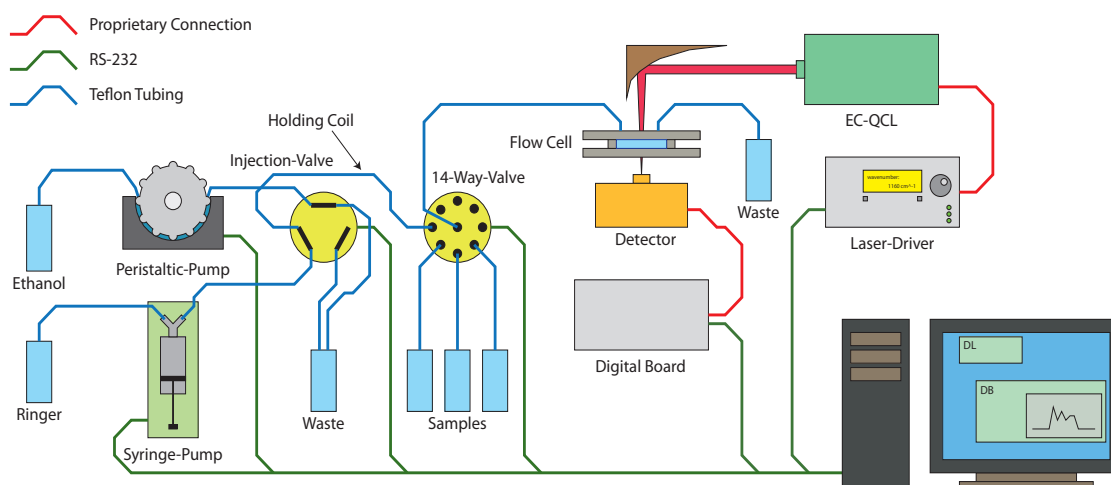


Fig. 6. Experimental setup for the measurement of lactate in Ringer solution using an External Cavity Quantum Cascade Laser.

converter (ADC) board which was read out by the *digital board* ATLAS client. Using a SIA system improves on manual sample injection by means of reproducibility and repeatability. Applying the SIA system also helps to reduce sample contaminations since the system can be cleaned automatically before a new sample is injected for the next measurement.

For this setup, shown in figure 6, the ATLAS clients for the digital board, the EC-QCL from Daylight Solutions Inc., the syringe pump from Cavo Inc., valves by Vici Inc. and the client for the Gilson Miniplus 3 peristaltic pump were connected to the ATLAS server. All hardware parts were connected to a notebook by RS-232 connections over USB-to-RS-232 converters. The peristaltic pump in the setup was only used if air bubbles were found in the tubings. In that case the system was purged with ethanol first to drive the bubbles out of the system and afterwards the ethanol flask was exchanged with Ringer solution manually and the tubings were filled with Ringer solution again.

In a first experiment lactate in Ringer matrix was pumped through the measurement spot repeatedly to examine the achieved flow profiles. Therefore, the whole system was filled with Ringer solution first. The laser parameters were sent by the client to the laser control unit and the emission wavenumber was tuned to  $1130\text{ cm}^{-1}$ . After initiating the emission of light the data acquisition was started and the intensity of the detected signal was streamed onto the hard drive continuously. In the meantime the syringe pump picked up the lactate sample through the 14-way-valve into the holding coil. After switching the 14-way-valve back to connect the holding coil with the measurement cell the syringe pump dispensed the lactate sample through the measurement cell. The pickup and dispense procedure was repeated while the data acquisition continued. In figure 7 the obtained flow profile for two repetitions is plotted against time. Whenever the sample solution passes the measurement cell the measured intensity on the detector decreases due to absorption taking place in the cell. The obtained flow profiles are in good agreement with theory. Optimization of the pumped lactate volume and the used flow rates allowed adjustments of the system in such a way that, at the maximum of the absorption, undiluted sample was measured. Knowing the exact time when this maximum reached the flow cell was crucial for the following experiment.

To obtain a calibration curve for lactate in Ringer solution a second command sequence was programmed. Firstly Ringer solution was pumped through the measurement cell utilizing a

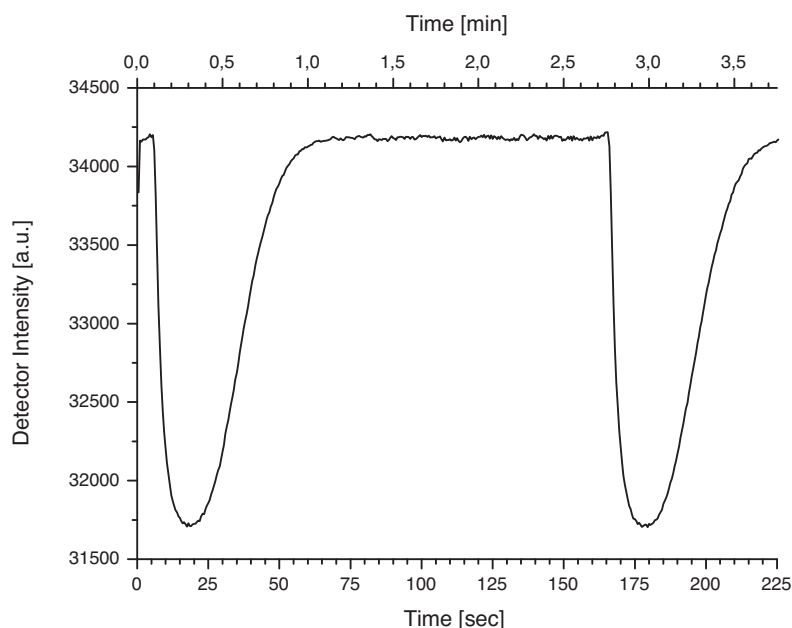


Fig. 7. Lactate solution was pumped through the measurement cell twice while the EC-QCL emitted light at  $1130\text{ cm}^{-1}$  and the digital board read out the detector values.

Cavro syringe pump. After the cell was purged the flow was stopped and the ATLAS server sent a signal to the digital board to start recording. Afterwards the EC-QCL was started by the server to scan over a wavenumber region ranging from  $1030$  to  $1230\text{ cm}^{-1}$ . This measurement served as  $I_0(\text{cm}^{-1})$  in equation (1). Then the valves switched positions allowing the syringe pump to pick up a sample of lactate into the holding coil. After the 14-way-valve was switched to connect the holding coil with the flow cell the sample was pumped into the measurement spot. Subsequently, the flow was stopped at the absorption maximum determined earlier. Now the EC-QCL received a trigger signal from the server to start another measurement, which gave  $I(\text{cm}^{-1})$  in equation (1). Then the valve of the syringe pump was switched to the opposite direction and picked up Ringer solution from the storage flask. After switching the valve back the whole system was purged again. This step was repeated twice to flush any possible remaining lactate out of the measurement spot.

The sequence described above was automatically repeated for all five sample concentrations by changing the 14-way-valve to the appropriate position in each of the measurement runs. Afterwards the absorbance spectra were calculated manually and the data shown in figure 8 were plotted in Origin. Calculating a linear calibration function for the measured absorbances at the band maxima gave a  $R^2$  value of 0.996.

In conclusion we can report that setting up a SIA system using ATLAS can be achieved easily. The integration of the EC-QCL and the data acquisition electronics into the SIA sequences was simple too after the ATLAS clients for the laser and the ADC board had been developed.

### 3.2 Example II: Using IR spectroscopy as a detector for liquid chromatography

Liquid chromatography (LC) is a widely used technique in analytical chemistry to separate mixtures of substances before detecting and quantifying them. The sample is injected onto a

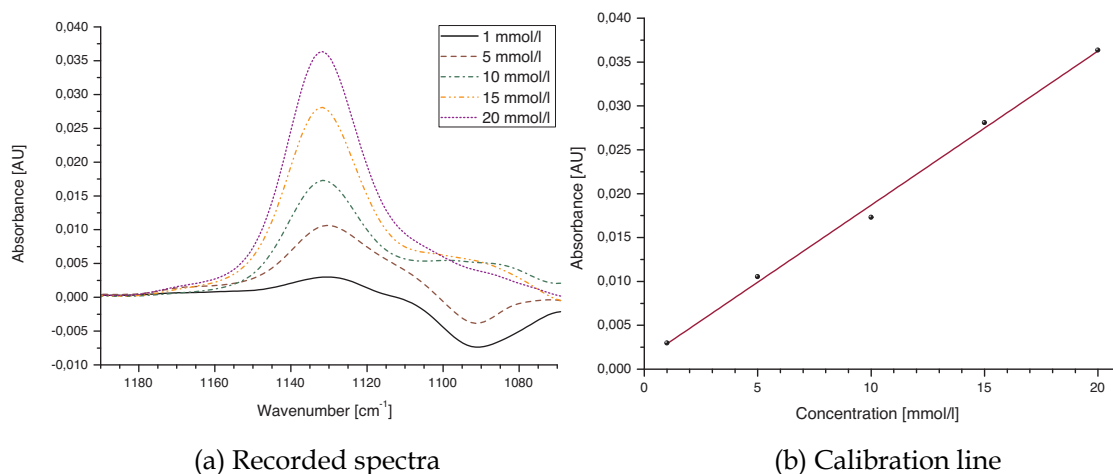


Fig. 8. 5 different concentrations of lactate in Ringer solution were measured and the absorbance values at 1131.7 cm<sup>-1</sup> are plotted as a calibration curve giving a  $R^2$  value of 0.996.

separation column where different molecules in the analyte mixture are retained for a varying time dependent on the nature of the column and the analyte itself. The analytes are driven through the column by a single solvent mixture, called isocratic mode, or the composition of the solvent mixture is changed during the elution, which is called gradient mode. Classical detectors used for detection in LC are mass spectrometry (MS) and UV-VIS spectroscopy. IR spectroscopy was not commercialized until today as a detection principle for LC because the solvents used cause high absorption in the infrared spectral region and overlap with the very small absorptions of the analyte molecules. However IR spectroscopy has some advantages as detection principle. First it is a non destructive detection principle, compared to MS. Second, the IR spectrum can be seen as a fingerprint of a target molecule which simplifies the identification of target molecules compared to UV-VIS spectroscopy.

Using IR spectroscopy as the detection principle in LC can be done in two ways. In the online method the exit of the separation column is connected to a flow cell and IR spectra are recorded during the elution of the analytes. Since the time resolution of the chromatogram depends mainly on the time needed to record a spectrum a tradeoff has to be made here. Increasing the spectral averaging will give better signal to noise levels and therefore better sensitivity. However, the time resolution of the chromatogram will decrease and two peaks, which are eluted shortly after each other, might be not detected separately. The strong absorption of the solvent can be easily subtracted in an isocratic elution whereas background correction algorithms have to be used in gradient elution (Quintás et al., 2009a;b).

The second possible method is based on physically eliminating the solvent from the sample and the IR spectra are measured afterwards as traces on an IR transparent substrate. This method enables averaging of as many spectra as needed without decreasing the time resolution of the chromatogram because the time resolution is mainly determined by the deposition method of the eluents on the measurement substrate.

Using ATLAS we have coupled a Dionex Ultimate 3000 capillary LC system to a micro dispenser (Laurell et al., 1999), which was used for eluate deposition on CaF<sub>2</sub> windows followed by subsequent IR detection. The setup described below was already used by manually controlling all components before ATLAS became available and proved capable of measuring pesticides down to concentrations of 2 µg/mL (Armenta & Lendl, 2010).

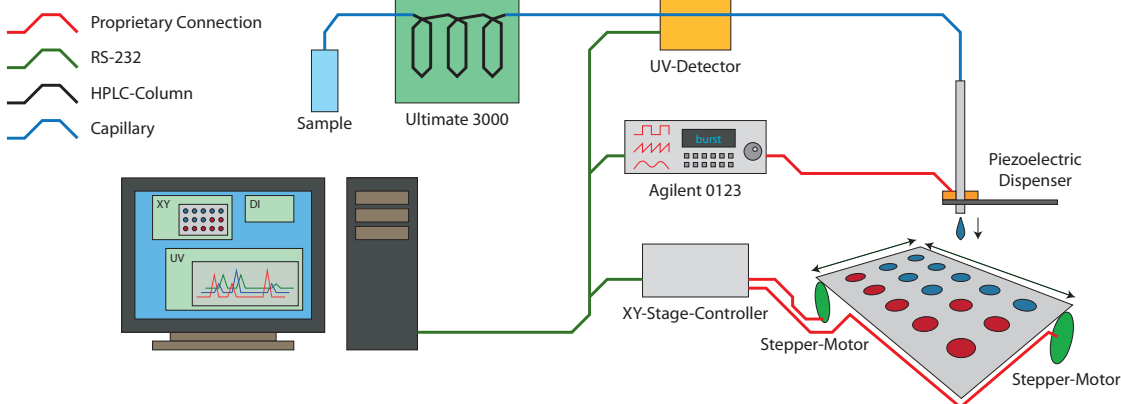


Fig. 9. Experimental setup for the coupling of a liquid chromatography system with offline IR detection utilizing a micro dispenser for sample deposition.

### 3.2.1 Experiment

Our system, as shown in figure 9, was built combining an Ultimate 3000 capillary LC system (Dionex, Sunnyvale, CA, USA), which is not implemented in ATLAS yet, a Dionex UV detector, a home built XY stage and a micro dispenser from Picology AB (Bjaerred, Sweden). The UV detector was configured and read out via a RS-232 connection by an ATLAS client. The stepping motors of the XY stage were connected to a controller board (Trinamic TCM-610) which was controlled by another ATLAS client. The piezo crystal of the micro dispenser was actuated by a specially designed electronics board which amplified a burst signal generated by an Agilent 33120A function generator. The burst period, giving the number of droplets dispensed each second, and the burst amplitude, giving the volume of each dispensed drop, were set by a dedicated dispenser ATLAS client. The droplets of the eluent were dispensed onto a heated plate of IR transparent  $\text{CaF}_2$  mounted on the XY stage moving the plate constantly during the deposition.

A typical experiment consisted of the following steps. First the injection of the sample onto the LC column was initiated manually since the LC system is not implemented into the ATLAS system yet. Immediately afterwards a preprogrammed ATLAS control sequence was started containing the following steps:

- The desired wavelengths for the UV measurement are set
- The absorbance signal of the UV detector is set to zero
- The dispenser parameters are set
- The movement of the XY stage is initiated at a certain speed and a programmed distance to travel
- The UV measurement is started
- The dispensing of the droplets is triggered

After the elution of the injected substances was completed the  $\text{CaF}_2$  plate was removed from the XY stage and was analyzed on a Hyperion 3000 IR microscope from Bruker Optics (Ettlingen, Germany). The plate was measured in transmission mode applying a line scan along the deposited material.

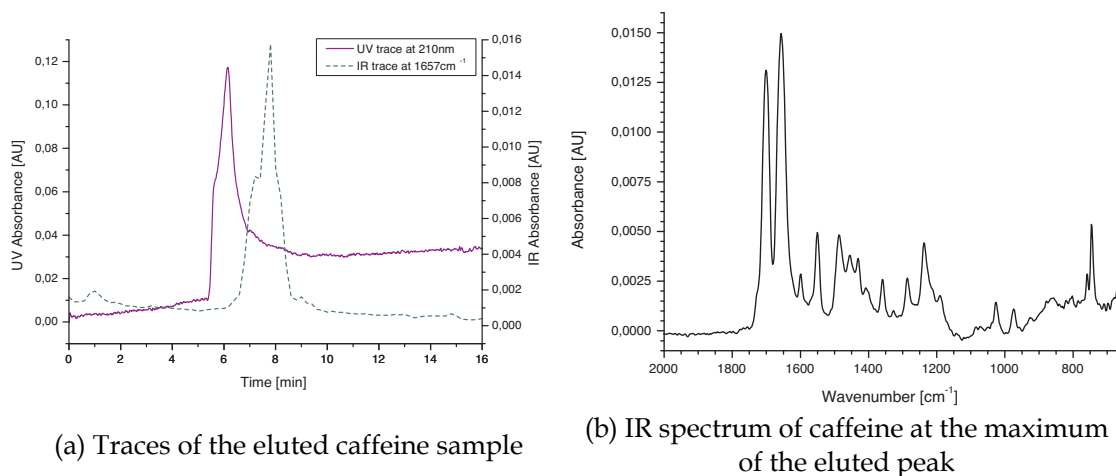


Fig. 10. Measurement results from the coupling of a liquid chromatography system with offline IR detection.

First results testing the ATLAS system were obtained by injecting 1  $\mu\text{L}$  of a 60 ppm solution of caffeine onto a C18 separation column. A mixture of water and acetonitrile (50:50 % v/v) with 0.1% acetic acid served as the mobile phase flowing at a speed of 2  $\mu\text{L}/\text{min}$ . The UV detector was set to measure at 200, 210, 250 and 350 nm wavelengths every 500 ms for 15 min and the XY stage was moved with 25  $\mu\text{m}/\text{s}$  for a distance of 3 cm. The dispense rate was set to 25 drops/s.

The obtained chromatogram of caffeine is plotted in figure 10. The time delay between the UV and IR measurement can be explained by the distance between the UV measurement cell and the micro dispenser. The IR trace was obtained by integration of the caffeine band located at 1657  $\text{cm}^{-1}$ . The plotted IR spectrum of caffeine represents the maximum of the IR trace.

Concluding we can state that using ATLAS enabled us to setup a measurement system coupling a LC system with online UV detection and offline IR detection. Inclusion of the Dionex Ultimate 3000 chromatograph would allow for fully automated measurements with this system eliminating the manual injection of the sample.

#### 4. Conclusion and Outlook

In this chapter we introduced ATLAS, our LabVIEW programmed lab automation system. While LabVIEW is routinely used in many labs to control laboratory equipment, usually these programs are ad-hoc solutions which are used for one type of experiment only and are never published. What sets our system apart from previously reported works are its expandability and flexibility. Through its Server-Client layout the ATLAS system can easily be expanded to be able to control a wide range of lab equipment – any instrument, that can be controlled by LabVIEW, can be controlled by our program – and experiment parameters can be easily changed.

To give the reader an idea of possible applications of ATLAS we described two ATLAS controlled experiments, which would have been very inconvenient to do manually, but were easily implemented with the help of the presented lab automation system.

In the future we plan to extend our program by the ability to send measurement data from clients to the server and have the server make decisions based on this data. Furthermore, the

final version and the source code of ATLAS will be made available on our website (<http://www.cta.tuwien.ac.at/cavs>), to allow other users to use and improve it.

## 5. Acknowledgment

The authors want to thank Eva Aguilera Herrador, Julia Kuligowski and Markus Brandstetter for supplying us with their measurement data which are presented in section 3.

## 6. References

- Armenta, S. & Lendl, B. (2010). Capillary liquid chromatography with off-line mid-ir and raman micro-spectroscopic detection: Analysis of chlorinated pesticides at ppb levels, *Anal Bioanal Chem* 397(1): 297–308.
- Barzin, R., Shukor, S. & Ahmad, A. (2010). New spectrophotometric measurement method for process control of miniaturized intensified systems, *Sensors and Actuators, B: Chemical* 146(1): 403–409.
- Brandstetter, M., Genner, A., Anic, K., Lendl, B. (2010). Tunable external cavity quantum cascade laser for the simultaneous determination of glucose and lactate in aqueous phase, *Analyst*, available online, doi: 10.1039/c0an00532k.
- Dominguez, R., Muñoz, R. & Araiza, H. (2010). Automated analytical system based on the sia technique, *Pan American Health Care Exchanges, PAHCE 2010* pp. 117–119.
- Faist, J., Capasso, F., Sivco, D., Sirtori, C., Hutchinson, A. & Cho, A. (1994). Quantum cascade laser, *Science* 264(5158): 553–556.
- Griffiths, P. R. & Haseeth, J. A. D. (2007). *Fourier Transform Infrared Spectrometry*, Wiley-Interscience.
- Jitmanee, K., Teshima, N., Sakai, T. & Grudpan, K. (2007). Drc™ icp-ms coupled with automated flow injection system with anion exchange minicolumns for determination of selenium compounds in water samples, *Talanta* 73(2): 352–357.
- Laurell, T., Wallman, L. & Nilsson, J. (1999). Design and development of a silicon microfabricated flow-through dispenser for on-line picolitre sample handling, *J. Micromech. Microeng* 9(4): 369–376.
- Quintás, G., Kuligowski, J. & Lendl, B. (2009a). On-line fourier transform infrared spectrometric detection in gradient capillary liquid chromatography using nanoliter-flow cells, *Analytical Chemistry* 81(10): 3746–3753.
- Quintás, G., Kuligowski, J. & Lendl, B. (2009b). Procedure for automated background correction in flow systems with infrared spectroscopic detection and changing liquid-phase composition, *Appl Spec* 63(12): 1363–1369.
- Růzicka, J. (1981). *Flow Injection Analysis*, Vol. 62 of *Chemical Analysis*, Wiley, John & Sons, Incorporated.
- Růzicka, J. (1992). The second coming of flow-injection analysis, *Analytica Chimica Acta* 261(1- 2): 3–10.
- Wagner, C., Armenta, S. & Lendl, B. (2010). Developing automated analytical methods for scientific environments using labview, *Talanta* 80(3): 1081–1087.

## Publication V

A. Kenda, M. Kraft, C. Wagner, B. Lendl, and A. Wolter, IEEE Sensors 2008, 724-727 (2008), DOI: 10.1109/ICSENS.2008.4716544.





# MEMS-based Spectrometric Sensor for the Measurement of Dissolved CO<sub>2</sub>

A. Kenda, M. Kraft  
Carinthian Tech Research AG  
Villach/St. Magdalen, Austria  
[andreas.kenda@ctr.at](mailto:andreas.kenda@ctr.at)

Ch. Wagner, B. Lendl  
Chemical Technologies and Analytics  
Vienna University of Technology  
Vienna, Austria

A. Wolter  
Hiperscan GmbH  
Dresden, Germany

**Abstract** — In the last few years several types of MEMS-based spectrometer systems emerged, mainly addressing the NIR spectral range. The presented MEMS-based sensor prototype operates in the mid-IR range between 2200 cm<sup>-1</sup> and 2500 cm<sup>-1</sup>. The main element is a blazed micro-electro-mechanical reflective grating device with an aperture of 3x3 mm<sup>2</sup>. The optical setup of the sensor corresponds to a Czerny-Turner type monochromator with an immense potential for further miniaturization due to its MEMS core. This allows designing and building competitively priced handheld analyzers for a range of applications that up to now has been restricted to large and expensive instruments. This work focuses on the development of an analyzer for dissolved CO<sub>2</sub> showing the methodology and also first implementation steps towards a sensor solution. CO<sub>2</sub>(aq) calibration samples were prepared by different NaHCO<sub>3</sub> concentrations in solution. Spectra and calibration data acquired with the prototype are presented.

## I. INTRODUCTION


The number one advantage of infrared (IR) spectroscopic sensors is their capability to directly and specifically detect and quantify (most) chemical substances by their inherent vibrational absorption properties [1,2]. An obstacle, however, is the limited availability of suitable, competitively priced sensor instrumentation, in particular in the mid-IR. Currently, most mid-IR sensors use non-dispersive (NDIR) technology, i.e. measure at a small number of wavelengths only. While simpler and hence smaller and cheaper in instrumentation, the reduction of the spectral information to a few pre-determined wavelengths forfeits the inherent capability of spectroscopic devices to selectively detect single substances even in the presence of spectrally interfering sample constituents. Fully spectroscopic sensors capable of scanning a wider spectral range around the target analytes' spectral absorption features would have significant advantages here, including the option of using smart chemometric algorithms for advanced data evaluation.

One such example where a fully spectroscopic sensor would have clear advantages over NDIR devices and other sensors is the detection of dissolved carbon dioxide in aqueous solu-

tions (CO<sub>2</sub>(aq)). The concentration of dissolved CO<sub>2</sub>, e.g. in carbonised beverages or beer, significantly influences the sensory experience during consumption. CO<sub>2</sub>(aq) levels hence are a key parameter in (on-line) quality control. Presently, CO<sub>2</sub>(aq) levels are mostly determined using gas extraction methods [3]. The classical technique is to expand the volume over a sample and measure the change in gas pressure due to out-gassing of CO<sub>2</sub>. While well proven, this method relies on sampling and thus is limited in its applicability for on-line process monitoring. An alternative is the use of semi-permeable membranes that allow a part of the dissolved CO<sub>2</sub> to diffuse into a measurement chamber, where it is detected directly using an NDIR detector or optically through its influence on a pH-sensitive dye. The chief limitation of these approaches is the limited compatibility with industrial food processing, in particular its stringent clean-in-place (CIP) requirements. Also, equilibrating between solutions and sensing devices may cause a time lag that limits the practical process applicability.

For industrial in-line monitoring, the ultimate solution would be a sensor that directly measures the dissolved carbon dioxide, e.g. in a process line or a storage tank. While well suited for measuring gaseous CO<sub>2</sub>, NDIR sensors have a problem with this, since the absorption band of CO<sub>2</sub>(aq) at 2343 cm<sup>-1</sup> / 4,27 μm overlaps with the short-wavelength tailing of the water combination band at 2130 cm<sup>-1</sup> / 4,7 μm (Figure 1). As mid-IR water absorptions are variable with temperature and the nature and concentration of chemically or physically dissolved substances, the shape and intensity of this interfering water band will change with e.g. the levels of sugars, alcohol or dissolved salts present in the beverage. Another complication is the pH-dependent equilibrium presence of spectrally different CO<sub>2</sub>-related chemical species, i.e. hydrogen carbonate (HCO<sub>3</sub><sup>-</sup>) and carbonate (CO<sub>3</sub><sup>2-</sup>) ions.

This clearly calls for the application of a sensor system capable of reliably discerning between the CO<sub>2</sub>(aq) feature and such interferences.

 This R&D project was co-financed within the Austrian Kplus Competence Centre programme.

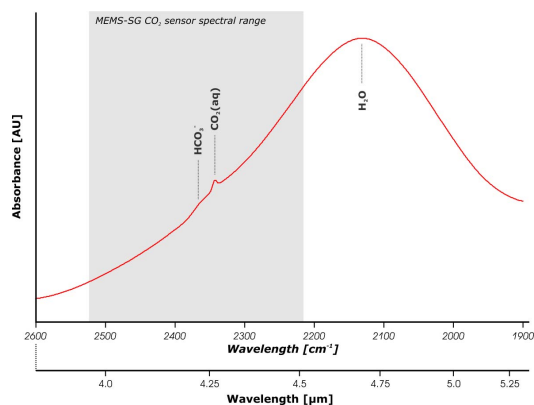


Figure 1. Absorption spectrum of an aqueous solution of 1.5 g/L carbon dioxide in water at 21 °C and pH 6; the shaded area indicates the spectral working range of the MEMS-GS CO<sub>2</sub> sensor prototype

## II. MEMS SPECTROMETER HARDWARE

To determine the relevant spectral range, the absorption spectra of various aqueous solutions containing dissolved carbon dioxide together with other typical beverage ingredients, such as sugars, artificial sweeteners, phosphates or alcohols, were measured under controlled laboratory conditions. The subsequent analysis resulted in the identification of a spectral range ( $2550\text{ cm}^{-1}$  -  $2200\text{ cm}^{-1}$  /  $3.9\text{ }\mu\text{m}$  -  $4.55\text{ }\mu\text{m}$ ) containing the significant spectral signatures of both the target analyte and relevant interferents. With a width of about  $0.6\text{ }\mu\text{m}$  this required spectral range is sufficiently narrow to be covered with a grating spectrometer device using a single refraction grating.

Based on that, a previously developed compact near-IR scanning grating (SG) spectrometer using a micro-electromechanical (MEMS) grating mirror [4,5] was redesigned to meet the specific needs of this application, i.e. operation in the mid-IR around  $4.2\text{ }\mu\text{m}$ . Implementing MEMS technology allows realising compact and reliable spectral analysers with good spectral properties and fast response times. Together with outstanding mechanical stability and a potentially low price due to the mass production of MEMS elements, such a system has the potential for being used as in-line sensor in industrial environments, e.g. directly flanged to a transfer line.

### A. Monochromator Layout

The spectral analyser was designed using a modified Czerny-Turner monochromator layout with  $15^\circ$  deviation angle (Figure 2). The incident light from the sample is collimated by an off-axis parabolic mirror with 10 mm focal length. Together with the  $3 \times 3\text{ mm}^3$  aperture of the scanning grating micro-element, this yields a good compromise between compact size, high radiation throughput ( $f/3.7$ ) and good spectral resolution. The first order diffractions are directed towards a spherical mirror focussing the beam through

an order-sorting filter (Spectrogon LP-3500) and an exit aperture onto a thermo-electrically cooled single-element MCT detector (Vigo PVI-2TE-5-0,5, BaF<sub>2</sub> window; VIGO S.A., Poland).

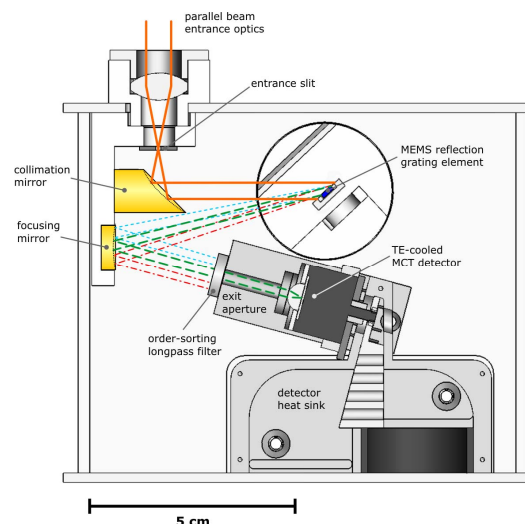


Figure 2. Optical layout of the prototype MEMS grating monochromator for operation in the  $4.0 - 4.5\text{ }\mu\text{m}$  range

### B. MEMS Component

To scan a grating monochromator through, the diffraction grating needs to be able to rotate or oscillate. On the micro-element scale, this translates favourably into a resonantly driven, electrostatically actuated oscillating micro-mirror device developed by the Fraunhofer Institute for Photonic Microsystems (IPMS) [6]. Using a number of in-plane comb electrodes to actuate an oscillatory movement around a central axis, large mechanical deflection angles can be achieved at low actuation voltages [7]. Depending on the design, oscillating micro-mirror components with deflection angles exceeding  $10^\circ$  can be driven at voltages less than 40 V. In order for such a component to function as a reflection grating element, the top surface of the mirror plate has to be modified by “cutting” a grating structure into it. In MEMS components, this can be achieved through anisotropic wet etching [8], followed by covering the structure with a thin metallic reflection coating, e.g. 100 nm aluminium, to ensure a high reflectivity in the mid-IR.

For the present study, a MEMS device with  $3 \times 3\text{ mm}^2$  aperture and a 400 grooves/mm V-shaped grating was used (Figure 3). Using a pulsed driving voltage of 36 V, the micro-mirror was operated at a mechanical deflection angle of  $\pm 7^\circ$  at an oscillation frequency of 130 Hz. Designed for the spectral range  $1.2 - 2.5\text{ }\mu\text{m}$ , operating this grating at a diffraction angle  $\beta = 66.5^\circ$  yields a first order centre wavelength of  $4.25\text{ }\mu\text{m}$  and allows covering the relevant spectral range from  $4.0$  to  $4.50\text{ }\mu\text{m}$ .

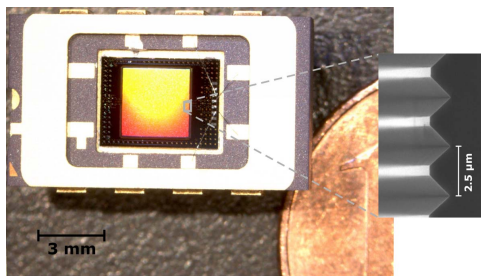


Figure 3. MEMS micro-mirror component with a 2.5  $\mu\text{m}$  spaced V-groove grating mirror, as used for the MEMS-SG  $\text{CO}_2$  sensor; on the right a part of one Euro-cent coin for size comparison.

### C. System Performance

The resulting spectrometric device covers a spectral range from 3,968  $\mu\text{m}$  to 4,520  $\mu\text{m}$  at a (simulated) spectral resolution of 10 nm; the experimental verification yields a spectral resolution better 15 nm, which is consistent. While not optimal in terms of grating efficiency (simulated average efficiency of 0.4) and effective grating aperture (the high angular inclination against the incident beam reduces the lateral aperture to approx. 1.2 mm), when compared to the effort of designing and producing a new grating the performance was deemed sufficient for proving or disproving the basic feasibility of the concept.

Another interesting feature of this device is its high scanning speed. At an oscillation frequency of 130 Hz the sensor can acquire one spectral scan every 7.7 ms, or one spectrum integrating 1000 scans within less than 8 s. It is thus easily possible to compensate for the inferior signal-to-noise ratio by co-adding a high number of spectral scans within a few seconds.

Encased in a robust standard housing, the MEMS-SG spectral transducer prototype has a typical footprint of 100 x 80 x 75  $\text{mm}^3$ , a weight of 0.6 kg and a typical power consumption of less than 5 W.

## III. EXPERIMENTAL

### A. Sample Preparation

As the equilibrium solubility of carbon dioxide in water is low, aqueous solutions containing dissolved  $\text{CO}_2$  need to be kept under pressure to avoid uncontrolled out-gassing. For this study, aqueous solutions containing controlled amounts of dissolved  $\text{CO}_2$  were produced in a closed flow system by mixing sodium hydrogen carbonate ( $\text{NaHCO}_3$ ) solutions in equal parts with a citrate buffer adjusted to pH 3.0. The change in the pH of the solution causes the hydrogen carbonate ( $\text{pK}_{a1}(\text{H}_2\text{CO}_3) = 6.35$ ) to transform into dissolved carbon dioxide, resulting in well-controlled standard solutions. In addition, a number of real samples (different mineral waters, dry sparkling wine, carbonated and sweetened dark coloured soft drink) were measured by pumping the respective sample through the measurement cell.

The measurement cell, a transmission flow cell with parallel  $\text{CaF}_2$  windows spaced 25  $\mu\text{m}$  apart, was directly connected to the flow system. The system proved pressure-stable up to 6 g/L  $\text{NaHCO}_3$  in the stock solution, equalling about 1.6 g/L dissolved carbon dioxide in the final standard solution. At higher concentrations the pressure provided by the peristaltic pump was no longer sufficient to reliably prevent the formation of gas bubbles in the flow cell.

### B. Data Acquisition & Post-Processing

All samples were measured in an open parallel beam setup consisting of a 20 W ceramic filament IR source, an off-axis parabolic mirror, the 25  $\mu\text{m}$  transmission flow cell and the MEMS-SG spectral analyser. The standard solutions were measured in flow at 1000 scans per spectrum (time resolution approx. 8 s) against a water/buffer background. To prevent water vapour or atmospheric carbon dioxide from interfering, the setup was encased in a glove box continuously flushed with dry nitrogen gas.

The measured absorption spectra were evaluated by integrating the peak area in the range 2327  $\text{cm}^{-1}$  to 2353  $\text{cm}^{-1}$  (4.30 – 4.25  $\mu\text{m}$ ), using a parabolic four-point baseline fit to compensate for baseline distortions due to the underlying water band.

## IV. RESULTS

Figure 4 shows some example spectra of  $\text{CO}_2(\text{aq})$  standard solutions. The strong variability of the baseline, in this case most likely due to temperature variations during the out-of-sequence measurement of the different standards, is clearly discernible, illustrating the need for a spectrometric analytical device able to identify and correct such baseline artefacts. A baseline-corrected integration of the area under the  $\text{CO}_2(\text{aq})$  peak yields a linear calibration curve (Figure 5,  $R^2=0.991$ ) with an estimated level of detection of 0,25 g/L.

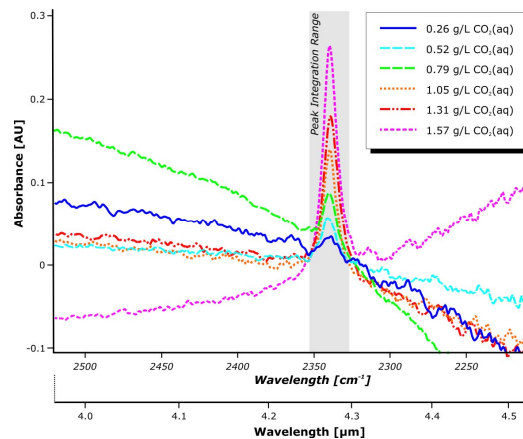


Figure 4. Absorption spectra of  $\text{CO}_2(\text{aq})$  solutions at different concentration levels, baseline offset corrected for the peak range. The shaded area indicates the peak integration range used for quantitative data evaluation.

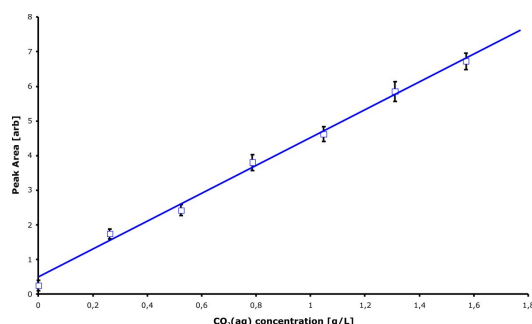


Figure 5.  $\text{CO}_2(\text{aq})$  calibration curve measured with the MEMS-SG  $\text{CO}_2$  sensor prototype

When attempting to measure strongly carbonated real samples out-gassing occurred, causing bubbles in the measurement cell. This out-gassing manifests itself also in the spectra (Figure 6), namely in a general decrease of intensity and the appearance of the characteristic double feature of gaseous  $\text{CO}_2$ .

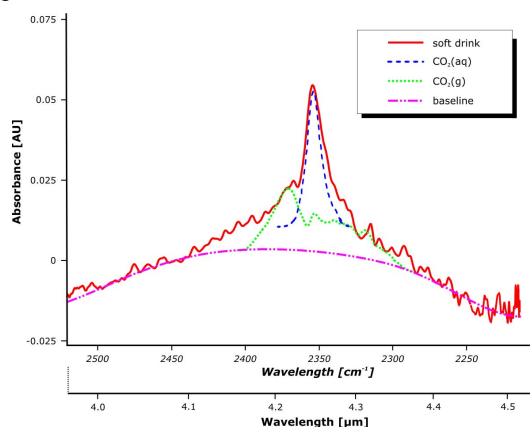


Figure 6. Typical absorption spectra of a strongly carbonated soft drink after partial out-gassing. The component spectra of dissolved  $\text{CO}_2$ , gaseous  $\text{CO}_2$  and the baseline distortion are shown in overlay.

## V. CONCLUSION & OUTLOOK

The findings of this study prove that using micro-electro-mechanical optical elements to build compact, robust spectrometric devices that could be used as the transducer core for dedicated IR sensors is feasible. Using dedicated gratings optimised for the respective wavelength range of interest, such devices can be tuned to specific analytes. Exploiting the fully spectroscopic measurement, multiple analytes absorbing in the same spectral region could be qualitatively and quantitatively detected, while interferences can be corrected

for. Exploiting the rapid scanning capabilities of the MEMS grating element, the limited optical signal throughput could be successfully compensated by co-adding large numbers of spectral scans in very short time. Thus, for the example application “dissolved  $\text{CO}_2$  in aqueous solutions” satisfactory results could be obtained even under less than optimal circumstances.

Next steps will include designing a mirror specifically for the spectral range 4 – 5  $\mu\text{m}$ . Besides improving the grating efficiency, this will allow increasing the f-number of the monochromator, thus improving the signal-to-noise characteristics. Combined with a high-pressure sample delivery system, this layout will be used for further measurements, including a wider study of real samples. Parallel to that, efforts will be made to further miniaturise the monochromator, with the aim of fitting it into a cube of about 5x5x5  $\text{cm}^3$ . Produced using standardised components, many of which can be produced cheaply using standard semiconductor processing technology, this could significantly reduce the prices for spectrometric analysers and thus make spectrometric IR competitive against their NDIR brethren.

## ACKNOWLEDGMENT

The cooperation of Dr. Harald Schenk and his work group at the Fraunhofer Institute of Photonic Microsystems in Dresden is gratefully acknowledged, as are the contributions by different co-workers and students involved in the technical development of the MEMS spectrometer prototype.

## REFERENCES

- [1] B. Mizaikoff, “Mid-Infrared Fiberoptic Sensors”, *Anal. Chem.* 75, 258A-267A, 2003
- [2] M. Kraft, “Vibrational spectroscopic sensors” in *Optical Chemical Sensors*, F. Baldini, A. Chester, J. Homola and S. Martellucci, Eds. NATO Science Series II, Vol. 224, Springer, 2006
- [3] R. Meyers (Ed), *Encyclopedia of analytical chemistry*. Wiley, 2000
- [4] M. Kraft, A. Kenda, A. Frank, W. Scherf, A. Heberer, T. Sandner, H. Schenk, F. Zimmer, „Single Detector Micro-Electro-Mechanical Scanning Grating Spectrometer“ *Anal. Bioanal. Chem.* 386, p. 1259-1266, 2006
- [5] A. Heberer; H. Gröger; F. Zimmer; H. Schenk; A. Kenda; A. Frank; W. Scherf, “Signal processing for a single detector MOEMS based NIR micro spectrometer“, *Proc. SPIE* 5964, p. 145–153, 2005
- [6] H. Schenk, P. Dürr, H. Kück, “Micromechanical components comprising an oscillating body”, *Eur. Patent* EP 1123526 B1 (1998)
- [7] H. Schenk, P. Dürr, D. Kunze, H. Lakner, H. Kueck, “Design and modeling of large deflection micromechanical 1D and 2D scanning mirrors”, *Proc. SPIE* 4178, p. 320–324 (1999)
- [8] F. Zimmer, H. Grueger, A. Heberer, Th. Sandner, H. Schenk, H. Lakner, A. Kenda, W. Scherf, „Development of high-efficient NIR-scanning gratings for spectroscopic applications“ *Proc. SPIE* Vol. 6114, p. 55-64, 2006

## Publication VI

A. Kenda, M. Kraft, A. Tortschanoff, C. Wagner, B. Lendl, T. Sandner, and H. Schenk, Proceedings of SPIE 7594, 75940U (2010), DOI: 10.1117/12.841957.



# Miniaturized MEMS-based spectrometric sensor for process control and analysis of carbonated beverages

A. Kenda<sup>\*a</sup>, M. Kraft<sup>a</sup>, A. Tortschanoff<sup>a</sup>, Ch Wagner<sup>b</sup>, B. Lendl<sup>b</sup>, T. Sandner<sup>c</sup>, H. Schenk<sup>c</sup>

<sup>a</sup>Carinthian Tech Research AG, Europastrasse 4/1, 9524 Villach, Austria

<sup>b</sup>Dept. of Chemical Technologies and Analytics, University of Technology, Vienna, Austria

<sup>c</sup>Fraunhofer Institute for Photonic Microsystems, Dresden, Germany

## ABSTRACT

With MEMS, it became possible to build pocket-sized spectrometers for various spectral ranges, including the near-IR or mid-IR. These systems are highly rugged and can measure spectral changes at ms time resolution or co-add several hundreds of scans to one spectrum achieving adequate signal-to-noise ratios. Two spectrometer systems a scanning grating based spectrometer and a FT-IR spectrometer both based on a micromechanical scanning mirror technology are presented. Furthermore, the focus of this work is on the development of an analyzer for dissolved CO<sub>2</sub> showing the methodology and also first implementation steps towards a sensor solution. CO<sub>2</sub>(aq) calibration samples were prepared by different NaHCO<sub>3</sub> concentrations in solution. Spectra and calibration data acquired with both MEMS based spectrometer prototypes are presented.

**Keywords:** MEMS; MOEMS; Scanning Grating Spectrometer; FT-IR Spectrometer; dissolved CO<sub>2</sub>; CO<sub>2</sub>(aq)

## 1. INTRODUCTION

With a definite trend towards the use of spectrometric systems in various fields of science and technology, there is an increased demand for compact spectrometers. Compact low-cost spectrometers for the near-IR above 1,7  $\mu\text{m}$  or even the mid-IR would be of high interest for numerous applications, such as industrial process control and chemical sensing. State of the art for wavelengths above 2  $\mu\text{m}$  are i) monochromator systems and ii) Fourier-Transform (FT) spectrometers, both using a single detector element but the necessity of having massive, moving optical components limit both the acquisition speed and the achievable degree of miniaturization. This is where MEMS components come in. MEMS components are usually produced using well-established semi-conductor production processes allowing for a convenient combination of e.g. semiconductor materials, dielectric layers and metals. Thus, intricate, powerful and highly reliable micro-devices can not only be produced in large quantities and at low cost but can also, within certain limits, be flexibly adapted to specific application requirements. Some efforts have been reported to miniaturize such instruments [1,2,3,4] based on various MEMS technologies. Furthermore the excellent mechanical stability of MEMS has the potential for being used as in-line sensor flanged directly to the main process pipeline. In this context a MEMS based sensor for the measurement of dissolved carbon dioxide for quality control of carbonized beverages and beer is of certain interest. At present dissolved CO<sub>2</sub> in beverages is determined mainly by measuring the partial gas pressure. This method is well proven but has several drawbacks e.g. the error of measurement introduced by other dissolved gases, and the need of complex and bulky mechanics leading to high costs especially in applications where in- or on-line measurements are demanded.

The spectrometric approach offers an alternative for the measurement of CO<sub>2</sub>(aq) with the advantage of not being interfered by other gases since IR spectrometry is a method of detection for (most) chemical substances by their inherent vibrational absorption properties [5,6]. Most industrial mid-IR sensors use non-dispersive (NDIR) technology, i.e. measure at a small number of wavelengths only. While simpler and hence smaller and cheaper in instrumentation, the reduction of the spectral information to a few pre-determined wavelengths forfeits the inherent capability of spectroscopic devices to selectively detect single substances even in the presence of spectrally interfering sample constituents. Fully spectroscopic sensors capable of scanning a wider spectral range around the target analytes' spectral absorption features would have significant advantages here, including the option of using smart chemometric algorithms for advanced data evaluation. One such example where a fully spectroscopic sensor would have clear advantages over NDIR devices and other sensors is the detection of dissolved carbon dioxide in aqueous solution (CO<sub>2</sub>(aq)).



Here we present two approaches towards a fully spectroscopic sensor, robust, fast and competitively priced to NDIR devices to observe the absorption band of  $\text{CO}_2(\text{aq})$  at  $2343\text{cm}^{-1}$ : A spectrometer based on a micro-electro-mechanical reflective scanning grating [7], and a recently developed FT-IR spectrometer [8] with the potential to yield extremely short measurement times.

## 2. INSTRUMENTATION DEVELOPMENT

### 2.1 MEMS Scanning Grating Spectrometer

The optical system of the spectrometer uses a Czerny-Turner monochromator setup where the spectrum is scanned across the detector on the basis of a rotating diffraction grating. As this system requires only a single detector, significant advantage over array spectrometers in terms of price as well as performance can be achieved especially in the NIR and mid-IR. While previously described MEMS scanners would be suitable in principle, the fact that these devices have to be operated at kilovolts makes integration into a portable instrument at least problematic.

Resonantly driven micro-mirrors developed by the Fraunhofer Institute for Photonic Microsystems (IPMS) yield large scanning amplitudes and optical apertures at comparatively low driving voltages [9,10]. The micromechanical scanning grating device is manufactured in a CMOS-compatible process. In an additional photolithographic step the mirror surface is structured with a high efficiency reflection grating [11].

For the present study, a MEMS device with  $3 \times 3\text{ mm}^2$  aperture and a 400 grooves/mm V-shaped grating was used (Figure 1). Using a pulsed driving voltage of 36 V, the reflection grating micro-device was operated at a mechanical deflection angle of  $\pm 7^\circ$  at an oscillation frequency of 130 Hz. The grating was originally designed and hence optimized for the spectral range 1.2 - 2.5  $\mu\text{m}$ . Aligning this grating to a diffraction angle  $\beta = 66.5^\circ$  yields a first order center wavelength of 4.25  $\mu\text{m}$  and allows covering the relevant spectral range from 4.0 to 4.50  $\mu\text{m}$ .

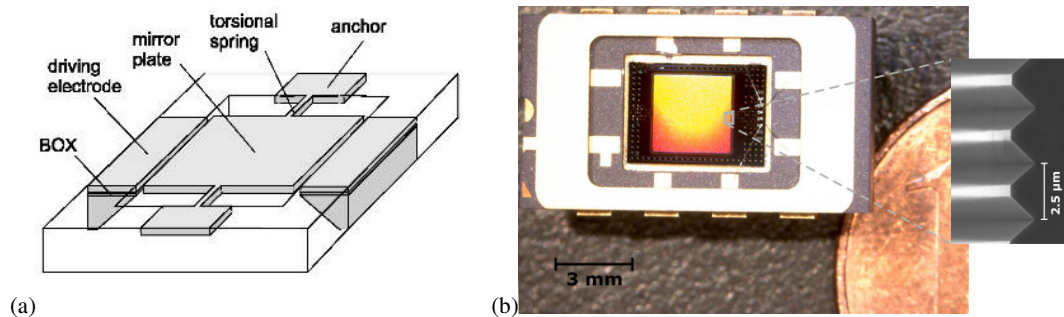


Figure 1: Micro scanner device (a) schematic and (b) housed device carrying a CMOS processed reflective grating with a 2.5  $\mu\text{m}$  spaced V-groove.

This device is the core of the spectral analyzer shown in Figure 2. After the incident light from the sample has been focused on an entrance slit, it is collimated by an off-axis parabolic mirror with 10 mm focal length. Together with the  $3 \times 3\text{ mm}^3$  aperture of the scanning grating micro-element, this yields a good compromise between compact size, reasonable radiation throughput ( $f/3.7$ ) and good spectral resolution. First order diffractions are directed towards a spherical mirror under  $15^\circ$  deviation angle. After passing an order-sorting filter, a second spherical mirror focuses the beam through an exit slit onto a thermo-electrically cooled single-element MCT detector.



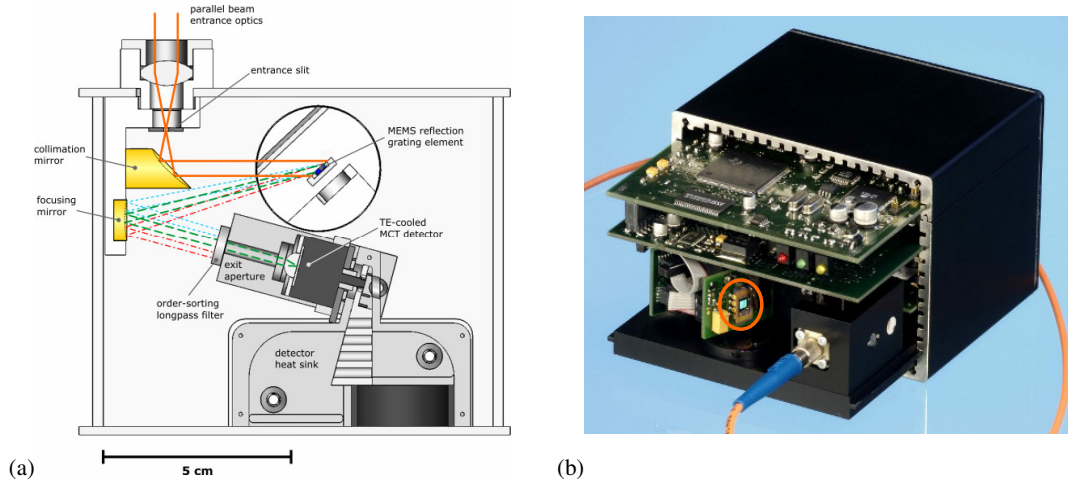


Figure 2: (a) layout of the optical bench, (b) scanning grating spectrometer prototype. The scanning micro grating is encircled. The shown fiber coupling was exchanged by a  $\text{CaF}_2$  for operation in the  $4.0 - 4.5 \mu\text{m}$  range as shown in the layout (a).

The resulting spectrometric device covers a spectral range from  $3.95 \mu\text{m}$  to  $4.52 \mu\text{m}$  at a spectral resolution of  $15 \text{ nm}$  as proved in Figure 3. While not optimal in terms of grating efficiency, the simulated average efficiency across the observed spectral range is  $0.4$ , and the reduced effective grating aperture of approx.  $1.2 \times 3 \text{ mm}^2$  due to the high angular inclination against the incident beam, when compared to the effort of designing and producing a new grating the performance was deemed sufficient for proving or disproving the basic feasibility of the concept.

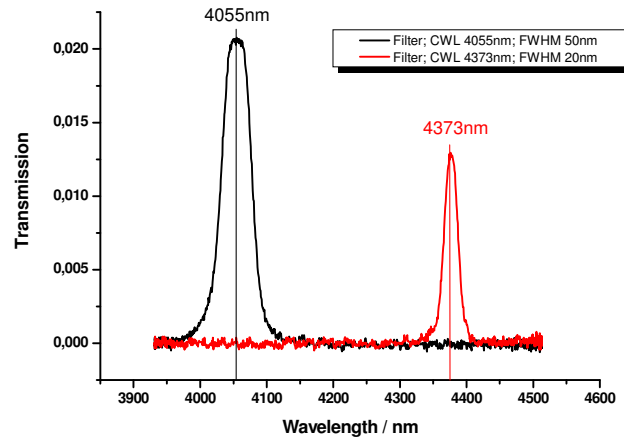


Figure 3: Transmission spectra of two interference filters (CWL 4055 nm and 4373 nm) for calibration and characterization of the scanning grating spectrometer prototype. The spectra were acquired averaging 1000 single scans.

Due to the high scanning speed it is easily possible to compensate for the perhaps insufficient signal-to-noise ratio (SNR) of a single scan by co-adding a high number of spectral scans within a few seconds. At an oscillation frequency of  $130 \text{ Hz}$  of the MEMS grating the spectrometer can acquire one spectral scan every  $7.7 \text{ ms}$ , or one spectrum integrating 1000 scans in less than  $8 \text{ s}$ .

## 2.2 MEMS FT-IR Spectrometer

A FT spectrometer requires a MEMS mirror component that is capable of linear movement. While a number of translatable MEMS elements have been described, the amount of linear travel is usually limited to several 10  $\mu\text{m}$ . Since spectral resolution is related to this parameter a maximum travel is favorable. Again, resonantly driven micro-mirrors developed by the Fraunhofer IPMS proved to be a feasible solution. The devices are electrostatically driven by applying a rectangular-shaped voltage to the in-plane inter-digital comb fingers [9,10]. When applying pulsed voltages the interlocking comb-structured electrodes induce electrostatic forces which actuate a sinusoidal forward-backward oscillation of the mirror plate. Since the electrostatic force always acts to pull the mirror from maximal elongation back towards the center, the frequency used for the driving signal must be twice the mechanical resonance frequency.

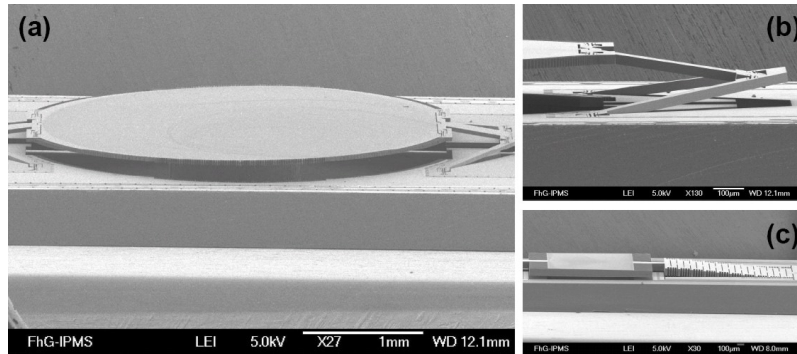


Figure 4: (a) SEM micrograph of a translatable micro-mirror component with pantograph-type suspensions. (b) suspension detail (c) SEM micrograph of the first generation mirror, used in an early FT-spectrometer prototype.

Figure 4 shows two different translatable mirror devices. These types of mirror devices have been described and characterized in [12,13,14]. Figure 4 (a) and (b) show a device with the mirror plate suspended by pantograph-type structures. Pantograph-type suspensions have the potential to enable mirror travels up to  $\pm 500 \mu\text{m}$  which would yield a spectral resolution of  $10 \text{ cm}^{-1}$  or better. A device showing this performance is currently under development and will be integrated in the next generation MEMS based FT-spectrometer which is the objective of the EU FP7 project 'MEMFIS'.

The mirror of the actual device, shown in Figure 4 (c), travels up to  $\pm 100 \mu\text{m}$ . When applying rectangular shaped voltages up to 40 V, the electrostatic forces actuate a quasi-harmonic oscillation of the mirror plate. This nonlinear motion has to be compensated at acquisition or the sampled interferogram has to be interpolated to get sample points which are equidistant in terms of optical path difference before applying the FFT. For this purpose the position of the MEMS mirror is monitored using the interference signal of a diode laser-reference interferometer, which uses the reflection from the backside of the actuator. The reference signal from the photodiode is used to precisely clock the IR interferogram, as outlined in much detail in [8]. From the interferogram, the IR spectrum is obtained via a Fourier transform. The system electronics are designed to perform averaging of multiple scans and calculation of the spectrum onboard, in order to provide a small standalone unit.

The layout optimization resulted in a classical Michelson arrangement, as illustrated in Figure 5. Encased in a rugged housing and using a thermo-electrically cooled MCT detector, the MEMS FT-spectrometer features a typical footprint of  $180 \times 120 \times 120 \text{ mm}^3$  and a weight of about 1.5 kg.

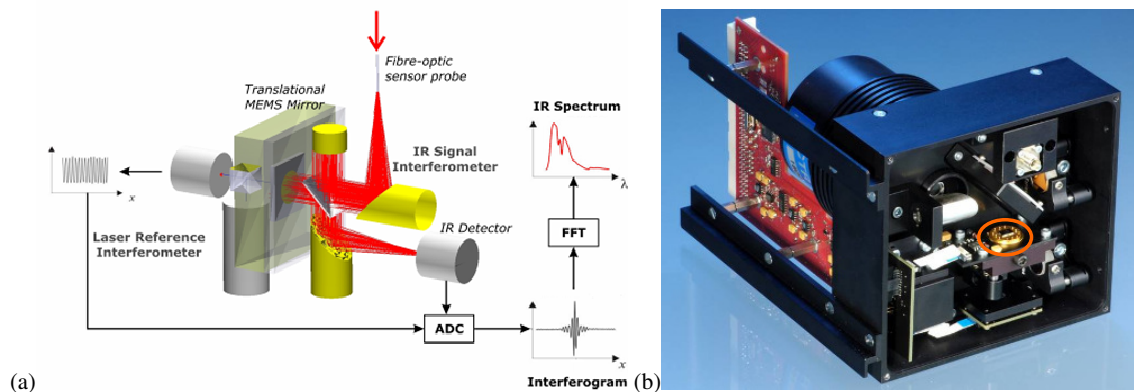


Figure 5: (a) FT-spectrometer optical layout and signal path (schematic). A laser reference interferogram is generated using the backside of the micro-mirror. The laser signal itself is used to clock the sampling. (b) Photograph of the FT-spectrometer prototype. The necessary vacuum chamber has been opened to show the translatory micro-mirror (encircled).

The prototype covers a spectral range from  $5000\text{ cm}^{-1}$  to  $1600\text{ cm}^{-1}$  at a spectral resolution of  $50\text{ cm}^{-1}$  as shown in Figure 6 (a). The current spectral resolution is likely not suitable for gas analysis but it is interesting for the addressed application due to the high potential of this spectrometer, namely the extremely high scanning speed and the expected improvements in terms of spectral resolution and throughput.

Due to the mirror oscillation frequency of  $>1\text{ kHz}$ , a single scan can be acquired within 1 ms. As an example for a time resolved plot with a resolution of 20 ms (20 scans averaged per spectrum) Figure 6 (b) shows two spectral features significant for aliphatic CH and  $\text{CO}_2$  in a flame of a Bunsen burner during ignition.

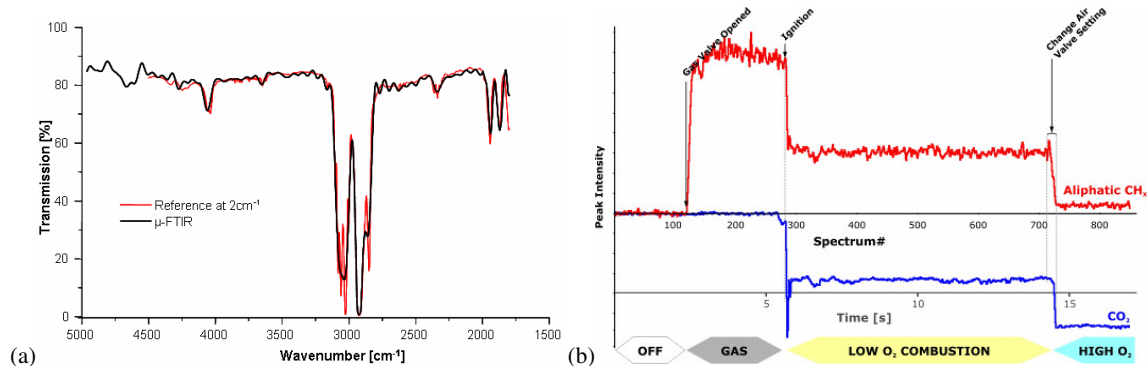


Figure 6: (a) Transmission spectrum of a Polystyrene film as a result of a 1000 scans average acquired within 1s compared to a reference acquired with a laboratory instrument at a resolution of  $2\text{ cm}^{-1}$ . (b) 20 ms time resolved spectral characteristics of different states of a Bunsen burner flame.

### 3. EXPERIMENTAL

#### 3.1 Sample Preparation

As the equilibrium solubility of carbon dioxide in water is low, aqueous solutions containing dissolved CO<sub>2</sub> need to be kept under pressure to avoid uncontrolled out-gassing. For this study, aqueous solutions containing controlled amounts of dissolved CO<sub>2</sub> were produced in a closed flow system by mixing sodium hydrogen carbonate (NaHCO<sub>3</sub>) solutions in equal parts with a citrate buffer adjusted to pH 2.8. The change in the pH of the solution causes the hydrogen carbonate ( $pK_{a1}(\text{H}_2\text{CO}_3) = 6.35$ ) to transform into dissolved carbon dioxide, resulting in well-controlled standard solutions. In addition, real samples (carbonated and sweetened soft drinks) were measured by pumping the respective sample through the measurement cell.

#### 3.2 Data Acquisition using the MEMS Scanning Grating Spectrometer

All samples were measured in an open parallel beam setup consisting of a 20 W ceramic filament IR source, an off-axis parabolic mirror, a measurement cell and the MEMS-SG spectral analyzer. The measurement cell, a transmission flow cell with parallel CaF<sub>2</sub> windows and 25 µm sample thickness was directly connected to the flow system. The system proved pressure-stable up to 6 g/L NaHCO<sub>3</sub> in the stock solution, equalling about 1.6 g/L dissolved carbon dioxide in the final standard solution. At higher concentrations the pressure provided by the peristaltic pump was no longer sufficient to reliably prevent the formation of gas bubbles in the flow cell. The standard solutions were measured in flow at 1000 scans per spectrum (time resolution approx. 8 s) against a water/buffer background. To prevent water vapour or atmospheric carbon dioxide from interfering, the setup was encased in a glove box continuously flushed with dry nitrogen gas.

The measured absorption spectra were evaluated by integrating the peak area in the range 2327 cm<sup>-1</sup> to 2353 cm<sup>-1</sup> / 4.30 – 4.25 µm, using a parabolic four-point baseline fit to compensate for baseline distortions due to the superimposed water band.

#### 3.3 Data Acquisition using the MEMS FT-IR Spectrometer

In this setup the samples were measured in a transmission flow cell with 100 µm layer thickness and sampling was accomplished using a special tap device. The advantages are that out-gassing of the sample was avoided as far as possible and the sample was flushed through the sample cell by its own overpressure. As IR source a 20 W ceramic filament was used. After transmitting the sample, the IR radiation is coupled into a Chalcogenide fiber leading into the MEMS interferometer. The samples were measured in flow with 512 scans per spectrum yielding a time resolution of approx. 0.7 s. against a water/buffer background. Also this setup was encased in a box flushed with dry nitrogen gas due to the reasons mentioned before.

### 4. RESULTS

For industrial in-line monitoring, the ultimate solution would be a sensor that directly measures the dissolved carbon dioxide, e.g. in a process line or a storage tank. NDIR sensors which are capable of measuring gaseous CO<sub>2</sub> are not straight forward applicable, since the absorption band of CO<sub>2</sub>(aq) at 2343 cm<sup>-1</sup> / 4.27 µm overlaps with the short-wavelength tailing of the water combination band at 2130 cm<sup>-1</sup> / 4.7 µm (Figure 7). As mid-IR water absorptions are variable with temperature and the nature and concentration of chemically or physically dissolved substances, the shape and intensity of this interfering water band will change with e.g. the levels of sugars, alcohol or dissolved salts present in the beverage. Another complication is the pH-dependent equilibrium presence of spectrally different CO<sub>2</sub>-related chemical species, i.e. hydrogen carbonates (HCO<sub>3</sub><sup>-</sup>) and carbonate (CO<sub>3</sub><sup>2-</sup>) ions.

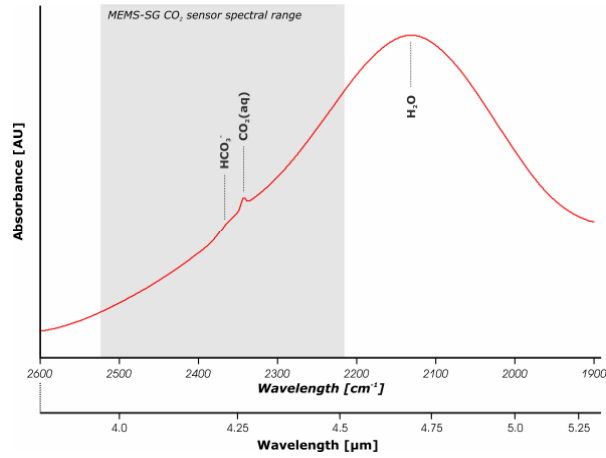


Figure 7: Absorption spectrum of an aqueous solution of 1.5 g/L carbon dioxide in water at 21 °C and pH 6; the shaded area indicates the spectral working range of the MEMS-Scanning Grating CO<sub>2</sub> sensor prototype. The working range of the MEMS-FT-IR CO<sub>2</sub> sensor prototype extends over a much wider spectral range as shown in Figure 6.

To determine the relevant spectral range, the absorption spectra of various aqueous solutions containing dissolved carbon dioxide together with other typical beverage ingredients, such as sugars, artificial sweeteners, phosphates or alcohols, were measured under controlled laboratory conditions. The subsequent analysis resulted in the identification of a spectral range (2550 cm<sup>-1</sup> – 2200 cm<sup>-1</sup> / 3.9 μm – 4.55 μm) containing the significant spectral signatures of both the target analyte and relevant interferences. With a width of about 0.6 μm this required spectral range is sufficiently narrow to be covered with a grating spectrometer device using the specified MEMS diffraction grating.

#### 4.1 MEMS Scanning Grating Spectrometer Measurements

Figure 8 (a) shows spectra of CO<sub>2</sub>(aq) standard solutions used for calibration. The strong variability of the baseline, in this case most likely due to temperature variations during the out-of-sequence measurement of the different standards, is clearly discernible, illustrating the need for a spectrometric analytical device able to identify and correct such baseline artefacts. A baseline-corrected integration of the area under the CO<sub>2</sub>(aq) peak yields a linear calibration curve (R<sup>2</sup>=0.991) with an estimated level of detection of 0.25 g/L as shown in Figure 8 (b).

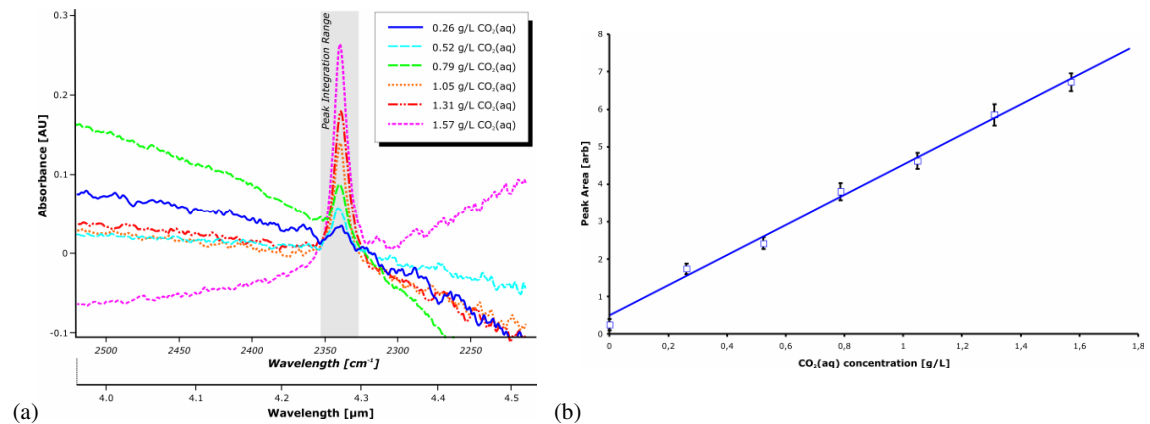


Figure 8: (a) Absorption spectra of CO<sub>2</sub>(aq) solutions at different concentration levels, baseline offset corrected for the peak range. The shaded area indicates the peak integration range used for quantitative data evaluation. (b) CO<sub>2</sub>(aq) calibration curve as a result of the integration.

When attempting to measure strongly carbonated real samples out-gassing occurred, causing bubbles in the measurement cell. This out-gassing manifests itself also in the spectra (Figure 9), namely in a general decrease of intensity and the appearance of the characteristic double feature of gaseous  $\text{CO}_2$ .

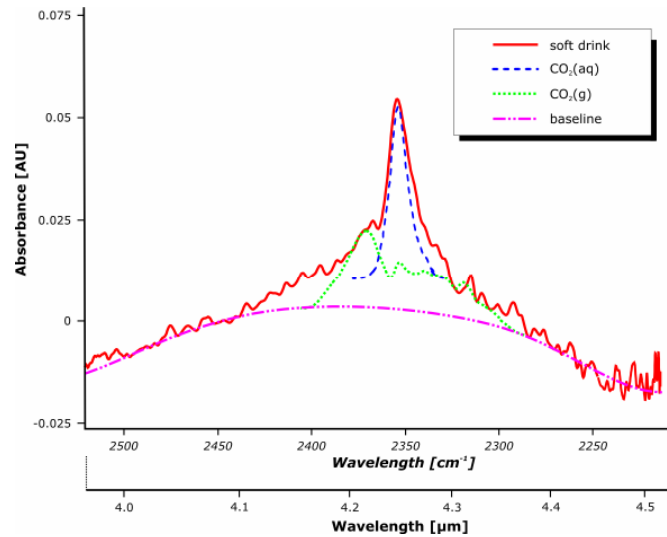


Figure 9: Typical absorption spectra of a carbonated soft drink after partial out-gassing. The component spectra of dissolved  $\text{CO}_2$ , gaseous  $\text{CO}_2$  and the baseline distortion are shown in overlay.

#### 4.2 MEMS FT-IR Spectrometer Measurements

Figure 10 shows  $\text{CO}_2(\text{aq})$  absorption spectra of various real beverage samples. Due to the more sophisticated sampling equipment and the better matched thickness of the flow cell, out-gassing and the formation of gas bubbles could be better controlled.

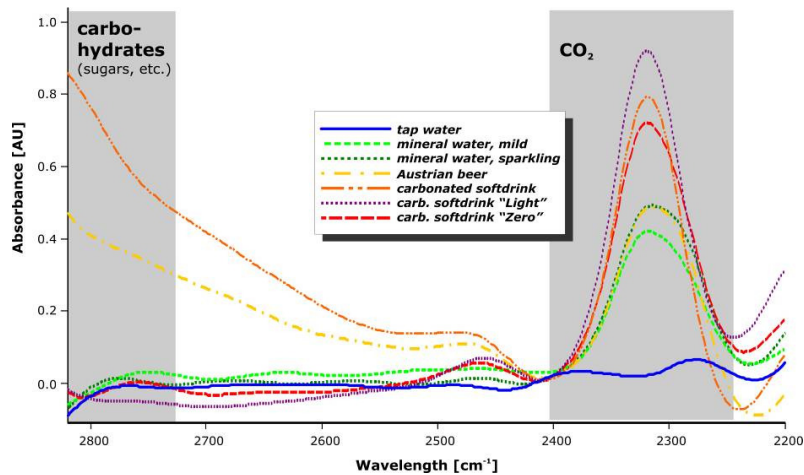


Figure 10: Absorption spectra of carbonated soft drinks, beer, carbonated water and tap water acquired with the MEMS FT-IR spectrometer. Due to the spectral range up to  $2850 \text{ cm}^{-1}$  absorption bands of CH compounds can be detected in parts.

The FT-IR spectra cover a wider spectral range but features a inferior spectral resolution of  $50\text{ cm}^{-1}$  which corresponds to a bandpass of  $90\text{ nm}$  at  $2343\text{ cm}^{-1}$  /  $4.27\text{ }\mu\text{m}$  (the central wavelength of the  $\text{CO}_2(\text{aq})$  peak) compared to the scanning grating spectrometer which shows a bandpass of  $15\text{ nm}$  (Figure 3). The spectral resolution of the MEMS FT-IR spectrometer is currently limited to this value [8]. Due to this factor the  $\text{CO}_2(\text{aq})$  peak could not be resolved in detail. Hence for quantitative analysis  $\text{CO}_2(\text{aq})$ ,  $\text{HCO}_3^-$  and gaseous  $\text{CO}_2$  remain indistinguishable. However, a calibration curve was derived based on standard solutions and the spectra of real samples were evaluated. The results are shown in Figure 11.

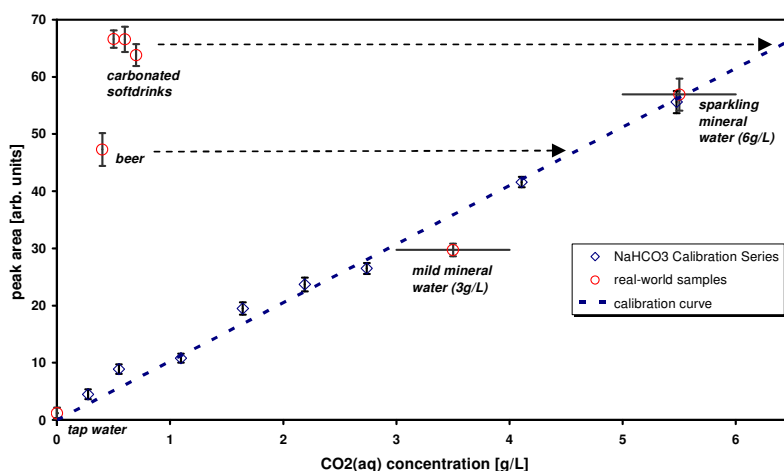


Figure 11: Peak integration values of baseline-corrected calibration solutions and the resulting linear calibration curve (dashed). Real samples are plotted according to their peak integration values. The corresponding peak integration area is indicated in Figure 10 as grey area labeled with  $\text{CO}_2$ .

Based on the FT-IR spectral data shown in Figure 10, we could determine the concentrations of dissolved  $\text{CO}_2$  as follows: Mild mineral water  $3.5\text{ g/L}$  and carbonated (sparkling) mineral water  $5.5\text{ g/L}$ . for these samples calibration data was known. The evaluation of the other samples is based on the derived calibration curve: Beer  $4.6\text{ g/l}$  and carbonated soft drinks about  $6.3\text{ g/L}$  dissolved  $\text{CO}_2$ . However, absorption spectra of carbonated soft drinks, beer and carbonated water also indicate the presence dissolved carbohydrates (sugar, etc.).

## 5. CONCLUSION & OUTLOOK

The findings of this study prove that using micro-electro-mechanical optical elements to build compact, robust spectrometric devices that could be used as the transducer core for dedicated IR sensors is feasible. Using dedicated gratings optimised for the respective wavelength range of interest, such devices can be tuned to specific analytes. Exploiting the fully spectroscopic measurement, multiple analytes absorbing in the same spectral region could be qualitatively and quantitatively detected, while interferences can be corrected for. Exploiting the rapid scanning capabilities of the MEMS grating element, the limited optical signal throughput could be successfully compensated by co-adding large numbers of spectral scans in very short time. Thus, for the measurement of dissolved  $\text{CO}_2$  in aqueous solutions encouraging results could be obtained even under less than optimal circumstances.

Next steps will include designing a MEMS grating specifically for the spectral range  $4 - 5\text{ }\mu\text{m}$ . Besides improving the grating efficiency, this will allow increasing the f-number of the scanning grating spectrometer, thus improving the SNR. Combined with a high-pressure sample delivery system, this layout will be used for further measurements, including a wider study of real samples.

In general, the first approaches to build practically applicable compact spectrometers based on MEMS devices with large amplitude in-plane actuators have exceeded initial expectations by far. The systems show the potential to be extremely fast and significantly cheaper than established spectrometers. Thus, MEMS spectrometers could significantly contribute to closer process surveillance and a better understanding of the underlying processes. For high-speed monitoring applications, spectral changes that could be monitored are at present restricted to more strongly absorbing substances or higher concentration levels. Still, improvement potentials, like increasing the spectral resolution and throughput, etc. will be exploited to facilitate such applications. Further developments will focus on hardware improvements, new applications and on implementing data evaluation algorithms directly into the spectrometer aiming at total analysis instruments that could provide the user directly with the relevant information and measures.

## ACKNOWLEDGEMENT

This R&D project was co-financed within the Austrian Kplus/COMET Competence Centre programme. The development of the MEMS based spectrometer systems was supported by the KWF – Kärntner Wirtschaftsförderungs Fonds within the “Technologiefonds Kärnten” programme.

Gratefully acknowledged is the cooperation of HiperScan GmbH as manufacturer and distributor of the scanning grating spectrometer (SGS) technology.

## REFERENCES

1. Beyer, T., Hahn, P., Hartwig, S., Konz, W., Scharring, S., Katzir, A., Steiner, H., Jakusch, M., Kraft, M., Mizaikoff, B., “Mini spectrometer with silver halide sensor fiber for in situ detection of chlorinated hydrocarbons”, *Sensors & Actuators B*, 90, 319-323 (2003).
2. Solf, C., Mohr, J., Wallrabe, U., “Miniaturized LIGA Fourier Transformation Spectrometer“, *Proc. IEEE Sensors*, 2, 773-776 (2003).
3. Manzardo, O., Herzig, H. P., Marxer, C. R., Rooij, N. F., “Miniaturized time-scanning Fourier transform spectrometer based on silicon technology”, *Opt. Lett.*, 24, 1705-1707 (1999).
4. Collins, S. D., Smith, R. L., González, C., Stewart, K. P., Hagopian, J. G., Sirota, J. M., “Fourier-transform optical microsystems”, *Opt. Lett.*, 24, 844-846 (1999).
5. Mizaikoff, B., “Mid-Infrared Fiberoptic Sensors”, *Anal. Chem.* 75, 258A-267A (2003).
6. Kraft, M., [Optical Chemical Sensors], Springer, Netherlands, 117-155 (2006).
7. Kraft, M., Kenda, A., Frank, A., Scherf, W., Heberer, A., Sandner, T., Schenk, H., Zimmer, F., “Single Detector Micro-Electro-Mechanical Scanning Grating Spectrometer“, *Anal. Bioanal. Chem.*, 386, 1259-1266 (2006).
8. Kenda, A., Drabe, Ch., Schenk, H., Frank, A., Lenzhofer, M., Scherf, W., “Application of a micromachined translatory actuator to an optical FTIR spectrometer”, *Proc. SPIE*, 6186, 72-88 (2006).
9. Schenk, H., Dürr, P., Kunze, D., Kück, H., “A new driving principle for micromechanical torsional actuators”, *Proc. of International Mechanical Engineering Congress and Exposition Nashville*, 1, 333-338 (1999).
10. Schenk, H., Dürr, P., Haase, Th., Kunze, D., Sobe, U., Lakner, H., Kück, H., “Large Deflection Micromechanical Scanning Mirrors for Linear Scans and Pattern Generation”, *Journal of Selected Topics in Quantum Electronics*, 6, 715-722 (2000).
11. Zimmer, F., Sandner, T., Grüger, H., Heberer, A., Wolter, A., Schenk, H., “Development of high-efficient NIR-scanning gratings for spectroscopic applications“, *Proc. SPIE*, 6114, 55-64 (2006).
12. Sandner, T., Drabe, Ch., Schenk, H., Kenda, A., Scherf, W., “Translatory MOEMS actuators for optical path length modulation in miniaturized Fourier-transform infrared spectrometers”, *Journal of Micro/Nanolithography MEMS and MOEMS*, 7, 21006 (2008).
13. Sandner, T., Drabe, Ch., Schenk, H., Kenda, A., “Large stroke MOEMS actuators for optical path length modulation in miniaturized FTIR spectrometers“, *Proc. SPIE*, 7319, 73190H (2009).
14. Tortschanoff, A., Lenzhofer, M., Frank, A., Wildenhain, M., Sandner, T., Schenk, H., Kenda, A., “Position encoding and phase control of resonant MOEMS-mirrors”, *Procedia Chemistry*, 1, 1315 (2009).



## Publication VII

M. Schleegeer, C. Wagner, M.J. Vellekoop, B. Lendl, and J. Heberle,  
Analytical and Bioanalytical Chemistry 394, 7, 1869-1877 (2009),  
DOI: 10.1007/s00216-009-2871-0.



## Time-resolved flow-flash FT-IR difference spectroscopy: the kinetics of CO photodissociation from myoglobin revisited

Michael Schleegeer · Christoph Wagner ·  
Michiel J. Vellekoop · Bernhard Lendl ·  
Joachim Heberle

Received: 9 April 2009 / Revised: 19 May 2009 / Accepted: 26 May 2009  
© The Author(s) 2009. This article is published with open access at Springerlink.com

**Abstract** Fourier-transform infrared (FT-IR) difference spectroscopy has been proven to be a significant tool in biospectroscopy. In particular, the step-scan technique monitors structural and electronic changes at time resolutions down to a few nanoseconds retaining the multiplex advantage of FT-IR. For the elucidation of the functional mechanisms of proteins, this technique is currently limited to repetitive systems undergoing a rapid photocycle. To overcome this obstacle, we developed a flow-flash experiment in a miniaturised flow channel which was integrated into a step-scan FT-IR spectroscopic setup. As a proof of principle, we studied the rebinding reaction of CO to myoglobin after photodissociation. The use of microfluidics reduced the sample consumption drastically such that a typical step-scan experiment takes only a few 10 ml of a millimolar sample solution, making this method particularly interesting for the investigation of biological samples that are only available in small quantities. Moreover, the flow cell provides the unique opportunity to assess the reaction

mechanism of proteins that cycle slowly or react irreversibly. We infer that this novel approach will help in the elucidation of molecular reactions as complex as those of vectorial ion transfer in membrane proteins. The potential application to the oxygen splitting reaction of cytochrome c oxidase is discussed.

**Keywords** Carbonmonoxymyoglobin ·  
Cytochrome c oxidase · Microfluidics ·  
Step-scan spectroscopy · Vibrational spectroscopy

### Introduction

Myoglobin is a monomeric oxygen transporting and storing protein of muscle tissue. The protein is well characterised and considered the hydrogen atom of biology [1]. The structure of the protein comprises eight helices A–H. The cofactor, heme b, is embedded in a hydrophobic pocket between helices E and F and ligated to the protein via a proximal histidine residue. The central ferric iron of heme b is able to bind oxygen and other small molecules, like carbon monoxide or nitric oxide. Substrate binding and rebinding kinetics after photolysis of myoglobin have been intensively studied, e.g. by X-ray crystallography [2, 3], time-resolved UV/Vis spectroscopy [4, 5] and time-resolved infrared spectroscopy [6, 7]. Instead of the natural ligand oxygen, infrared (IR) spectroscopy mostly uses the polar CO as IR probe which is photo-labile with a quantum efficiency of photolysis of close to unity [7]. Photodissociation of carbonmonoxymyoglobin (Mb-CO) yields a short-lived photoproduct, which relaxes to the deoxy form of myoglobin (deoxy-Mb) [8]. Deoxy-Mb exhibits several structural differences to Mb-CO, in particular heme-doming

M. Schleegeer · J. Heberle (✉)  
Biophysical Chemistry, Bielefeld University,  
Universitätsstr. 25,  
33615 Bielefeld, Germany  
e-mail: joachim.heberle@uni-bielefeld.de

C. Wagner · B. Lendl  
Institute of Chemical Technologies and Analytics,  
Vienna University of Technology,  
Getreidemarkt 9/164 AC,  
1060 Vienna, Austria

M. J. Vellekoop  
Institute of Sensor and Actuator Systems,  
Vienna University of Technology,  
Gusshausstraße 27-29 /E366,  
1040 Vienna, Austria

Published online: 12 June 2009

 Springer

due to the out-of-plane movement of the heme iron, protein backbone displacements of helices B, C and E and, to a lesser extent, of helices F and G. As a consequence, single amino acids change their positions: H64 (sperm whale numbering) moves into the heme pocket, and the side chain of L29 rotates [2, 9]. The photo-dissociated CO is able to exit the protein through transiently opened cavities [10]. Rebinding of CO from the solution to the heme recovers the initial Mb-CO state. This recovery, which takes several milliseconds, has shown to be an intricate reaction with a number of intermediate states. The intermediates were studied with spatially resolved techniques such as crystallography with kinetic resolutions down to the sub-nanosecond time range [2, 3, 11].

To study the rebinding kinetics and the subsequent protein relaxation, step-scan Fourier-transform infrared (FT-IR) spectroscopy with high time resolution was also employed [6, 7, 12]. This method takes advantage from both the sensitivity of IR spectroscopy to electronic changes of the heme cofactor and structural changes of the apo-protein, as well as from the multiplex advantage of FT spectroscopy.

Up to now, most of the applications of step-scan FT-IR spectroscopy to biological samples are restricted to reversible or fast cycling systems. The reason is the necessity to record hundreds of time traces at the various sampling positions of the interferometer to generate the time-resolved data set. It is mandatory that the reaction under study must be precisely synchronised and strictly reversible for the ~1.000 sampling points that constitute the interferogram at a given optical resolution of  $4\text{ cm}^{-1}$ . In total, as much as 100.000 repetitions of the same experiment are not uncommon to achieve sufficient signal-to-noise ratio in a time-resolved step-scan experiment of a large protein [13]. This is most practically realised in studies of light-activated proteins by the use of pulsed laser sources [14, 15]. The sample is optically excited and measured and eventually recovers back to the initial state before the next reaction is induced.

For the investigation of irreversible reactions, it is essential that each measurement is performed on a fresh sample of identical concentration. Rödiger and Siebert implemented a sample-changing wheel to provide fresh sample after each reaction [16]. Rammelsberg et al. reported a step-scan experiment using an IR microscope and an xy-stage that moves the sample after each excitation [17]. A major problem in both approaches is the change in optical path length when moving from one sampling position to the next because absorption changes as small as <1% are recorded on a film thickness of <10  $\mu\text{m}$ ! Moreover, both experiments employed hydrated films of membrane protein in which the concentration of compounds is difficult to control.

Here, we present a novel approach to perform step-scan FT-IR experiments for kinetic investigations of irreversible reactions of biological samples in solution. In our setup, the fresh sample condition is provided by continuously pumping the protein solution through a miniaturised flow cell with a sampling volume of only a few nanoliters. The rebinding reaction of CO to myoglobin was studied as a model for the catalytic reaction performed by highly complex heme proteins, like e.g. cytochrome c oxidase. The investigation of the mechanism of the irreversible reaction of cytochrome c oxidase with molecular oxygen was pioneered by Gibson and Greenwood when they developed the so-called flow-flash technique [18, 19]. There, a solution of the CO complex of reduced cytochrome c oxidase was mixed with oxygenated buffer in an observation tube. Heme-bound CO was displaced by a short photolysis flash, molecular oxygen binds to the vacant position and is immediately split [19]. Our experimental setup is designed to finally perform a time-resolved flow-flash IR experiment on the oxygen reaction of cytochrome c oxidase, the terminal enzyme of the mitochondrial respiratory chain.

## Experimental section

**Optical setup** All measurements were carried out on an IFS 66v/S FT-IR spectrometer (Bruker Optics, Rheinstetten, Germany) which was controlled by OPUS<sup>TM</sup> software. The collimated infrared light beam exiting the spectrometer through an external port was focused (focal diameter 1.0 mm) onto a microfluidic flow cell by a homemade focusing unit described in Fig. 9a [20]. The micro-fluidic device is positioned within the focus using an xyz-stage. The transmitted light is collected by the second off-axis parabolic mirror (B in Fig. 1) and transferred to a LN<sub>2</sub>-cooled MCT detector. To limit the IR radiation to the range(s) of interest, suitable interference filters (E in Fig. 1; OCLI, Santa Rosa, CA, USA and Spectrogon, Täby, Sweden) were inserted into the beam path. Photodissociation of Mb-CO was initiated with a 10 ns, 540 nm light pulse that is absorbed by the  $\beta$ -band of CO-bound heme of myoglobin. Laser pulses were produced by a tuneable optical parametric oscillator (OPO) system (Opta GmbH, Bensheim, Germany) pumped by the third harmonic of a Nd:YAG laser (Quanta-Ray Lab-150, Spectra Physics, Mountain View, CA, USA) at a repetition rate of 10 Hz. The laser pulse was enlarged by a concave lens (C in Fig. 1), and the diameter was adjusted by an aperture. The laser beam is made colinear to the IR beam via a dichroic mirror (3×3 in. MirrIR plate, Kevley Technologies, Chesterland, OH, USA; item A in Fig. 1) that is highly reflective to the

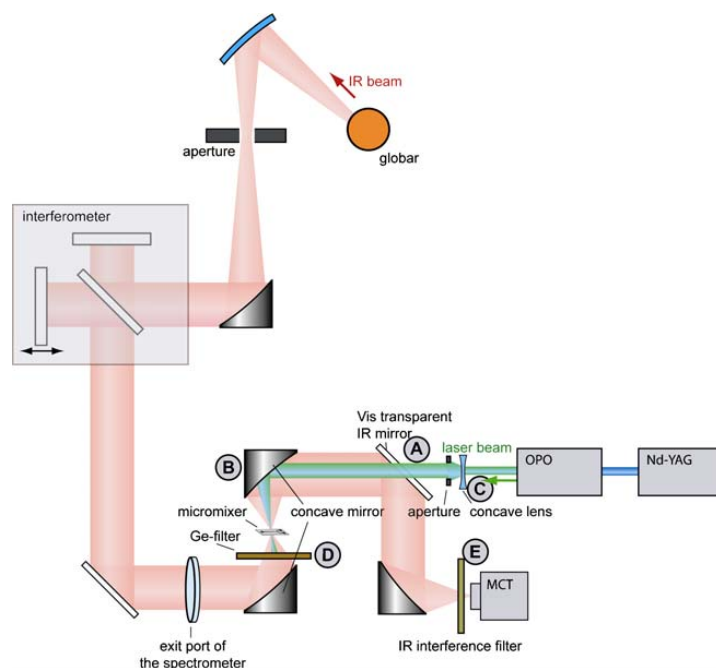


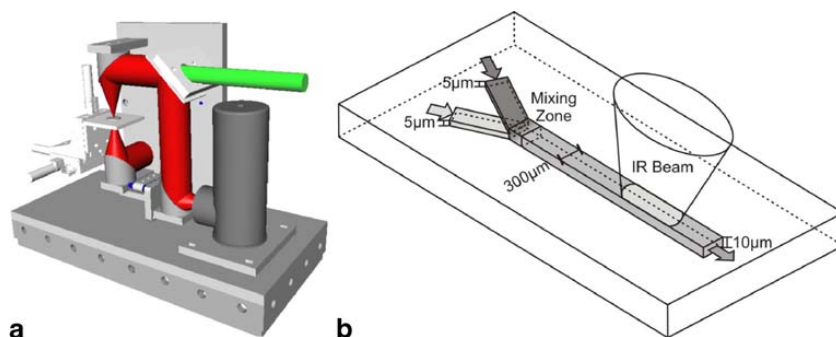
**Fig. 1** Setup of the combination of the flow-flash and the time-resolved step-scan FT-IR experiment using the flow-channel of the micromixer. The black-body emission from the globar source is collimated before passing the interferometer and the exit port of the spectrometer and is focussed on the micromixer by a concave mirror (B). After transmitting the micromixer and reflection via a series of mirrors, the IR beam is fed onto the MCT detector. Before hitting the

detector, the IR beam is filtered by interference filters (E) that limit the free spectral range of detection. The pulsed laser emission from the OPO, driven by the third harmonic of the Nd:YAG laser, is coupled into the path of the focusing optic by the use of a dichroitic mirror that is transmissive to visible light but reflective to IR radiation (A). After photoexcitation of the sample, the intense laser pulse is blocked by a germanium filter (D) from entering the spectrometer

infrared radiation but transmissive to the visible laser light. The laser pulse was focused onto the micro fluidic device by the same parabolic mirror that collects the transmitted infrared radiation (B in Fig. 1). To avoid damage to the spectrometer, the intense laser pulse was blocked by an infrared transparent germanium filter after it passed the micro fluidic device (D in Fig. 1). The whole optical setup was encased by a Plexiglas box that was purged by dry air (dew point  $-70^{\circ}\text{C}$ ).

**Micro mixer/liquid handling** A previously described micro-mixer was used as a flow cell [21]. This microfluidic device consists of micro-channels made of SU8 epoxy resin that are embedded between two 1-mm thick  $\text{CaF}_2$  windows. As illustrated in Fig. 2, the measurement channel itself is  $300\text{ }\mu\text{m}$  wide and  $10\text{ }\mu\text{m}$  deep. With the diameter of  $1,000\text{ }\mu\text{m}$  of the IR beam, a volume of  $3\text{ nl}$  is sampled. Two inlet channels having a height of  $5\text{ }\mu\text{m}$  are superimposed in the measurement channel where diffusion-based mixing

**Fig. 2** **a** Optical setup of the focusing unit with the IR beam shown in red and the laser beam in green. The microfluidic device (**b**) is placed in the focal point of the IR beam. **b** Schematic layout of the micromixer with the dimensions as indicated. The IR beam probes an area of about  $0.3\text{ mm}^2$  of the measuring channel



takes place due to the forced laminar flow. The mixer was pressed onto a special mounting made of stainless steel by two PEEK clamps, and the openings between the  $\text{CaF}_2$  of the mixer and the support are sealed by O-rings. The support connects two inlet and one outlet capillary made of PEEK with the microfluidic device. Solution was pumped through the mixer with the help of two 1-ml Hamilton syringes simultaneously driven by a syringe pump (KDS Model 200, Novodirect, Kehl/Rhein, Germany). Because the micromixer was used as a continuous flow cell in this experiment, both syringes were filled with the same solution. The solution was filtered with 0.2  $\mu\text{m}$  PEEK in-ferrule frits (Upchurch Scientific) to avoid blockage of the measurement cell by solid particles. A flow rate of 8  $\mu\text{L}/\text{min}$  was chosen to ensure that no more than 10% of the sample volume was exchanged during the sampling time of a single step-scan experiment of 2.5 ms. The sample volume was exchanged more than four times from one laser pulse to the next which ensures that fresh sample was in the measurement spot before the next photo-excitation.

**Sample preparation** A 4 mM solution of myoglobin (from horse heart 90%, Sigma) was prepared in 25 mM phosphate buffer at pH 7.0. The solution was placed in an ultrasonic bath for 1 h and centrifuged at  $21,900\times g$  (Hettich, Micro 22R, Tuttlingen, Germany). The supernatant was sterile filtrated (0.2  $\mu\text{m}$  cutoff) to remove insoluble components. The resulting myoglobin solution was chemically reduced by the addition of dithionite (final concentration of 16 mM) under anaerobic conditions at a Schlenk line (five cycles of vacuum and purging by Argon). In the final step, Argon was replaced by carbon monoxide, and the resulting solution was stirred for 30 min, yielding a solution of Mb-CO in the presence of an excess of 1 mM non-bound carbon monoxide. The formed Mb-CO complex is stable in solution but photolabile. For UV/Vis spectroscopy, the sample was diluted by 1:100 with 16 mM  $\text{Na}_2\text{S}_2\text{O}_4$  in water to control the formed Mb-CO state of the protein. Shortly before the time-resolved FT-IR experiments were started, the two gastight Hamilton syringes were filled with sample and connected to the inlets of the microfluidic cell under a stream of argon.

**Time-resolved FT-IR experiments and data analysis** Step-scan spectroscopy was performed with a spectral resolution of 4.5  $\text{cm}^{-1}$  and a time resolution of 5  $\mu\text{s}$ . Other technical details have been previously described [22]. The FT-IR experiments were performed in two different spectral regions, 2,429–1,669  $\text{cm}^{-1}$  and 1,973–0  $\text{cm}^{-1}$ , by using suitable broadband and long-pass interference filters, respectively (E in Fig. 1). Ten time traces were co-added for each mirror position of the interferometer. Each step-scan experiment was repeated four times for the spectral

region 2,429–1,669  $\text{cm}^{-1}$  and 15 times for the region 1,973–0  $\text{cm}^{-1}$ . At the given flow rate of the myoglobin solution, these acquisition conditions resulted in a total sample consumption of 22.4  $\mu\text{L}$  for measuring the first spectral range 2,429–1,669  $\text{cm}^{-1}$ , 469 mirror positions, four averaged full spectral datasets) and 229.5  $\mu\text{L}$  for the second spectral range (1,973–0  $\text{cm}^{-1}$  and 1,024 mirror positions, 15 averaged full spectral datasets). The first 36 spectra of a step-scan experiment, before the laser flash hits the sample, were averaged and used as the reference spectrum to calculate the difference spectra. The resulting difference spectra after photo-activation covered the time range from 5  $\mu\text{s}$  to 2.5 ms. After generation of the matrix of 500 IR difference spectra at the respective time, singular value decomposition (SVD analysis) was applied [13, 23]. Global fit analysis was used to analyse the spectral range of 1,800–1,500  $\text{cm}^{-1}$  as described by Majerus et al. [24].

## Results and discussion

The functionality of proteins is critically dependent on the water content, calling for an aqueous environment. Unlike UV/Vis spectroscopy, the strong absorptivity of water presents a problem in IR spectroscopy of proteins. Thus, an optical path length of a few micrometres is typically used, and hydrated films are often employed to maximise the protein concentration. The challenge of time-resolved IR spectroscopy is to record difference spectra in the presence of the strong background absorption by the aqueous protein solution. IR spectroscopy of proteins in solution suffers from the fact that proteins are difficult to be concentrated to higher than a few millimolar. These considerations set the limits to the design of a microfluidic cell for IR spectroscopy as described in the experimental section. The optical path length of the mixer is 10  $\mu\text{m}$  allowing FT-IR measurements in the spectral regions of water absorptions. The width of the measurement channel of 300  $\mu\text{m}$  compromises adequate transmission of the focussed measuring beam and minimal sample consumption. The sample volume in the measuring spot is exchanged within 23 ms at the chosen flow of 8  $\mu\text{L}\cdot\text{min}^{-1}$ . Thus, sample consumption is minimised to about 250  $\mu\text{L}$  of 4 mM protein solution for the entire time-resolved step-scan experiments.

The microfluidic cell was filled with an anaerobic solution of Mb-CO. Figure 3a shows the single-beam IR spectrum which reflects the spectral emission of the global source limited primarily by the detector's spectral response. The strong absorption bands of water (3,360, 2,130 and 1,641  $\text{cm}^{-1}$ ) overlapped by the weak bands of the protein backbone (amide A at 3,300  $\text{cm}^{-1}$ , amide I at 1,650  $\text{cm}^{-1}$  and amide II at 1,549  $\text{cm}^{-1}$ ) are evident. Small contribu-

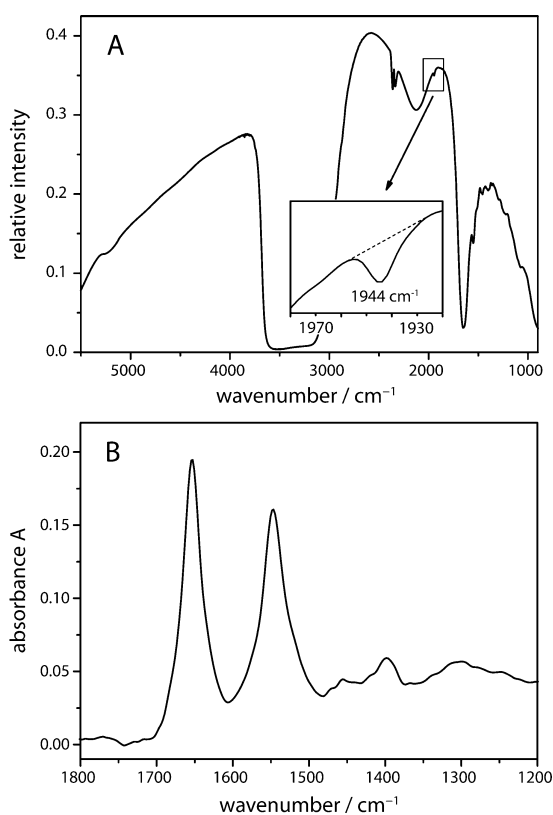


**Fig. 3** **a** Spectral intensity of 4 mM Mb-CO in 25 mM phosphate buffer pH 7.0 measured in the flow channel of the micro mixer. The very weak absorption of the bound CO at 1,943  $\text{cm}^{-1}$  was detectable even in the single beam spectrum (see *inset* for the zoom-out). **b** Absorption spectrum of the aqueous Mb-solution with the IR spectrum of buffer solution as reference. The short path length of the microcell allows for the clear detection of the amide I and amide II absorption bands of the protein backbone

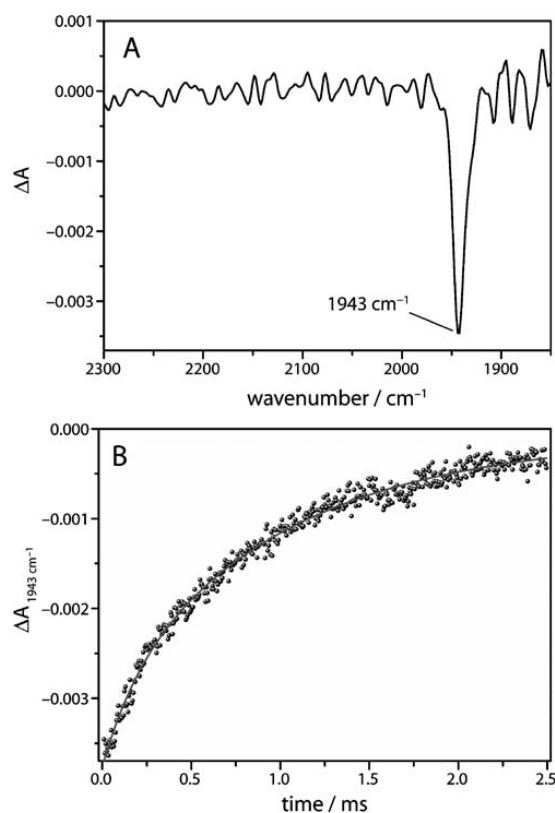


**Fig. 4** **a** Time-resolved step-scan difference spectrum of the photodissociation of CO from myoglobin at  $t=10 \mu\text{s}$  after pulsed laser excitation. The negative band at 1,943  $\text{cm}^{-1}$  corresponds to the stretching vibration of the photolabile CO ligand. **b** Time trace of the C–O stretching vibration at 1,943  $\text{cm}^{-1}$ . The *solid line* is a bi-exponential fit to the data with time constants  $\tau_1=185 \mu\text{s}$  and  $\tau_2=1.0 \text{ ms}$  and relative amplitudes of 21% and 79%, respectively

tions from atmospheric  $\text{CO}_2$  are visible at 2,362 and 2,336  $\text{cm}^{-1}$ . The inset of Fig. 3a depicts the band of the stretching vibration of heme-bound CO (1,943  $\text{cm}^{-1}$ ). The absorption spectrum of the protein (Fig. 3b) is calculated from the single-beam spectrum of the Mb-CO solution and of pure water. The latter was manually corrected for the displaced water, giving a flat baseline between 1,700 and 1,800  $\text{cm}^{-1}$ . The amide I and II absorption bands show maxima at 1,654 and 1,547  $\text{cm}^{-1}$ , respectively, characteristic for the predominant  $\alpha$ -helical structure of myoglobin.

For time-resolved experiments, the photoreaction of Mb-CO was induced by a nanosecond laser pulse to dissociate bound CO from myoglobin. The laser pulse was spatially overlapped with the measuring IR beam (Fig. 1). Absorption changes were recorded with the step-scan technique where the intensity changes at each position of the moving

mirror were recorded over time. To follow the kinetics of CO dissociation, the spectral range was limited by an interference filter to the 2,300–1,850  $\text{cm}^{-1}$  range where the C–O stretching vibration of the ligand absorbs. The filter also blocked stray light of the exciting laser from hitting the detector and prevented spectral aliasing. As an additional benefit, undersampling was applied which effectively reduced the number of sampling positions required for a full interferogram.

As a consequence of the photodissociation of CO, a pronounced negative difference band appears at 1,943  $\text{cm}^{-1}$  (Fig. 4), indicating the loss of absorption in the newly generated state of the protein (deoxy-Mb). Due to the time-resolution of 5  $\mu\text{s}$  of the setup, this band appears instantaneously. At room temperature, the released carbon monoxide is able to leave the protein through exit pathways



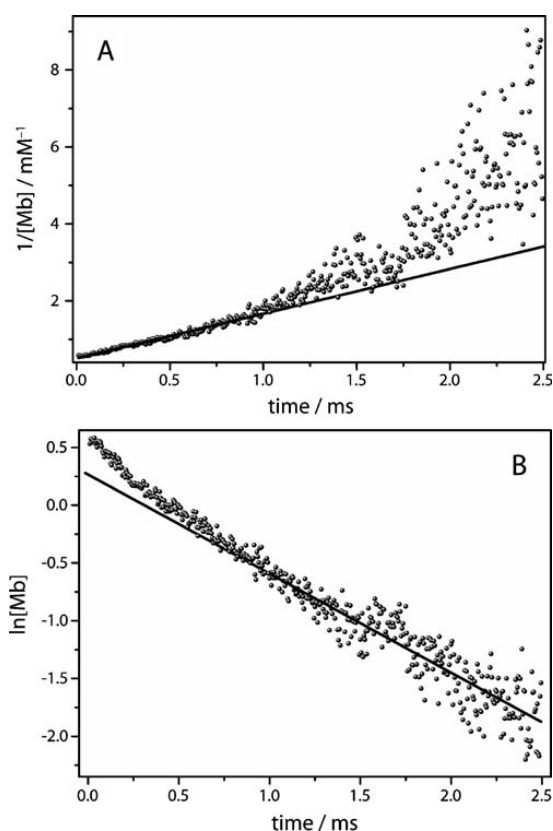


**Fig. 5** Kinetic analysis of the recovery of the C–O stretching vibration. **a** The early kinetics (5  $\mu$ s to 1 ms) exhibit second-order recovery kinetics as shown by the linear behaviour of the plot  $1/[Mb]$  vs time. **b** The later part of the recovery kinetics display first-order kinetics as shown by the linear behaviour of the plot  $\ln\{[Mb]/mM\}$  vs time

that are transiently opened by protein fluctuations [2]. Re-binding of carbon monoxide from the solvent to the heme iron of myoglobin results in the decay of the negative difference band over time (Fig. 4b). The difference band at  $1,943\text{ cm}^{-1}$  corresponds to the  $A_1$ -band of the CO-stretching vibration. A shoulder corresponding to the  $A_0$ -band is expected at  $1,963\text{ cm}^{-1}$ , but this band is difficult to be distinguished from noise [6, 25]. The time trace of the absorption at  $1,943\text{ cm}^{-1}$  is plotted in Fig. 4b. The absence of large fluctuations in the kinetics of the change in absorbance demonstrates the constant optical path length during the experiment. The time trace is fitted using the sum of two exponentials (solid trace) which yields phenomenological time constants of  $185\text{ }\mu\text{s}$  and  $1\text{ ms}$ , respectively. A detailed kinetic analysis revealed that the reaction of the deoxy state of myoglobin to carbonmonoxymyoglobin obeys

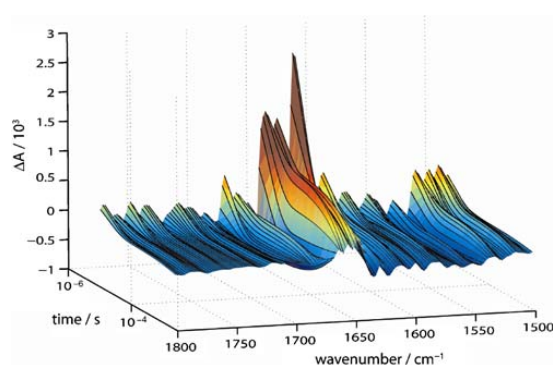


**Fig. 6** Time course of the FT-IR difference spectra of CO recombination to myoglobin. The spectral range is  $1,800\text{--}1,500\text{ cm}^{-1}$  and covers the amide I and amide II vibrational bands. The time range of  $10\text{ }\mu\text{s}$  to  $2.5\text{ ms}$  is plotted on the logarithmic scale. Data shown are those reconstructed from fitting the absorbance changes to a sum of three exponentials (see text for details on the global fitting analysis)

(pseudo-) first-order kinetics, if the concentration of carbon monoxide does not change significantly during reaction [25]. Thus, the kinetics of the reaction are described by simple integration of the differential rate law of a first-order reaction which results in:

$$\ln[Mb] = k_1 \times t + c$$

where  $[Mb]$  is the concentration of the decaying deoxy state of myoglobin,  $k_1$  the first-order rate constant,  $t$  the reaction time and  $c$  a constant that depends on the initial concentration. A plot of  $\ln[Mb]$  vs  $t$  should result in a straight line if

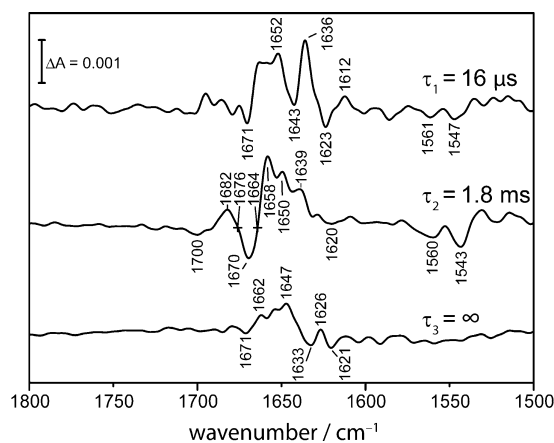


**Fig. 7** Species-associated difference spectra (SADS) as a result of the global fitting to the step-scan difference spectra of CO-poised myoglobin. Three intermediate spectra were identified with time constants of  $\tau_1=16\text{ }\mu\text{s}$ ,  $\tau_2=1.8\text{ ms}$  and  $\tau_3=\infty$  with the latter not decaying during the recording range of  $2.5\text{ ms}$ . The calculation of the spectra from the raw data is described in the text



the assumption of a first-order reaction is valid. For the case where the concentration of carbon monoxide affects the reaction rate, the integrated rate law of the reaction corresponds to

$$\frac{1}{[\text{Mb}]_t} - \frac{1}{[\text{Mb}]_0} = k_2 \times t$$

with  $k_2$  as the second-order rate constant and  $[\text{Mb}]_0$  as the initial concentration of deoxy myoglobin. The temporal change of  $[\text{Mb}]_t$  was derived from the absorption difference at  $1,943 \text{ cm}^{-1}$  using the extinction coefficient  $\varepsilon_{\text{CO}} = 1.920 \text{ M}^{-1} \text{ cm}^{-1}$  as described by Plunkett et al. [7]. The plot of  $1/[\text{Mb}]$  vs.  $t$  yields a linear relationship, if the reaction follows a second-order rate law. In agreement with Dixon et al. [25], the first part of the reaction ( $t < 1 \text{ ms}$ ) exhibits second-order kinetics that depend on the concentrations of both the unbound myoglobin and the free carbon monoxide (Fig. 5a). The initial concentration of photolysed CO significantly exceeds the concentration of dissolved CO in the buffer solution because of the high concentration of

myoglobin used in the experiment (Fig. 5b). After the concentration of free carbon monoxide is reduced to the level of dissolved carbon monoxide ( $\sim 1 \text{ mM}$  at  $293 \text{ K}$ ), the kinetic behaviour changes to pseudo first-order behaviour (Fig. 5b). In our experiment, this takes place for rebinding kinetics at  $t > 1 \text{ ms}$ .

In a second set of step-scan experiments, the spectral range of  $1,800\text{--}1,500 \text{ cm}^{-1}$  was studied where the structural response of the protein is examined after CO dissociation. Because of the smaller magnitude of the difference bands as compared to the C-O stretching vibration band (*vide supra*), it was necessary to average more experiments for a sufficient signal-to-noise ratio. To further reduce the noise level, SVD analysis was applied, and the 3D data set was reconstructed using the three most significant components (see Fig. 6 for a 3D representation) [22]. It is evident that the vibrational changes across the spectral region of  $1,800\text{--}1,500 \text{ cm}^{-1}$  are much more complex than those reflected in the CO kinetics at  $1,943 \text{ cm}^{-1}$  (Fig. 4b). Therefore, global kinetic analysis was applied which identified three species-

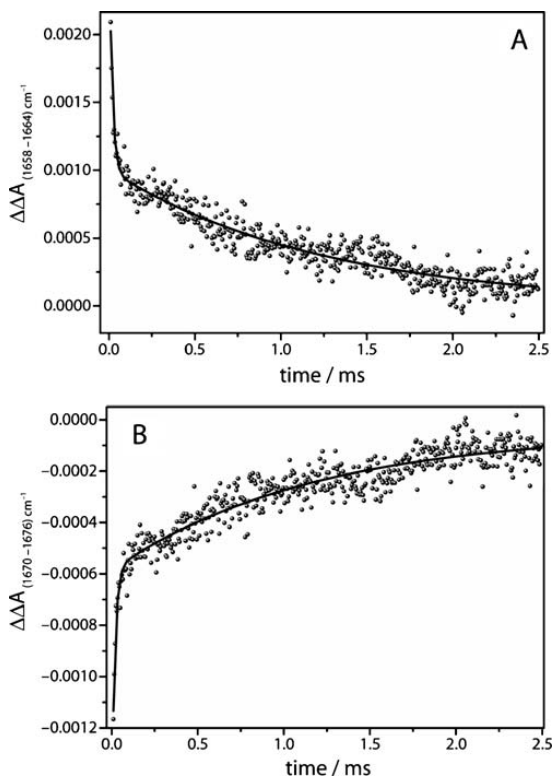


**Fig. 8** Time trace of two difference bands in the amide I spectral region **a** at  $1,658\text{--}1,664 \text{ cm}^{-1}$ , **b** at  $1,670\text{--}1,676 \text{ cm}^{-1}$ . Solid line Bi-exponential fit to the data. The slow components agree well to the slow component of the C-O stretching band kinetics (see Fig. 5b)

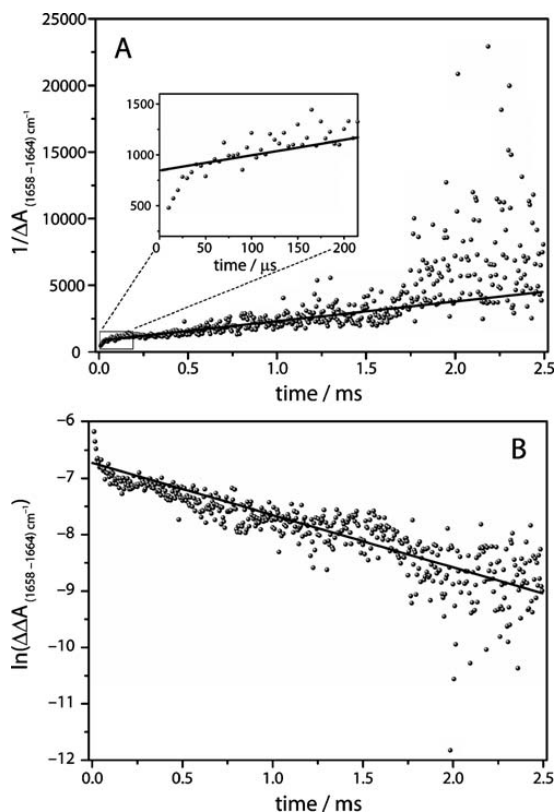


**Fig. 9** Kinetic analysis of the decay of the difference band  $1,658\text{--}1,664 \text{ cm}^{-1}$ . **a** The plot of  $1/\Delta A$  vs time exhibits linear behaviour in the time range of  $15 \mu\text{s}$  to  $1 \text{ ms}$ . **b** The plot of  $\ln(\Delta A)$  ( $1,658\text{--}1,664 \text{ cm}^{-1}$ ) shows linear behaviour between  $1 \text{ ms}$  and  $2.5 \text{ ms}$

associated difference spectra (SADS): a fast decaying component ( $\tau_1=16\ \mu\text{s}$ ) which is followed by a second component ( $\tau_2=1.8\ \text{ms}$ ). The final SADS ( $\tau_3=\infty$ ) corresponds to the difference spectrum at the end of data recording because rebinding of CO from the bulk has not reached completion.

The difference bands shown in the spectra of Fig. 7 were assigned to specific structural changes mainly in secondary structure with weak contributions from amino acid side chain vibrations [7, 8, 26, 27]. The differential shaped feature at  $1,701\ (-)$  and  $1,683\ \text{cm}^{-1}\ (+)$  represents a shift of the C–O stretching band of the terminal –COOH of the heme-propionic acid [8, 9]. The difference bands in the amide I range are indicative for changes in the structure of the protein backbone. The bleach at  $1,669\ \text{cm}^{-1}\ (-)$  was assigned to a change in a turn structure, the band at  $1,658\ \text{cm}^{-1}\ (+)$  to a shift of an  $\alpha$ -helix, the band at  $1,650\ \text{cm}^{-1}\ (+)$  to an unordered structure and the features at  $1,637\ (+)$  and  $1,624\ \text{cm}^{-1}\ (-)$  to  $\beta$ -type turn structures [28]. The negative bands at  $1,561$  and  $1,543\ \text{cm}^{-1}$  are related to the structural changes in the amide II region, corresponding to the aforementioned changes in  $\beta$ -turn and  $\alpha$ -helical structures [28].

The kinetics of two distinct difference absorption bands in the range of the amide I vibrations are plotted exemplarily at  $1,658\ \text{cm}^{-1}$  in Fig. 8a and at  $1,670\ \text{cm}^{-1}$  in Fig. 8b. To account for baseline drifts, the difference to nearby isosbestic points ( $1,664\ \text{cm}^{-1}$  in Fig. 8a and  $1,676\ \text{cm}^{-1}$  in Fig. 8b) were taken. Analogous to the rebinding kinetics of carbon monoxide to myoglobin, the kinetics of the protein structural changes do not exhibit simple mono-exponential behaviour. Again, a bi-exponential fit is used to describe the decay of these bands. While the fast components of the fit are too fast to be correlated to the CO-recombination process ( $\tau=17\ \mu\text{s}$ ), the slower components exhibit a time constant of  $1.2\ \text{ms}$  that corresponds well to the slow time constant of CO recombination (see Fig. 4b). The kinetics of secondary structure changes, as monitored by the changes of amide I difference bands, should tally to the rebinding kinetics of CO, if the binding of CO to the heme is the rate-limiting step in the formation of Mb-CO from deoxy-Mb and if the relaxed deoxy-state is already formed at the start of the measurement due to the fast relaxation of the ligated conformation of myoglobin after photolysis. Although the kinetics of the band at  $1,658\ \text{cm}^{-1}$  are noisier than those determined at  $1,943\ \text{cm}^{-1}$  (Fig. 5), it is evident that the fast kinetics exhibit linear behaviour in the time range up to  $1\ \text{ms}$ . This contrasts to later times ( $>1\ \text{ms}$ ) where a clear deviation from a linear fit is observed (see Fig. 9a). The early secondary structure changes exhibit second-order kinetics as it was observed for the CO rebinding kinetics. Plotting the reaction time of  $1$  to  $2.5\ \text{ms}$  against the natural

logarithm of the absorption reveals the first-order behaviour for later timescales (Fig. 9b).

A detailed view on the early time range ( $5$  to  $30\ \mu\text{s}$  in Fig. 9a) shows that the kinetics exhibit a significant deviation from the linear behaviour demonstrating that these structural changes are not correlated to the CO rebinding kinetics. A possible interpretation of this behaviour is an ongoing relaxation of the ligated conformation of myoglobin to deoxy-Mb after photolysis. Step-scan FT-IR experiments on myoglobin from horse-heart in  $\text{D}_2\text{O}$  performed by Plunkett et al. agree with our data [7]. These authors found that the decay of the amide I difference band exhibited faster second-order kinetics than the recovery of CO. In contrast, studies on sperm-whale myoglobin in  $\text{D}_2\text{O}$  using a tuneable CW lead salt diode infrared probe laser, concluded that protein relaxation after photolysis of CO from Mb-CO is complete after  $100\ \text{ns}$  [8]. The variation in the experimental results may be attributed to the different behaviour of myoglobin from different organism (horse heart vs. sperm whale) and to the influence of the solvent isotope effect ( $\text{H}_2\text{O}$  vs.  $\text{D}_2\text{O}$ ).

## Conclusion

It is demonstrated that the combination of microfluidics with time-resolved step-scan FT-IR spectroscopy can be successfully applied to studies of the reaction kinetics of proteins in solution. As a proof of concept, we studied the kinetics after CO photodissociation from myoglobin. Rebinding of CO from solution to the heme-iron was monitored together with the subsequent protein structural changes. The major technological advance of this novel spectroscopic approach lies in the fact that it allows for step-scan spectroscopy on non-cyclic reactions of proteins in aqueous solution. Previous step-scan studies were commonly performed on hydrated films to reduce the absorption of water in the IR range. We minimised the sample consumption by using a microfluidic flow cell which enables to record multiple co-additions to improve the signal-to-noise ratio while keeping the sample consumption at realistic levels of milligram amounts of protein for a full step-scan experiment. The noise level is reduced by using a dedicated focusing unit which optimises optical throughput of our microfluidic setup.

An additional benefit lies in the opportunity to mix two solutions immediately before excitation. This flow-flash approach has provided valuable insights into the mechanism of the oxygen splitting reaction of cytochrome c oxidase by monitoring the visible absorption of the heme and copper cofactors [18, 19]. Up to now, the short optical path length of  $\sim 10\ \mu\text{m}$  mandatory for mid-IR spectroscopy of aqueous solutions has prevented the application of the

classical flow-flash technique to time-resolved IR spectroscopy. As mixing experiments have been successfully performed with the micromixer [21, 29], an oxygen-containing solution will be rapidly mixed with the reduced and CO-bound cytochrome c oxidase, and the irreversible reaction of the enzyme with oxygen is initiated by photodissociation of the carbon monoxide complex. Temporal synchronisation of the flow, photolysis and mirror movement of the interferometer was achieved as demonstrated by the experiments shown here. Thus, the experimental prerequisites are now implemented to perform a flow-flash experiment with FT-IR detection on cytochrome c oxidase in order to study the oxygen-splitting reaction of this central membrane complex of the respiratory chain. These experiments are currently under way.

**Acknowledgements** Financial support for the German part of this research was provided by the Volkswagen Foundation (“Intra- und intermolekulare Elektronenübertragung”). Support for the Austrian part from Carinthian Tech Research AG and the COMET Competence Centre Programme of the Austrian Government is gratefully acknowledged.

**Open Access** This article is distributed under the terms of the Creative Commons Attribution Noncommercial License which permits any noncommercial use, distribution, and reproduction in any medium, provided the original author(s) and source are credited.

## References

- Frauenfelder H, McMahon BH, Fenimore PW (2003) *Proc Natl Acad Sci U S A* 100:8615–8617
- Ostermann A, Waschipky R, Parak FG, Nienhaus GU (2000) *Nature* 404:205–208
- Schotte F, Lim M, Jackson TA, Smimov AV, Soman J, Olson JS, Phillips GN Jr, Wulff M, Anfinsen PA (2003) *Science* 300:1944–1947
- Frauenfelder H, Alberding NA, Ansari A, Braunstein D, Cowen BR, Hong MK, Iben IET, Johnson JB, Luck S, Marden MC, Mourant JR, Ormos P, Reinisch L, Scholl R, Schulte A, Shyamsunder E, Sorensen LB, Steinbach PJ, Xie AH, Young RD, Yue KT (1990) *J Phys Chem* 94:1024–1037
- Gibson QH, Regan R, Elber R, Olson JS, Carver TE (1992) *J Biol Chem* 267:22022–22034
- Rödig C, Siebert F (1995) Rebinding and concomitant protein relaxation of photodissociated CO-myoglobin studied by time-resolved FTIR spectroscopy. Dyer, R. B., Martinez, M. D., Shreve, A., and Woodruff, W. A. Proceedings of the 7th International Conference on Time-Resolved Vibrational Spectroscopy, 291–292. 1997. Los Alamos National laboratory, Los Alamos, New Mexico. Ref Type: Conference Proceeding
- Plunkett SE, Chao JL, Tague TJ, Palmer RA (1995) *Appl Spectrosc* 49:702–708
- Causgrove TP, Dyer RB (1993) *Biochemistry* 32:11985–11991
- Kuriyan J, Wilz S, Karplus M, Petsko GA (1986) *J Mol Biol* 192:133–154
- Olson JS, Phillips GN Jr (1996) *J Biol Chem* 271:17593–17596
- Schmidt M, Nienhaus K, Pahl R, Krasselt A, Anderson S, Parak F, Nienhaus GU, Srajer V (2005) *Proc Natl Acad Sci U S A* 102:11704–11709
- Hu X, Frei H, Spiro TG (1996) *Biochemistry* 35:13001–13005
- Heitbrink D, Sigurdson H, Bolwien C, Brzezinski P, Heberle J (2002) *Biophys J* 82:1–10
- Uhmman W, Becker A, Taran C, Siebert F (1991) *Appl Spectrosc* 45:390–397
- Zscherp C, Heberle J (1997) *J Phys Chem B* 101:10542–10547
- Rödig C, Siebert F (1999) *Vib Spectrosc* 19:271–276
- Rammelsberg R, Boulas S, Chorongiewski H, Gerwert K (1999) *Vib Spectrosc* 19:143–149
- Gibson QH, Greenwood C (1963) *Biochem J* 86:541–554
- Greenwood C, Gibson QH (1967) *J Biol Chem* 242:1782–1787
- Hinsmann P, Haberkorn M, Frank J, Svasek P, Harasek M, Lendl B (2001) *Appl Spectrosc* 55:241–251
- Kaun N, Kulka S, Frank J, Schade U, Vellekoop MJ, Harasek M, Lendl B (2006) *Analyst* 131:489–494
- Heberle J, Zscherp C (1996) *Appl Spectrosc* 50:588–596
- Shrager RI, Hendler RW (1998) *J Biochem Biophys Methods* 36:157–173
- Majerus T, Kottke T, Laan W, Hellingwerf K, Heberle J (2007) *ChemPhysChem* 8:1787–1789
- Dixon AJ, Glyn P, Healy MA, Hodges PM, Jenkins T, Poliakov M, Turner JJ (1988) *Spectrochim Acta A* 44:1309–1314
- Schlereth DD, Mantle W (1992) *Biochemistry* 31:7494–7502
- Dong A, Huang P, Caughey B, Caughey WS (1995) *Arch Biochem Biophys* 316:893–898
- Krimm S, Bandekar J (1986) *Adv Protein Chem* 38:181–364
- Svasek P, Svasek E, Lendl B, Vellekoop M (2004) *Sens Actuators A* 115:591–599



## Publication VIII

C. Wagner, W. Buchegger, M.J. Vellekoop, M. Kraft, and B. Lendl,  
Analytical and Bioanalytical Chemistry 400, 8, 2487-2497 (2011),  
DOI: 10.1007/s00216-010-4643-2.



# Time-resolved mid-IR spectroscopy of (bio)chemical reactions in solution utilizing a new generation of continuous-flow micro-mixers

Christoph Wagner · Wolfgang Buchegger ·  
Michael Vellekoop · Martin Kraft · Bernhard Lendl

Received: 10 November 2010 / Revised: 9 December 2010 / Accepted: 21 December 2010  
© Springer-Verlag 2011

**Abstract** A specially designed micro-mixer made of silicon, calcium fluoride, and silicone with an optical transmission path of 8  $\mu\text{m}$  has been used for mid-IR spectroscopy monitoring of mixing-induced chemical reactions in the low millisecond time regime. The basic principle of the proposed continuous-flow technique is to mix two liquids introduced in two times two alternatingly stacked layers through diffusion at the entrance of a 200  $\mu\text{m}$  wide, 1 cm long micro-fluidic channel also serving as measurement area. By using this special, dedicated arrangement, diffusion lengths and hence the mixing times can be significantly shortened and the overall performance improved in comparison to previous systems and alternative methods. Measurements were carried out in transmission mode using an Fourier transform infrared (FTIR) microscope, recording spectra with spot sizes of  $180 \times$

100  $\mu\text{m}^2$  each at defined spots along this channel. Each of these spots corresponds to a specific reaction time: moving the measurement spot towards the entry yields shorter reaction times, moving it towards the channel's end gives longer reaction times. This principle is generic in nature and provides a solution for accurate, chemically induced triggering of reactions requiring the mixing of two liquid reagents or reagent solutions. A typical experiment thus yields up to 85 time-coded data points, covering a time span from 1 to 80 ms at a total reagent consumption of only about 125  $\mu\text{L}$ . Using the fast neutralization reaction of acetic acid with sodium hydroxide as a model, the time required for 90% mixing was determined to be around 4 ms. Additionally, first experiments on ubiquitin changing its secondary structure from native to "A-state" were carried out, illustrating the potential for time-resolved measurements of proteins in aqueous solutions.

Published in the special issue *Analytical Sciences in Austria* with Guest Editors G. Allmaier, W. Buchberger, and K. Francesconi

C. Wagner · B. Lendl (✉)  
Institute of Chemical Technologies and Analytics,  
Vienna University of Technology,  
Getreidemarkt 9/164AC,  
1060 Vienna, Austria  
e-mail: [bernhard.lendl@tuwien.ac.at](mailto:bernhard.lendl@tuwien.ac.at)  
URL: <http://www.cta.tuwien.ac.at/cavs>

W. Buchegger · M. Vellekoop  
Institute of Sensor and Actuator Systems,  
Vienna University of Technology,  
Gusshausstraße 27-29/E366,  
1040 Vienna, Austria

M. Kraft  
Carinthian Tech Research AG,  
Europastraße 4/1,  
9524 Villach, Austria

**Keywords** IR spectroscopy · Microfluidics · Kinetics

## Introduction

*Time-resolved IR measurements* Today, infrared spectroscopy knows two well-established techniques with which to follow chemical reactions over time. The first, *rapid scanning*, operates on a time scale in the low millisecond range. Here, the moving mirror of the infrared spectrometer is moved rapidly and as many interferograms as possible are recorded and stored separately, with the Fourier transformations calculated after the end of the experiment. In theory, state-of-the-art rapid-scan spectrometers with rotating mirrors can thus measure at time resolutions of down to 1 ms [1]. Recent efforts have been made to minimize the moving parts in classical IR spectrometers in order to

further increase scanning rates [2,3]. Chase and Rabolt developed an alternative method that decouples the temporal resolution from the speed of the moving mirror. Their so-called planar array infrared spectrograph uses a grating to disperse the infrared light over a focal plane array (FPA) detector. Initially, this instrument covered only a spectral range from 3,400–2,000  $\text{cm}^{-1}$  [4], but with advances in FPA technology also the IR fingerprint region is now accessible [5]. Still, rapid-scanning approaches can only be applied to reactions with sufficient signal-to-noise ratios requiring only little averaging, or the time advantage will be lost. Applying a Manning Applied Technology URS-FTIR spectrometer coupled to a modified Olis stopped-flow system, time resolutions of 5 ms have been successfully realized for monitoring chemical reactions in  $\text{CH}_2\text{Cl}_2$  [6]. Kötting et al. averaged four interferograms recorded during one complete mirror movement of a Bruker IFS 66v/s to follow drug protein interactions at a time resolution of around 100 ms using a static sample [7].

For further increased temporal resolution, the method of choice is usually *step-scanning* [8]. There, the time resolution is no longer dependent on the speed of the moving mirror, but only on the detector's rise time and signal digitization. With this technique, temporal resolutions on the order of 10 ns have been achieved [9] and with improvements in technology even higher time resolutions may be possible in the future. Yet, in practice the step-scanning approach suffers from some major drawbacks: the reaction under investigation needs to be repeatable many times to record all data points required to generate time-resolved interferograms, and only chemical reactions that can be triggered by an external stimulus can be studied, due to the need to start the reaction over and over again with very precise timing to ensure an accurate starting point. Together with the often limited amount of available sample, this often limits step-scanning techniques to cyclic reactions where the same sample can be excited repeatedly, resulting in little sample consumption—a necessary pre-condition for studying most biochemical reactions. Measuring non-cyclic reactions is significantly more complex. Rammelsberg et al. developed a system to monitor non-cyclic reactions of biological reactions in thin films [10]. More recently, a technique using a micro-fluidic cell was developed for studying non-cyclic reactions in solutions with step scan technology at low sample consumption [11], facilitating the measurement of biological systems in their natural environments. Another approach to facilitate step-scanning measurements of non-cyclic reactions uses caged compounds, which can be released by a laser flash to start the chemical reaction under investigation [12].

*Micro-fluidic mixers* Despite the range of optical, electrical, thermal and other triggering methods described in the

literature, the most convenient and simplest way to initiate a reaction would still be to simply mix the chemicals involved in the reaction. In UV/VIS spectroscopy, this can be easily achieved using a stopped-flow apparatus. In IR spectroscopy, however, certain limitations need to be considered, especially the intense absorptions of water in the mid-infrared range, limiting the maximum transmission pathlength to 8–50  $\mu\text{m}$ . Of particular importance for the study of biological molecules are the amide I and II bands, as they reflect the structural composition of proteins [13]. Thus, the overlap of the amide I band with the deformation vibration of water at 1,645  $\text{cm}^{-1}$  is a significant problem, making it necessary to either reduce the optical pathlengths to 8  $\mu\text{m}$  or smaller, or work in  $\text{D}_2\text{O}$ , which enables transmission pathlengths of 30  $\mu\text{m}$  for measurements in the region of the amide I band. In any case, the tradeoff of this technique is a lower sensitivity caused by the smaller pathlength, a fact that can only be partially compensated for by using solutions with higher concentrations.

Given these dimensions, stopped-flow measurements are notoriously difficult, mainly due to the high pressures required for pumping liquids through a narrow measurement cell, and then stop them abruptly. An alternative would be the continuous-flow mode, where the reactants under investigation are constantly flowing through the mixing channel. This is of high practical interest also since the reaction evolves further with the observation window being moved downstream from the point of mixing [14]. Still, this approach requires fast mixing times to ensure a precise starting point of the reaction. As the narrow channels allow only laminar flow conditions, efficient and fast mixing cannot be easily achieved the standard way, i.e., through creating turbulences in the flow [15], an obstacle that can be circumvented in two ways.

The first and more complex way is to design an active mixer element that utilizes external forces to perturb the laminar flow. Ahmed et al. demonstrated a single-bubble-based acoustic streaming mixer where an air bubble trapped in a horseshoe-like structure is excited at its resonance frequency by a piezo transducer [16]. In other approaches, an oscillating micro-cantilever implemented in a micro-mixing channel by Williams et al. showed a significant impact on the laminar flow [17], as did ultrasonic transducers [18], surface acoustic wave elements [19], and magneto-hydrodynamic actuators inducing body forces in the fluid [20].

The second fundamental method for inducing mixing in strictly laminar flow regimes is through diffusion. Since the mixing time in such a device is proportional to the square of the diffusion lengths in the channel ( $t_{\text{mix}} \sim l_D^2$ ), the most promising approach to shorten mixing times is to reduce these distances to a minimum. In the past, a few different approaches have been developed to ensure fast mixing

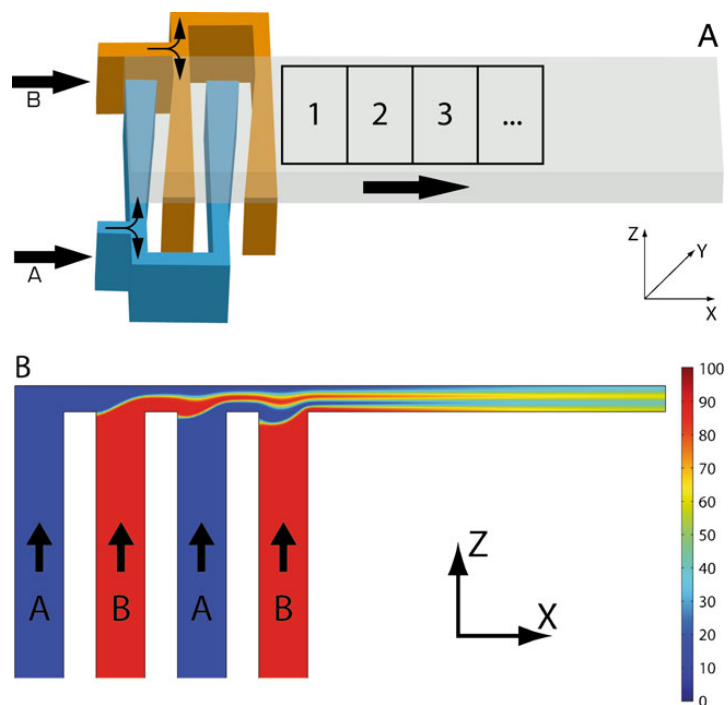


times. The split and recombine (SAR) technique splits the liquid up horizontally and recombines it vertically (or vice versa) to reduce the diffusion lengths [21,22]. In chaotic advection mixers, static elements in the mixing channel induce steady chaotic flows and thereby reduce the diffusion lengths [23]. Finally, a third way to passively mix liquids is laminar diffusion mixing, where laminar flow sheets are formed in the mixing channel [24]. One such micro-mixer, designed by Manz et al. [25], was used to investigate the folding of ubiquitin via both infrared spectroscopy [26] and NMR spectroscopy [27]. Also, a special embodiment of laminar flow mixers where the analyte is pumped through a narrow nozzle and sandwiched between two thicker reagent streams [28], often referred to as hydrodynamic focusing, was successfully used by Hertzog et al. to study protein folding by Förster resonance energy-transfer measurements [29].

Still, given various limitations most of these designs are not suitable for time-resolved IR measurements. Most active mixer designs require, e.g., electrodes or transducers in or over the measurement channel, thus obstructing the infrared measurement beam. The same applies to passive mixers based on SAR or built-in elements in the mixing channel; even if the materials used were transparent in the mid-infrared region, they would still distort the transmitted

beam. To ultimately combine time resolutions achievable with a stopped-flow-rapid-scanning approach with low channel heights and thus transmission pathlengths enabling mid-infrared detection in aqueous systems in one device, several different continuous-flow micro-mixers have been designed and tested over the years. Hinsmann et al. proposed a “spaghetti mixer” design where two feeding channels produce an alternating sequence of 50 streams with a thickness of 20  $\mu\text{m}$  each [30], facilitating mixing times of around 100 ms. In a later design, two fluid layers with a thickness of 5  $\mu\text{m}$  were superimposed horizontally, resulting in shorter mixing times [14,31]. Kaufmann et al. added a third fluid layer and investigated the  $\beta$ -sheet  $\rightarrow$   $\alpha$ -helix transition of  $\beta$ -lactoglobulin [32], with the protein fed into the middle channel while buffer was added to the top and bottom layers. Yet, one critical drawback of this design is that the cross section of the mixing channel exhibits severe inhomogeneities in mixing quality, in particular at the side of the fluid inlets. To overcome this obstacle affecting the actual analytical performance of the system, we used a novel four-layered micro-mixer with wedge-shaped inlet channels [33,34] (Fig. 1) specially designed to overcome the inhomogeneous concentration distribution of the chemicals over the width of the mixing channel observed by Kaufmann et al. [32].

**Fig. 1** **a** Basic measurement principle for time-resolved measurements in a laminar continuous-flow micro-mixer, shown for a device with hydrodynamically optimized wedge-shaped inlet channels. Measurements are carried out along the mixing channel in consecutive order (positions 1, 2, 3, etc.) by moving the mixer under the microscope. Measuring further downstream from the point of mixing gives longer reaction times. **b** CFD simulation results of inlet streams and diffusive mixing in a side view of the micro-mixer: each inlet channel forms one fluid layer in the mixing channel, thus minimizing the diffusion lengths and enable faster mixing



As can be seen in Fig. 1, the measurements may take place anywhere along the mixer channel, starting right after the last inlet channel. The actual reaction time can be calculated by dividing the cross section area of the mixer by the flow rate inside the channel and multiplying it with the distance from the chosen zero-point. The corresponding time resolution of the experiment is determined mainly by two factors: the *spot size* of the microscope and the *flow rate* of the liquids in the mixing channel. Generally, the smaller the spot size of the IR beam and the faster the flow rate, the better the time resolution. The spot size can be easily controlled by the aperture of a state-of-the-art IR microscope, but only to the point where the signal-to-noise ratio becomes a limiting factor. The flow rate of the liquids is limited by the mechanical designs of the mixer holder and the mixer, by the pumps used and by the permissible reagent consumption. With the system reported here, a maximum flow rate of 30  $\mu\text{L}/\text{min}$  could be achieved for aqueous solutions having roughly the same viscosity as water.

**System characterization** To characterize the system's time behavior, we first evaluated the mixer performance with a fast acid–base reaction [35,36] mixing acetic acid with sodium hydroxide. To characterize the mixing performance across the width of the mixing channel, a  $64 \times 64$  pixel focal plane array detector was then used to monitor the formation of HDO from  $\text{D}_2\text{O}$  and  $\text{H}_2\text{O}$ , allowing to directly compare mixers equipped with hydrodynamically optimized wedge-shaped inlet channels with those with straight, parallel standard inlet channels. To directly compare the mixing times and performance with our previous two-layered mixer, we revisited the formaldehyde–sulfite clock reaction used by Kaun et al. [37], and finally demonstrated the feasibility of our new mixer for measuring biochemical reactions by mixing ubiquitin with methanol and following the resulting changes in the protein's secondary structure.

## Experimental

### Mixing device

The micro-mixer used in this work [33,34] was specially designed to meet the requirements for the measurements of dissolved proteins in aqueous solutions in the mid-infrared, using IR-transparent materials like silicon and  $\text{CaF}_2$ , a mixing channel height of 8  $\mu\text{m}$  and a channel width of 200  $\mu\text{m}$ . The latter follows geometric considerations regarding the mixing quality, as do the wedge-structure inlet channels shown in Fig. 1. Widening from 10 to 22  $\mu\text{m}$ , they render a homogeneous concentration distribu-

tion possible, a design that was determined by a series of computational fluid dynamic (CFD) simulations. An additional special feature is that, to further minimize the effective diffusion lengths, the top and bottom layers are thinner than the middle layers sandwiched in between. This is achieved by carefully designed, slight pressure loss differences of the different distribution channels between the split and the wedge-shaped outlets. These distribution channels simultaneously split the two liquids entering the mixing chip through two inlet holes at the bottom of the chip into the four streams forming the four layers.

The micro-fluidic devices were produced using a series of standard semiconductor processing steps, including photo structuring, deep reactive ion etching and chemical etch steps, and special procedures like cold bonding of the  $\text{CaF}_2$  [34], making the micro-mixers potentially suitable for production in larger quantities. As a special measure, a metal layer with a 180  $\mu\text{m}$  wide slit was deposited on the  $\text{CaF}_2$  window, serving as an integrated optical aperture. For measuring, the assembled mixers were mounted in stainless steel supports, using a typically 200  $\mu\text{m}$  thick silicone foil as sealing layer. These supports were specially designed to keep the dead volume of the liquid handling system as low as possible to minimize sample consumption, and feature integrated titanium frits with a pore size of 0.2  $\mu\text{m}$  located immediately before the support-mixer interface. The design thus effectively prevents any contamination of the mixer with small particles that could affect the desired formation of undisturbed laminar flow sheets.

### Reagents

Formaldehyde (37 wt.% aqueous solution), heavy water ( $\text{D}_2\text{O}$ , 99.8%), methanol ( $\geq 99.9\%$ ), and ubiquitin (from bovine erythrocytes, 98%) were purchased from Sigma-Aldrich (Schnelldorf, Germany). Sodium sulfite and sodium hydroxide, both of analytical grade, were purchased from Merck (Darmstadt, Germany). Acetic acid (99.8 wt. %) was purchased from Riedel-de Haen.

All solutions used for the experiments were made with deionized water additionally filtered through a 0.2  $\mu\text{m}$  pore size filter to remove any particle contamination that might get stuck in the micro-mixer, as this could lead to a reduction of the mixing quality.

### Infrared measurements

All experiments were carried out in transmission mode on a Hyperion 3000 microscope with a 15-fold Cassegrain objective, attached to a Tensor 37 spectrometer (Bruker Optics, Ettlingen, Germany), with the micro-mixer in its support mounted onto the automated XY stage of the microscope. The measurements were conducted with a

150×150  $\mu\text{m}^2$  single-element MCT detector and a 64×64 pixel FPA detector with a total element size of 2.5×2.5  $\text{mm}^2$ , respectively. For single-element measurements, the rectangular aperture of the microscope was closed to 100  $\mu\text{m}$  in width; the height was limited to 180  $\mu\text{m}$  by the aperture of the mixer. The first measurement spot along the mixing channel was placed 50  $\mu\text{m}$  downstream from the last inlet channel, so that no light could pass through this channel and affect the measurement; the further measurement spots were then each spaced 100  $\mu\text{m}$  apart from the previous. The spectra were recorded at 4  $\text{cm}^{-1}$  spectral resolution, averaging 32 scans for each measurement spot. When using the FPA detector, the aperture was left open, and only one image located in the upper left corner of the mixing channel, with the first pixels overlapping with the last inlet channel on the left side and the aperture of the mixer at the top to accurately determine the beginning of the mixing channel, was recorded for each experiment. Here, 128 scans were averaged at a spectral resolution of 4  $\text{cm}^{-1}$ , and the resulting image data processed with Cytospec ([www.cytospec.com](http://www.cytospec.com)).

Each time-resolved measurement consisted of two measurement runs. Firstly, background reference spectra were acquired for each measurement position of the micro-mixer, through which deionized water was being pumped at the respective flow rate. Afterwards, the sample solutions were pumped through the mixer at the same speed, and measurements at the same spots were taken. This measure was taken to account for slight differences in the absorption characteristics of the micro-mixer filled with sample at different measurement spots. The absorbance spectra were then calculated manually using the OPUS software.

The two reagents used in each experiment were pumped through the mixer by two 500  $\mu\text{l}$  Hamilton glass syringes driven by a kDS100 syringe pump (KD Scientific Inc., MA, USA) at a constant flow rate; thus, the flow rate in the mixing channel equals twice the flow rate of each single reagent. The measurements were initiated around 2 min after the pump was started so that the pressure conditions inside the flow system could stabilize.

## Results and discussion

Calculating the zero-absorption lines of the water-filled mixers for a spectral resolution of 4  $\text{cm}^{-1}$  and 128 co-added scans per spectrum yielded a root mean square noise level of  $2.1 \times 10^{-4}$  for the spectral range 1,500–1,700  $\text{cm}^{-1}$ , i.e. region of the water's strong deformation vibration absorptions, and of  $1.0 \times 10^{-4}$  for the region 1,900–2,100  $\text{cm}^{-1}$ . With this first step proving the basic spectroscopic suitability of the measurement setup for the intended applications, examining the actual mixing characteristics

of the micro-mixer requires choosing a chemical reaction in which the diffusive process in the mixer is the time-limiting factor. Both acid–base reactions and the proton–deuterium exchange between water and heavy water meet this requirement.

**Temporal mixing characterization** Knowledge of the actual mixing performance of a given mixer is important, as it allows correcting the actual starting point of the chemical reaction under investigation by the delay caused by the mixing process. For the characterization, 0.2 M acetic acid was mixed with 0.1 M sodium hydroxide solution at constant reagent flow rates of 10  $\mu\text{l}/\text{min}$ , with 60 spectra recorded for different positions along the mixing channel. The substances involved in this reaction exhibit four strong absorption bands in the mid-IR region: the asymmetric and symmetric stretch vibrations of the acetate ion at 1,525 and 1,416  $\text{cm}^{-1}$  respectively, the stretching vibration of the carbonyl group at 1,710  $\text{cm}^{-1}$  and a fourth band at 1,280  $\text{cm}^{-1}$  assigned to the C–O stretching vibration of the protonated acid.

Figure 2 shows the integrated areas of the 1,416  $\text{cm}^{-1}$  (acetate) and 1,710  $\text{cm}^{-1}$  (acetic acid) bands plotted against time. Obviously, for the first measurement spot in the mixing channel, roughly two thirds of the equilibrium amount of acetate were already formed. After around 7 ms both liquids have mixed completely, resulting in an equilibrium state in the mixer. Exponential fits applied to both bands yielded time constants of 1.80 ms for the acetate and 1.87 ms for the acetic acid band. Extrapolating the exponential fit for the acetate band towards zero, i.e., the

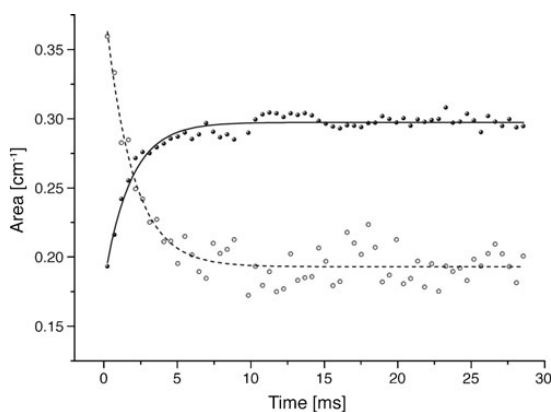


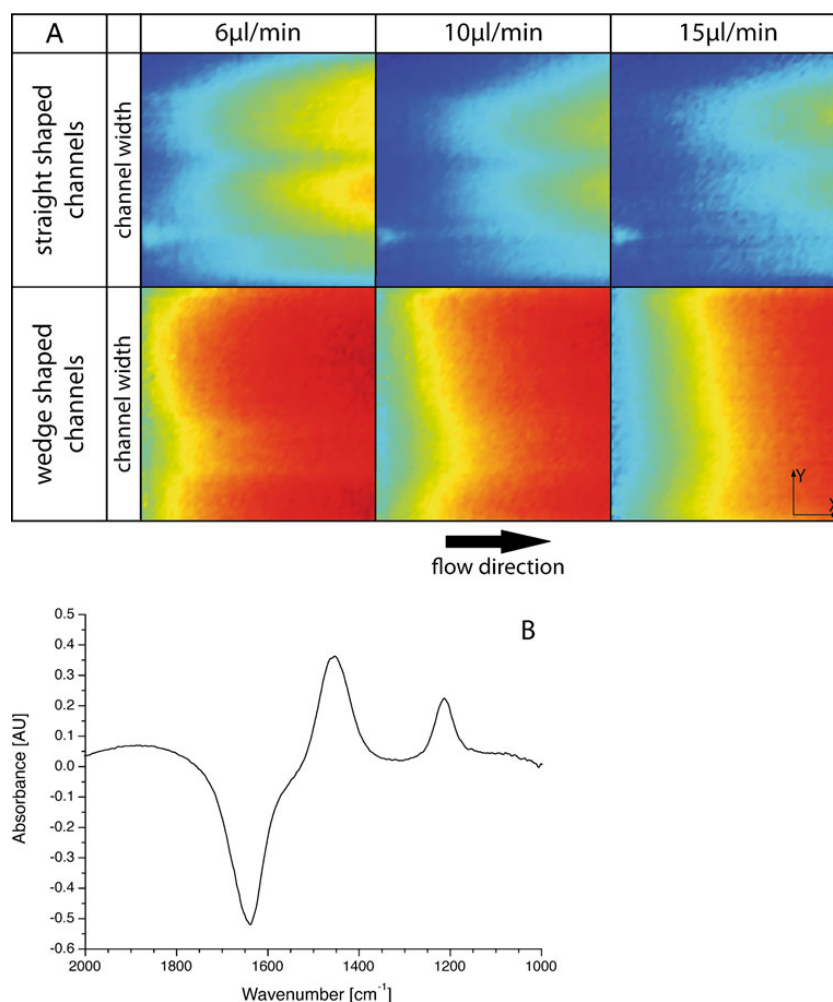
**Fig. 2** Time traces of the rising acetate band at 1,416  $\text{cm}^{-1}$  (black solid spheres) and the falling acetic acid band at 1,710  $\text{cm}^{-1}$  (hollow spheres), recorded at a flow rate of 20  $\mu\text{l}/\text{min}$  in the mixing channel. The black and dashed lines show exponential fits to the data, yielding time constants of 1.8 ms

factual reaction start, and applying a 90% mixing quality criteria yielded a mixing time of about 4 ms. This is in acceptable agreement to the results of corresponding CFD simulations. Using standard thermodynamic and hydrodynamic properties of the liquid (water) at the given temperature (293 K) and setting the binary diffusion coefficient to  $D=2\times 10^{-9}\text{m}^2\text{s}^{-1}$ , which is a typical value for small molecules like  $\text{H}_2\text{O}$  in liquid form [38], the simulations yielded a 90% mixing time of about 1 ms for a channel flow rate of  $20\text{ }\mu\text{L}/\text{min}$ . The deviation between the experimental and the theoretical mixing times could be explained by the difference of the real binary diffusion coefficients of acetic acid and water. Furthermore, the mixing time can only be derived from an extrapolation and the exact reaction speed at

the beginning remains unknown, adding an additional uncertainty factor. The effect will be the objective of further studies.

**Spatial mixing characterization** In a further study, we aimed at confirming CFD simulation results indicating that traditional straight inlet channels yield less effective and homogenous mixing in comparison to wedge-shaped channels. According to the CFD calculation, the overall mixing process of fast reactions should be completed within the first  $200\text{ }\mu\text{m}$  when using a channel flow rate of  $30\text{ }\mu\text{L}/\text{min}$  [39]. These investigations were performed with a  $64\times 64$  focal plane array detector, allowing to simultaneously acquire 4096 IR spectra covering an area of  $170\times 170\text{ }\mu\text{m}^2$ .

**Fig. 3 a** FPA images of HDO formation (integration of the HDO deformation vibration with integration boundaries set to  $1,335\text{--}1,530\text{ cm}^{-1}$ ; blue indicates low and red higher HDO concentrations) recorded at the beginning of the mixing channel for different reagent flow rates (i.e. flow rate per syringe) and micro-mixer designs. **b** Absorption spectrum obtained from one FPA pixel in the center of the channel for a well-advanced reaction state, clearly showing the negative absorption feature of  $\text{H}_2\text{O}$  at  $1,640\text{ cm}^{-1}$  and the positive bands of HDO at  $1,456\text{ cm}^{-1}$  and  $\text{D}_2\text{O}$  at  $1,212\text{ cm}^{-1}$  (measured against water background)



As the noise levels of these FPA pixel spectra are higher than the ones obtainable with a single-element MCT detector in the same experimental setup, the proton exchange reaction induced by mixing D<sub>2</sub>O with H<sub>2</sub>O was chosen as a model system with strong absorption features and fast reaction kinetics.

Different flow rates were applied to both micro-mixer types, i.e., such with straight channels and such with wedge-shaped inlets, to study the stability of the mixing process also for different reagent throughputs. As shown in Fig. 3a for the formation of HDO, reagent flow rates of 6, 10, and 15  $\mu\text{l}/\text{min}$  yield well comparable mixing behaviors. Comparing the distribution of HDO between the straight and the wedge-shaped mixer design furthermore shows that the mixers containing wedge-shaped inlet channels have a significantly more homogenous distribution of the fed liquids across the mixer's width ( $y$ -axis).

Integrating the area under the HDO band for all pixels along the center of the channel in downstream direction and plotting them against time yields the correlations shown in Fig. 4. Again applying exponential fits to the curves obtained for different flow rates, the time constant of the reaction of H<sub>2</sub>O with D<sub>2</sub>O can be derived as consistently 0.45 ms for all investigated flow rates, proving the suitability of the mixer for kinetic measurements at different flow rates.

**Reaction monitoring and kinetics studies** Following the fundamental system characterization, we examined a more complex reaction: the sulfite-formaldehyde acid-to-alkali clock reaction of a 0.2 M sodium sulfite solution with a 0.2 M

formaldehyde solution. Figure 5 illustrates the spectral changes occurring over time for different flow rates. The strong band at  $940\text{ cm}^{-1}$  is a result of the S–O stretching vibration, whereas the band at  $1,027\text{ cm}^{-1}$  is due to the C–O stretching vibration of the methylene glycol form of formaldehyde in water. The product band rising at  $1,180\text{ cm}^{-1}$  results from the antisymmetric stretching vibration of SO<sub>2</sub>, and the split in the band at  $1,027\text{ cm}^{-1}$  is caused by an overlap of the C–O stretching and the symmetric stretching vibration of SO<sub>2</sub>.

In a comparison of different reagent flow rates (4, 5, 6, and 7  $\mu\text{l}/\text{min}$ ), the evolution of the product band at  $1,180\text{ cm}^{-1}$  shows a very similar progress (Fig. 6), proving that the mixing is dominated by diffusion, and also takes place reproducibly at low flow rates. The underlying sigmoidal time dependency, which was never observed in previous studies using slower mixers [37,40], can be related to the complex interacting reaction kinetics of the reaction that are not yet fully elucidated [41]. Comparing our results with results obtained by Kaun et al. using the two-layered mixing design with two 5  $\mu\text{m}$  thick flow sheets, we found an improvement in mixing efficiency by a factor of  $\sim 25$ . This realized improvement is a prerequisite to study this complicated inorganic reaction in more detail, showing for instance the illustrated sigmoid behavior at the reaction start for the first time, and a starting point for future investigations in the field.

**Protein folding studies** Finally, first experiments on protein folding were carried out in the mixer using ubiquitin, the smallest naturally occurring protein. A 6 mM solution of ubiquitin acidified with hydrochloric acid was mixed with acidified methanol (both pH 2). According to Brutscher et al., methanol induces a transition from the ubiquitin's native state to its "A-state", changing the structure of the C-terminal from  $\beta$ -sheet structures to a predominantly  $\alpha$ -helical character [42] and thus causing a shift of the amide I band to higher wavenumbers [13].

As the comparatively high concentration of ubiquitin caused negative water absorptions when referenced to the corresponding water background, a data processing step was required prior to the actual data evaluation. A pure water spectrum was added manually to each ubiquitin spectrum acquired along the time axis to compensate this negative absorption. Afterwards, the spectra were normalized to the amide I band. The following data evaluation of the amide I band position showed a band center position shift from  $1,640$  to  $1,646.7\text{ cm}^{-1}$  within 72 ms, reflecting the change from  $\beta$ -sheet to  $\alpha$ -helical secondary protein structures (Fig. 7). Future work will aim at reducing the presently significantly disturbing effect of changing water vapor interferences in the open beam-path

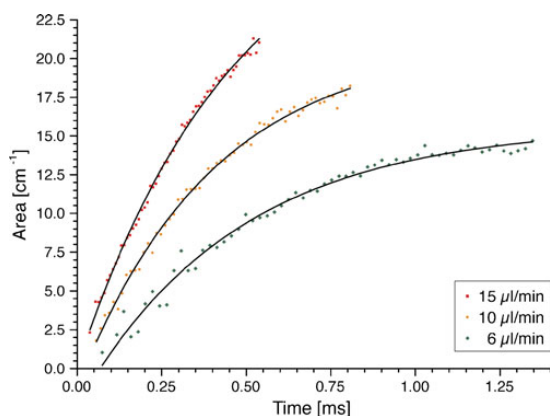
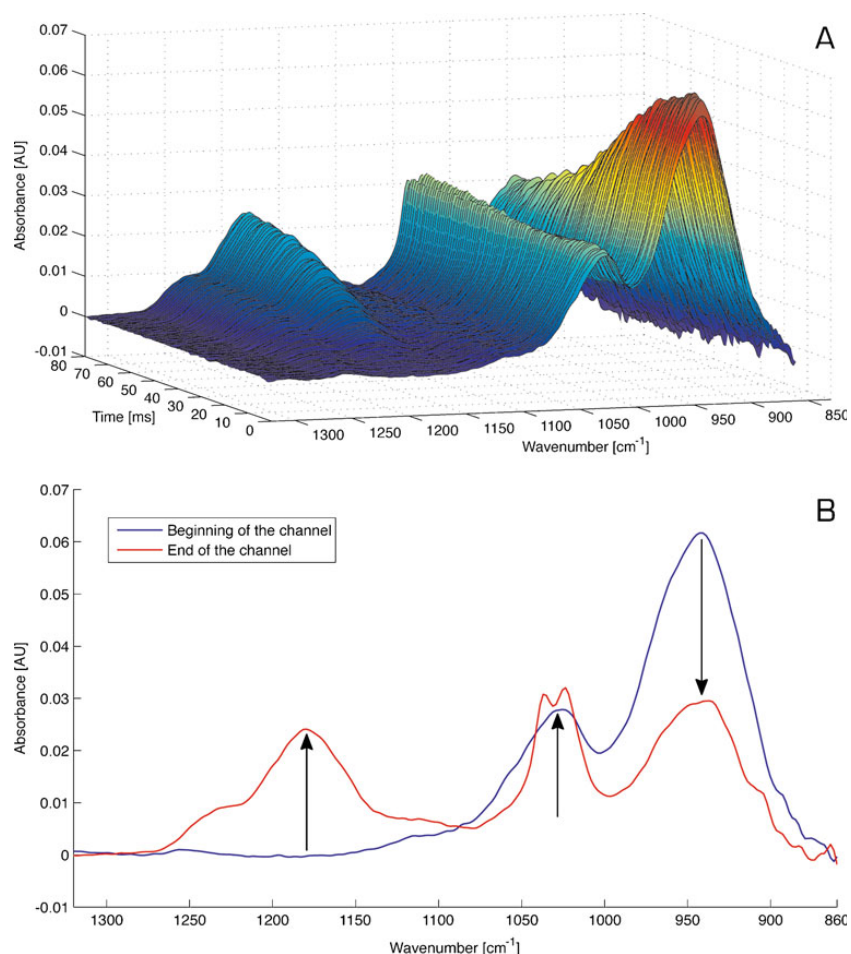


**Fig. 4** Integration of the HDO band along the middle of the mixing channel. Black lines show exponential fits to the data points, yielding a uniform time constant of 0.45 ms that is independent of the reagent flow rate per syringe



**Fig. 5** **a** Time-resolved measurement of the sulfite-formaldehyde clock reaction followed over 80 ms at a channel flow rate of 10  $\mu\text{l}/\text{min}$ . **b** Spectral changes caused by the sulfite-formaldehyde clock reaction; see text for band assignments



experimental setup, allowing to take full advantage of the experimental possibilities offered and conduct, e.g., detailed kinetic analyses of the conformational protein changes.

## Conclusions

With a height of only 8  $\mu\text{m}$  and effective 90% mixing times of 4 ms, the specially designed four-layered laminar micro-mixer investigated in this work has proven its suitability for time-resolved IR measurement of reactions and has clearly outperformed previous two-layered designs with mixing times of typically 45 ms [37]. Vibrational images using a focal plane array detector showed that using wedge-shaped inlet channels indeed significantly improves the mixing homogeneity across the mixing channel in comparison to

previous designs featuring linear structures, a fact that is of particular importance when using the mixer with single-element detectors.

The theoretically predicted mixing times could be experimentally verified using two independent reactions with high-reaction kinetics, the hydrogen–deuterium exchange between water and heavy water and the neutralization reaction of acetic acid with sodium hydroxide. Both verified the range of mixing times to be in the low single-digit ms range, and both showed the expected exponential reaction kinetics. For the much more complex multi-species reaction between formaldehyde and sulfite, entirely different reaction kinetic pattern matching dose response curves were observed for the first 100 ms of the reaction. This data clearly indicate complex, intricate reaction kinetics for this type of clock reaction, which have been recorded in the mid-IR spectral range for the first time.

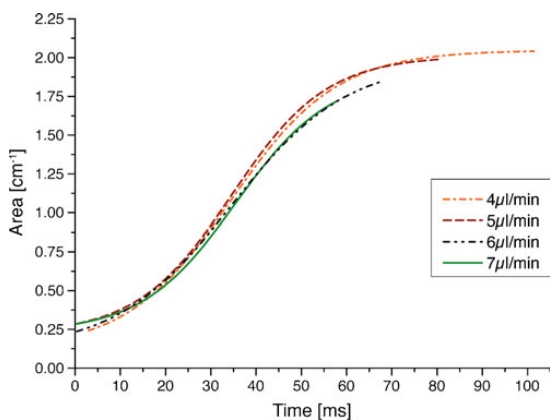
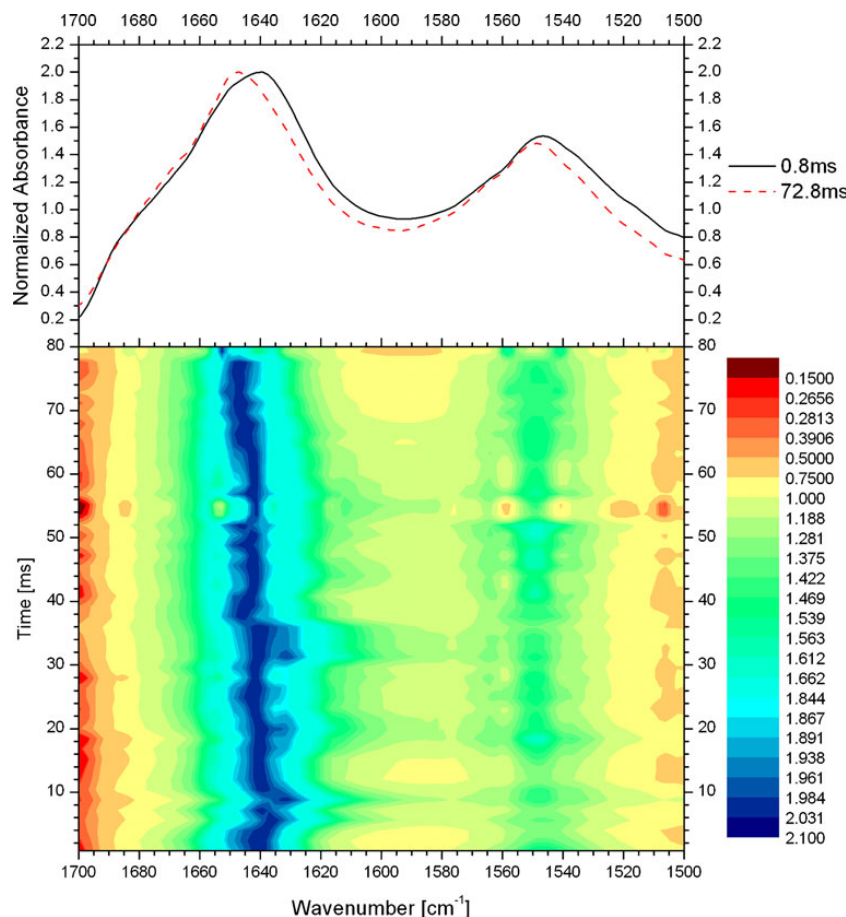


**Fig. 6** Dose response fits for the evolution of the  $1,180\text{ cm}^{-1}$  band during the sulfite-formaldehyde clock reaction, showing that the mixing behavior is quite similar for different flow rates. The stated flow rates denote the reagent flow for each of the two inlet channels; given a 1:1 mixture of the reagents, the corresponding channel flow rate in the mixing channel is twice that number

**Fig. 7** Mixing-induced conformation changes of ubiquitin. Mixing ubiquitin with methanol induces a secondary structure change to the “A-state”; the wavenumber shift of the amide I band to higher wavenumbers reflects the corresponding transition from  $\beta$ -sheet to  $\alpha$ -helical structures



Finally, the low optical path of the developed mixer allowed measuring changes of the amide I band in aqueous solution during conformational changes of a proteins secondary structure. The change of the conformation of an acidified aqueous solution of ubiquitin upon mixing with acidified methanol was successfully recorded, proving that micro-mixers can be a key asset in the elucidation of (bio) chemical reactions using infrared microscopy.

In future works, we plan to continue to improve the robustness and performance of the overall experimental setup. This concerns an improved purge for reducing interference from changing water vapor in the experimental setup. Furthermore, since achieving acceptable signal-to-noise ratios for limited path lengths of  $8\text{ }\mu\text{m}$  poses quite a challenge, strategies to increase the signal-to-noise ratio have to be developed. Current plans in this direction include increasing the light throughput through the mixer by applying antireflection coatings to one side of the Si-wafer. Additionally, we consider replacing the employed FTIR spectrometer by external cavity quantum cascade

lasers. Their meanwhile achieved high spectral power density along with tuning ranges of  $200\text{ cm}^{-1}$  and more makes them very promising light sources to be used in the field of time-resolved IR spectroscopy of chemical reactions in solutions in the near future.

**Acknowledgment** We gratefully acknowledge the financial support by the COMET Competence Centre Program of the Austrian Government. The authors also want to thank Greta Lindermuth and Karin Wieland, who contributed to this paper during their B.Sc. theses.

## References

- Griffiths PR, Hirsche BL, Manning CJ (1999) Ultra-rapid-scanning Fourier transform infrared spectrometry. *Vib Spectrosc* 19(1):165–176
- Kenda A, Kraft M, Wagner C, Lendl B, Wolter A (2008) MEMS-based spectrometric sensor for the measurement of dissolved CO<sub>2</sub>. *Sensors*, 2008 IEEE:724–727
- Kraft M, Kenda A, Frank A, Scherf W, Heberer A, Sandner T, Schenk H, Zimmer F (2006) Single-detector micro-electromechanical scanning grating spectrometer. *Anal Bioanal Chem* 386(5):1259–1266. doi:10.1007/s00216-006-0726-5
- Elmore D, Tsao M, Frisk S, Chase D, Rabolt J (2002) Design and performance of a planar array infrared spectrograph that operates in the 3400 to 2000  $\text{cm}^{-1}$  region. *Appl Spectrosc* 56(2):145–149
- Pellerin C, Snively C, Chase D, Rabolt J (2004) Performance and application of a new planar array infrared spectrograph operating in the mid-infrared (2000–975  $\text{cm}^{-1}$ ) fingerprint region. *Appl Spectrosc* 58(6):639–646
- Reback M, Roske C, Bitterwolf T, Griffiths PR, Manning CJ (2010) Stopped-flow ultra-rapid-scanning fourier transform infrared spectroscopy on the millisecond time scale. *Appl Spectrosc* 64(8):907–911
- Kötting C, Suveyzdis Y, Bojja R, Metzler-Nolte N, Gerwert K (2010) Label-free screening of drug–protein interactions by time-resolved fourier transform infrared spectroscopic assays exemplified by ras interactions. *Appl Spectrosc* 64(9):967–972
- Uhmman W, Becker A, Taran C, Siebert F (1991) Time-resolved FT-IR absorption spectroscopy using a step-scan interferometer. *Appl Spectrosc* 45(3):390–397
- Chen P, Palmer R (1997) Ten-nanosecond step-scan FT-IR absorption difference time-resolved spectroscopy: Applications to excited states of transition metal complexes. *Appl Spectrosc* 51(4):580–583
- Rammelsberg R, Boulas S, Chorongiewski H, Gerwert K (1999) Set-up for time-resolved step-scan FTIR spectroscopy of noncyclic reactions. *Vib Spectrosc* 19:143–149
- Schleeger M, Wagner C, Vellekoop MJ, Lendl B, Heberle J (2009) Time-resolved flow-flash FT-IR difference spectroscopy: the kinetics of CO photodissociation from myoglobin revisited. *Anal Bioanal Chem* 394(7):1869–1877. doi:10.1007/s00216-009-2871-0
- Cheng Q, Steinmetz MG, Jayaraman V (2002) Photolysis of  $\gamma$ -( $\alpha$ -carboxy-2-nitrobenzyl)-L-glutamic acid investigated in the microsecond time scale by time-resolved FTIR. *J Am Chem Soc* 124(26):7676–7677
- Barth A (2007) Infrared spectroscopy of proteins. *Biochimica et Biophysica Acta (BBA)-Bioenergetics* 1767 (9):1073–1101. doi:10.1016/j.bbabi.2007.06.004
- Kaun N, Kulka S, Frank J, Schade U, Vellekoop MJ, Harasek M, Lendl B (2006) Towards biochemical reaction monitoring using FT-IR synchrotron radiation. *Analyst* 131(4):489–494. doi:10.1039/b514102h
- Brody JP, Yager P, Goldstein RE, Austin RH (2005) Biotechnology at low Reynolds numbers. *Biophys J* 71(6):3430–3441. doi:10.1016/S0006-3495(96)79538-3
- Ahmed D, Mao X, Shi J, Juluri BK, Huang TJ (2009) A millisecond micromixer via single-bubble-based acoustic streaming. *Lab Chip* 9(18):2738–2741. doi:10.1039/b903687c
- Williams AM, Griffiths DJ, Vlachos PP (2009) Laminar mixing using oscillating cantilevered ionic polymer actuators. *Sens Actuators A* 153(1):105–113. doi:10.1016/j.sna.2009.04.028
- Johansson L, Johansson S, Nikolajeff F, Thorslund S (2009) Effective mixing of laminar flows at a density interface by an integrated ultrasonic transducer. *Lab Chip* 9(2):297–304. doi:10.1039/b815114h
- Renaudin A, Chabot V, Grondin E, Aimez V, Charette PG (2010) Integrated active mixing and biosensing using surface acoustic waves (SAW) and surface plasmon resonance (SPR) on a common substrate. *Lab Chip* 10(1):111. doi:10.1039/b911953a
- Bau H, Zhong J, Yi M (2001) A minute magneto hydro dynamic (MHD) mixer. *Sens Actuators B* 79(2–3):207–215
- Schwesinger N, Frank T, Wurmus H (1996) A modular microfluid system with an integrated micromixer. *J Micromech Microeng* 6(1):99–102
- Fang W-F, Yang J-T (2009) A novel microreactor with 3D rotating flow to boost fluid reaction and mixing of viscous fluids. *Sens Actuators B Chem* 140(2):629–642. doi:10.1016/j.snb.2009.05.007
- Stroock AD, Dertinger SKW, Ajdari A, Mezić I, Stone HA, Whitesides GM (2002) Chaotic mixer for microchannels. *Science* 295(5555):647–651
- Hessel V, Hardt S, Löwe H, Schönfeld F (2003) Laminar mixing in different interdigital micromixers: I. Experimental characterization. *AIChE J* 49(3):566–577
- Bessoth F, deMello A, Manz A (1999) Microstructure for efficient continuous flow mixing. *Anal Commun* 36(6):213–215
- Kakuta M, Hinsmann P, Manz A, Lendl B (2003) Time-resolved Fourier transform infrared spectrometry using a microfabricated continuous flow mixer: application to protein conformation study using the example of ubiquitin. *Lab Chip* 3(2):82–85. doi:10.1039/b302295a
- Kakuta M, Jayawickrama D, Wolters A, Manz A, Sweedler J (2003) Micromixer-based time-resolved NMR: applications to ubiquitin protein conformation. *Anal Chem* 75(4):956–960. doi:10.1021/ac026076q
- Knight JB, Vishwanath A, Brody JP, Austin RH (1998) Hydrodynamic focusing on a silicon chip: mixing nanoliters in microseconds. *Phys Rev Lett* 80(17):3863–3866
- Hertzog D, Michalet X, Jager M, Kong X, Santiago J, Weiss S, Bakajin O (2004) Femtomole mixer for microsecond kinetic studies of protein folding. *Anal Chem* 76(24):7169–7178. doi:10.1021/ac048661s
- Hinsmann P, Frank J, Svasek P, Harasek M, Lendl B (2001) Design, simulation and application of a new micromixing device for time resolved infrared spectroscopy of chemical reactions in solution. *Lab Chip* 1(1):16–21. doi:10.1039/b104391a
- Kaun N, Vellekoop MJ, Lendl B (2006) Time-resolved fourier transform infrared spectroscopy of chemical reactions in solution using a focal plane array detector. *Appl Spec* 60(11):1273–1278
- Kauffmann E, Darnton N, Austin R, Batt C, Gerwert K (2001) Lifetimes of intermediates in the sheet to-helix transition of lactoglobulin by using a diffusional IR mixer. *PNAS* 98(12):6646–6649
- Rigler A, Wagner C, Svasek P, Jachimowicz A, Hudek P, Kraft M, Vellekoop MJ (2008) Improved lamination micromixer with



- wedge shaped inlet channels for IR spectroscopy. In: Proceedings EUROSENSORS XXII:187–190
34. Buchegger W, Wagner C, Kraft M, Lendl B, Vellekoop M A (2010) Highly uniform lamination micromixer with wedge shaped inlet channels for time resolved infrared spectroscopy. Microfluid Nanofluid (available online) doi:[10.1007/s10404-010-0722-0](https://doi.org/10.1007/s10404-010-0722-0)
35. Rini M, Pines D, Magnes B, Pines E, Nibbering E (2004) Bimodal proton transfer in acid-base reactions in water. J Chem Phys 121 (19):9593–9610. doi:[10.1063/1.1804172](https://doi.org/10.1063/1.1804172)
36. Cox MJ, Timmer RLA, Bakker HJ, Park S, Agmon N (2009) Distance-dependent proton transfer along water wires connecting acid-base pairs. J Phys Chem A 113(24):6599–6606
37. Kaun N, Vellekoop MJ, Lendl B (2006) Time-resolved fourier transform infrared spectroscopy of chemical reactions in solution using a focal plane array detector. Appl Spectrosc 60(11):1273–1278
38. Mills R (1973) Self-Diffusion in normal and heavy water in the range 1–45 °C. J Phys Chem Us 77(5):685–688
39. Buchegger W, Kraft M, Vellekoop MJ (2010) Characterization of a vertical lamination micromixer for IR spectroscopy. Procedia Engineering 5 (C):1348–1351. doi: [10.1016/j.proeng.2010.09.364](https://doi.org/10.1016/j.proeng.2010.09.364)
40. Hinsmann P, Haberkorn M, Frank J, Svasek P, Harasek M, Lendl B (2001) Time-resolved FT-IR spectroscopy of chemical reactions in solution by fast diffusion-based mixing in a micromachined flow cell. Appl Spectrosc 55(3):241–251
41. Kovacs K, McIlwaine R, Gannon K, Taylor A, Scott S (2005) Complex behavior in the formaldehyde-sulfite reaction. J Phys Chem A 109(1):283–288
42. Brutscher B, Bruschweiler R, Ernst R (1997) Backbone dynamics and structural characterization of the partially folded A state of ubiquitin by H-1, C-13, and N-15 nuclear magnetic resonance spectroscopy. Biochemistry 36(42):13043–13053



# List of available clients for ATLAS

---

AC: Self-developed 230 VAC power socket.

The AC-Client can switch a power socket and is connected to the PC via a RS-232-port.

BC: Self-developed Boxcar-Integrator.

This client reads the data, whereas the gating- and trigger-delay have to be set manually at the device.

BP: Beep client.

If the ATLAS server has to alert the user, the BP client can be used. It produces an audible tone with a certain frequency for 100 ms and is already included in the ATLAS server.

CA: Syringe pumps by Cavo Scientific Instruments (Sunnyvale, CA, USA).

Liquids can be aspirated and dispensed from two liquid connections at different speeds. The ramping up and down to the programmed speed can also be programmed.

DB: A digital board from TVE Elektronische Systeme GmbH (Vienna, Austria)

This board is a combination of a 16-bit-AD converter for a thermoelectrical cooled infrared detector. The integrated CPU supports features such as trigger delay, internal averaging and base line correction and is connected to the PC via USB.

DI: Micro dispenser from Picology AB (Sweden).

The piezo-element of the dispenser is controlled by burst signals from an Agilent 33120A function generator. The size of the dispensed drops and the number of drops per second can be adjusted.

DL: External cavity quantum cascade laser from Daylight Solutions Inc. (CA, USA).

The wavenumber and the intensity of the emitted light can be set among other laser parameters. The DL client also supports a scanning mode, where the emission wavenumber of the laser is tuned automatically.

GI: The Miniplus 3 peristaltic pump from Gilson Inc. (Middleton, WI, USA). The speed as well as the pumping direction can be controlled.

HV: CZE 1000R high voltage supply from Spellman (NY, USA).

It is supported via an DAC module from National Instruments. The output voltage of the module is transformed into high voltage output (10 V equal 30 kV).

LC: Waverunner 64-Xi oscilloscope from LeCroy Corp. (NY, USA).

Only the most important features such as setting V/div, timebase and trigger-parameters are implemented. Single pulses can be read and stored.

OP: FTIR spectrometers from Bruker Optik GmbH (Ettlingen, Germany).

This client connects to OPUS over a DDE connection and can trigger measurements utilizing predefined experiment files. Single and repeated measurements are supported.

TE: TDS 220 oscilloscope by Tektronix (OR, USA).

Only the most important features such as setting V/div, timebase and trigger-parameters are implemented. Single pulses can be read and stored.

UV: Capillary UV-Detector from Dionex (Sunnyvale, CA, USA).

The client allows to set four wavelengths for absorption measurements. It can autozero the absorbance values and record the absorbance over time.

VI: Valves from Vici AG (Switzerland).

Injection and selection valves are supported by this client.

WA: Wait client

The wait client allows a delay of the execution of the next command by a defined time period. It is also included in the ATLAS server as for the BP client.

XY: Custom-built XY stage.

The XY stage is operated by a Trinamic TMC610 stepper motor control, which is controlled by the XY client. This client allows the user to move the stage for a certain distance by a predefined speed.



APPENDIX C

# Curriculum Vitae

---





# Christoph Wagner

Vienna, 17. August 2012

Dammstrasse 21/46  
1200 Vienna, Austria  
+43 699 19994335  
christoph@freizeitgeek.net  
www.freizeitgeek.net

---

## Personal Information

Born 31. January 1981, Vienna, Austria  
Nationality Austria  
Marital Status engaged  
Military Service fulfilled

---

## Academic Education

### PhD “Technical Chemistry”

Since 10/2007 at the Vienna University of Technology

Title *Application of microfluidic devices for time resolved FTIR spectroscopy*

Supervisor Dr. techn. Bernhard Lendl

### Master “Technical Chemistry”

10/2000 - 6/2007 at the Vienna University of Technology, *graduated with distinct*

23/May/2007 Masterthesis

Title *Entwicklung eines IR Sensors für Erdgas*

Supervisor Dr. techn. Bernhard Lendl

2006 Merit Scholarship

---

## Education

9/1991 - 6/1999 Bundesrealgymnasium “Wasagasse” - 1090 Wien

9/1987 - 6/1991 Volksschule - 1180 Wien

---

## Work Experience

Since 9/2010 Project Manager MP1 Project of the PAC K-Project (FFG)

Since 3/2007 “Projektassistent” Vienna University of Technology

2003 & 2004 Webdesign Freelancer

---

## Internships

2001 & 2002 OMV, Analysis of Petrochemical Products

2001 AGES, Analysis of pesticide residues

---

## Advanced Training

2009 Laser Safety Training according to ÖNORM S 1100

2009 Advanced Study Course on Optical Chemical Sensors and Biosensors, Madrid, Spanien

- 2007 CAMO Workshop “Multivariate analysis spectroscopic data”, Innsbruck, Austria
- 2000 6 weeks English course at the “EF International School of English”, Northridge, USA

## Language Skills

- German mother tongue
- English fluent in writing and speaking
- French basic knowledge

## Software Kenntnisse

- OS Windows, Mac OS X, Linux
- Office Microsoft Office, L<sup>A</sup>T<sub>E</sub>X
- Data Analysis OPUS, Matlab, Unscrambler, Origin, LabVIEW
- Graphics Adobe Photoshop, Adobe Illustrator, Corel Draw
- Webdesign PHP, MySQL, HTML, CSS

## Interests

- Photography, Geocaching
- Cycling, Badminton, Skiing, Hiking

## Academic Dissemination

### Journal Publications

11. A. Limbeck, **C. Wagner**, B. Lendl, A. Mukhtar. *Determination of water soluble trace metals in airborne particulate matter using a dynamic extraction procedure with on-line inductively coupled plasma optical emission spectrometric detection*. Analytica Chimica Acta (2012) accepted for publication
10. G. Steinhauser, G. Giester, **C. Wagner**, P. Weinberger, B. Zachhuber, G. Ramer, M. Villa, B. Lendl. *Nitrogen-rich compounds of the actinoids: dioxouranium(VI) 5,5'-azobis[tetrazolide] pentahydrate and its exceptionally small uranyl angle*. Inorganic Chemistry 51 (12), 6739-6745 (2012)
9. D. Lumpi, **C. Wagner**, M. Schöpf, E. Horkel, G. Ramer, B. Lendl, J. Fröhlich. *Fibre optic ATR-IR spectroscopy at cryogenic temperatures: in-line reaction monitoring on organolithium compounds*. Chemical Communications 48, 2451-2453 (2012)
8. W. Buchegger, **C. Wagner**, P. Svasek, B. Lendl, M. Kraft, M.J. Vellekoop. *Fabrication and characterization of a vertical lamination micromixer for mid-IR spectroscopy*. Sensors and Actuators B: Chemical 159 (1), 336-341 (2011)
7. W. Buchegger, **C. Wagner**, B. Lendl, M. Kraft, M.J. Vellekoop. *A highly uniform lamination micromixer with wedge shaped inlet channels for time resolved infrared spectroscopy*. Microfluidics And Nanofluidics 10 (4), 889-897 (2011).

6. **C. Wagner**, W. Buchegger, M.J. Vellekoop, M. Kraft, B. Lendl. *Time-resolved mid-IR spectroscopy of (bio)chemical reactions in solution utilizing a new generation of continuous-flow micromixers*. Analytical and Bioanalytical Chemistry 400 (8), 2487-2497 (2011)
5. **C. Wagner**, S. Armenta, B. Lendl. *Developing automated analytical methods for scientific environments using LabVIEW*. Talanta 80 (3), 1081-1087 (2010)
4. G. Steinhauser, G. Giester, N. Leopold, **C. Wagner**, M. Villa, A. Musilek. *Nitrogen-Rich Compounds of the Lanthanoids: Highlights and Summary*. Helvetica Chimica Acta 93 (2), 183-202 (2010)
3. M. Schleege, **C. Wagner**, M. Vellekoop, B. Lendl, J. Heberle. *Time-Resolved Flow-Flash FT-IR Difference Spectroscopy: The Kinetics of CO-Photodissociation from Myoglobin Revisited*. Analytical and Bioanalytical Chemistry 394 (7), 1869-1877 (2009)
2. G. Steinhauser, G. Giester, N. Leopold, **C. Wagner**, M. Villa. *Nitrogen-Rich Compounds of the Lanthanoids: the 5,5'-Azotetrazolates of the Light Rare Earths (Ce, Pr, Nd, Sm, Eu, Gd)*. Helvetica Chimica Acta 92 (10), 2038-2051 (2009)
1. G. Steinhauser, G. Giester, **C. Wagner**, N. Leopold, J.H. Sterba, B. Lendl, M. Bichler. *Nitrogen-Rich Salts of the Lanthanoids: the 5,5'-Azotetrazolates of some Yttrium Earths (Tb, Dy, Ho, Er, Tm, Yb, Lu)*. Helvetica Chimica Acta 92 (7), 1371-1384 (2009)

#### Book Chapters

1. **C. Wagner**, A. Genner, G. Ramer, and B. Lendl. *Advanced Total Lab Automation System (ATLAS)*. in LabVIEW - Modeling, Programming and Simulations, (INTECH), 3-20, (2011), ISBN: 978-953-307-521-1

#### Proceedings

3. A. Kenda, M. Kraft, A. Tortschanoff, **C. Wagner**, B. Lendl, T. Sandner, H. Schenk. *Miniaturized MEMS-based spectrometric sensor for process control and analysis of carbonated beverages*. Proceedings of SPIE 7594 (2010)
2. A. Kenda, M. Kraft, **C. Wagner**, B. Lendl, A. Wolter. *MEMS-based Spectrometric Sensor for the Measurement of Dissolved CO<sub>2</sub>*. Proceedings IEEE Sensors, 724-727, (2008)
1. A. Rigler, **C. Wagner**, P. Svasek, A. Jachimowicz, P. Hudek, M. Kraft, J. Vellekoop. *Improved Lamination Micromixer With Wedge Shaped Inlet Channels For IR Spectroscopy*. Proceedings EUROSENSORS XXII, (2008), ISBN: 978-3-00-025217-4

#### Conference Contributions

- 2010 FACSS 2010, Raleigh, USA  
 Poster: *Time resolved Fourier transform infrared (TR-FTIR) studies employing micro fluidic mixers*

- 2009 IRDG Christmas Meeting, London, Great Britain  
 Poster: *Reaction induced protein folding in a four layer lamination mixing device*
- 2009 Euroanalysis 2009, Innsbruck, Österreich  
 Poster: *Micro Mixers used for light induced time-resolved Flow-Flash experiments on proteins* **2<sup>nd</sup> Place Poster Award**  
 Poster: *Time resolved FTIR spectroscopy using a four-layer lamination micro mixing device*
- 2009 ICAVS 5, Melbourne, Australia, **ASAG Mobility Scholarship**  
 Poster: *Evaluation of a four-layer lamination micro mixer used for time resolved FTIR spectroscopy on the low ms time scale*  
 Poster: *Light induced time resolved Flow-Flash FTIR investigation in micro mixing cells*
- 2007 IRDG Christmas Meeting, London, Great Britain  
 Poster: *Development of an IR-MEMS Sensor for aqueous CO<sub>2</sub> in Beverages*
- 2007 ICAVS 4, Corfu, Greece  
 Development of an IR-based Sensor for Natural Gas